

# Development and optimisation of advanced auxiliary ion heating schemes for 3D fusion plasma devices

Thèse N°9167

Présentée le 1<sup>er</sup> février 2019  
à la Faculté des sciences de base  
SPC - Théorie  
Programme doctoral en physique

pour l'obtention du grade de Docteur ès Sciences

par

**HAMISH WILLIAM PATTEN**

Acceptée sur proposition du jury  
Prof. S. Manley, présidente du jury  
Dr J. Graves, directeur de thèse  
Dr E. Lerche, rapporteur  
Dr J. Geiger, rapporteur  
Dr S. Coda, rapporteur

2019



Dedicated to my family: Mum, Dad, Jonny, Rory, Harry and Ali.  
You shaped the person I am, and so are all to blame.

*“Regarding life,  
the wisest men of all ages have judged alike:  
it is worthless.”*

- Friedrich Nietzsche -

# Abstract

The magnetic confinement fusion devices known as the tokamak and the stellarator are progressing towards becoming viable commercial nuclear fusion reactor designs. Both approaches require improvements in the applied heating sources and in the particle and energy confinement in order to become power efficient and cost effective. A better understanding of the physics associated to the different heating techniques is required to optimise performance. Ion Cyclotron Range-of-Frequency (ICRF) waves and Neutral Beam Injection (NBI) are two auxiliary fast-ion heating methods that are commonly used in tokamak and stellarator fusion devices. This thesis is relevant to research in preparation for the large fusion projects being developed at present. The largest tokamak in the world, ITER, is currently being built in Cadarache, France, and the largest stellarator project, Wendelstein 7-X (W7-X), started operation in 2015. For the latter, NBI operation will start in 2018, and ICRF experiments are foreseen in 2020. The heating scenarios to be applied experimentally in both of these machines are currently being developed. This requires the development of an understanding of how the heating methods work, proposals to be made for optimisation, and theoretical and numerical predictions to be made in advance. A known issue for stellarator devices is the relatively poor confinement of energetic particles. This is an issue for the auxiliary power efficiency of the device. Fusion reactions produce alpha particles of large energies ( $\sim 3.6\text{MeV}$ ) that should be well confined and collide with the background plasma such that the plasma becomes self-heating. This reduces the requirements on the external heating sources to maintain ideal fusion conditions, assuming these fusion alphas are themselves confined. The work presented in this thesis uses the SCENIC code package to calculate the heating performance and energetic particle production and confinement of a range of basic and advanced heating scenarios involving ICRF and NBI. The SCENIC code self-consistently calculates the magnetic equilibrium, the RF-wave propagation and absorption, the neutral beam injection ionisation and deposition, and evaluates the energetic particle distribution function evolution in the presence of the applied heating scheme. The main results of this thesis indicate that for the Wendelstein 7-X stellarator, both the 3-ion species and the synergetic RF-NBI Doppler shifted resonance heating schemes, developed in this thesis, generate highly energetic ion populations. However, the 3-ion species scheme is shown to not be ideal for energetic particle experiments for multiple reasons. The results for this heating scheme are very sensitive to the magnetic equilibrium. In particular, it is found that the standard mirror equilibrium produces and confines only up to  $0.15\text{MeV}$  ions. Moreover, the densities of such fast ion populations are



---

low, such that experimental detection from probes such as Fast Ion Loss Detectors (FILD) is not feasible. The 3-ion species scheme is only capable of producing particles that are deeply trapped with a strong peaking in the pitch angle at  $\lambda = v_{\parallel} / v = 0$ . Typically, such particles have worse confinement in the 3D equilibrium. With respect to the heating transferred to the core background plasma and the generation of highly energetic particles, the most successful heating scheme applied to W7-X is the synergetic RF-NBI doppler shifted resonance heating scheme, developed for the first time in W7-X in this thesis. Large densities of MeV-range ions are produced isotropically in pitch-angle space. The results are also less sensitive to the magnetic equilibrium than pure RF schemes.

Keywords: Magnetic confinement fusion, plasma, tokamak, stellarator, Ion Cyclotron Range-of-Frequency, Neutral Beam Injection, fast ion confinement, minority species scenario, harmonic scenario, 3-ion species scenario, RF-NBI synergetic scenario.

# Résumé

Les machines à confinement magnétique que sont le tokamak et le stellarator sont en phase de démontrer leur viabilité en tant que reacteurs nucléaires. Chacune des deux approches exige l'amélioration du confinement de l'énergie et des particules ainsi que celle des méthodes de chauffage afin d'améliorer à la fois le rendement et le coût énergétique. Un progrès dans la recherche est nécessaire à la compréhension du fonctionnement des méthodes de chauffage, et à leur optimisation. L'utilisation d'ondes radio à la Fréquence Cyclotronique Ionique (ICRF) et l'Injection de Faisceau de Neutre (NBI) sont deux méthodes de chauffage auxiliaire des ions rapides couramment utilisées dans les tokamaks et les stellarators. L'importance du travail effectué au cours de cette thèse est fortement liée à la recherche en cours pour les plus grands projets de fusion à confinement magnétique. Le tokamak ITER est le plus grand tokamak du monde en cours de construction à Cadarache, en France. Le stellarator Wendelstein 7-X (W7-X) quant à lui est fonctionnel depuis 2015. A W7-X, les expériences impliquant l'utilisation du NBI ont commencées en 2018 et des expériences utilisant l'ICRF sont prévues pour 2020.

La conception des scénarios de chauffage pour les expériences futures est en cours de réalisation. Une connaissance profonde du fonctionnement de chaque méthode, de son optimisation, ainsi que la connaissance au préalable des prédictions théoriques et numériques sont nécessaires. Qui plus est, un enjeu bien connu des stellarators est le confinement des particules rapides. C'est un problème qui concerne directement le rendement énergétique du réacteur. Les réactions nucléaires produisent des particules alpha avec de très grands niveaux d'énergie ( $\sim 3.6\text{MeV}$ ). Un bon confinement de ces particules permet leur collision avec le plasma de fond et la transmission de leur énergie, rendant le système plus autonome énergétiquement. Cette phase d'opération que l'on appelle "ignition" réduit les exigences des méthodes de chauffage auxiliaires tout en présentant les meilleures conditions d'existence des réactions de fusion nucléaire.

Dans cette thèse, le code SCENIC est utilisé pour calculer la performance et la production de particules énergétiques pour une gamme de scénarios de chauffage basiques et avancés impliquant le NBI et le ICRF. Le code SCENIC calcule de manière autonome l'équilibre des surfaces de flux, la propagation et l'absorption des ondes de fréquence radio, l'ionisation et la déposition du faisceau de neutres et l'évolution de la fonction de distribution des ions énergétiques en présence de chauffages auxiliaires. Les résultats montrent aussi que le scénario à trois ions ne sera pas idéal pour les raisons suivantes : les résultats pour ce scénario sont très sensibles à l'équilibre magnétique. En particulier, l'équilibre standard prévu ne produira

---

que très peu d'ions rapides et avec des énergies de seulement 0.15 MeV. De plus, les densités des populations des ions rapides seront très faibles, à tel point que leur détection des sondes de type FILD n'est pas envisageable. Le scénario à trois ions n'aura la capacité que de produire des particules qui sont profondément piégées avec un angle d'incidence maximum de  $\lambda = v_{\parallel} / v = 0$ . Les résultats principaux de cette thèse indiquent que pour le stellarator W7-X, le scénario RF-NBI synergique à résonance à décalage Doppler produit les plus grandes populations d'ions énergétiques. En ce qui concerne le chauffage transmis au cœur du plasma et la génération d'ions rapides, la scénario qui a connu le plus de succès à W7-X dans les simulations calculées est la scénario RF-NBI synergique à résonance à décalage Doppler. De grandes densités d'ions de la gamme du MeV d'énergie est produite de manière isotropique dans l'espace de phase des angles d'incidence. Les résultats obtenus pour ce scénario seront aussi moins sensibles à l'équilibre magnétique que les scénarios purement RF.

Mots clefs : fusion par confinement magnétique, plasma, tokamak, stellarator, fréquence cyclotronique ionique, injection de faisceau de neutre, confinement des ions rapide, scénario minoritaire, scénario trois ions, scénario harmonique, scénario RF-NBI synergique à résonance à décalage Doppler.



# Acronyms

**FLR:** Finite Larmor Radius

**FOW:** Finite Orbit Width

**HFS:** High Field Side

**ICRF:** Ion Cyclotron Range of Frequency

**ITER:** International Thermonuclear Experimental Reactor

**JET:** Joint European Torus

**LCFS:** Last Closed Flux Surface

**LFS:** Low Field Side

**MCF:** Magnetic Confinement Fusion

**MHD:** Magneto-HydroDynamic

**NBI:** Neutral Beam Injection

**PIC:** Particle-In-Cell

**PINI:** Positive Ion Neutral Injector

**QLO:** Quasi-Linear Operator

**W7-X:** Wendelstein 7-X



# Contents

<b>Abstract (English/Français)</b>	<b>iv</b>
<b>Acronyms</b>	<b>ix</b>
<b>Acronyms</b>	<b>ix</b>
<b>1 Introduction</b>	<b>1</b>
1.1 Fusion Devices . . . . .	2
1.2 Tokamaks . . . . .	3
1.3 Stellarators . . . . .	4
1.4 Thesis Contribution . . . . .	5
1.5 Outline . . . . .	6
<b>2 Equilibria, Waves and Fast Ions: the SCENIC Code Package</b>	<b>9</b>
2.1 Magneto-HydroDynamic Equilibria and Anisotropic VMEC . . . . .	9
2.1.1 Calculating Ideal MHD Equilibria: ANIMEC . . . . .	10
2.1.2 2D Stellarator Symmetry and 3D Equilibria . . . . .	11
2.1.3 W7-X Equilibria . . . . .	12
2.2 RF-Wave Propagation and LEMan . . . . .	16
2.2.1 Fast and Slow Wave Cut-offs and Resonances . . . . .	16
2.2.2 RF-Resonant Surface . . . . .	18
2.2.3 Polarisation . . . . .	22
2.2.4 Simulating RF-propagation: LEMan . . . . .	23
2.3 NBI injection and the VENUS-NBI Module . . . . .	24
2.3.1 Cross Sections . . . . .	24
2.3.2 Important NBI Parameters . . . . .	26
	xi

## Contents

---

2.4	Fast Ion Orbits, Drifts and VENUS-LEVIS . . . . .	28
2.4.1	Orbit Types in Tokamaks . . . . .	29
2.4.2	Radial Electric Field in W7-X . . . . .	30
2.4.3	Collisionality . . . . .	32
2.4.4	Wave-Particle Interaction : Quasi-Linear Operator . . . . .	33
2.5	The Self-Consistent Iterative Method . . . . .	36
2.6	Summary . . . . .	38
<b>3</b>	<b>Numerical Advancements and Application for ICRF Optimisation</b>	<b>41</b>
3.1	Updating the LEMan Dielectric tensor to Include Higher Order (Hot Plasma) Effects . . . . .	41
3.1.1	Comparison of full and second order Dielectric Tensors . . . . .	48
3.1.2	$k_{\perp}$ and the Full-Hot Plasma Dispersion Relation . . . . .	50
3.2	Generalised Magnetic Coordinate Systems in LEMan . . . . .	54
3.3	N-Species . . . . .	55
3.4	Benchmarking . . . . .	55
3.4.1	Up-Down Asymmetric Magnetic Equilibrium . . . . .	58
3.4.2	RF-Power Absorption in Minority Species Heating Scenarios . . . . .	60
3.5	RF-Antenna . . . . .	61
3.5.1	In Tokamak Geometries . . . . .	61
3.5.2	In Stellarator Geometries . . . . .	64
3.6	Minority Species Heating . . . . .	66
3.6.1	JET . . . . .	66
3.6.2	W7-X . . . . .	92
3.6.3	RF in the Presence of Helical Cores . . . . .	99
3.7	Summary . . . . .	103
<b>4</b>	<b>Numerical Advancements and Applications for NBI</b>	<b>107</b>
4.1	Simulating NBI heating . . . . .	107
4.1.1	Equal Marker Weighting . . . . .	107
4.1.2	Voxelisation Method . . . . .	108
4.1.3	Benchmarking . . . . .	109



4.2	W7-X . . . . .	111
4.2.1	NBI Ionisation . . . . .	112
4.2.2	NBI Losses . . . . .	114
4.2.3	Slowing Down Distribution . . . . .	116
4.3	Summary . . . . .	124
<b>5</b>	<b>Advanced Heating Schemes</b>	<b>127</b>
5.1	3-Ion Species Heating Scheme . . . . .	127
5.1.1	W7-X . . . . .	128
5.2	RF-NBI Synergetic heating Scheme . . . . .	138
5.2.1	Numerical Methods . . . . .	140
5.2.2	JET Shot 91256 . . . . .	143
5.2.3	W7-X . . . . .	147
5.3	Summary . . . . .	171
<b>6</b>	<b>Conclusion and Outlook</b>	<b>173</b>
6.1	Outlook . . . . .	175
	<b>Acknowledgements</b>	<b>177</b>
	<b>Bibliography</b>	<b>182</b>
	<b>Curriculum Vitae</b>	<b>183</b>



# 1 Introduction

The potential for an energy crisis to occur in the future is becoming increasingly more apparent in society, a problem for which the solution heavily depends on scientific solutions. At present, commercialised sustainable energy sources are at best unreliable, and despite the exceptional improvement in technology, windfarms, for example, will unfortunately never be able to generate electricity when there is no wind. The issues with radioactive fission products and general fission powerplant safety imply that current commercial fission reactors are unlikely to replace the energy demand. Additionally, battery technology cannot keep up with the demand to store the energy from solar, wind, and other natural energy farms. Batteries themselves have a finite lifetime, and have an environmental impact, as do the electronics on which storage systems depend. Fossil fuels may be contributing to accelerated global temperatures. Therefore, there exists a place in the energy market for some new ideas. The new idea that will be explored in this study is far from new. In fact, pilot reactors were designed after the second world war.

Nuclear fusion is what powers a star. In fission reactors, heavy elements like uranium are split into two elements, and this process releases energy according to Einstein's equation  $E = mc^2$ . The energy comes from something called the 'binding energy' of the element. The larger the element is beyond iron, the more energy is released from the fission reaction. Fusion works inversely to this. Small elements such as hydrogen combine together to form the heavier element helium, releasing energy. One fusion reaction with two hydrogen ions releases roughly six times more energy than the fission splitting of one uranium ion. Nuclear fusion in the sun occurs rather simply: the enormous mass holds the 'reactor' together simply via gravity. On earth, we unfortunately do not have the luxury of a confining localised gravitational field. The approach described in this thesis is called Magnetic Confinement Fusion (MCF). This involves using powerful magnets to ensure good confinement of the fuel inside the reactor. This can only be achieved if the fuel is hot enough that the state of matter of the fuel is a plasma.

Plasma is a state of matter aside from solid, liquid and gas. State transitions of materials occur when a certain amount of heat is applied (ice melts as it warms to room temperature). A plasma can be achieved if a gas is heated up such that particles begin to ionise. Above certain

## Chapter 1. Introduction

---

temperatures, electrons will cease to be bound to its corresponding ion and will freely move around in its surrounding environment. This ‘soup’ of electrically charged particles will therefore respond to electric and magnetic fields, and they collectively produce electromagnetic fields. A more rigorous definition of a plasma is as follows:

- The ionised gas obeys quasi-neutrality: on scales larger than the Debye length  $\lambda_D^2 \simeq en_e/\epsilon_0 k_B T_e$  ( $n_e$  and  $T_e$  the electron density and temperature respectively), the plasma obeys  $n_e \simeq \sum_\alpha Z_\alpha n_\alpha$ . The quasi-neutral system size must therefore be considerably larger than the Debye volume such that  $(4/3\pi\lambda_D^3 \ll V)$ . On scales the size of the Debye volume, particles are free to move around.
- The ionised gas is sufficiently dense: many particles are required inside a Debye volume such that charged particle screening occurs.
- Collisions between neutrals and ions must be infrequent, such that the charged particles in the system do not neutralise over the timescale of some characteristic frequency of interest (e.g. a wave or plasma oscillation).

Producing a fusion-relevant plasma requires high temperatures, densities and plasma energy confinement time. In order for the system to self-sustain the fusion processes, the Lawson criterion must be met:

$$nT\tau > 3 \times 10^{21} \text{ keVs/m}^{-3}, \quad (1.0.1)$$

with  $\tau$  the energy confinement time. An ideal steady-state nuclear fusion reactor would ideally approach or exceed this value. To do so would require: good particle and energy confinement, as well as efficient heating sources capable of delivering high power over sustained periods. When two hydrogen isotopes fuse, an alpha particle (a helium nucleus) is produced with high energies ( $\sim 3.6$  MeV). Collisions with the background plasma result in a transfer of energy from the alpha population, heating the plasma. Confinement of these fusion-born alpha particles over long enough timescales results in a more efficient reactor. The two main approaches towards a commercially viable nuclear fusion reactor are currently the tokamak and the stellarator.

### 1.1 Fusion Devices

Using magnetic fields, charged particles can be confined based on the property that a particle will gyrate around a magnetic field line, and travel freely along it. The basic concept of modern magnetic confinement fusion devices is to use closed magnetic field lines where the plasma can move along without interacting with the reactor wall. The poloidal and toroidal directions of the magnetic field lines are illustrated in figure 1.1. Unfortunately, highly energetic charged particles in curved magnetic geometries tend to drift in directions normal to the field lines. The application of the basic equations of plasma physics indicate that if the magnetic field does not have a poloidal component, then the plasma confinement is severely degraded. This

poloidal component creates a field line pitch, such that a field line will rotate infinitely many times around the device in both the poloidal and toroidal angles. The tokamak and stellarator, shown in figure 1.2, have two different approaches to generating this poloidal magnetic field component.

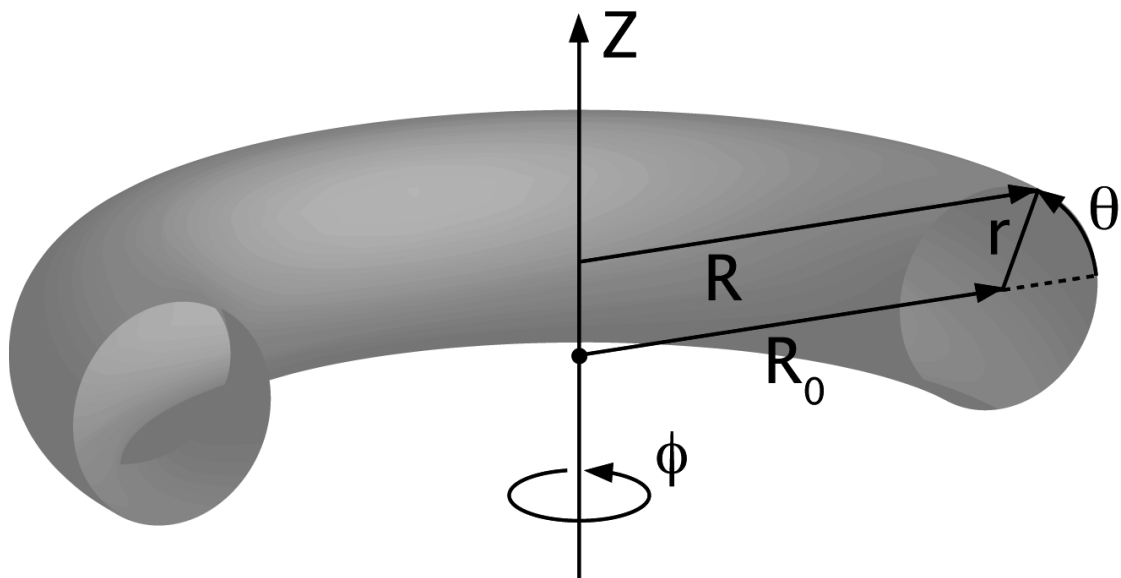


Figure 1.1 – Defining poloidal  $\theta$  and toroidal  $\phi$  directions in magnetic fusion configurations. Image courtesy of *fusionwiki*.

## 1.2 Tokamaks

The tokamak approach to magnetic confinement fusion is through the induction of a toroidal plasma current. By Ampère's law, this induces a poloidal magnetic field. This can be obtained using different sources. The most prevalent is Ohmic induction, requiring the presence of a large solenoid running through the middle of the device, as shown in figure 1.2 (left). The disadvantage of inducing a poloidal magnetic field via a plasma current is that the plasma can easily become unstable. Current-induced instabilities can cause unpredictable global plasma movement that can catastrophically disrupt the fusion device. The use of an external transformer to generate the plasma current is also inherently non-steady state. Thus a major disadvantage of the tokamak approach: how to drive a plasma current whilst ensuring steady-state conditions which are a necessity for commercial nuclear reactors. The largest fusion experiment is currently being built in France: ITER, a tokamak which is expected to run experiments within the next ten to twenty years. The aims of which are to demonstrate long duration quasi-steady state experiments which will produce more energy than is input into the system. In order to achieve this, the tokamak requires highly optimised heating methods that result in more favourable conditions for fusion reactions.

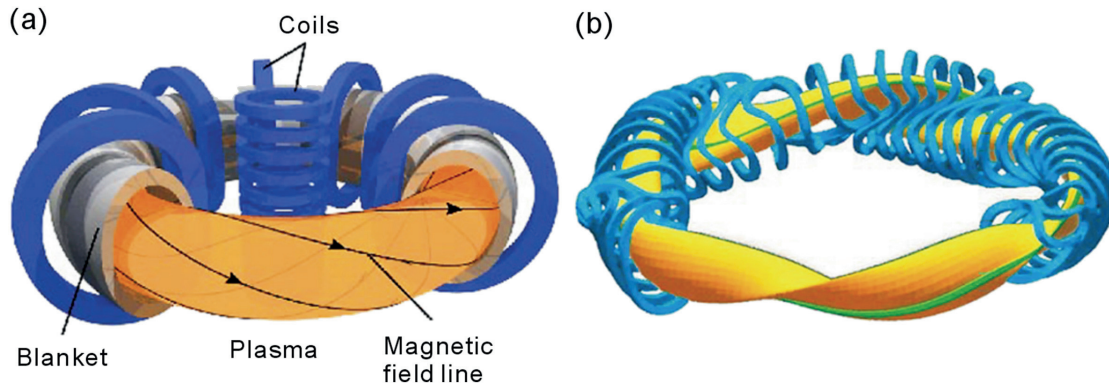


Figure 1.2 – The magnetic coil configurations and the resultant effect on plasma geometry, and magnetic field lines (tokamak left and stellarator right). Image courtesy of Yuhong Xu (2016) [1].

### 1.3 Stellarators

Removing the need for solenoids, stellarators generate the magnetic field line pitch purely from the magnetic coil configuration. There are two different approaches for generating magnetic fields without plasma current: through a 3D distortion of the magnetic axis, known as magnetic torsion, or through a non-circular deformation of the magnetic flux surface shapes (further details in section 2.1.2). Often this involves combinations of poloidal, toroidal and helical coil configurations, for which the engineering constraints are extremely challenging. Implementation of plasma diagnostics to measure quantities such as the temperature and density becomes difficult with so many coils, and the production of coil components of such sizes is also challenging. The approach taken for the largest stellarator currently in operation is through the application of modular coils. Figure 1.3 illustrates that if one superimposes the magnetic fields from combinations of toroidal and helical coils, one can generate the corresponding magnetic field by sets of deformed modular coils, shown for the W7-X device in figure 1.2 (right).

Like the tokamak, the stellarator still requires significant scientific investment before a commercial reactor can be foreseen. Issues such as the heat loading of the plasma on the vessel, or the efficiency of the heating methods are problems that both fusion devices share, but the 3D magnetic geometry of the stellarator results in both advantages and disadvantages over the tokamak. Stellarators are inherently steady-state: without the need for plasma current drive. Therefore, stellarators are ideally stable to current driven instabilities. In tokamak experiments, often the plasma terminates unexpectedly due to large energy disruptions, or edge localised modes occur that pose challenges for the design of plasma facing components. For the ITER tokamak reactor, one disruption or a handful of edge localised modes could permanently damage the 19-billion euro machine. Stellarators so far do not experience such events. However, one of the main problems that the stellarator must overcome is the confinement of

particles and energy. Due to the 3D magnetic geometry, particles can become trapped in magnetic wells, becoming quickly lost from the system. The confinement of energetic particles in tokamaks is generally better than in stellarators. This problem becomes increasingly more severe proportionally with the particle energy. This creates significant problems for alpha particle confinement, a requirement for an efficient fusion reactor design. While stellarators such as W7-X have been optimised for good particle confinement, the confinement of fast ions remains much poorer than in most tokamak devices.

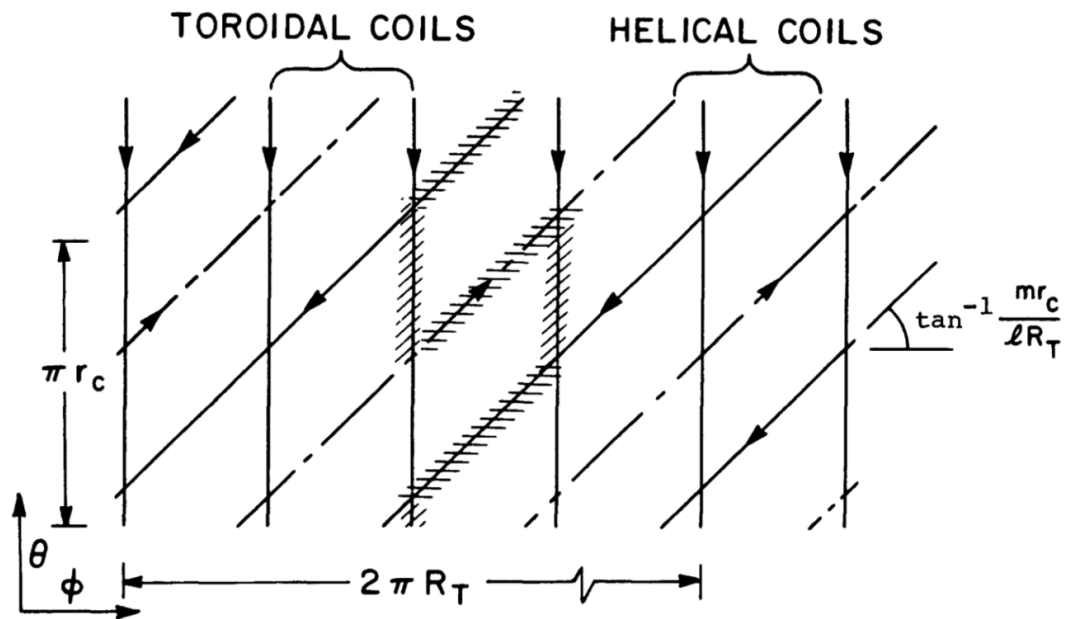


Figure 1.3 – The modular field coil concept of the modern stellarator. Image taken from *The Modular Stellarator Reactor: A Fusion Power Plant*, R.L. Miller *et al* (1983).

## 1.4 Thesis Contribution

The auxiliary fast-ion heating methods investigated in this thesis are Ion Cyclotron Range of Frequency (ICRF) and Neutral Beam Injection (NBI) heating. The former involves propagating a wave into the plasma such that the frequency of the wave permits particle-wave resonance and energy exchange to heat the plasma. The frequency of the wave launched is in the range of the gyration frequency (cyclotron frequency) of the resonating ion species around the magnetic field lines. NBI heating involves the injection of highly energetic neutrals into the plasma, which ionise and deposit their energy upon colliding with the background plasma. There are other methods, such as Electron Cyclotron Resonance Heating (ECRH) and Lower Hybrid (LH) heating, which will not be explored in this thesis. In terms of direct ion heating, ICRF and NBI heating are the most commonly applied methods at present. However, the resulting fast ions from each method have very different properties. The main aims of this thesis are to study tokamak and stellarator fusion devices for the following:

- To improve the understanding of the current auxiliary fast-ion heating methods ICRF and NBI.
- Apply this knowledge to optimise such methods, with the aim to enhance fusion conditions in tokamak and stellarator devices.
- Development of novel or little-explored heating scenarios to generate energetic ions for fast ion particle confinement studies in strongly 3D plasmas, especially the W7-X stellarator. W7-X must demonstrate reasonable fast ion confinement in order to keep the stellarator concept for fusion along a path to success.

### 1.5 Outline

The thesis is organised as follows. In chapter 2, an introduction to the basic physics and the relevant equations is given. These basics are required in order to understand the following chapters, in which the scientific results will be explained. The different codes that comprise the SCENIC numerical code package will also be introduced, explaining how the SCENIC code suite can be applied to resolve ICRF and NBI physics in 3D magnetic confinement fusion devices.

Over the period of this thesis, many significant modifications have been made to the SCENIC package in terms of the ICRF wave propagation code LEMan. Chapter 3 explains these updates, and applies them to optimise the commonly used minority species RF-heating scheme. For the JET tokamak, a broad parameter scan has been made in order to thoroughly investigate the performance of ICRF in various plasma conditions. This also includes second harmonic (parasitic) deuterium heating effects on the Fokker-Planck evolution of the majority thermal deuterium. Simulations of ICRF in the Wendelstein 7-X stellarator for different magnetic equilibria are presented. The final part of the chapter shows results never before calculated numerically: wave propagation and absorption in 3D internal helical-core deformed tokamak equilibria. These simulations are made for the ITER tokamak.

The SCENIC package has also been modified to numerically simulate NBI ionisation and ion accumulation in 3D magnetic equilibria, amongst other updates. Chapter 4 presents the numerical approach and application of the code suite to the Wendelstein 7-X stellarator for different magnetic equilibria.

After having presented the basic heating scenarios of both ICRF and NBI, chapter 5 focuses on the development and application of more advanced heating scenarios. This includes the RF 3-ion species heating. The final section of this chapter presents a heating scenario that, to date, has never been applied to stellarator devices: synergetic RF-NBI heating through multiple-species Doppler shifted resonance. Two numerical approaches explain how to calculate the performance and characteristics of this heating scheme. Simulations are made for the JET tokamak and W7-X stellarator, with particular emphasis on the latter.



The final chapter summarises the research made throughout the thesis. Future modifications and improvements to both the work and the SCENIC code package are also described.



## 2 Equilibria, Waves and Fast Ions: the SCENIC Code Package

The aims of this thesis are to accurately simulate and explore the physics of auxiliary heating methods in magnetised 3D plasmas. This requires an understanding of the generation of closed magnetic flux surface topologies in tokamak and stellarator devices, the propagation, absorption and reflection of ICRF waves, the injection of NBI beam ions and the fast ion orbit motion and RF-wave power transfer in such equilibria. This chapter presents the basic theory and numerical approach taken in this work to calculate and explore such physics.

### 2.1 Magneto-HydroDynamic Equilibria and Anisotropic VMEC

A plasma fluid can be represented (neglecting resistive effects) by the ideal MHD force balance equation:

$$\vec{j} \times \vec{B} = \nabla \bar{P}. \quad (2.1.1)$$

This equation represents the plasma equilibrium as a set of closed magnetic flux surfaces, provided that the confining magnetic field and induced current density obeys Maxwell's equations

$$\nabla \times \vec{B} = \mu_0 \vec{j}, \quad (2.1.2)$$

$$\nabla \cdot \vec{B} = 0. \quad (2.1.3)$$

This closed set of flux surfaces are best described in curvilinear flux coordinates  $(s, u, v)$ . With these coordinates the magnetic field in a covariant basis

$$\vec{B} = B_s \nabla s + B_u \nabla u + B_v \nabla v, \quad (2.1.4)$$

where  $u$  and  $v$  are in general functions of both the geometrical poloidal and toroidal directions, and  $s$  is the flux surface label variable (though  $v$  is mostly toroidal, and  $u$  mostly poloidal).

The parameter  $s$  is usually related to either the normalised toroidal

$$\psi_v = \int_{S(v)} \vec{B} \cdot d\vec{S}, \quad (2.1.5)$$

or poloidal

$$\psi_u = \int_{S(u)} \vec{B} \cdot d\vec{S}, \quad (2.1.6)$$

magnetic flux, with

$$s = \left| \frac{\psi_{u,v}}{\psi_{u,v}(LCFS)} \right|, \quad (2.1.7)$$

where LCFS is the Last Closed Flux Surface. This parameter has the range  $0 \leq s \leq 1$ . In concentric circular flux surface tokamak equilibria  $s = (r/a)^2$ , where  $a$  is the minor radius and  $r$  the minor radial variable that varies linearly  $0 \leq r \leq a$ . The magnetic field can also be described in the Clebsch representation

$$\vec{B} = \nabla v \times \nabla \psi_u + q \nabla \psi_u \times \nabla u, \quad (2.1.8)$$

with the local safety factor  $q_l$  defined as the local field line pitch angle

$$\left. \frac{dv}{du} \right|_{\vec{B}} = \frac{\vec{B} \cdot \nabla v}{\vec{B} \cdot \nabla u} = q_l(s, u, v). \quad (2.1.9)$$

The safety factor is defined as  $q(s) = \langle q_l(s, u, v) \rangle$ , where  $\langle \dots \rangle$  denotes an average over a flux surface with respect to poloidal  $u$  and toroidal  $v$  angles. Variables such as the poloidal and toroidal magnetic flux, the safety factor and therefore the magnetic field of the plasma magnetic equilibrium are dictated by a combination of the induced poloidal and toroidal currents as well as the plasma pressure as functions in  $s$ .

### 2.1.1 Calculating Ideal MHD Equilibria: ANIMEC

Codes such as ANIMEC [2] read as input the flux surface average profiles of the parallel plasma pressure of the thermal species  $\langle P_\alpha(s) \rangle$ , fast ion parallel pressure  $\langle p_\parallel^h(s, B) \rangle$ , fast ion anisotropy  $\langle T_\perp^h(s) \rangle / \langle T_\parallel^h(s) \rangle$  and either the (local flux surface) safety factor  $q(s)$  or the (local flux surface) toroidal current  $I(s)$  and solve the ideal MHD equations to evaluate the nested flux surface equilibrium. Such a solution can be analytically found in simple toroidally axisymmetric tokamak equilibria, but for 3D tokamak and stellarator configurations solutions can only be evaluated numerically. The ANIMEC code calculates this via a variation of the plasma energy integral

$$W = \int \left( \frac{B^2}{2\mu_0} + \frac{p_\parallel}{\gamma - 1} \right) dV, \quad (2.1.10)$$

where  $\gamma$  is the adiabatic index and  $p_{\parallel}(s, B) = \langle p_{\parallel}^h(s, B) \rangle + \langle p_{\alpha}(s) \rangle$ . One of the outputs of the code is to map the magnetic flux surface geometry into cylindrical coordinates in the Fourier representation

$$|B|(s, u, v) = \sum_{m,n} (B_{m,n}^S(s) \sin(mu - nv) + B_{m,n}^C(s) \cos(mu - nv)), \quad (2.1.11)$$

$$R(s, u, v) = \sum_{m,n} (R_{m,n}^S(s) \sin(mu - nv) + R_{m,n}^C(s) \cos(mu - nv)), \quad (2.1.12)$$

$$Z(s, u, v) = \sum_{m,n} (Z_{m,n}^S(s) \sin(mu - nv) + Z_{m,n}^C(s) \cos(mu - nv)), \quad (2.1.13)$$

$$\phi(s, u, v) = v, \quad (2.1.14)$$

noting that the toroidal angle is therefore the geometrical toroidal angle. ANIMEC uses the normalised toroidal magnetic flux coordinate for the flux surface label  $s$ . The additional inputs to the code required are either a LCFS shape for a fixed boundary solver, or a discretised description of the toroidal and poloidal coil currents for a free-boundary equilibrium solution.

### 2.1.2 2D Stellarator Symmetry and 3D Equilibria

Equations 2.1.16-2.1.19 can be further simplified using what is known as stellarator symmetry (or up-down symmetry for a toroidally axisymmetric equilibrium) such that a vector represented in curvilinear coordinates obeys

$$[A_s(s, u, v), A_u(s, u, v), A_v(s, u, v)] = [-A_s(s, -u, -v), A_u(s, -u, -v), A_v(s, -u, -v)]. \quad (2.1.15)$$

Most of the magnetic field coil configurations of tokamak and stellarator devices around the world are designed with stellarator symmetry. Ampère's law yields that if the coil current is stellarator symmetric then so is the magnetic field. This results in the simplification

$$|B|(s, u, v) = \sum_{m,n} B_{m,n}(s) \cos(mu - nv), \quad (2.1.16)$$

$$R(s, u, v) = \sum_{m,n} R_{m,n}(s) \cos(mu - nv), \quad (2.1.17)$$

$$Z(s, u, v) = \sum_{m,n} Z_{m,n}(s) \sin(mu - nv), \quad (2.1.18)$$

$$\phi(s, u, v) = v. \quad (2.1.19)$$

Stellarator symmetry significantly simplifies the calculation of stellarator equilibria. There are examples such as the generation of internal-kink like magnetic flux surface deformations which exist in tokamaks and stellarators that would break such an assumption.

### 2.1.3 W7-X Equilibria

Stellarator research investigated in this thesis is primarily concerned with the W7-X device. Optimisation of a magnetic confinement fusion machine requires the optimisation of an array of engineering systems and constraints. If an unexpected plasma current is generated it will deform the flux surface equilibrium, which can result in the breakdown of closed magnetic surfaces. For this reason, self-induced plasma currents usually need to be minimised. Other concerns are particle and energy confinement, especially the effects of neoclassical and turbulent transport. The term neoclassical connects to classical transport due to the toroidal effect of trapping/detrapping in magnetic wells. The W7-X device is five-fold toroidally periodic. Built to minimise such neoclassical transport, the machine has been designed to be quasi-omnigeneous.

#### Quasi-omnigeneity

The definition of omnigeneity is related to the radial displacement  $\Delta\psi$  of a single particle at different bounce points,

$$\Delta\psi = \oint_b (\vec{v}_D \cdot \vec{\nabla}\psi) dt = 0, \quad (2.1.20)$$

with  $\vec{v}_D$  the drift velocity of the particle across magnetic field lines, and the integration limit indicating integration between two consecutive bounce points. In an axisymmetric tokamak configuration, a single particle moving through the magnetic topology (thus without the presence of Coulomb collisions, turbulence, etc) satisfies equation 2.1.20 exactly. The particle will therefore remain confined, with a bounce average motion that is purely toroidal (toroidal precession). To lowest order, equation 2.1.20 can be represented as the integration along the magnetic field strength along a particle trajectory between bounce points,

$$\Delta\psi = 2 \sum_{\sigma} \sigma \int_{B_{min}}^{B_{ref}} \frac{B dB}{|v_{\parallel}| \vec{B} \cdot \vec{\nabla} B} \vec{v}_D \cdot \vec{\nabla}\psi, \quad (2.1.21)$$

with  $\sigma = v_{\parallel}/|v_{\parallel}|$ . Integration of the radial drift over the magnetic field strength provides the definition of an omnigeneous magnetic field configuration. If the contours of the magnetic field strength are connected around the torus either poloidally, toroidally, or both then the magnetic geometry is omnigeneous as particles do not have a net radial drift between bounce points. Wendelstein 7-X does not satisfy this condition, however, it is designed to be *nearly*

omnigenous. This means that the entire stellarator has been optimised such that over many bounce points, equation 2.1.20 tends towards zero. This has significant benefits for particle and energy confinement of the device.

### Toroidal Magnetic Mirroring

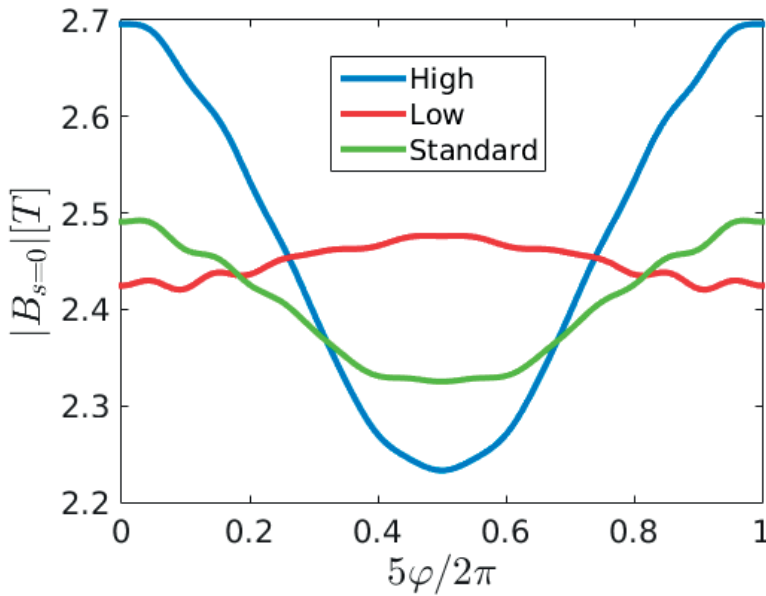


Figure 2.1 – Toroidal (Boozer) variation of the magnetic field strength along the magnetic axis in one W7-X period comparing three different coil current configurations.

In addition to quasi-omnigenicity, optimisation of the stellarator can be achieved by modifying the coil configuration. The currents in the modular coil sections can be adjusted to produce a broad array of magnetic equilibria. The work in this thesis investigates the influence of the toroidal magnetic mirror on ICRF, NBI and fast ion confinement. The degree of magnetic mirroring,

$$MR = \frac{B_{\phi=0}(s=0) - B_{\phi=\pi/5}(s=0)}{B_{\phi=0}(s=0) + B_{\phi=\pi/5}(s=0)}. \quad (2.1.22)$$

represents the difference in the magnetic field strength along the magnetic axis in the two toroidal sections of W7-X: the bean ( $\phi = 2n\pi/5$ ,  $n = 0, \dots, 4$ ) and the triangular ( $\phi = (n+1)\pi/5$ ,  $n = 0, \dots, 4$ ) section. Three magnetic configurations with different values of the toroidal magnetic mirror are used in this work: low, standard and high mirror. A comparison of the magnetic field strength on-axis for the three configurations is given in figure 2.1. Further illustration of the differences between the three equilibria is given in table 2.1.

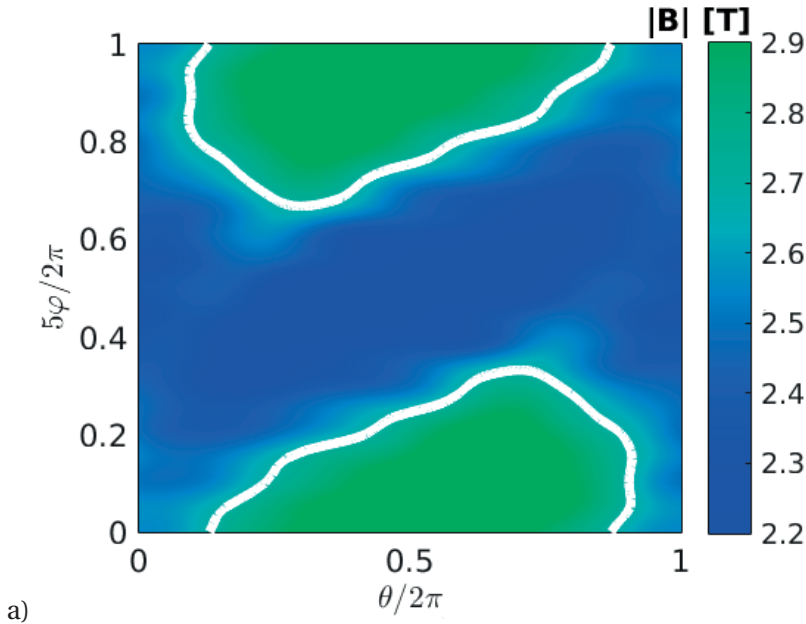
	MR %	max( $B$ ) [T]	min( $B$ ) [T]
High	9.4	3.14	2.14
Standard	3.5	2.95	2.22
Low	-0.8	2.92	2.28

Table 2.1 – Comparison of the low, standard and high mirror equilibria, including the global maximum and minimum values of the magnetic field strength.

Each of these equilibria were calculated such that the global  $\beta$  value of the plasma was fixed at 3%, defined as

$$\langle \beta \rangle = \frac{2\mu_0 \int p dV}{\int |B|^2 dV}. \quad (2.1.23)$$

The experimental profiles for these equilibria will be described in chapter 3. Figure 2.2 illustrates the magnetic field strength on the LCFS as a contour plot varying in the toroidal and poloidal directions, plotted in Boozer coordinates. The choice of Boozer curvilinear coordinates is chosen such that the poloidal coordinate  $u \rightarrow \theta$  and the toroidal coordinate  $v \rightarrow \varphi$ . The low mirror equilibrium therefore most closely resembles a classical stellarator such that the magnetic field strength is almost constant for all toroidal angles. The high mirror equilibrium has been optimised for high  $\beta$  performance, with respect to a variety of different parameters so as to reduce anomalous transport, bootstrap currents, heating of the divertor, etc.





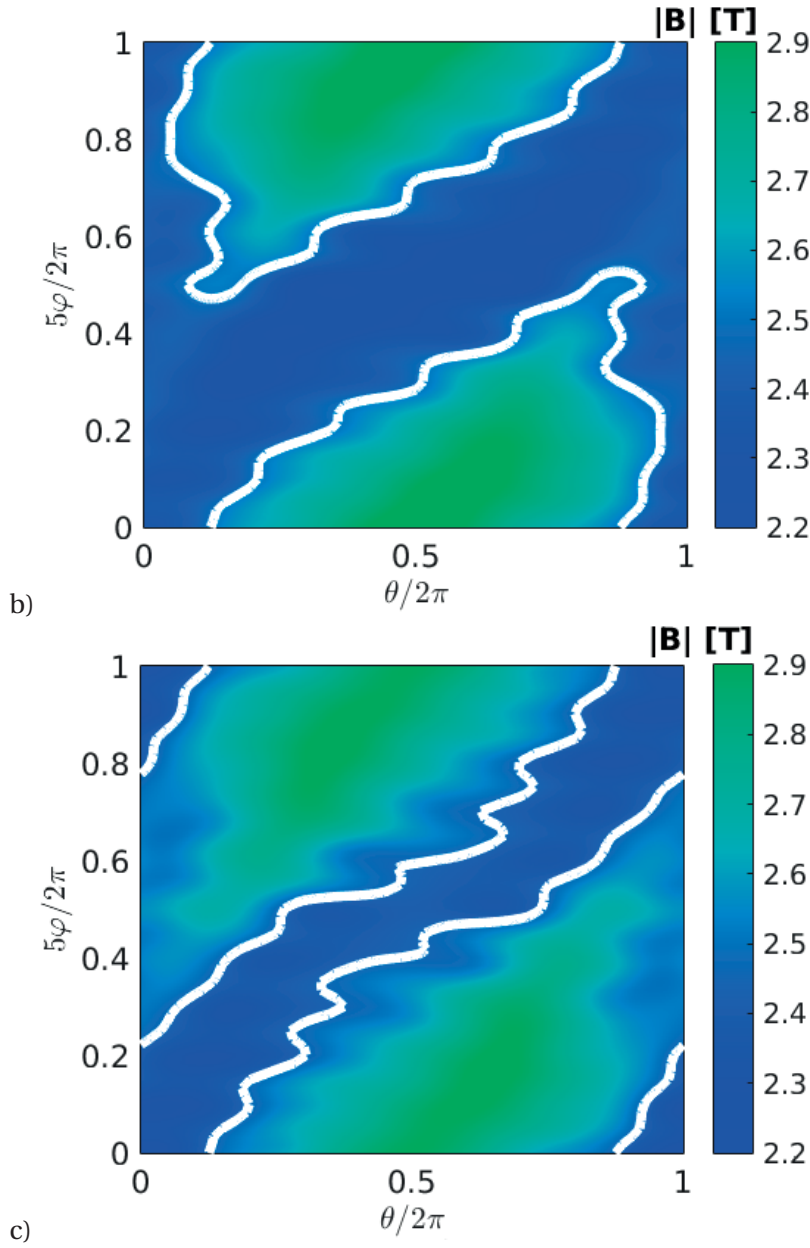


Figure 2.2 – Magnetic field strength contour on the last closed flux surface. a), b) and c) illustrate the three magnetic configurations (high, standard and low mirror respectively). The solid white line reflects the magnetic resonant surface described in section 2.2.2.

One of the most significant differences between the three equilibria is the toroidal precession of trapped particles within the equilibria. For example, trapped particles with  $B_{ref} = E/\mu < 2.4\text{T}$  would toroidally precess in the low but not the high or standard mirror equilibria (where trapped particles would only poloidally precess). The consequence of a lack of toroidal drift precession of trapped particles is that they are locked into one period of the device, until

knocked out by collisional detrapping or e.g. RF-wave resonant effects. Figure 2.2 indicates the presence of the large toroidal magnetic well in between the bean sections in the high mirror equilibrium, influencing the toroidally trapped population. However, other examples indicate improved confinement in the standard or high mirror [3]. This plays a crucial role in ICRF and NBI performance and energetic ion confinement in the magnetic configurations.

## 2.2 RF-Wave Propagation and LEMan

Ion Cyclotron Resonance Heating involves the induction of a current in an antenna located on the vessel wall. This current then produces an electric field which propagates into the plasma. Based upon certain plasma and magnetic geometry conditions, resonance occurs between the wave and the different species present. Introductory courses on magnetised plasmas tends to use the cold plasma model ( $T \rightarrow 0$ ) and separates the allowed resonances into different groups: wave absorption from wave propagation purely parallel or perpendicular to the magnetic field  $B_0$ . This leads to classifications of the RF wave according to the wave vector  $\vec{k}$  to be the cyclotron  $L$  and  $R$  waves, rotating in the direction of the ions or electrons respectively, for  $\vec{k} \perp \vec{B}_0$  and either the Ordinary-Mode (OM) or Extraordinary-Mode (XM) for  $\vec{k} \parallel \vec{B}_0$ . This depends on the electric field alignment to the magnetic field,  $\vec{E} \parallel \vec{B}_0$  is OM and  $\vec{E} \perp \vec{B}_0$  is XM. In toroidal, warm ( $T \neq 0$ ) and magnetised ICRF experiments, this basic theory breaks down. Toroidal geometry (as opposed to a cylindrical magnetic geometry) introduces refraction of the wave, and this in turn leads to the presence of components of the electric field and wave-vector that propagate both parallel and perpendicular to the magnetic field, connecting certain branches of the L, R, OM and EM waves. A more general classification is to describe ‘fast’ and ‘slow’ waves. With respect to experiments, these two are generally used to refer to whether the RF-antenna induces waves that propagate predominatly in the perpendicular (ICRF) or parallel (Lower Hybrid (LH)) directions. However, this definition is not exact, as mentioned in [4]. This chapter is focused on the fast wave and its propagation, absorption and reflection in magnetised plasmas. Once an important theoretical basis is established, the aims of this chapter is to provide an understanding of how to apply RF-waves to heat the plasma in tokamak and stellarator devices.

### 2.2.1 Fast and Slow Wave Cut-offs and Resonances

Starting from a combination of Maxwell’s equations, the electric field can be related to a current density by:

$$\nabla \times (\nabla \times \vec{E}) = -\mu_0 \frac{\partial \vec{j}}{\partial t} - \frac{1}{c^2} \frac{\partial^2 \vec{E}}{\partial t^2}. \quad (2.2.1)$$

Illustrating the influence of an antenna current to induce an electric field to disperse through the plasma. Assuming Ohm’s law  $\vec{j} = \vec{\sigma} \cdot \vec{E}$ , equation 2.2.1 can be written in the following form:

$$\left\{ n^2 \left[ \frac{\vec{k}\vec{k}}{k^2} - \mathbb{1} \right] + \vec{\epsilon} \right\} \cdot \vec{E} = 0, \quad (2.2.2)$$

where  $\bar{\epsilon}$  is the dielectric tensor and  $n^2 = k^2 c^2 / \omega^2$  the plasma refractive index. To zeroth order in Finite Larmor Radius (the influence of all FLR orders is described in 3.1) this can be written as [5]:

$$\begin{vmatrix} S - n_{\parallel}^2 & -iD & n_{\perp} n_{\parallel} \\ iD & S - n^2 & 0 \\ n_{\perp} n_{\parallel} & 0 & P - n_{\perp}^2 \end{vmatrix} = 0. \quad (2.2.3)$$

Using the cold plasma model, (hot effects will be included in section 3.1.2), the components of equation 2.2.3 can be written as:

$$S = 1 - \sum_{\alpha} \frac{\omega_{p,\alpha}^2}{\omega^2 - \Omega_{c,\alpha}^2}, \quad (2.2.4)$$

$$D = \sum_{\alpha} \frac{\Omega_{c,\alpha} \omega_{p,\alpha}^2}{\omega(\omega^2 - \Omega_{c,\alpha}^2)}, \quad (2.2.5)$$

$$P = 1 - \sum_{\alpha} \frac{\omega_{p,\alpha}^2}{\omega^2}, \quad (2.2.6)$$

$$\omega_{p,\alpha}^2 = \frac{n_{\alpha} Z_{\alpha}^2}{m_{\alpha} \epsilon_0}, \quad (2.2.7)$$

with  $\alpha$  the plasma species,  $\omega_{p,\alpha}$  the plasma frequency and  $\Omega_{c,\alpha} = Z_{\alpha} B / m_{\alpha}$  the cyclotron frequency. In ICRF and LH tokamak experiments, it is most common that  $\omega \ll \omega_{p,\alpha}$  and thus solutions to equation 2.2.3 are:

$$n_{\perp}^2 = \frac{(S - n_{\parallel}^2)^2 - D^2}{S - n_{\parallel}^2} = \frac{(R - n_{\parallel}^2)(L - n_{\parallel}^2)}{S - n_{\parallel}^2}, \quad (2.2.8)$$

$$n_{\perp}^2 = \frac{P(S - n_{\parallel}^2)}{S}, \quad (2.2.9)$$

where

$$L = 1 - \sum_{\alpha} \frac{\omega_{p,\alpha}^2}{\omega(\omega - \Omega_{c,\alpha})}, \quad (2.2.10)$$

and

$$R = 1 - \sum_{\alpha} \frac{\omega_{p,\alpha}^2}{\omega(\omega + \Omega_{c,\alpha})}. \quad (2.2.11)$$

Note that  $S = \frac{1}{2}(R + L)$  and  $D = \frac{1}{2}(R - L)$  from equations 2.2.4 and 2.2.5. The resonance and cut-off regions of the plasma are the regions where  $n_{\perp} \rightarrow \infty$  and  $n_{\perp} \rightarrow 0$  respectively. Resonance indicates wave-particle energy exchange whereas the cut-off region refers to where the plasma medium results in reflection of the wave. Equation 2.2.8 corresponds to the fast wave and equation 2.2.9 to the slow wave dispersion relation. Regarding the dispersion relation for the slow wave, if launched from the low field side of a tokamak, it experiences strong damping ( $n_{\perp} \rightarrow \infty$ ) as the magnetic field increases and it approaches  $\omega \simeq \Omega_{c,\alpha}$ . Thus for on-axis resonance the slow wave cannot propagate into the core and no energy can be exchanged to the ions unless they are highly energetic. This effect is known as the ‘magnetic beach’. The fast wave is able to propagate into the core depending upon the value of the parallel wave-vector. The slow wave heats predominantly in parallel direction and therefore heats the electrons through Landau damping and electron Transit Time Magnetic Pumping (eTTMP). The resulting TTMP force exerted on the particle is:

$$\vec{F}_{TTMP} = -\hat{e}_{\parallel,0} \cdot \nabla(\mu B_{\parallel,0}). \quad (2.2.12)$$

The importance of TTMP effects is often neglected as these result in additional terms added to the dielectric tensor, which are neglected in the limit of zero FLR. If the ions are highly energetic (such as alpha particle populations) then the slow wave can also heat ions in the perpendicular direction. The fast wave heats the electrons in the parallel direction and ions in the both the parallel and perpendicular directions. The amount of energy transferred between ions and electrons depends on the plasma conditions such as density, temperature and location of the resonant surface. Additionally, for large temperatures and certain plasma conditions, an injected fast wave can be partially or entirely converted to a slow wave, known as the Ion Bernstein Wave (IBW). This is produced close to the fast wave resonance  $S - n_{\parallel}^2 \rightarrow 0$ . This wave resonates with electrons in the parallel direction and is generally referred to as ‘mode-conversion’ power absorption by the electrons. Note that for both the fast and slow wave, outside of the LCFS where the density (and thus  $\omega_{p,\alpha}$ ) falls to low values this wave is actually reflected. To avoid wave reflection and a consequential damaging of the RF-antenna, gas is puffed in front of the antenna. This also prevents the RF-wave from melting the divertor component and vessel wall.

### 2.2.2 RF-Resonant Surface

The location of where wave-particle energy is transferred is dictated by the resonance condition:  $\omega_a = k_{\parallel} v_{\parallel} + n\Omega_{c,\alpha}$ , where  $n \in \mathbb{Z}$  is the harmonic cyclotron resonance index. This implies that, based upon the spatial variation of  $k_{\parallel}$  and  $\Omega_{c,\alpha}$ , wave-particle resonance can only occur for particles with a specific parallel velocity, belonging to the set:

$$v_{\parallel,res} = \left[ \min_{\{k_{\parallel}^+, \Omega\}} \left( \left| \frac{\omega_a - \Omega}{k_{\parallel}^+} \right| \right), \max_{\{k_{\parallel}^+, \Omega\}} \left( \left| \frac{\omega_a - \Omega}{k_{\parallel}^+} \right| \right) \right]$$

$$\cup \left[ \min_{\{k_{\parallel}^-, \Omega\}} \left( \left| \frac{\omega_a - \Omega}{k_{\parallel}^-} \right| \right), \max_{\{k_{\parallel}^-, \Omega\}} \left( \left| \frac{\omega_a - \Omega}{k_{\parallel}^-} \right| \right) \right]. \quad (2.2.13)$$

The importance of the unity in this equation will become more important in section 5.2. For standard ICRF scenarios where the antenna frequency resonates on-axis with the fundamental ion cyclotron frequency, this can be reduced to:

$$\nu_{\parallel, res} = \left[ \min_{\{k_{\parallel}, \Omega\}} \left( \left| \frac{\omega_a - \Omega}{k_{\parallel}} \right| \right), \max_{\{k_{\parallel}, \Omega\}} \left( \left| \frac{\omega_a - \Omega}{k_{\parallel}} \right| \right) \right]. \quad (2.2.14)$$

For a given value of  $\nu_{\parallel}$ , the regions where wave-particle resonance can occur can be plotted using the magnetic geometry and the values of  $k_{\parallel}$  calculated by LEMan.

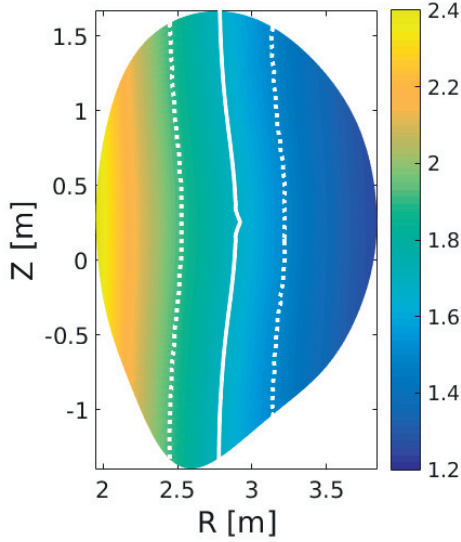


Figure 2.3 – Contour plot of the total magnetic field strength  $|B|$  [T] for the JET tokamak, experiment 91610. The solid white line indicates the resonance for particles with  $E_{\parallel} = 0$  and dotted lines  $E_{\parallel} = 100\text{keV}$ .

In a 2D tokamak geometry this is shown in figure 2.3. For particles with  $E_{\parallel} \in [0, 100]\text{keV}$  the possible regions of the plasma where wave-particle energy exchange can occur is between the two dotted lines (representing  $E_{\parallel} = 100\text{keV}$ ). In 3D stellarator geometry, this becomes more complicated, and is not easy to visualise. Figure 2.4 shows the line of resonance in the poloidal (a) and toroidal (b) plane respectively. A comparison between the RF-resonant surface for JET and W7-X indicates the influence 3D magnetic fields can have on ICRF as a heating method. In W7-X, the resonant surface adjusts toroidally to the change in magnetic field. Regions such as the triangular section ( $\varphi = \pi/5$ ) indicate that particles with  $E_{\parallel} < 100\text{keV}$  cannot resonate on-axis at this toroidal location.

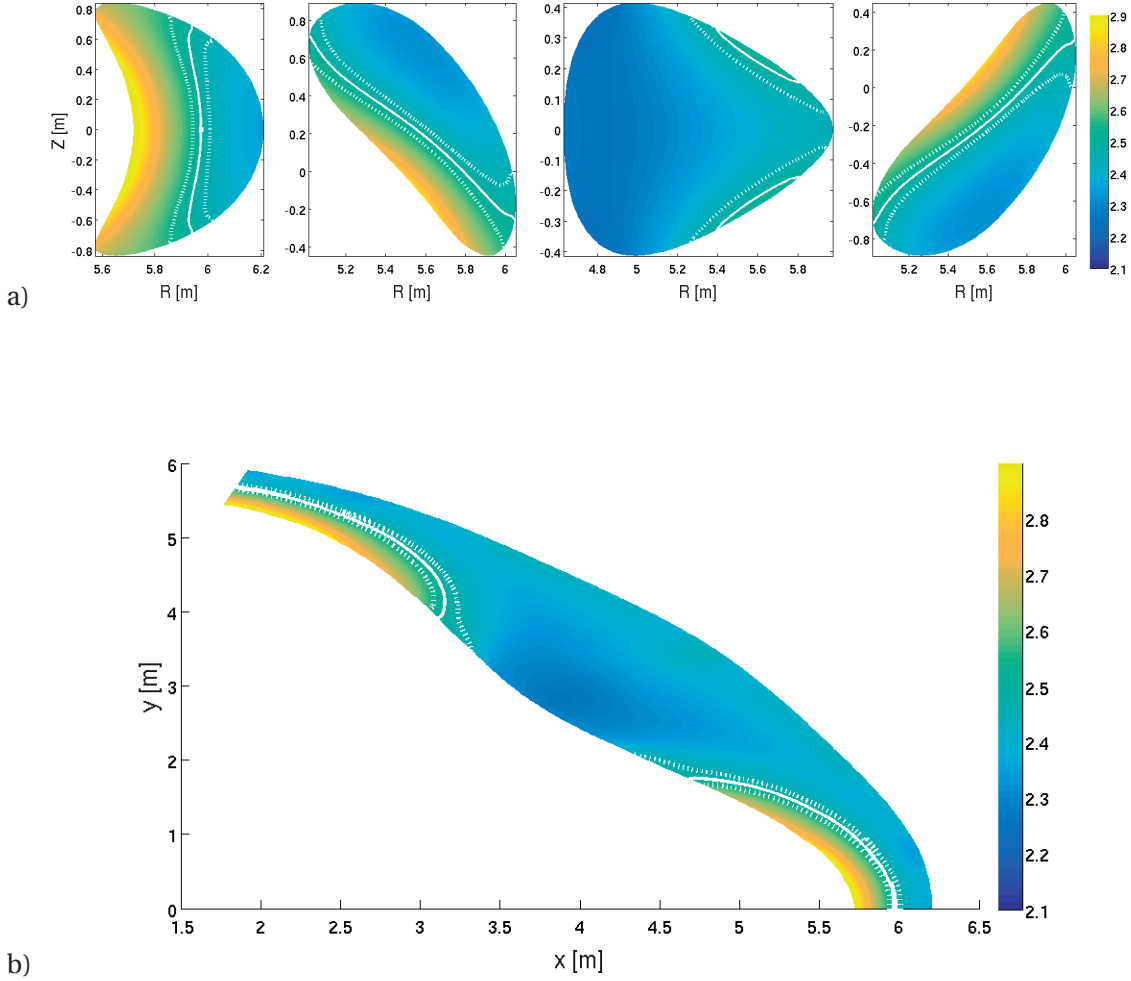


Figure 2.4 – Contour plot of the magnetic field strength [T] for the standard mirror W7-X stellarator equilibrium, showing a) poloidal cross-sections at  $\varphi = [0, \pi/10, \pi/5, 3\pi/10]$  and b) a toroidal cross-section for one field period. The solid white line indicates the resonance for particles with  $E_{\parallel} = 0$  and dotted lines  $E_{\parallel} = 100\text{keV}$ .

In section 2.4.1 it will be shown that RF-resonant trapped particles tend to align their bounce tip to the resonant surface in tokamak geometries. If this same physics were to be applied to the stellarator then it would imply that ICRF would strongly decrease the core confinement time of resonant particles. In 2D and 3D magnetic geometries, particles bounce not just poloidally, but also toroidally. The conservation of the canonical toroidal momentum  $p_{\phi}$  in 2D tokamak equilibria leads to a toroidal precession of trapped particles. A toroidally precessing particle means that the particle motion will trace over all toroidal angles. In 3D tokamak and stellarator equilibria, this toroidal precession is not guaranteed for all particles that bounce toroidally if  $p_{\phi}$  is not conserved. The resulting orbit motion is therefore much more complicated and so particles do not tend to align to the resonant surface in the same way. Additionally, if the electric field of the RF-wave is well localised in front of the antenna, then the

majority of the power will be transferred to particles on-axis. This means that even if particles can resonate away from the antenna, no energy is available at these locations. Comparing the toroidal magnetic mirror terms described in section 2.1.3 the radial location of the resonant surface at different toroidal values varies significantly between the three equilibria, shown in figure 2.5. The location of the ion cyclotron resonant surface in figure 2.5 already indicates the potential RF-heating performance for the different equilibria. The low mirror configuration (c) can be seen to allow on-axis heating of the resonant particles at (almost) all toroidal locations. In contrast, it can be seen that the resonant surface moves out of the plasma for the high mirror equilibrium (a) at  $\varphi = \pi/5$  (triangular section). This means that there is no possible means for wave-particle energy exchange for thermal particles in the high mirror configuration.

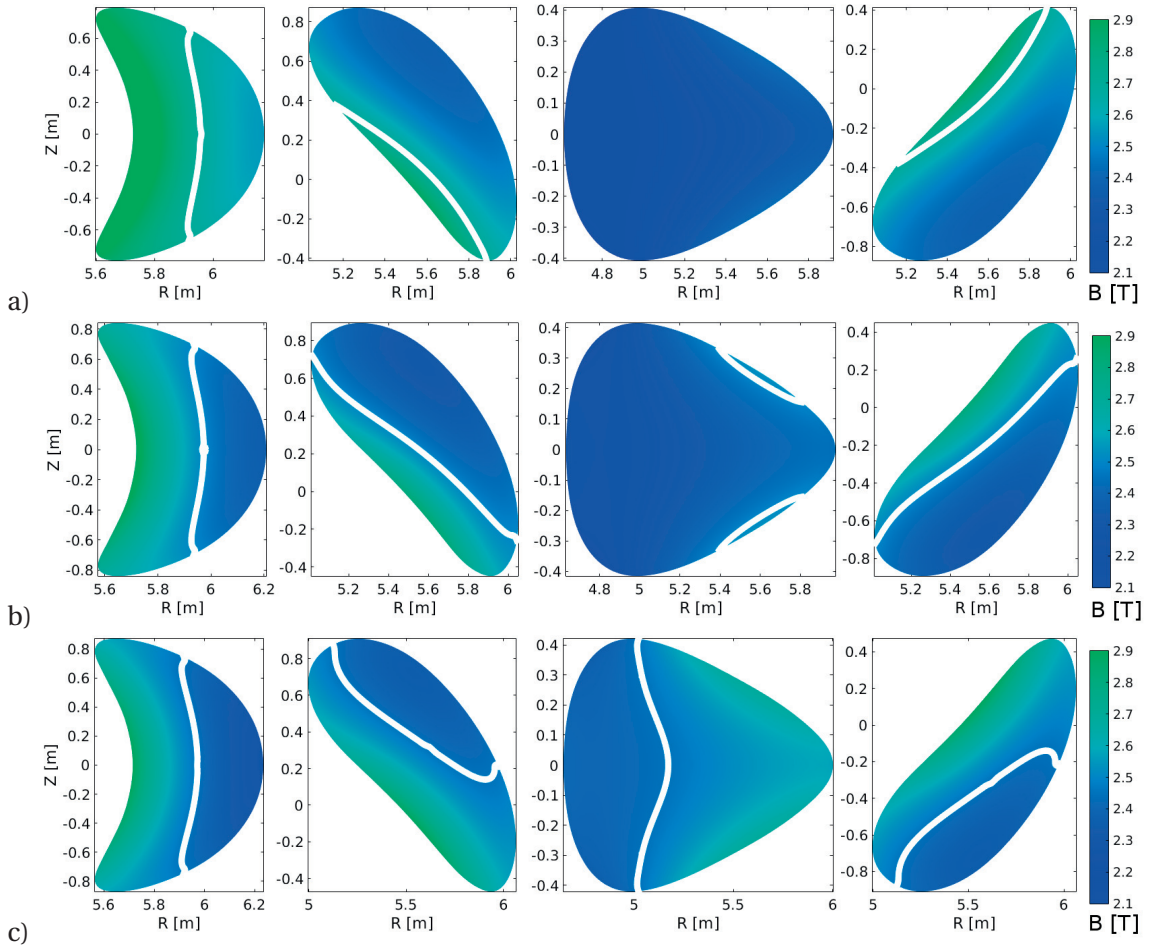


Figure 2.5 – The toroidal dependence of the resonance location as compared to the the magnetic field strength contours, for  $\varphi = 0, \pi/10, \pi/5$  and  $3\pi/10$  (from left to right). The different rows represent the influence of the toroidal mirror term of the equilibria: a) High, ( $B_{res} = 2.7 T$ ) b) Standard, ( $B_{res} = 2.5 T$ ) and c) Low, ( $B_{res} = 2.45 T$ ).  $B_{res} = m_{\alpha} \omega_{ant} / Z_{\alpha}$ . The solid white line indicates location of the on-axis ion cyclotron resonance layer  $B_{res}$  at the toroidal RF-antenna position (6.7 degrees).



### 2.2.3 Polarisation

At the resonant surface, the RF-power absorbed by the resonant particles from the wave is  $P_{abs} \propto |E^+ J_0(\frac{1}{2} k_{\perp}^2 \rho_L)^2|^2$ , where  $\rho_L$  is the Larmor radius, and  $J_n(\lambda)$  is the Bessel function. For fundamental heating, the majority of the the wave energy absorbed by the ions is through  $|E^+|$ . To ensure efficient ion heating the ratio  $|E^+ / E^-|$  should be maximised. This parameter is known as the polarisation of the wave:  $|E^+ / E^-|$ . This relates the electric field of the wave rotating in the direction of the ions (+) with the electrons (-). Taking the two electric field components  $x$  and  $y$  as perpendicular to the magnetic field,

$$E^+ = E_x - iE_y, \quad (2.2.15)$$

$$E^- = E_x + iE_y. \quad (2.2.16)$$

With respect to ICRF, the polarisation of the wave places an upper limit on the RF power absorption by the resonant ion species. This limits the maximum efficiency of the RF-heating to the ion population. Using the two-fluid cold plasma model, the polarisation can be approximated as [5]:

$$\left| \frac{E^+}{E^-} \right|^2 \simeq \left( \frac{R - n_{\parallel}^2}{L - n_{\parallel}^2} \right)^2. \quad (2.2.17)$$

For a single species plasma:

$$\left| \frac{E^+}{E^-} \right|^2 \leq \left( \frac{\omega - \Omega_{c,res}}{\omega + \Omega_{c,res}} \right)^2, \quad (2.2.18)$$

implying that, in the region where the fast wave becomes resonant ( $\omega \rightarrow \Omega_{c,res}$ ), the polarisation approaches zero, such that little energy is absorbed by the ions. This scenario results in almost all RF-power transferred by mode conversion to the electrons. For harmonic heating ( $n > 1$ ):

$$\left| \frac{E^+}{E^-} \right|^2 \leq \left( \frac{n-1}{n+1} \right)^2, \quad (2.2.19)$$

with  $n$  the harmonic number. Harmonic heating requires high temperatures as the coupled power per harmonic decreases for increasing harmonic number. This is a result of the harmonic heating relying on the inclusion of higher order FLR effects, where the Larmor radius increases with temperature. For the minority species scheme in the limit of small minority species concentrations the polarisation limit is:

$$\left| \frac{E^+}{E^-} \right|^2 \leq \left( \frac{\tilde{Z}_{min} - \tilde{Z}_{maj}}{\tilde{Z}_{min} + \tilde{Z}_{maj}} \right)^2, \quad (2.2.20)$$



where  $\tilde{Z}$  is the atomic charge to mass ratio, with *min* and *maj* the minority and majority species respectively (for a two-species plasma). The resonant layer for the minority species heating scheme appears between the two cyclotron frequencies of the majority and minority ions, known as the ion-ion hybrid resonant layer. This region lies close to the L-cutoff where the polarisation is maximised. The ion-ion hybrid resonant layer approaches the fundamental minority cyclotron resonance position for decreasing  $n_{min}/n_{maj}$  where  $n$  refers to the density. Thus, the aim is to have the minority cyclotron frequency resonance  $\Omega_{c,res} = \omega_{ant}$  as close to the L-cutoff as possible, where the polarisation is maximised and efficient RF heating occurs. The limit for the polarisation of RF heating for minority species heating of hydrogen in a deuterium plasma is  $|E^+/E^-| \leq 1/3$ . The same polarisation limit can be calculated for second harmonic heating in a pure hydrogen plasma. Advanced RF-heating schemes have been recently developed aiming to maximise the polarisation such that  $|E^+/E^-| \gg 1$ . Such schemes are described in chapter 5.

### 2.2.4 Simulating RF-propagation: LEMan

Wave propagation, absorption by the plasma species (including the influence of the resonant surface), reflection and polarisation are calculated in the LEMan code [6]. The code solves the wave equation (equation 2.2.1) for the vector and scalar potential, assuming a time-independent solution:

$$\nabla^2 \vec{A} + k_0^2 \vec{\epsilon} \cdot \vec{A} + i k_0 \vec{\epsilon} \cdot \nabla \tilde{\phi} = -\frac{4\pi}{c} \vec{j}_{ant}, \quad (2.2.21)$$

$$\nabla \cdot (\vec{\epsilon} \cdot \nabla \tilde{\phi}) - i k_0 \nabla \cdot (\vec{\epsilon} \cdot \vec{A}) = -4\pi \rho_{ext}. \quad (2.2.22)$$

The assumption of time-independence is based on the wave time-scales being shorter than any other relevant time-scale of the system. In order to numerically evaluate equations 2.2.21 and 2.2.22, the scalar and vector potential is decomposed in the toroidal and poloidal directions using a Fourier spectrum, and with cubic Hermite polynomials in the radial direction with  $\psi_j$  the radial basis decomposition function,

$$f(s, \theta, \phi) = \sum_{j,l,m,n} \hat{f}_{j,l,m,n} \psi_j(s) e^{i(m\theta+n\phi)}. \quad (2.2.23)$$

The wave equations 2.2.21 and 2.2.22 can be projected into a finite element basis by using the test functions F and G,

$$\int_{\Omega} dV [ -(\nabla \times \vec{F}^*) \cdot (\nabla \times \vec{A}) - (\nabla \cdot \vec{F}^*) \cdot (\nabla \cdot \vec{A}) + k_0^2 \vec{F}^* \cdot (\vec{\epsilon} \cdot \vec{A}) + i k_0 \vec{F}^* \cdot (\vec{\epsilon} \cdot \nabla \tilde{\phi}) ] + \int_{\sigma\Omega} d\vec{S} \cdot [ \vec{F}^* \times (\nabla \times \vec{A}) + \vec{F}^* \cdot (\nabla \times \vec{A}) ] = \frac{4\pi}{c} \int_{\Omega} dV \vec{F} \cdot \vec{j}_{ant}, \quad (2.2.24)$$

and

$$\int_{\Omega} dV [\nabla G^* \cdot (\bar{\epsilon} \cdot \nabla \tilde{\phi}) - i k_0 \nabla G^* \cdot (\bar{\epsilon} \cdot \vec{A})] + \int_{\sigma\Omega} d\vec{S} \cdot [i k_0 G^* \bar{\epsilon} \cdot \vec{A} - G^* \bar{\epsilon} \cdot \nabla \tilde{\phi}] = -4\pi \int_{\Omega} dV G^* \rho_{ant}. \quad (2.2.25)$$

For the solution of the vector potential, equations 2.2.24 and 2.2.25 result in the calculation of a large matrix inversion problem. This is solved in LEMan using Gaussian elimination via the ‘BABE’ (Burn At Both Ends) method. Updates and the application of the LEMan code is to be further described in sections 3 and 5.

### 2.3 NBI injection and the VENUS-NBI Module

In magnetised plasmas, beam injection heating into the core region is only feasible using a beam of neutral particles, capable of penetrating into the plasma without influence of the magnetic field. The process for the generation of neutrals is as follows: ionise the particles, accelerate them to the required energy, neutralise using a neutral gas (including removing the remaining ions that did not neutralise). This will therefore form a beam of neutral particles that will continue their trajectory into the plasma unaffected by electromagnetic fields until they become ionised by various interaction processes with particles from the background plasma. Ideally this will occur in the core of the plasma for effective heating. The beam deposition can be calculated using the following equation:

$$\frac{N_{beam}(l)}{N_{beam,0}} = e^{-\int_0^l n(l') \sigma_{eff}(l') dl'}, \quad (2.3.1)$$

with  $l$  the distance from the beam entry into the plasma and  $\sigma_{eff}$  the interaction cross-section. The neutrals can ionise through a process known as charge exchange, they can ionise directly by collision with plasma electrons or ions, or can go through a multistep ionisation process.

#### 2.3.1 Cross Sections

The probability of ionising a neutral beam particle in a plasma is described in [7, 8]. Formulas to calculate the cross section of each ionisation process have been taken from these two articles in order to predict the neutral beam ionisation and penetration in the plasma. Charge exchange involves the electron bound to the neutral beam particle being exchanged with an ion in the plasma and can be numerically evaluated using

$$\sigma_{cx} = 0.6937 \times 10^{-18} \frac{(1 - 0.155 \log_{10} E)^2}{1 + 0.1112 \times 10^{-14} E^{3.3}}, \quad (2.3.2)$$

where the beam particle energy  $W_b$  is normalised by its mass  $E = W_b/m_b$  [eV/amu]. For the neutral-ion ionisation cross sections, a differentiation is made between the background plasma protons-deuterons-tritons and the background impurities. For the former, two differ-

ent functions are used depending on the beam particle energy. For  $E > 150\text{keV}$ :

$$\sigma_{i,+} = 3.6 \times 10^{-16} \log_{10}(0.1666E)/E. \quad (2.3.3)$$

For  $E \leq 150\text{keV}$ :

$$\sigma_{i,-} = 10^{-0.8712 \log_{10}(E)^2}. \quad (2.3.4)$$

For the high-Z impurities:

$$\sigma_Z = Z_{eff} \left( 7.457 \times 10^{-20} \left( \frac{1}{1 + 0.08095w} \right) + 2.754 \frac{\log_n(1 + 1.27w)}{64.58 + w} \right), \quad (2.3.5)$$

where  $w = E/(Z_{eff} \times 10^3)$ . The cross-section for electrons is the only contribution to the beam deposition effective cross-section  $\sigma_{eff}$  that is a function of the beam line coordinate  $l$ . For W7-X, the beam injection energy ( $\sim 55\text{keV}$ ) is low enough that the cross section for charge exchange and ions are significantly larger than that for the electron ionisation, see figure 2.6.

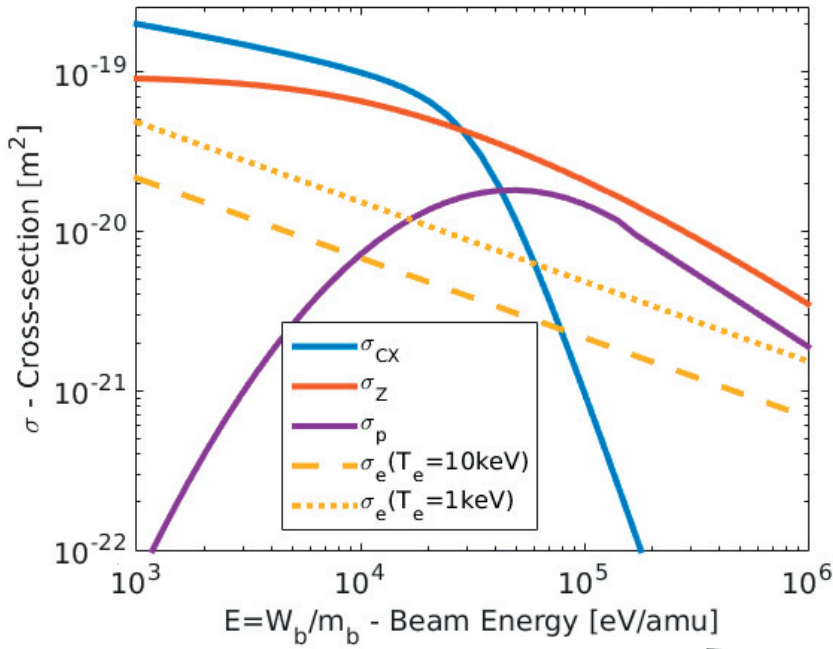


Figure 2.6 – Ionisation cross section  $\sigma$  against hydrogen beam energies  $E = W_b/m_b$ .  $\sigma_e$  was made using a temperature of 1 and 10keV and  $\sigma_Z$  with  $Z_{eff} = 1.25$ .

The effective electron ionisation cross-section is averaged over a Maxwellian electron distribution:

$$\bar{\sigma}_e = \frac{\langle \sigma_e v_e \rangle}{1.3715 \times 10^4 \sqrt{E}}, \quad (2.3.6)$$

where the electron ionisation cross-section is calculated for energies  $E > I$ ,  $I = 13.6\text{eV}$ , using the formula:

$$\sigma_e = \frac{1 \times 10^{-17}}{I \cdot E} \left[ 0.1845 \log_n \left( \frac{E}{I} \right) + \sum_{i=1}^5 B_i \left( 1 - \frac{I}{E} \right)^i \right], \quad (2.3.7)$$

using the constants  $B_i \in \{-0.032226, -0.034539, 1.4003, -2.8115, 2.2986\}$ . The multistep ionisation process accounts for the influence of the energy states of the neutral beam on the ionisation. As the neutral passes through the plasma, it can be excited into higher energy states by collisions with the plasma until ionisation occurs. The increase in the interaction cross-section is calculated as shown in [9], as a function of the electron density and plasma  $Z_{eff}$ . For values of  $1 < Z_{eff} < 2$ , the increase in cross section  $\sigma_{eff} \rightarrow \sigma_{eff}(1 + \delta)$  is approximated by  $\delta = 0.4 \times 10^{-5}$ . A plot of the cross sections against the mass normalised beam energy is shown in figure 2.6, including the influence of the multistep ionisation.

### 2.3.2 Important NBI Parameters

The total effective cross-section depends mostly on charge-exchange and ionisation with ions and impurities for core plasma temperatures above 3keV and injection energies around 50 – 150keV. This is common for NBI injection in most current tokamak and stellarator devices (note ITER will have 1MeV beams using negative ion beam technology). For such plasma temperatures the penetration depth is a function of the density of the ion species along the beam line direction  $l$ . For flat-top density profiles, such as in W7-X (shown in figure 3.46), the mean free path of the beam is  $\lambda_{mfp} \sim 1/(\sigma_{CX} + n_{e,0} \sum_i X_i \sigma_i)$  with  $X$  the concentration of the species and  $i$  indicating ion and impurity species only. The mean free path is therefore also proportional to the beam injection energy. In order to understand the evolution of the beam species, the beam particle distribution function is calculated from a balance between collisions, sources and losses (see equation 2.4.15 for further explanations):

$$\frac{\partial f_{0,\alpha}}{\partial t} = \sum_{\beta} \mathcal{C}[f_{\alpha}, f_{\beta}] + S_0 - L. \quad (2.3.8)$$

When NBI heating is applied, the three terms on the RHS eventually balance to form a slowing down distribution. The collisional term  $\mathcal{C}$  in equation 2.3.8 indicates the transfer of energy from the NBI particles to the background plasma. This means that NBI results in both electron and ion heating. The interactions of one test particle with background species (assumed Maxwellian) leads to an equation representing the change in energy of the particle. Assuming that  $v_e \gg v_b \gg v_i$ :

$$\frac{dE_b}{dt} = -\frac{2E_b}{\tau_s} \left[ 1 + \left( \frac{E_{crit}}{E_b} \right)^{(3/2)} \right], \quad (2.3.9)$$

$$E_{crit} = 14.8 A_{NBI} T_e \left[ \sum_{\alpha} \frac{n_{\alpha} Z_{\alpha}^2}{n_e A_{\alpha}} \right]^{2/3}, \quad (2.3.10)$$

where  $\tau_s$  is the Spitzer resistivity slowing down time:

$$\tau_s = 6.3 \times 10^2 \frac{A_b}{Z_b^2} \frac{T_e^{3/2}}{n_e \log_n(\Lambda_e)}. \quad (2.3.11)$$

For large injection energy levels  $E_{inj} > E_{crit}$  and close-to Maxwellian background distribution functions, the power is predominantly transferred to the electrons and not the background ions. Determining the slowing down distribution function of the NBI cannot be accurately evaluated analytically due to the complicated motion of the beam ions through the magnetic geometry. This is evaluated numerically, as described in section 4.1. Equation 2.3.10 also reflects that the choice of the beam ion element is also of important consideration in terms of the amount of power transferred to the ions over the electrons. The beam penetration depth is inversely proportional to the element charge. Additionally, for approximately the same injection energy, the velocity of the particle in the plasma is inversely proportional to the mass of the element, a factor that strongly influences the Doppler-shift. This will become important when considering RF-NBI synergetic heating in section 5.2.

The use of tritium as an NBI injection fuel is possible in tokamaks [10], but for steady-state operation of a reactor device concerns for the radioactivity of the NBI modules will prevent the use of such beam element source. The neutralisation process inside the NBI module results in not only the production of single neutral beam particles, but also molecules of neutrals. Commonly found in NBI systems are bonds of neutral molecules of two or three neutrals. There are different fractions for each of the molecular species produced depending on the beam element used as an NBI source. In the JET tokamak and the W7-X stellarator the particle (and therefore power) fractions are shown in tables 2.2 and 2.3 respectively [11, 12].

Species	max( $W_b$ ) [keV]	$M^1$	$M^2$	$M^3$
H	90	0.28	0.44	0.28
D	125	0.52	0.38	0.1
T	118	0.63	0.26	0.11

Table 2.2 – NBI beam source information for the JET tokamak.

Species	max( $W_b$ ) [keV]	$M^1$	$M^2$	$M^3$
H	55	0.54	0.31	0.15
D	60	0.55	0.20	0.05

Table 2.3 – NBI beam source information for the W7-X stellarator.

A known experimental limit of increasing the beam particle energies of tables 2.2 and 2.3 is that the neutralisation process inside the NBI module reduces in efficiency for positive ions that are accelerated. A technique to overcome this is through the use of negative ions[13]. JT60-U injects 350keV energy negative beam ions and ITER is foreseen to deploy 1MeV beams.

The VENUS-NBI module [14] combines equation 2.3.1 with the inclusion of a numerical representation of the NBI injector geometry in order to simulate NBI ionisation in tokamak and stellarator magnetic geometries. This module has been updated as part of the work of this thesis. A more detailed explanation of how the code works will be given in section 4.

## 2.4 Fast Ion Orbits, Drifts and VENUS-LEVIS

In the presence of a uniform, homogeneous magnetic field, an unperturbed particle will continuously perform gyro-orbits around the field lines such that its motion can be described by

$$v_{\parallel} = \frac{\vec{v} \cdot \vec{B}}{B} = \text{const}, \quad (2.4.1)$$

$$\vec{v}_{\perp} = \vec{v} \cdot \begin{bmatrix} \cos \Omega t & \sin \Omega t \\ -\sin \Omega t & \cos \Omega t \end{bmatrix}. \quad (2.4.2)$$

In tokamak and stellarator devices, the magnetic field is no longer uniform nor homogeneous, and particles can interact with electric fields present in the equilibrium. These effects introduce particle drifts from the magnetic field lines. The general guiding-centre drift equations in general coordinates can be written in the simple form:

$$\dot{\vec{X}} = v_{\parallel} \frac{\vec{B}^*}{B_{\parallel}^*} + \frac{\vec{E}^* \times \vec{b}}{B_{\parallel}^*}, \quad (2.4.3)$$

$$\dot{v}_{\parallel} = \frac{q}{m} \frac{\vec{B}^* \cdot \vec{E}^*}{B_{\parallel}^*}, \quad (2.4.4)$$

Using the following definitions of the modified electric, magnetic and parallel magnetic fields respectively,

$$\vec{E}^* = \vec{E} - \left( \frac{\mu}{q} + v_{\parallel} \rho_{\parallel} \right) \vec{\nabla} B - \rho_{\parallel} \dot{\vec{B}}, \quad (2.4.5)$$

$$\vec{B}^* = \vec{B} + \rho_{\parallel} \vec{\nabla} \times \vec{B}, \quad (2.4.6)$$

$$B_{\parallel}^* = \vec{b} \cdot \vec{B}^*. \quad (2.4.7)$$

The magnetic field in tokamak and stellarator devices is curved and particles travelling along field lines experience a change in the magnetic field throughout their motion, giving rise to the curvature and grad-B drifts that can be identified from equations 2.4.3, 2.4.5-2.4.7.

$$\vec{v}_\kappa = v_\parallel \rho_\parallel \frac{\vec{B} \times \vec{\kappa}}{BB_\parallel^*}, \quad (2.4.8)$$

$$\vec{v}_{\nabla B} = \frac{\mu}{q} \frac{\vec{B} \times \nabla B}{BB_\parallel^*}, \quad (2.4.9)$$

where the magnetic field line curvature  $\kappa$  is defined as

$$\vec{\kappa} = -\frac{\vec{B}}{B} \times \left( \nabla \times \frac{\vec{B}}{B} \right). \quad (2.4.10)$$

From equations 2.4.3, the particle drift induced by the presence of an electric field can also be extracted

$$\vec{v}_{\vec{E} \times \vec{B}} = \frac{\vec{E} \times \vec{B}}{BB_\parallel^*}. \quad (2.4.11)$$

The guiding centre equations and therefore the particle drifts shown here are calculated by the VENUS-LEVIS code[15].

### 2.4.1 Orbit Types in Tokamaks

A particle in a tokamak equilibrium with no externally applied electric or magnetic fields can be approximated to have three constants of motion. The particles energy is a constant of motion when the electromagnetic fields are time-independent, balancing the magnetic potential energy with the kinetic energy of the particle. The canonical toroidal momentum  $p_\phi$  is conserved in axisymmetric magnetic equilibria such as tokamaks. The magnetic moment  $\mu = mv_\perp^2/2B$  is always *nearly* constant, assuming that particle adiabaticity is respected. Considering these constants of motion, especially the toroidal momentum  $p_\phi$ , allows the identification of the orbit type of a particle in toroidally axisymmetric tokamaks. The method was illustrated in [16]. The canonical toroidal momentum is defined as

$$p_\phi/q = -\psi + mv_\parallel B_\phi/q|B| = -\psi + \frac{\sigma m B_\phi |v|}{q B_0} \sqrt{H(H - \Lambda)}, \quad (2.4.12)$$

where  $\psi$  is the poloidal magnetic flux (zero at the magnetic axis),  $B_0$  is the magnetic field at the magnetic axis,  $\sigma = v_\parallel/|v_\parallel|$ ,  $H = B_0/B$  (the denominator is the magnetic field evaluated at the position of the particle) and  $\Lambda = \mu B_0/E_{kin}$ . Rearranging equation(2.4.12) in terms of the

guiding centre constants of motion  $p_\varphi$ ,  $\mu$ ,  $E_{kin}$  and  $\sigma$ ,

$$H = \frac{1}{2}\Lambda \pm \frac{1}{2}\sqrt{\Lambda^2 + \left(\frac{2B_0(p_\varphi + q\psi)}{m\sigma|v|B_\varphi}\right)^2}. \quad (2.4.13)$$

Knowing the maximum and minimum values of  $B_\varphi$  on a flux surface allows the calculation of the orbit type of a particle, located at B, with the constants of motion  $(p_\varphi, \mu, E)$ . For example, knowing the value of the magnetic field where the particle would bounce  $B_b = B_0/\Lambda$  indicates whether the particle is trapped or passing. This can provide insight into the drift a particle will undergo from its average flux surface during its motion around the tokamak [17]. Therefore, orbit types such as co and counter passing, trapped and even more exotic orbits such as potato and cherry orbits can be identified using this method.

For stellarators, orbit types are more difficult to evaluate, as conservation in the toroidal canonical momentum is lost with the presence of a 3D magnetic field. The main methods used in this thesis use numerical techniques to evaluate particle orbit types. The Fokker-Planck code VENUS-LEVIS uses numerical markers to represent groups of particles by assigning each marker a weight. To determine the number of markers that are passing or trapped, symmetries in  $v_\parallel$  can be exploited. For simulations with equal marker weights, the weightings of the markers are modified (unphysically) according to whether the marker has a positive or negative value of  $v_\parallel$ . For unequal marker weights, markers with either positive or negative  $v_\parallel$  have their weights set to zero. The marker distribution is then simulated without Monte-Carlo processes using the Fokker Planck code over multiple bounce time-scales. A rough estimate of how many markers are passing is to see how many markers remain with the same value of  $v_\parallel$ , checking the sign of  $v_\parallel$  over many simulation diagnostics.

### 2.4.2 Radial Electric Field in W7-X

For W7-X experiments with plasma collisionalities in the banana regime, ion radial transport would be significantly different from that of the electrons in the case of a vanishing electric field. Radial currents are negated by the establishment of an ambipolar electric field, which also serves to preserve quasineutrality for tokamak and stellarator magnetic devices. Such an electric field is purely in the radial direction. The  $\vec{E} \times \vec{B}$  drift term in equation 2.4.11 will therefore have both poloidal and toroidal components but no radial component

$$v_{\vec{E} \times \vec{B}} = \frac{E_r}{|\nabla s|B\sqrt{g}B_\parallel^*} (B_\theta \hat{e}_\varphi - B_\varphi \hat{e}_\theta). \quad (2.4.14)$$

For any given plasma profiles and magnetic equilibrium, this radial electric field can be calculated by stellarator transport codes such as the NEO-2 package [18] (which includes neoclassical transport coefficient calculation using DKES [19]). The resulting radial electric field for the low, standard and high mirror is shown in figure 2.7.



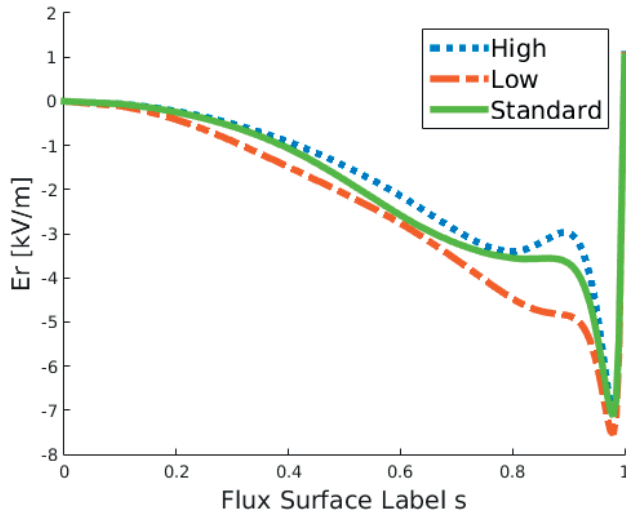
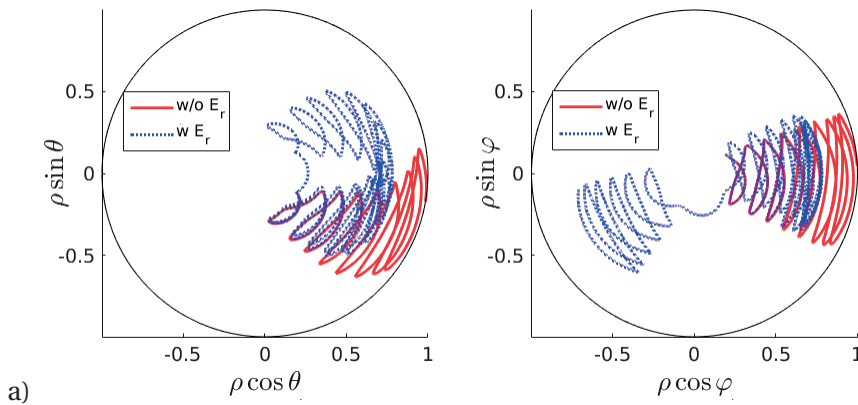


Figure 2.7 – Radial electric field  $E_r$  calculated for each of the three toroidal magnetic mirror configurations with the NEO-2 code package.

The ambipolar electric field has an effect also on the fast ions, provided that the kinetic energy of the fast ion is not too large. In essence, the  $\nabla B$  and  $\vec{\kappa}$  drifts of equations 2.4.8 and 2.4.9 should not be so large that a particle completes a bounce orbit before the  $\vec{E} \times \vec{B}$  drift of equation 2.4.11 can force a particle to complete a full circuit either in the toroidal or poloidal direction. Ion confinement with and without the presence of  $E_r$  in the different mirror equilibria indicate significant improvement with the inclusion of  $E_r$ . The influence of the poloidal and toroidal drifts induced by the radial electric field help ions to not become trapped in the magnetic wells that would otherwise induce large radial transport and thus losses. Examples of the improved confinement in the low and high mirror are shown in figure 2.8. The right hand side plots in 2.8 (a) and (b) mix the toroidal and radial directions whilst neglecting the poloidal direction, reflecting, for example, if a particle is trapped in one toroidal period. These simulations were carried out without the presence of Coulomb collisions using thermal particle energies (4keV) and a pitch angle of 0.3.



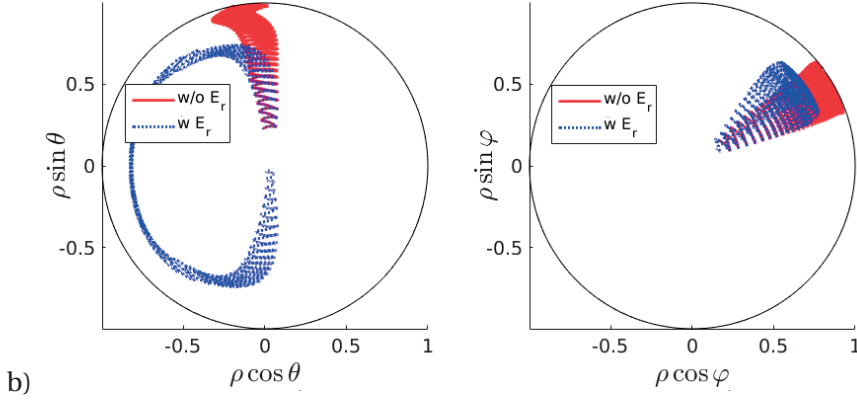


Figure 2.8 – Ion orbits in the a) low and b) high mirror configurations with and without the presence of the radial electric field. The plots are made using pseudo-coordinates in the left) poloidal and right) toroidal planes.

### 2.4.3 Collisionality

In addition to a particle's velocity drift caused by the curvature,  $\nabla B$  and  $\vec{E} \times \vec{B}$ , particle movement is also induced from collisions with the background plasma. Without the presence of ICRF the evolution of the distribution function for plasma species  $\alpha$  is

$$\frac{df_\alpha}{dt} = \sum_\beta \mathcal{C}_{\alpha,\beta}[f_\alpha, f_\beta] + S - L, \quad (2.4.15)$$

where  $S$  is a source term (e.g. NBI) and  $L$  is the particle loss term. The collision operator,  $\mathcal{C}_{\alpha,\beta}$ , is known as the Landau operator and calculates the collisions between the species alpha with all other plasma species. It can be written as

$$\mathcal{C}_{\alpha,\beta} = \frac{1}{2} v_{\alpha,\beta}^\lambda \left[ \frac{\partial}{\partial \lambda} (1 - \lambda^2) \frac{\partial}{\partial \lambda} \right] f_\alpha - \frac{1}{v^2} \frac{\partial}{\partial v} \left[ v^2 v_{\alpha,\beta}^{E_{\alpha,\beta}} \left( \frac{T_\beta}{m_\alpha} \frac{\partial}{\partial v} f_\alpha + v_\alpha f_\alpha \right) \right]. \quad (2.4.16)$$

The first term corresponds to pitch angle ( $\lambda = v_\parallel / v$ ) scattering from Coulomb collisions, the second representing scattering in energy and for highly energetic particle distributions this term would predominately act as a slowing down interaction due to Coulomb collisions. The pitch angle and energy collision frequencies are

$$v_{E_{\alpha,\beta}} = v_0 \frac{m_\alpha}{m_\beta} \frac{\Psi(x)}{v_{th,\beta}^2 v_\alpha}, \quad (2.4.17)$$

$$v_{\lambda_{\alpha,\beta}} = v_0 \frac{\phi(x) - \Psi(x)}{v_\alpha^3}, \quad (2.4.18)$$

$$v_0 = n_\beta \frac{Z_\alpha^2 Z_\beta^2 \ln \Lambda_\beta}{4\pi m_\alpha^2 \epsilon_0^2}, \quad (2.4.19)$$

with  $\phi(x)$  the error function,  $x = v_\alpha / v_{th,\beta}$  and

$$\Psi(x) = \frac{\phi(x) - x\phi'(x)}{2x^2}. \quad (2.4.20)$$

The mean and standard deviation of the values from the Coulomb scattering in pitch angle and energy space can be used to form a Monte-Carlo operator. This numerically represents the interactions between the individual numerical marker and the background plasma

$$\delta E = -2 \sum_\beta v_{E\alpha,\beta} \delta t \left[ E - \left( \frac{3}{2} + \frac{E}{v_{E\alpha,\beta}} \frac{dv_{E\alpha,\beta}}{dE} \right) T_\beta \right] + 2\mathbb{R}_E \sqrt{\sum_\beta v_{E\alpha,\beta} T_\beta E} \delta t, \quad (2.4.21)$$

$$\delta \lambda = - \sum_\beta v_{\lambda\alpha,\beta} \lambda \delta t + \mathbb{R}_\lambda \sqrt{(1 - \lambda^2) \sum_\beta v_{\lambda\alpha,\beta}} \delta t, \quad (2.4.22)$$

for  $\mathbb{R}_{\lambda,E}$  as the sign of random numbers taken between  $[-1,1]$ . Equations 2.4.21 and 2.4.22 are implemented in VENUS-LEVIS to simulate collisions between a numerical marker and the background plasma.

#### 2.4.4 Wave-Particle Interaction : Quasi-Linear Operator

Wave-particle resonance in a Fokker-Planck code can also be calculated using Monte-Carlo operators. The first derivation of velocity diffusion in magnetised plasmas can be found in [20]. During wave-particle interaction, energy is transferred from the wave to the particle or vice-versa, modifying both the particle distribution function and the wave propagation and absorption. This is a non-linear kinetic process that is difficult to numerically evaluate for tokamak or stellarator plasmas. The Quasi-linear Diffusion (QLO) model was developed on the assumption that only a small amount of particles resonate and exchange energy with the wave, which implies that on RF-diffusion time-scales the perturbed distribution function will not grow large enough to influence to propagation of the wave. Linearisation of the particle distribution function  $f = f_0 + \delta f$  requires that the resonant particle distribution  $\delta f$  remains small compared to the background distribution function  $f_0$ . The final distribution function is obtained by a balance between the quasi-linear velocity diffusion, the collisional power transfer, the lost particles and the source of particles:

$$\frac{df_\alpha}{dt} = \mathcal{Q}_{\perp,RF} \frac{\partial^2 f_\alpha}{\partial v_\perp^2} + \sum_\beta \mathcal{C}_{\alpha,\beta}[f_\alpha, f_\beta] + S_0 - L = 0, \quad (2.4.23)$$

where  $\mathcal{Q}_{\perp,RF}$  is the perpendicular velocity diffusion operator induced by the presence of the RF-wave. Over longer time-scales than the wave-particle interaction time, such as collisional time-scales, the energies of the resonant particle population will produce a non-negligible fast ion pressure. The energetic resonant species will have a back-influence on the magnetic equilibrium and wave-propagation. The SCENIC code package [21] has been created to self-consistently include the effects of the fast ion distribution function, including the effect of anisotropy due to the localisation of fast ion pressure at the resonant particle bounce tips, which is aligned to the RF-resonant surface. For the derivation of the QLO used in SCENIC, see the thesis of M. Jucker [21], or a more complete derivation in the books [5, 22]. Averaging the Vlasov equation over the gyro angle  $\phi$ , the time evolution of the resonant species distribution function in resonance with an electromagnetic wave can be written as [20]:

$$\left\langle \frac{\partial f_{\alpha}}{\partial t} \right\rangle = - \lim_{V \rightarrow \infty} Z_{\alpha} \int \frac{d^3 \vec{k}}{V} \int_0^{2\pi} \frac{d\phi}{2\pi} \nabla_p \cdot [(\vec{E}_k + \vec{v} \times \vec{B}_k) \tilde{f}_{\alpha}^{-k}]. \quad (2.4.24)$$

Integration over the gyro-angle is simplified by use of the Bessel functions

$$\left\langle \frac{\partial f_{\alpha}}{\partial t} \right\rangle = - \lim_{V \rightarrow \infty} \pi Z_{\alpha}^2 \sum_{n=-\infty}^{\infty} \int \frac{d^3 \vec{k}}{V} \mathcal{L} \left[ p_{\perp} \delta(\omega_k - k_{\parallel} v_{\parallel} - n\Omega_{c,\alpha}) |\Gamma_{n,k}|^2 p_{\perp} \mathcal{L} \tilde{f}_{\alpha}^{-k} \right], \quad (2.4.25)$$

$$\mathcal{L} = \left( 1 - \frac{k_{\parallel} v_{\parallel}}{\omega_k} \right) \frac{1}{p_{\perp}} \frac{\partial}{\partial p_{\perp}} + \frac{k_{\parallel} v_{\perp}}{\omega_k} \frac{1}{p_{\perp}} \frac{\partial}{\partial p_{\parallel}}, \quad (2.4.26)$$

$$\Gamma_{n,k} = \frac{1}{2} \left[ E_k^+ e^{-i\psi} J_{n-1}(Y) + E_k^- e^{+i\psi} J_{n+1}(Y) \right] + \frac{v_{\parallel}}{v_{\perp}} E_k^{\parallel} J_n(Y), \quad (2.4.27)$$

where  $p_{\parallel,\perp}$  is the parallel and perpendicular momentum respectively, and  $Y = k_{\perp} v_{\perp} / \Omega_c$ . From these relations the perpendicular diffusion coefficient  $\mathcal{Q}_{\perp}$  can be extracted, as shown in equation 2.4.29. For the Monte-Carlo operators in the Fokker-Planck code VENUS-LEVIS, the ‘kick’ in the perpendicular velocity is determined by neglecting the influence of the parallel field  $E^{\parallel}$ . This assumption comes from  $\omega_{p,e} \gg \omega_k$  for ICRF heating, which leads to  $E^{\parallel} \ll E^{+,-}$ . The perpendicular velocity diffusion for an individual resonant particle is therefore:

$$(\Delta v_{\perp})^2 = 4\tau \mathcal{Q}_{\perp} = 2\pi\tau\gamma \frac{Z_{\alpha}^2}{m_{\alpha}^2} \delta(\omega_a - k_{\parallel} v_{\parallel} - n\Omega_{c,\alpha}) \left| E^+ e^{-i\psi} J_{n-1}(Y) + E^- e^{+i\psi} J_{n+1}(Y) \right|^2. \quad (2.4.28)$$

When a particle crosses the line of resonance the energy the particle receives is related to the length of time, known as the correlation time  $\tau$ , that the wave and particle have interacted for. This results in the use of the Airy functions. Note that, like in section 3.1, the Bessel functions illustrate the dependence of the interaction on FLR effects. The inclusion of  $E^-$  indicates that energetic ions will also receive energy from the electric field rotating in the direction of the electrons, due to their large Larmor radii. Extracting the mean and standard deviation

provides the quasi-linear Monte Carlo kick in the perpendicular direction

$$\Delta v_{\perp} = \frac{\langle \Delta v_{\perp}^2 \rangle}{2v_{\perp}} + \mathbb{R} \sqrt{2\langle \Delta v_{\perp}^2 \rangle}, \quad (2.4.29)$$

with  $\mathbb{R}$  a random number generated in the interval  $[0, 1]$ ,  $\gamma$  the scaling factor and

$$\langle \Delta v_{\perp}^2 \rangle = \tau^2 \gamma \frac{Z_{\alpha}^2}{m_{\alpha}^2} \left| E^{+} e^{-i\psi} J_{n-1}(Y) + E^{-} e^{+i\psi} J_{n+1}(Y) \right|^2. \quad (2.4.30)$$

Equation 2.4.29 (combined with equation 2.4.30) is the Monte-Carlo stochastic parameter used by the QLO of VENUS-LEVIS to simulate RF-heating in perpendicular velocity space. The scaling factor  $\gamma$  ensures that the RF-power transferred to the plasma equals that of the antenna power. Quasi-linear diffusion also occurs in the parallel velocity. An important feature of the  $\mathcal{L}$  operator in equation 2.4.26 is that for particle resonance with one specific  $k_{\parallel}$ , a distribution function  $f = f[v_{\perp}^2 + (v_{\parallel} - \omega_a/k_{\parallel})^2]$  will remain at a constant energy along the curves in velocity space:

$$v_{\perp}^2 + \left( v_{\parallel} - \frac{\omega_a}{k_{\parallel}} \right)^2 = \text{const.} \quad (2.4.31)$$

Particles moving at the wave parallel velocity will therefore have constant energy unless they become resonant with the wave. In a region of physical space which would be dominated by a single  $k_{\parallel}$  value, particles would move along concentric circles in  $(v_{\perp}, v_{\parallel})$  until a resonance occurs, where a change in the perpendicular velocity (given by 2.4.29) would move particles between these curves to increase or decrease  $v_{\perp}$  depending upon the sign of  $\nabla_{\perp} f_0$ . The stochastic Monte-Carlo operator in the parallel direction implemented into the QLO in VENUS-LEVIS is therefore

$$\Delta v_{\parallel} = \frac{k_{\parallel}}{\Omega_c} v_{\perp} \Delta v_{\perp}. \quad (2.4.32)$$

Rearranging equations 2.4.29 and 2.4.32 relates the change in the perpendicular velocity to the respective change in the parallel velocity

$$\frac{\Delta v_{\parallel}}{\Delta v_{\perp}} = \frac{v_{\perp}}{v_{\parallel}} \left( \frac{\omega_a}{n\Omega} - 1 \right). \quad (2.4.33)$$

The SCENIC package makes the assumption that there is one dominant  $k_{\parallel}$  value for each point in physical space. In toroidally axisymmetric equilibria, the  $n_{\phi}$  are not coupled, allowing one value of  $n_{\phi}$  to be used as an initial condition on  $k_{\parallel}$  for the LEMan simulation. After completion of the simulation, a convolution of the electric field is made according to the mode number spectrum excited by the RF-antenna. Note that this does not apply to stellarators due to the absence of toroidal axisymmetry. If multiple wave-vectors (mode numbers) are excited by the RF-antenna, the theory of quasi-linear diffusion breaks down. In the presence of multiple resonances, particles can move from one characteristic to another. The marginal stability

indicated by the H-theorem is therefore not guaranteed. Multiple  $k_{\parallel}$  values can be included in the Monte Carlo simulation, provided that the resulting resonant surfaces values are not close to one another in velocity space. This is important when considering the choice and number of values of  $n_{\phi}$ , the toroidal wave-number, to accurately represent the RF antenna in 2D equilibria.

## 2.5 The Self-Consistent Iterative Method

Fast ion densities of typical resonant minority populations are usually of low concentrations. However, the strong anisotropies in the fast ion pressure can have a large influence on both the magnetic equilibrium and the wave-propagation. This is because trapped resonant particles tend to align their bounce tips at the resonant surface, where the particles tend to spend the most amount of time throughout a full orbit. The build up of fast ion pressure at the resonance location can heavily modify the wave-propagation and resonance such that absorption by the resonant species is increased. In order to simulate this self-consistent influence of the resonant ion distribution on the magnetic equilibrium and wave-propagation, moments of the distribution are taken and fed back through the other codes, iterating until convergence is reached. For the fast ion fraction of the Fokker Planck simulation (fast defined as particles with  $E > nT_e$ , with  $n > 1$ ) a bi-Maxwellian is used. For the thermal fraction of the remaining particles a Maxwellian distribution is used to evaluate the moments. The SCENIC package uses the zeroth-order Vlasov bi-Maxwellian distribution function[23],

$$f_h(\bar{s}, E, \mu) = \aleph_h(\bar{s}) \left( \frac{m_h}{2\pi T_{\perp}(\bar{s})} \right)^{\frac{3}{2}} \exp \left\{ -m_h \left( \frac{\mu B_c}{T_{\perp}(\bar{s})} + \frac{|E - \mu B_c|}{T_{\parallel}(\bar{s})} \right) \right\}, \quad (2.5.1)$$

with  $\bar{s}$  the binned value in the radial direction  $s$ . The fast particle density is related to the fast particle density coefficient by,

$$n_h(\bar{s}, B) = \aleph_h(\bar{s}) A(\bar{s})^{-\frac{1}{2}} C(\bar{s}, B), \quad (2.5.2)$$

with  $A = T_{\perp}/T_{\parallel}$  and the constant term  $C$  has a value that depends upon the value of the magnetic field strength. For  $B > B_c$

$$C(\bar{s}, B) = \frac{(B/B_c)}{[1 - A(\bar{s})(1 - (B/B_c))]} \quad (2.5.3)$$

For  $B < B_c$

$$C(\bar{s}, B) = \frac{B}{B_c} \frac{[1 + A(\bar{s})(1 - (B/B_c)) - 2A(\bar{s})^{\frac{3}{2}}(1 - (B/B_c))^{\frac{3}{2}}]}{1 - [A(\bar{s})(1 - (B/B_c))]^2}. \quad (2.5.4)$$

In addition,

$$p_{\parallel}(\bar{s}, B) = p(\bar{s}) + \aleph_h(\bar{s}) T_{\parallel}(\bar{s}) H(\bar{s}, B) = p(\bar{s}) + p_{\parallel}^h(\bar{s}, B), \quad (2.5.5)$$

and

$$p_{\perp}(\bar{s}, B) = p_{\parallel}(\bar{s}, B) - B \left. \frac{\partial p_{\parallel}}{\partial B} \right|_{\bar{s}}. \quad (2.5.6)$$

The constant term  $H$  depends upon the value of the magnetic field strength. For  $B > B_c$

$$H(\bar{s}, B) = \frac{(B/B_c)}{[1 - A(\bar{s})(1 - (B/B_c))]} \quad (2.5.7)$$

For  $B < B_c$

$$H(\bar{s}, B) = \frac{B}{B_c} \frac{[1 + A(\bar{s})(1 - (B/B_c)) - 2A(\bar{s})^{\frac{5}{2}}(1 - (B/B_c))^{\frac{5}{2}}]}{1 - [A(\bar{s})(1 - (B/B_c))]^2}. \quad (2.5.8)$$

To fit the bi-Maxwellian to the Fokker-Planck marker population, first the particles are binned in 3D space

$$n^h(\bar{s}, \theta, \phi) = \sum_{i \in \text{fast}} \frac{w_i}{\delta V}, \quad (2.5.9)$$

$$p_{\parallel}^h(\bar{s}, \theta, \phi) = \sum_{i \in \text{fast}} v_{\parallel}^2 \frac{w_i}{\delta V}, \quad (2.5.10)$$

$$p_{\perp}^h(\bar{s}, \theta, \phi) = \sum_{i \in \text{fast}} \frac{v_{\perp}^2}{2} \frac{w_i}{\delta V}. \quad (2.5.11)$$

The anisotropy can be obtained by equating  $p_{\perp}^h/p_{\parallel}^h$  from equations 2.5.10 and 2.5.11 with 2.5.5 and 2.5.6 to give, for  $B > B_c$

$$\left\langle A \frac{B}{B_c} (1 - A(1 - B/B_c)^{-1}) \right\rangle = \left\langle \frac{\sum_{i \in \text{fast}} \frac{v_{\perp}^2}{2} \frac{w_i}{\delta V}}{\sum_{i \in \text{fast}} v_{\parallel}^2 \frac{w_i}{\delta V}} \right\rangle = \left\langle \frac{p_{\perp}^h}{p_{\parallel}^h} \right\rangle, \quad (2.5.12)$$

and for  $B < B_c$

$$\begin{aligned} & \left\langle A \frac{B}{B_c} \frac{(1 - A(1 - B/B_c))^2 - 5(1 - A(1 - B/B_c))^{3/2} + (A(-B/B_c))^{7/2}}{(1 - A^2(1 - B/B_c)^2)(1 + A(1 - B/B_c)) - 2(A(1 - B/B_c))^{5/2}} \right\rangle \\ & = \left\langle \frac{\sum_{i \in \text{fast}} \frac{v_{\perp}^2}{2} \frac{w_i}{\delta V}}{\sum_{i \in \text{fast}} v_{\parallel}^2 \frac{w_i}{\delta V}} \right\rangle = \left\langle \frac{p_{\perp}^h}{p_{\parallel}^h} \right\rangle, \end{aligned} \quad (2.5.13)$$

with the angular brackets indicating the flux surface average. Thus, equations 2.5.12 and 2.5.13 are solved for  $A(\bar{s}) = T_{\perp}^h/T_{\parallel}^h$ . Knowing the flux surface anisotropy, one can obtain the density

factor  $\aleph_h$  from equating equation 2.5.9 with 2.5.2

$$\langle \aleph_h(\bar{s}) A(\bar{s})^{-\frac{1}{2}} C(\bar{s}, B) \rangle = \left\langle \sum_{i \in \text{fast}} \frac{w_i}{\delta V} \right\rangle = \langle n_h(\bar{s}, B) \rangle. \quad (2.5.14)$$

Finally,  $T_{\parallel}^h$  is obtained by equating 2.5.10 with 2.5.11,

$$\langle \aleph_h(\bar{s}) T_{\parallel}^{\frac{1}{2}} C(\bar{s}, B) \rangle = \left\langle \sum_{i \in \text{fast}} v_{\parallel}^2 \frac{w_i}{\delta V} \right\rangle = \langle p_{\parallel}^h(\bar{s}, B) \rangle. \quad (2.5.15)$$

This also leads to the calculation of  $T_{\perp}^h(\bar{s}) = A(\bar{s}) T_{\parallel}^h(\bar{s})$ . The marker distribution taken from the VENUS-LEVIS Fokker Planck simulation can be used in a Particle-In-Cell (PIC) like method to self-consistently calculate the back-influence of the fast ion population on the magnetic flux surface  $(p_{\parallel}^h, p_{\perp}^h)$  geometry and the RF-wave propagation and absorption  $(T_{\parallel}, A, \aleph_h)$ .

## 2.6 Summary

This chapter introduced the basics of the physics investigated in this thesis, including the analytical theory and numerical tools implemented to resolve and explore such physics. The SCENIC package is a Particle-In-Cell like code package to investigate the self-consistent influence of ICRF interaction with a resonant plasma species in full 3D magnetic equilibria, as well as the tools to simulate NBI ionisation and motion in such 3D magnetic topologies. This self-consistency includes important effects such as the Finite Orbit Width (FOW) and anisotropies of the energetic ions, even for synergetic ICRF-NBI heating. The basics of Magneto-HydroDynamic ideal MHD closed flux surface geometries and how they are calculated by ANIMEC was presented. This included important parameters such as stellarator symmetry and toroidal magnetic mirroring in the W7-X stellarator. The auxiliary heating method ICRF was introduced with a description of the appropriate wave launched into the plasma for such heating. This included a brief explanation of the cold dielectric tensor as a means to evaluate wave propagation, absorption and reflection in magnetised plasmas. The resonance condition for wave-particle interaction was shown to produce resonant magnetic surfaces, the location of which depends on the antenna frequency, the parallel velocity of the particle and the dominant parallel wave-vector near the resonant layer. Significant differences between the resonant surface in tokamaks and in the W7-X stellarator show that, depending on the toroidal magnetic mirror strength of W7-X, certain toroidal locations may not permit wave-particle energy exchange. The LEMAN code package was introduced and the basic equations solved were illustrated. Throughout this thesis, many updates have been made to the codes and so a more in-depth explanation of the current code status is given in section 3 and 4. Calculation of the NBI ionisation into a magnetised plasma has been described and key influential parameters on the deposition explored. A brief introduction of particle motion, radial drifts and the VENUS-LEVIS Fokker Planck solver are presented. The code calculates particle motion in full-3D magnetic geometries with the inclusion of curvature  $\kappa$ ,  $\nabla B$  and  $\vec{E} \times \vec{B}$  radial drifts as well as particle perturbations from Coulomb collisions and the presence of



ICRF waves using a Quasi-Linear Operator. The latter two are numerically implemented in the code via the use of Monte-Carlo operators. An additional parameter was mentioned that is crucial to accurately simulate particle motion in W7-X: the radial electric field  $E_r$  that arises from the ambipolarity condition, ensuring quasineutrality. In order to iterate self-consistently between these codes, the moments of the fast ion population calculated by the Fokker Planck code VENUS-LEVIS allows the influence of RF-induced fast ion pressures and anisotropies to have a back-influence on both the magnetic equilibrium, NBI ionisation and the RF-wave propagation, absorption and reflection.



## 3 Numerical Advancements and Application for ICRF Optimisation

Many significant updates have been made to the LEMan wave-propagation code in the frame of this thesis. This chapter aims to describe why and how these have been numerically implemented. This includes application of the updates to tokamak and stellarator ICRF scenarios to illustrate the relevance and importance of the code modifications. The chapter describes the updates to the dielectric tensor and the calculation of the perpendicular wave vector using a hot plasma dispersion relation. In addition, it describes the generalisation of the magnetic coordinate system input into the code, and the ability to simulate multiple plasma species. The code is then benchmarked against other similar codes. The method that LEMan deploys for simulating the RF-antenna geometry in tokamak and stellarator devices is also described. The SCENIC code package is applied to investigate minority species heating in 2D and 3D tokamak and 3D stellarator magnetic geometries, with the intention for providing a theoretical and numerical based optimisation of the application of ICRF for such fusion devices. The final section concerns harmonic heating in the JET tokamak, in order to assess the influence of the majority plasma heating in minority species heating schemes.

### 3.1 Updating the LEMan Dielectric tensor to Include Higher Order (Hot Plasma) Effects

The propagation of an electromagnetic wave through a magnetised plasma is a complicated process, and is governed by the dielectric tensor  $\bar{\bar{\epsilon}}$  of the plasma. It will be shown in this section that the physics of wave propagation, refraction, reflection and absorption are all contained in the dielectric tensor. There are many different methods to calculate  $\bar{\bar{\epsilon}}$ . Originally, the LEMan code [6] started with the cold plasma model, mentioned in [24]. The cold model solves the reduced MHD equations whilst retaining the two-fluid properties of the electron and ion populations. The limitation of the cold model is that no plasma velocity distribution effects can be included, and hence no Doppler shift broadening of the absorption profile. In [6], the dielectric tensor was modified to include warm effects through a first order expansion

### Chapter 3. Numerical Advancements and Application for ICRF Optimisation

---

of the distribution function with respect to the FLR parameter

$$\lambda_\alpha = \frac{k_\perp^2 v_{th,\alpha}^2}{2\Omega_{c,\alpha}^2}, \quad (3.1.1)$$

For this expansion, the assumption  $\lambda \ll 1$  was applied. Intuitively, this implies that over one period of a particle's gyro orbit the phase of the wave does not significantly vary and so resonance will only occur with the fundamental harmonic. This assumption is consistent with retaining only the zeroth and first order terms with respect to the gyro-angle  $\phi$  and the wave-phase  $\psi$ . The approximation made which limits the model to first order is that  $\phi = \psi$ , which allows the plasma distribution function to be simplified by Fourier decomposing in  $\chi = \{\phi, \psi\}$ :

$$\tilde{f}_\alpha = \int_{-\infty}^{\infty} \tilde{f}_{l,\alpha} e^{il\chi} d\chi, \quad (3.1.2)$$

The basic FLR reduction of the dielectric tensor developed in [6] is used for the description of many of the ICRF heating schemes discussed in chapter 3 and 5. However, advanced effects such as harmonic heating, a heating method commonly used in ICRF fusion experiments, cannot be described under this approximation. Additionally, the off-axis diagonal dielectric tensor elements  $\varepsilon_{l,\parallel}$  or  $\varepsilon_{\parallel,l}$  (with  $l \in \{n, b\}$ ) are zero (see equation 3.1.24) in the basic FLR reduction of [6]. This neglects terms such as the Transit Time Magnetic Pumping (TTMP) effects, resulting in strongly unphysical absorption of wave power by the electron population even for fundamental harmonic simulations, as described in this section.

The analytical solution for the dielectric tensor recently implemented in the LEMan code retains FLR effects to all orders, and thus wave-particle resonance is included even for high harmonics, and includes important off-diagonal terms such as TTMP effects. The analytical approach is to solve for the distribution function along unperturbed (by the presence of an externally applied electric field) particle orbits via the method of characteristics. Intuitively speaking, the distribution function of each plasma species is integrated along the trajectory of the unperturbed orbit, and any perturbation of the particle from this orbit must directly relate to some interaction with the wave. Using this approach one can calculate the small perturbation to the distribution function via the influence of the electromagnetic wave amplitude on the background plasma. This method is already well explained in multiple plasma physics books [5, 22, 25]. The basics are outlined here. On RF-wave propagation time-scales, the Fokker-Planck equation 2.4.23 can be reduced to neglect the influence of collisionality and plasma sources and losses. Projecting the Vlasov equation along the unperturbed, zero-order orbit  $\vec{R} = \vec{R}[\vec{r}(t), \vec{v}(t), t]$ :

$$\left. \frac{df_\alpha}{dt} \right|_{\vec{R}} = \left. \frac{df_{\alpha,0}}{dt} \right|_{\vec{R}} + \left. \frac{d\delta f_\alpha}{dt} \right|_{\vec{R}} = \left[ \frac{\partial}{\partial t} + \vec{v} \cdot \nabla + \frac{q}{m} [\vec{E}(r, t) + \vec{v} \times \vec{B}(r, t)] \cdot \nabla_v \right] \{f_{\alpha,0} + \delta f_\alpha\} = 0. \quad (3.1.3)$$

The linearisation of the Vlasov equation leads to a simplification of the resonant ion distribution function to become a background and a resonant distribution  $f \rightarrow f_0 + \delta f$ . The

### 3.1. Updating the LEMan Dielectric tensor to Include Higher Order (Hot Plasma) Effects

background magnetic field amplitude is assumed to be much larger than the RF wave such that  $\vec{E} \rightarrow \vec{E}_0 + \delta\vec{E}$  with  $\vec{E}_0 = 0$ , and  $\vec{B} \rightarrow \vec{B}_0 + \delta\vec{B}$  with  $\vec{B}_0 \gg \delta\vec{B}$ . All zeroth order terms  $df_0/dt|_{\vec{R}}$  relating the background magnetic field to  $f_0$  are removed due to the integral along the orbit. Second order terms are neglected due to the negligible amplitude. The result can then be rearranged in terms of the perturbed distribution function:

$$\delta f_\alpha(r, v, t) = -\frac{q_\alpha}{m_\alpha} \int_{-\infty}^t \{\delta\vec{E}(r', t') + \vec{v}' \times \delta\vec{B}(r', t')\} \cdot \nabla_{v'} f_{0,\alpha}(v') dt'. \quad (3.1.4)$$

Applying the Maxwell-Faraday law

$$\delta\vec{B} = \frac{\vec{k} \times \delta\vec{E}}{\omega}, \quad (3.1.5)$$

leads to an equation directly relating the perturbed distribution function to the electric field perturbation produced by the RF-wave. Fourier decomposition results in:

$$\delta f_\alpha(r, v, t) = -\frac{q_\alpha}{m_\alpha} \int_{-\infty}^t \delta\vec{E}(r', t') \left\{ \mathbb{1} + \frac{\cdot v' k - v' \cdot k}{\omega} \right\} \cdot \nabla_{v'} f_{0,\alpha}(v') dt' e^{i(\vec{k} \cdot \vec{r}' - \omega t')}. \quad (3.1.6)$$

The trajectory of the particle is assumed to be cylindrical due to its guiding centre motion, such that the relation between  $v'$  and  $v$  is given by:

$$\frac{d\vec{v}'}{dt} = \epsilon \vec{v} \times \Omega_c \hat{e}_\parallel, \quad (3.1.7)$$

with  $\epsilon = q/|q|$ . Assuming cylindrical guiding centre orbits, the translation  $[\vec{r}'(t'), \vec{v}'(t'), t'] \rightarrow [\vec{r}(t), \vec{v}(t), t]$  is given by:

$$v'_n = v_n \cos \Omega_c \tau - \epsilon v_b \sin \Omega_c \tau,$$

$$v'_b = v_b \cos \Omega_c \tau + \epsilon v_n \sin \Omega_c \tau,$$

$$v'_\parallel = v_\parallel,$$

$$r'_n = r_n - \frac{v_n}{\Omega_c} \sin \Omega_c \tau + \frac{\epsilon v_b}{\Omega_c} (1 - \cos \Omega_c \tau),$$

$$r'_b = r_b - \frac{\epsilon v_n}{\Omega_c} (1 - \cos \Omega_c \tau) - \frac{v_b}{\Omega_c} \sin \Omega_c \tau,$$

$$r'_{\parallel} = r_{\parallel} - v_{\parallel} \tau, \quad (3.1.8)$$

with  $\tau = t - t'$ . The coordinates  $\{n, b, \parallel\}$  refer to directions normal to flux surfaces, the binormal coordinate and parallel to the magnetic field respectively. The Fourier amplitude of the perturbed distribution function can then be written as:

$$\begin{aligned} \delta \tilde{f}_{\alpha} = & -\frac{q_{\alpha}}{m_{\alpha}} \int_0^{\infty} d\tau e^{i(\omega - k_{\parallel} v_{\parallel})\tau - i\chi_n v_n - i\chi_b v_b}, \\ & \cdot \left[ E_n \left\{ f'_{\alpha|n} \cos \Omega_{c,\alpha} \tau - \epsilon f'_{\alpha|b} \sin \Omega_{c,\alpha} \tau - \frac{v_{\parallel} k_{\parallel}}{\omega} (f'_{\alpha|n} \cos \Omega_{c,\alpha} \tau - \epsilon f'_{\alpha|b} \sin \Omega_{c,\alpha} \tau), \right. \right. \\ & - \frac{v_b}{\omega} (f'_{\alpha|n} k_b + \epsilon f'_{\alpha|\parallel} k_{\parallel} \sin \Omega_{c,\alpha} \tau) + \frac{v_n}{\omega} (f'_{\alpha|b} k_b + f'_{\alpha|\parallel} k_{\parallel} \cos \Omega_{c,\alpha} \tau) \left. \right\}, \\ & + E_b \left\{ f'_{\alpha|b} \cos \Omega_{c,\alpha} \tau + \epsilon f'_{\alpha|n} \sin \Omega_{c,\alpha} \tau - \frac{v_{\parallel} k_{\parallel}}{\omega} (f'_{\alpha|b} \cos \Omega_{c,\alpha} \tau + \epsilon f'_{\alpha|n} \sin \Omega_{c,\alpha} \tau), \right. \\ & + \frac{v_b}{\omega} (f'_{\alpha|n} k_n + f'_{\alpha|\parallel} k_{\parallel} \cos \Omega_{c,\alpha} \tau) - \frac{v_n}{\omega} (f'_{\alpha|b} k_n - \epsilon f'_{\alpha|\parallel} k_{\parallel} \sin \Omega_{c,\alpha} \tau) \left. \right\}, \\ & + E_{\parallel} \left\{ f'_{\alpha|\parallel} + \frac{v_b f'_{\alpha|\parallel}}{\omega} (\epsilon k_n \sin \Omega_{c,\alpha} \tau - k_b \cos \Omega_{c,\alpha} \tau) - \frac{v_b f'_{\alpha|\parallel}}{\omega} (k_n \cos \Omega_{c,\alpha} \tau + \epsilon k_b \sin \Omega_{c,\alpha} \tau), \right. \\ & \left. \left. + \frac{v_{\parallel}}{\omega} ((f'_{\alpha|n} k_n + f'_{\alpha|b} k_b) \cos \Omega_{c,\alpha} \tau - \epsilon \sin \Omega_{c,\alpha} \tau (f'_{\alpha|b} k_n - f'_{\alpha|n} k_b)) \right\} \right], \quad (3.1.9) \end{aligned}$$

$$\chi_n = \frac{1}{\Omega_{c,\alpha}} [k_n \sin \Omega_{c,\alpha} \tau + \epsilon k_b (1 - \cos \Omega_{c,\alpha} \tau)], \quad (3.1.10)$$

$$\chi_b = \frac{1}{\Omega_{c,\alpha}} [k_b \sin \Omega_{c,\alpha} \tau - \epsilon k_n (1 - \cos \Omega_{c,\alpha} \tau)], \quad (3.1.11)$$

where  $f'|_g$  is the derivative of the zeroth order distribution function with respect to  $g \in \{n, b, \parallel\}$ . In order to evaluate the dielectric tensor, the current induced by the perturbed distribution

### 3.1. Updating the LEMan Dielectric tensor to Include Higher Order (Hot Plasma) Effects

function can be related to the plasma conductivity tensor:

$$\begin{bmatrix} j_n \\ j_b \\ j_{\parallel} \end{bmatrix} = \sum_{\alpha} q_{\alpha} \int d^3v \begin{bmatrix} v_n \\ v_b \\ v_{\parallel} \end{bmatrix} \delta f_{\alpha} = \overline{\overline{\sigma}} \cdot \vec{E}.$$

Single elements of the dielectric tensor can now be extracted from the equation relating  $\delta f$  to  $E$  using its relation with the conductivity tensor:

$$\overline{\overline{\epsilon}} = \mathbb{1} - \frac{\overline{\overline{\sigma}}}{i\omega\epsilon_0}. \quad (3.1.12)$$

The method to calculate  $\epsilon_{nn}$  will now be shown. This involves integrating equation 3.1.9 and extracting the component multiplied by  $E_n$ . To implement this into the LEMan code, an analytical distribution function must be provided to represent the plasma species (including the NBI beam slowing down distribution). A first step is to use an isotropic Maxwellian distribution function:

$$f_M(v_n, v_b, v_{\parallel}) = \left( \frac{1}{\pi v_{th,\alpha}^2} \right)^{\frac{3}{2}} \exp \left\{ -\frac{(v_n^2 + v_b^2 + v_{\parallel}^2)}{v_{th,\alpha}^2} \right\}. \quad (3.1.13)$$

The approach taken here is first to integrate over the perpendicular velocities, then over  $\tau$  and finally over the parallel velocity. Integrating over the perpendicular velocities involves solving integrals with the error function. For definite integrals (which is not the case for the zeroth order Vlasov bi-Maxwellian distribution function (see equation 2.5.1) adopted by the SCENIC package), then the solutions to such a problem are of the form:

$$A_l = \frac{1}{\sqrt{\pi} v_{th,\alpha}} \int_{-\infty}^{\infty} v^l e^{-i\chi v - v^2/v_{th,\alpha}^2} dv,$$

$$A_0 = e^{-\chi^2 v_{th,\alpha}^2/4},$$

$$A_1 = e^{-\chi^2 v_{th,\alpha}^2/4} \left( -\frac{i\chi v_{th,\alpha}^2}{2} \right),$$

$$A_2 = e^{-\chi^2 v_{th,\alpha}^2/4} \left( \frac{v_{th,\alpha}^2}{2} - \frac{\chi^2 v_{th,\alpha}^4}{4} \right). \quad (3.1.14)$$

### Chapter 3. Numerical Advancements and Application for ICRF Optimisation

Using these equations one arrives at:

$$\varepsilon_{nn} = 1 + \frac{iq^2}{2\sqrt{\pi}v_{th,\alpha}m\varepsilon_0\omega} \int dv_{\parallel} \int d\tau e^{i(\omega - k_{\parallel}v_{\parallel})\tau - \lambda(1 - \cos\Omega_{c,\alpha}\tau) - v_{\parallel}^2/v_{th,\alpha}^2},$$

$$\cdot \left\{ (2 - v_{th,\alpha}^2\kappa_n^2) \cos\Omega_{c,\alpha}\tau + v_{th,\alpha}^2\varepsilon\kappa_n\kappa_b \sin\Omega_{c,\alpha}\tau \right\}. \quad (3.1.15)$$

Noting the presence of  $\lambda$  which is as a result of  $v_{th,\alpha}^2(\kappa_n^2 + \kappa_b^2)/4 = \lambda(1 - \cos\Omega_{c,\alpha}\tau)$ . The use of modified Bessel functions of the first kind helps to overcome the issue with the cosine term in the exponential:

$$e^{\lambda \cos\Omega_{c,\alpha}\tau} = \sum_{n=-\infty}^{\infty} I_n(\lambda_{\alpha}) e^{in\Omega_{c,\alpha}\tau}. \quad (3.1.16)$$

To integrate this over  $\tau$ , simplification of the sine and cosine terms is necessary:

$$2 \cos\Omega_{c,\alpha}\tau - v_{th,\alpha}^2\kappa_n(\kappa_n \cos\Omega_{c,\alpha}\tau - \varepsilon\kappa_b \sin\Omega_{c,\alpha}\tau)$$

$$= 2 \cos\Omega_{c,\alpha}\tau + \frac{v_{th,\alpha}^2\kappa_n}{\Omega_{c,\alpha}}(\varepsilon\kappa_b - \varepsilon\kappa_b \cos\Omega_{c,\alpha}\tau - \kappa_n \sin\Omega_{c,\alpha}\tau). \quad (3.1.17)$$

Using the orthogonality relation of the Bessel functions simplifies the integral over  $\tau$ :

$$\sum_{n=-\infty}^{\infty} \int_0^{\infty} d\tau I_n(\lambda_{\alpha}) e^{i(\omega - k_{\parallel}v_{\parallel} + n\Omega_c)\tau} \left\{ \begin{array}{c} 1 \\ \cos\Omega_c\tau \\ \sin\Omega_c\tau \\ \cos\Omega_c\tau \sin\Omega_c\tau \\ \sin\Omega_c\tau^2 \end{array} \right\}$$

$$= \sum_{n=-\infty}^{\infty} \left\{ \begin{array}{c} iI_n(\lambda_{\alpha}) \\ iI'_n(\lambda_{\alpha}) \\ \frac{n}{\lambda}I_n(\lambda_{\alpha}) \\ \frac{n}{\lambda^2}[\lambda I'_n(\lambda_{\alpha}) - I_n(\lambda_{\alpha})] \\ \frac{i}{\lambda^2}[\lambda I'_n(\lambda_{\alpha}) - n^2 I_n(\lambda_{\alpha})] \end{array} \right\} \frac{1}{(\omega - k_{\parallel}v_{\parallel} + n\Omega_c)},$$

with the derivative  $I'_n(\lambda_{\alpha}) = \frac{\partial I_n}{\partial \lambda_{\alpha}}$ . The final step is to integrate over the parallel velocity:

$$\varepsilon_{nn} = 1 + \frac{iq^2}{\sqrt{\pi}v_{th,\alpha}m\varepsilon_0\omega} \int dv_{\parallel} \frac{1}{(\omega - k_{\parallel}v_{\parallel} + n\Omega_c)} e^{-\lambda - v_{\parallel}^2/v_{th,\alpha}^2}$$

$$\cdot \left\{ 2 \sin^2\psi^2 \lambda_{\alpha} [I_n(\lambda_{\alpha}) - I'_n(\lambda_{\alpha})] + \frac{n^2}{2\lambda} I_n(\lambda_{\alpha}) \right\}, \quad (3.1.18)$$



### 3.1. Updating the LEMan Dielectric tensor to Include Higher Order (Hot Plasma) Effects

where the perpendicular wave-vector has been transformed into cylindrical coordinates  $k_n = k_\perp \cos \psi$  and  $k_b = k_\perp \sin \psi$  for convenience. Integrating over the parallel velocity involves the plasma dispersion function [26]:

$$Z(\xi) = \frac{\xi}{\sqrt{\pi}} \int_{-\infty}^{\infty} \frac{1}{\xi - x} e^{-x^2} dx \quad (\text{Im}\{\xi\} > 0) \quad (3.1.19)$$

and

$$Z'(\xi_{n,\alpha}) = -2(1 + \xi_{n,\alpha} Z(\xi_{n,\alpha})), \quad (3.1.20)$$

where

$$\xi_{n,\alpha} = \frac{\omega_{ant} - n\Omega_{c,\alpha}}{k_\parallel v_{th,\alpha}}. \quad (3.1.21)$$

Thus the  $nn$ -th component of the dielectric tensor is:

$$\epsilon_{nn} = 1 + \sum_{\alpha} \mu_{\alpha} \sum_{n=-\infty}^{n=\infty} \left\{ 2 \sin^2 \psi \lambda_{\alpha} [I_n(\lambda_{\alpha}) - I'_n(\lambda_{\alpha})] + \frac{n^2}{2\lambda} I_n(\lambda_{\alpha}) \right\} Z(\xi_{n,\alpha}), \quad (3.1.22)$$

where

$$\mu_{\alpha} = \frac{\omega_{p,\alpha}^2 e^{-\lambda_{\alpha}}}{\omega k_\parallel v_{th,\alpha}}. \quad (3.1.23)$$

It can be seen that the term involving  $\sin^2 \psi$  is of first-order in  $\lambda_{\alpha}$ . Therefore, in order to easily observe the influence of terms like this, all the dielectric tensor components can be separated such that terms tend to repeat ( $K_0, K_4, K_5$ ):

$$\bar{\epsilon} = \begin{bmatrix} K_1 + \sin^2 \psi K_0 & K_2 - \cos \psi \sin \psi K_0 & \cos \psi K_4 + \sin \psi K_5 \\ -K_2 - \sin \psi \cos \psi K_0 & K_1 + \cos^2 \psi K_0 & \sin \psi K_4 - \cos \psi K_5 \\ \cos \psi K_4 - \sin \psi K_5 & \sin \psi K_4 + \cos \psi K_5 & K_3 \end{bmatrix}, \quad (3.1.24)$$

$$K_0 = 2 \sum_{\alpha} \mu_{\alpha} \lambda_{\alpha} \sum_{n=-\infty}^{n=\infty} \{I_n(\lambda_{\alpha}) - I'_n(\lambda_{\alpha})\} Z(\xi_{n,\alpha}), \quad (3.1.25)$$

$$K_1 = 1 + \sum_{\alpha} \frac{\mu_{\alpha}}{2\lambda_{\alpha}} \sum_{n=-\infty}^{n=\infty} n^2 I_n(\lambda_{\alpha}) Z(\xi_{n,\alpha}), \quad (3.1.26)$$

$$K_2 = \iota \sum_{\alpha} \epsilon_{\alpha} \mu_{\alpha} \sum_{n=-\infty}^{n=\infty} \{I_n(\lambda_{\alpha}) - I'_n(\lambda_{\alpha})\} Z(\xi_{n,\alpha}), \quad (3.1.27)$$

$$K_3 = 1 - \sum_{\alpha} \mu_{\alpha} \sum_{n=-\infty}^{n=\infty} I_n(\lambda_{\alpha}) \xi_{n,\alpha} Z'(\xi_{n,\alpha}), \quad (3.1.28)$$

$$K_4 = \sum_{\alpha} \frac{\mu_{\alpha}}{\sqrt{2\lambda_{\alpha}}} \sum_{n=-\infty}^{n=\infty} n I_n(\lambda_{\alpha}) Z'(\xi_{n,\alpha}), \quad (3.1.29)$$

$$K_5 = i \sum_{\alpha} \epsilon_{\alpha} \mu_{\alpha} \sqrt{\frac{\lambda_{\alpha}}{2}} \sum_{n=-\infty}^{n=\infty} \{I_n(\lambda_{\alpha}) - I'_n(\lambda_{\alpha})\} Z'(\xi_{n,\alpha}). \quad (3.1.30)$$

This calculation implements the hot plasma effects into the dielectric tensor for thermal species represented by an isotropic Maxwellian distribution function (equation 3.1.13). As shown in chapter 2, the SCENIC code implements the zeroth order Vlasov bi-Maxwellian distribution function for the fast ion distribution (equation 2.5.1). The current version of LEMan implements full-FLR effects for particle distributions that are assumed to be isotropic Maxwellian, and first order effects for the Bi-Maxwellian fast distribution. For higher harmonic heating, an isotropic Maxwellian is currently applied for the fast ion distribution function. Future work that should be carried out is the derivation and implementation of the dielectric tensor into LEMan using this distribution function. This would be implemented for the fast species in order to allow self-consistent calculation of the influence of the fast pressure on the wave-propagation and power damping.

### 3.1.1 Comparison of full and second order Dielectric Tensors

The updates made to the LEMan dielectric tensor are difficult to implement numerically. It is therefore necessary to verify if mistakes or bugs are present in the new updates. For example, the calculation of modified Bessel functions of the first kind, including with a complex input, is something that is not straight-forward. It is additionally useful to have a more simplistic dielectric tensor that retains second-order FLR effects. A comparison will be made between this full-FLR order dielectric tensor with a second order reduced dielectric tensor. The latter can be numerically evaluated from the former using the expansions of  $I_n(\lambda_{\alpha})$ :

$$I_n(\lambda_{\alpha}) = i^{-n} J_n(i\lambda_{\alpha}) = \sum_{m=0}^{\infty} \frac{1}{m! \Gamma(m+n+1)} \left(\frac{\lambda_{\alpha}}{2}\right)^{2m+n} \quad (3.1.31)$$

$$= \frac{1}{n!} \left(\frac{\lambda_{\alpha}}{2}\right)^n \left[ 1 + \frac{(\lambda_{\alpha}/2)^2}{1(n+1)} + \frac{(\lambda_{\alpha}/2)^4}{1 \cdot 2(n+1)(n+2)} + \frac{(\lambda_{\alpha}/2)^6}{1 \cdot 2 \cdot 3(n+1)(n+2)(n+3)} + \dots \right], \quad (3.1.32)$$

### 3.1. Updating the LEMan Dielectric tensor to Include Higher Order (Hot Plasma) Effects

$$I_n(\lambda_\alpha)e^{-\lambda_\alpha} = \frac{1}{n!} \left( \frac{\lambda_\alpha}{2} \right)^n \left[ 1 - \lambda_\alpha + \left( \frac{\lambda_\alpha}{2} \right)^2 \left( 2 + \frac{1}{n+1} \right) + \dots \right]. \quad (3.1.33)$$

This leads to the following second order FLR dielectric tensor elements:

$$K_0 = \sum_{\alpha} \mu'_{\alpha} \lambda_{\alpha} Z(\xi_{0,\alpha}), \quad (3.1.34)$$

$$K_1 = 1 + \sum_{\alpha} \frac{\mu'_{\alpha}}{2} [(1 - \lambda)\{Z(\xi_{-1}) + Z(\xi_1)\} + \lambda\{Z(\xi_{-2}) + Z(\xi_2)\}]_{\alpha}, \quad (3.1.35)$$

$$K_2 = \iota \sum_{\alpha} \epsilon_{\alpha} \frac{\mu'_{\alpha}}{2} [(1 - 2\lambda)\{Z(\xi_{-1}) - Z(\xi_1)\} + \lambda\{Z(\xi_{-2}) - Z(\xi_2)\}]_{\alpha}, \quad (3.1.36)$$

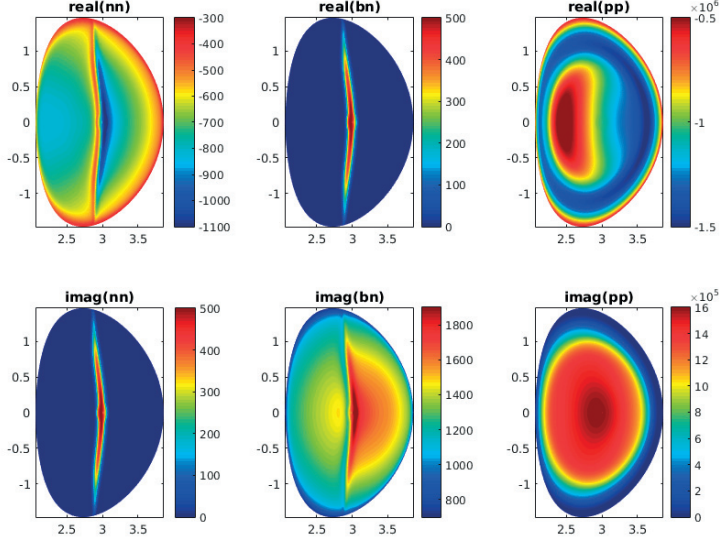
$$K_3 = 1 - \sum_{\alpha} \mu'_{\alpha} [(1 - \lambda)\xi_0 Z'(\xi_0) + \frac{\lambda}{2}\{\xi_{-1} Z'(\xi_{-1}) + \xi_1 Z'(\xi_1)\}]_{\alpha}, \quad (3.1.37)$$

$$K_4 = \sum_{\alpha} \frac{\mu'_{\alpha} \sqrt{\lambda}}{2\sqrt{2}} [\{Z'(\xi_1) - Z'(\xi_{-1})\}]_{\alpha}, \quad (3.1.38)$$

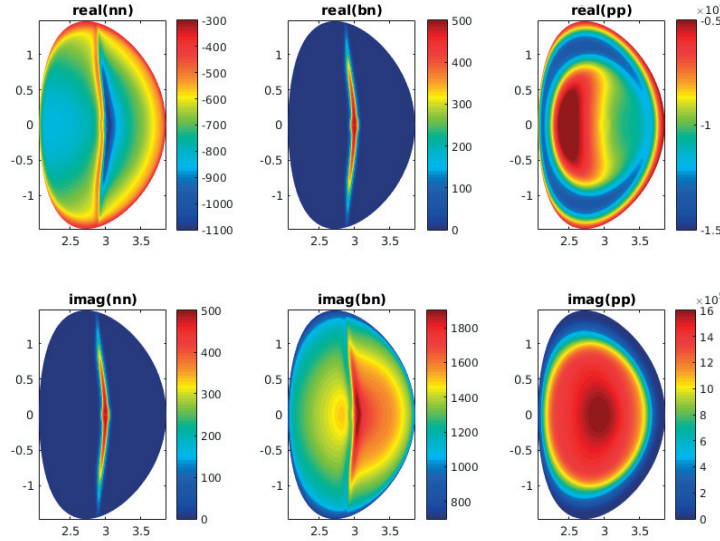
$$K_5 = \iota \sum_{\alpha} \frac{\epsilon_{\alpha} \mu'_{\alpha} \sqrt{\lambda}}{2\sqrt{2}} [Z'(\xi_0) - \frac{1}{2}\{Z'(\xi_1) + Z'(\xi_{-1})\}]_{\alpha}. \quad (3.1.39)$$

The second order dielectric tensor elements can be used to calculate fundamental and second harmonic heating. Simulations have been made to calculate the differences between second and full-FLR effects on the second harmonic RF-heated JET pulse 91610. The pure hydrogen plasma (assumed here) had a central electron temperature of 2keV and a central electron density of  $3.5 \times 10^{19}$ . Figure 3.1 plots the real and imaginary components of the dielectric tensor elements  $\epsilon_{nn} = K_1 + \sin^2 \psi K_0$ ,  $\epsilon_{bn} = K_2 - \cos \psi \sin \psi K_0$  and  $\epsilon_{pp} = K_3$  from equation 3.1.24. The second-order FLR dielectric tensor equations are calculated for figure 3.1 (a) and the full-FLR dielectric tensor for in figure 3.1 (b). The comparison illustrates minimal differences between the full and reduced dielectric tensor. The only noticeable difference is visible in the real part of  $\epsilon_{\parallel\parallel}$ . This is due to the inclusion of important higher order FLR terms in the parallel component of  $\bar{\epsilon}$  that were neglected in the reduction of the model. A more directly comparable 1D plot of the radial power deposition is explained in section 3.1.2 in figure 3.2. The verification of the full-FLR dielectric tensor implementation into SCENIC allows benchmarking against other RF-wave codes, shown in section 3.4. The full-FLR dielectric tensor will be the default choice for future isotropic wave-propagation calculations with the

SCENIC package.



a)



b)

Figure 3.1 – Comparison of the Stix components of the dielectric tensor for the a) full-FLR order and b) reduced-second order dielectric tensors. The terms ‘nn’, ‘bn’ and ‘pp’ refer to  $\epsilon_{nn} = K_1 + \sin^2 \psi K_0$ ,  $\epsilon_{bn} = K_2 - \cos \psi \sin \psi K_0$  and  $\epsilon_{pp} = K_3$  respectively from equation 3.1.24.

### 3.1.2 $k_{\perp}$ and the Full-Hot Plasma Dispersion Relation

The LEMan code uses an iterative method to calculate the wave-propagation. The iteration occurs over wave-vector space. Using the warm dielectric tensor of [6], these equations are reduced such that only the parallel wave-vector  $k_{\parallel}$  is required, as  $k_{\perp}$  and  $\psi$  played no role in

### 3.1. Updating the LEMan Dielectric tensor to Include Higher Order (Hot Plasma) Effects

the dielectric tensor calculated by the code. With the full-FLR (and reduced-second) order dielectric tensor,  $k_{\perp}$  and  $k_{\parallel}$  henceforth play an important role in the convergence. The three equations for  $\psi$ ,  $k_{\perp}$  and  $k_{\parallel}$  are now described. The first equation is taken directly from the electric field scalar potential:

$$|k_{\parallel,i+1}| = |k_{\parallel,i}| + \lambda_c \sqrt{\frac{|\nabla_{\parallel}\phi|^2}{|\phi|^2}}, \quad (3.1.40)$$

with  $\lambda_c$  the relaxation method parameter. An initial guess of  $k_{\parallel} \simeq n_{\phi}/R$  is taken from the specific details of the RF antenna geometry. For the wave-vector phase  $\psi$ , the symmetry in the dielectric tensor elements allows us to make the approximation  $\cos(\psi) = 0$ , a common assumption amongst RF-wave propagation codes[27]. However,  $\psi$  does become important in the quasi-linear operator, shown in equations 2.4.24 and 2.4.29. Upon convergence, the wave phase is calculated by:

$$\psi = \arctan \sqrt{\frac{|\nabla_n \phi|^2}{|\nabla_b \phi|^2}}. \quad (3.1.41)$$

The perpendicular wave-vector  $k_{\perp}$  requires an additional equation. This can be calculated using the plasma dispersion relation, which relates the wave-vector to the components of the dielectric tensor:

$$\begin{aligned} & [\gamma(\gamma - K_0 + n_{\perp}^2) + K_2^2] K_3 + n_{\perp}^2 [(\gamma - K_0 + n_{\perp}^2)K_1 - K_2^2] + \\ & K_4(\gamma - K_0 + n_{\perp}^2)(2n_{\perp} n_{\parallel} + K_4) - K_5[\gamma K_5 + 2K_2(n_{\perp} n_{\parallel} + K_4)] = 0, \end{aligned} \quad (3.1.42)$$

$$\gamma = n_{\parallel}^2 - K_1.$$

The iteration in  $k_{\perp}$  is made within the calculation of the dielectric tensor. The process is as follows: the initial guess  $\lambda = 0$  is provided to the second order FLR dielectric tensor (equations 3.1.34-3.1.39).  $k_{\perp}$  can be recalculated using equation 3.1.42. The full-FLR order dielectric tensor (equations 3.1.25-3.1.30) is now given the updated value of  $k_{\perp}$ , which is further iterated upon until a convergence such that  $|k_{\perp,i+1} - k_{\perp,i}| < 10^{-3} m^{-1}$ . In order to resolve  $k_{\perp}$  from equation 3.1.42, the Newton-Raphson numerical method is applied. Both the real and complex components of  $k_{\perp}$  are retained in the calculation of the dielectric tensor elements. Often codes neglect the contribution of the complex part, for numerical reasons concerning the calculation of the Bessel functions. The complex part is generally one order of magnitude smaller than the real part, but its influence near the resonant surface is non-negligible. This can be seen by the presence of the  $e^{-\lambda}$  term in the dielectric tensor components. Complex values result in an oscillatory term that is of significant importance near the resonant surface.

The dielectric tensor can be directly related to the power absorbed by the plasma:

$$P_{pla}(s) = \frac{\omega}{8\pi} \int_{\Omega(s<s')} dV' \left[ |B|^2 - E^* \bar{\epsilon} E \right]. \quad (3.1.43)$$

The dielectric tensor can still be separated as a sum over the plasma species, allowing the calculation of the contribution of each species to the wave-power absorption. Figure 3.2 illustrates the 1D total power absorption density calculated using the dielectric tensor equations 3.1.25-3.1.30, comparing the results from using a real  $k_{\perp}$  against the full complex  $k_{\perp}$ . The results show differing values of the total RF-power absorption in the core region. The increased power absorption when including  $\text{Im}\{k_{\perp}\}$  is due to the resulting increase in the FLR parameter  $\lambda_{\alpha}$ . The presence of the complex part of  $\lambda_{\alpha}$  in equations 3.1.25-3.1.30 increases the dielectric tensor components of the resonant species near the resonant surface, which increases the absorbed power density (see equation 3.1.43) in the core for on-axis heating.

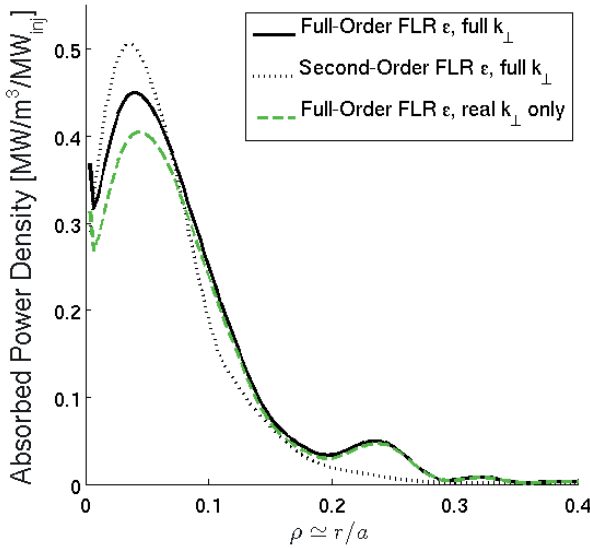


Figure 3.2 – The total radial wave power deposition for JET shot number 91610. A comparison is made between the results when calculating the dielectric tensor with the following: the full dielectric tensor in equations 3.1.25-3.1.30 where  $k_{\perp}$  has both imaginary and real components (solid black line), the full dielectric tensor in equations 3.1.25-3.1.30 where  $k_{\perp}$  has real components only (dashed black line) and the reduced second-order dielectric tensor in equations 3.1.34-3.1.39 where  $k_{\perp}$  has both imaginary and real components (dashed green line).

Inaccurate calculation of  $k_{\perp}$  can also lead to errors in the wave-particle energy transfer. Error of the type shown in figure 3.2 will have a significant effect on the Bessel functions that appear in the QLO described in section 2.4.4. Previously, calculating the warm dielectric tensor as described in [6] calculated  $k_{\perp}$  using the scalar vector potential (as is still used for the parallel

### 3.1. Updating the LEMan Dielectric tensor to Include Higher Order (Hot Plasma) Effects

wave-vector shown in equation 3.1.40),

$$|k_{\perp,i+1}| = |k_{\perp,i}| + \lambda_c \sqrt{\frac{|\nabla_b \phi|^2 + |\nabla_n \phi|^2}{|\phi|^2}}. \quad (3.1.44)$$

LEMan has been updated to take the  $k_{\perp}$  value calculated by the full-hot plasma dispersion relation (equation 3.1.42) instead of from equation 3.1.44.

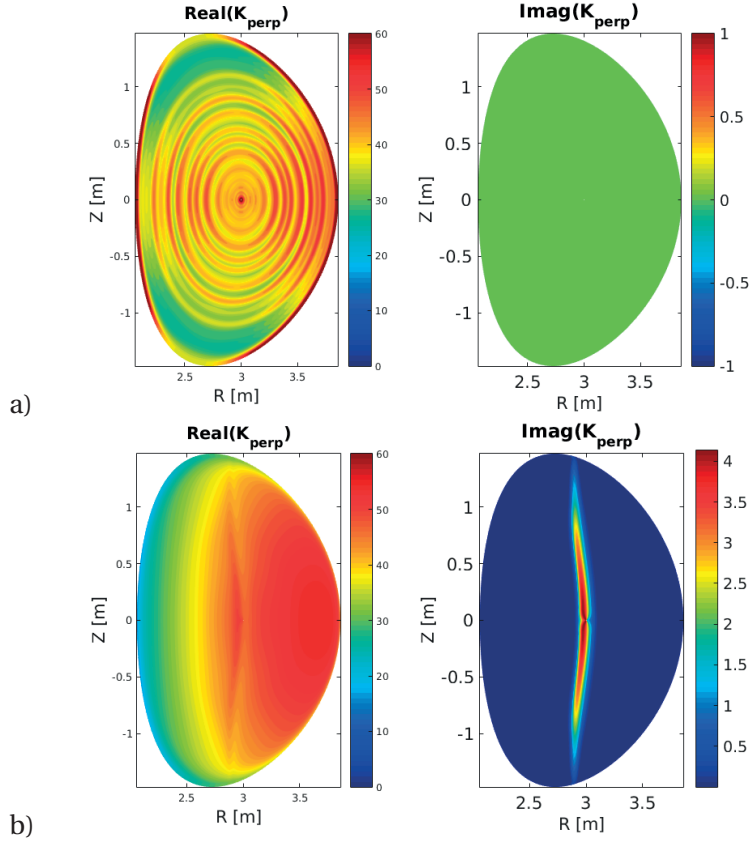


Figure 3.3 – Comparison of the left) real and right) imaginary values of  $k_{\perp}$  calculated from a) the electric field scalar potential shown in [28] and b) from the full-hot plasma dispersion relation.

Figure 3.3 shows contour plots of the real (left) and complex (right) components of  $k_{\perp}$ , comparing the scalar vector potential calculation (equation 3.1.44) and the recently implemented hot plasma dispersion relation calculation (equation 3.1.42). Using the full-hot plasma dispersion relation calculation allows for the wave-particle energy transfer to be more reliably calculated. This has a significant impact upon the energy transferred at the resonant surface. In the core region, the values of  $\text{Re}\{k_{\perp}\}$  are  $\sim 35 - 40 m^{-1}$  for both 3.3 (a) and (b). Outside of the core region, the values differ, which will have an influence mostly in the Bessel functions of the QLO in the VENUS-LEVIS code. Note that the imaginary part, which is related to the wave

absorption, was previously unused. Benchmarking of the LEMan code with the implemented changes to  $k_{\perp}$  is described in section 3.4.

### 3.2 Generalised Magnetic Coordinate Systems in LEMan

The dielectric tensor derivation requires a physical coordinate system to describe the plasma behaviour parallel to the magnetic field separately to the perpendicular direction. The vector potential is therefore written as

$$\vec{A} = A_n \nabla s |\nabla s| + A_b \frac{\vec{B} \times \nabla s}{|\vec{B} \times \nabla s|} + A_{\parallel} \frac{\vec{B}}{B}, \quad (3.2.1)$$

where  $n$  and  $b$  refer to the normal and binormal components respectively. Equations 2.2.24 and 2.2.25 are also calculated in these coordinates. In order to convert between this physical system and that of any curvilinear magnetic flux coordinate system  $(s, u, v)$ , one can project onto the basis vectors, for example, on a contravariant basis:

$$A^s = \vec{A} \cdot \nabla s = A_n |\nabla s|, \quad (3.2.2)$$

$$A^u = \vec{A} \cdot \nabla u = A_n \frac{\nabla s \cdot \nabla u}{|\nabla s|} + A_b \frac{(\vec{B} \times \nabla s) \cdot \nabla u}{B |\nabla s|} + A_{\parallel} \frac{\vec{B} \cdot \nabla u}{B}, \quad (3.2.3)$$

$$A^v = \vec{A} \cdot \nabla v = A_n \frac{\nabla s \cdot \nabla v}{|\nabla s|} + A_b \frac{(\vec{B} \times \nabla s) \cdot \nabla v}{B |\nabla s|} + A_{\parallel} \frac{\vec{B} \cdot \nabla v}{B}. \quad (3.2.4)$$

The transformation between the magnetic coordinate system and the physical LEMan system can therefore be represented by the matrices  $\hat{U}$  and  $\hat{L}$  to project into the contravariant and covariant basis respectively. In Boozer flux coordinates  $(s, \theta, \phi)$

$$\hat{U} = \begin{bmatrix} \nabla s & 0 & 0 \\ \frac{\nabla s \cdot \nabla \theta}{|\nabla s|} & -\frac{I}{B |\nabla s| \sqrt{g}} & \frac{\psi'_{\theta}}{B \sqrt{g}} \\ \frac{\nabla s \cdot \nabla \phi}{|\nabla s|} & -\frac{J}{B |\nabla s| \sqrt{g}} & \frac{\psi'_{\phi}}{B \sqrt{g}} \end{bmatrix}, \quad (3.2.5)$$

$$\hat{L} = \begin{bmatrix} \frac{1}{\nabla s} & -\frac{g_{s,\theta} I + g_{s,\phi} J}{B |\nabla s| \sqrt{g}} & \frac{g_{s,\theta} \psi'_{\theta} + g_{s,\phi} \psi'_{\phi}}{B \sqrt{g}} \\ 0 & \frac{\psi'_{\theta} |\nabla s|}{B} & \frac{J}{B} \\ 0 & -\frac{\psi'_{\phi} |\nabla s|}{B} & -\frac{I}{B} \end{bmatrix}. \quad (3.2.6)$$

The original version of LEMan was only capable of solving the wave equation with magnetic equilibria calculated in Boozer coordinate systems. One of the recent updates made to the code has been to generalise the  $\hat{U}$  and  $\hat{L}$  matrices such that any flux surface coordinate



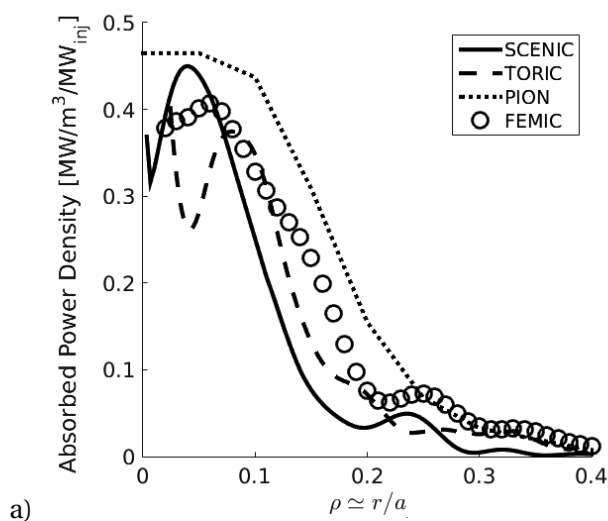
system with differentially continuous metric elements can be used in the code. This permits RF-wave calculation of up-down asymmetric equilibria and can reduce the numerical error via the direct deployment of the ANIMEC equilibrium coordinate system, without having to transition to Boozer coordinates with the TERPSICHORE code [29] (introducing some additional numerical error, and restricting to up-down symmetric equilibrium in tokamaks). An example of the wave propagation with up-down asymmetry is shown in the benchmarking performed in section 3.4 in figure 3.7.

### 3.3 N-Species

An additional update to the LEMan code is the inclusion of an unlimited number of plasma species into the wave calculation. Only one species is evaluated using the bi-Maxwellian distribution function described in chapter 2, and all other species with a Maxwellian. This addition is of significant importance when studying the influence of plasma impurities on the wave-propagation, simulations of which are investigated in section 3.6.

### 3.4 Benchmarking

The updates to the LEMan code were benchmarked for the second harmonic hydrogen heating JET experiment 91610 against three other codes: TORIC [30], a 2D code which includes mode conversion effects, FEMIC [31], a 2D (being developed into a 3D) code with an accurate RF-antenna coupling model and PION [32], a 1D code with a cold plasma dielectric tensor. A pure hydrogen plasma with  $X[\text{Be}]=0.5\%$  was considered; the ICRF antenna frequency applied resonated with the second harmonic cyclotron frequency of the hydrogen near to the magnetic axis. The 1D absorbed RF-power density predicted by each code is shown in figure 3.4. Note that  $B_0(\text{at } R_0 = 2.96\text{m}) = 1.72\text{T}$  and  $f_{RF} = 51\text{MHz}$ .



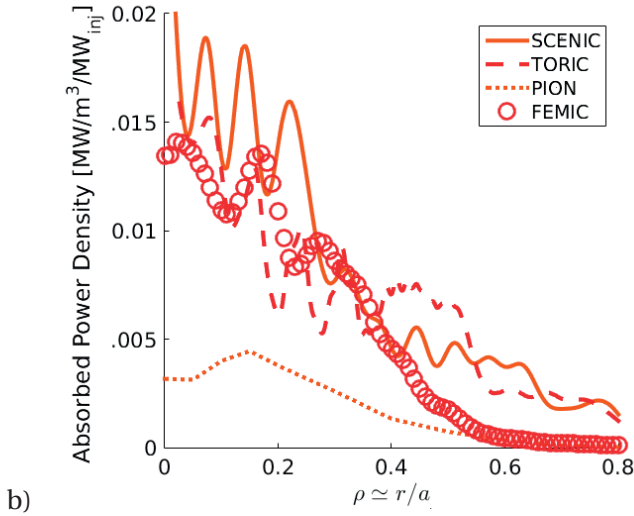


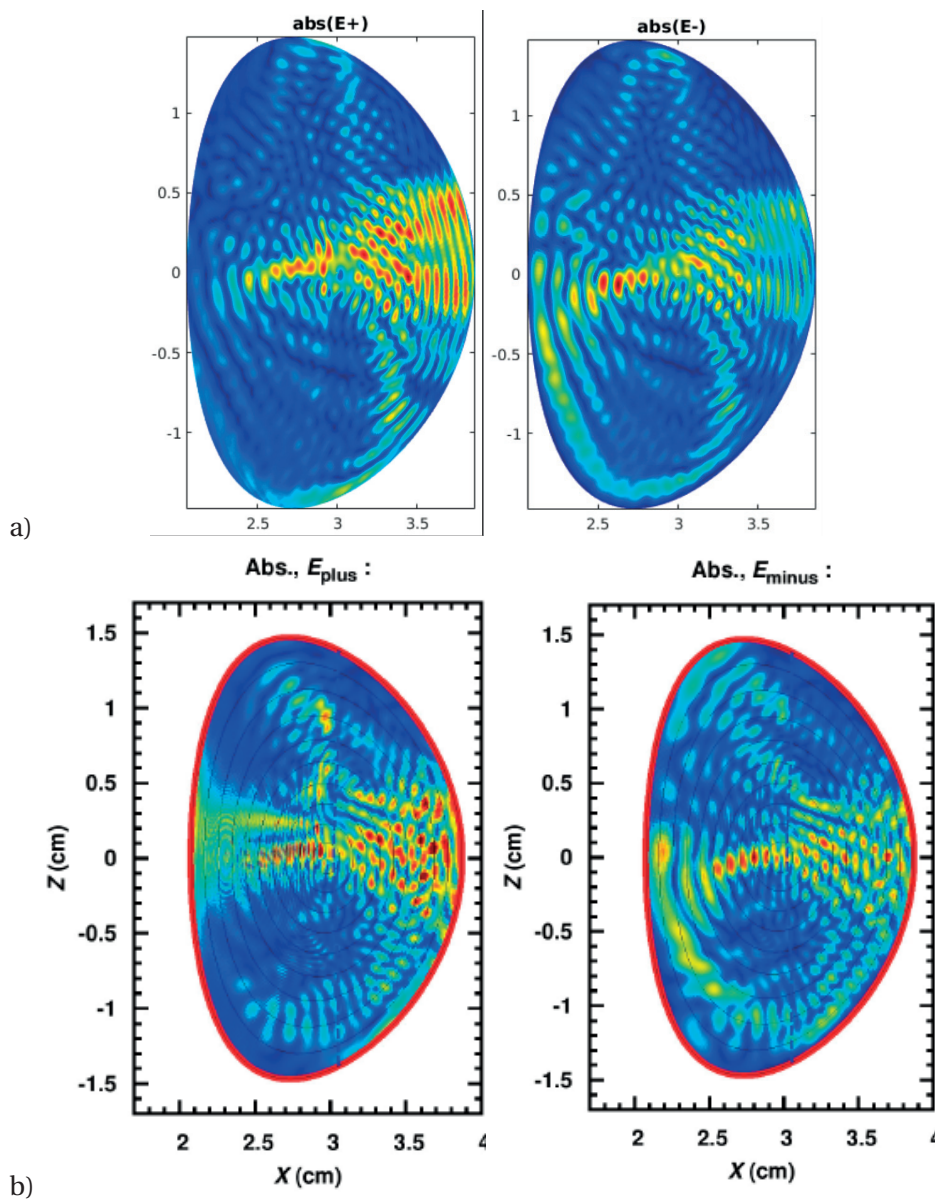
Figure 3.4 – A comparison of the toroidal and poloidal summation of the 1D RF-power absorption for the different codes: SCENIC, FEMIC, PION and TORIC for a) total and b) electron RF-power absorption. JET pulse 91610:  $B_0 = 1.72\text{T}$ ,  $f_{RF} = 51\text{MHz}$ .

The results show a promising comparison between the RF-power deposition as a summation over the toroidal and poloidal angles. The two dimensional (TORIC and FEMIC) and three dimensional (LEMan) wave-propagation codes find two peaks in the total RF-power absorption shown in figure 3.4, in the core  $\rho = 0$  and the second at  $\rho \sim 0.08$ . It is also clear that the majority of the energy is absorbed by the hydrogen for this experiment due to the relatively high temperature profiles in the core. A table of the power fractions absorbed by each species is given in table 3.1. The TORIC code is the only code capable of including the effects of mode conversion and therefore predicts the lowest amount of energy transferred to the ions. The power transferred to the electrons through mode conversion (through the Ion Bernstein Wave) was predicted to be only 4.35%. This small degree of mode conversion explains the relatively small difference between SCENIC and TORIC.

	Hydrogen %	Electrons %
SCENIC	85.5	14.5
TORIC	80.66	19.44
FEMIC	87	13
PION	96	4

Table 3.1 – A comparison of the total power absorbed by hydrogen and electrons between the codes.

Comparison of one-dimensional profiles can be useful, but comparison of RF-wave propagation can be assisted by inspection of 2D plots of the electric field produced by the wave. Figure 3.5 shows the absolute values of the electric field components  $E^-$  and  $E^+$  for the codes SCENIC, TORIC and FEMIC. Note that the amplitude of the electric field is not important as it is related to the injected RF-antenna power and can therefore be normalised. The three codes show a very good agreement. The poloidal magnetic field and the complex component of  $k_\perp$  is not taken into account in the wave calculation of the FEMIC code. The antenna model implemented by the FEMIC code is much more complicated than that implemented in SCENIC. The additional difference could be the use of an up-down asymmetric last closed flux surface, but this has also been studied with the SCENIC code in the next subsection 3.4.1.



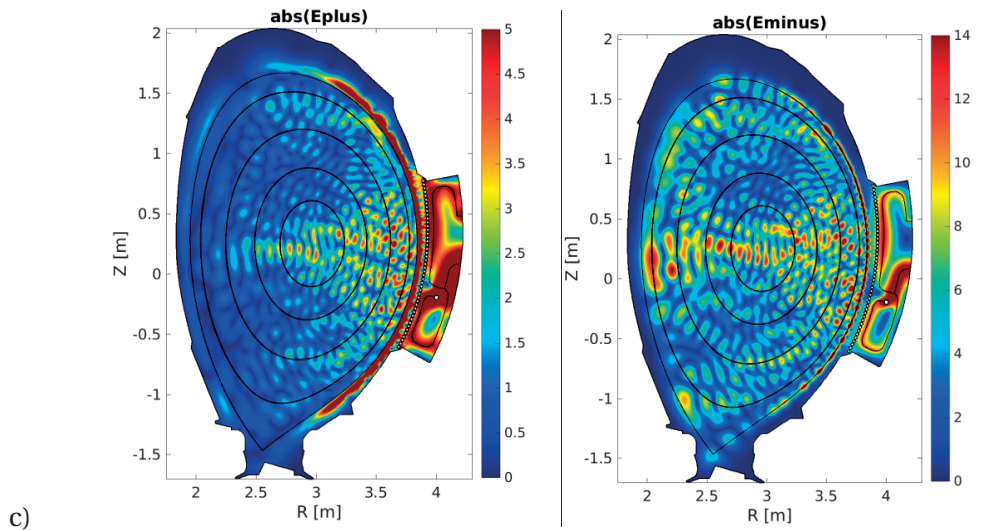


Figure 3.5 – A comparison of the absolute electric field left)  $E^+$  and right)  $E^-$  between the codes a) SCENIC, b) TORIC and c) FEMIC.

### 3.4.1 Up-Down Asymmetric Magnetic Equilibrium

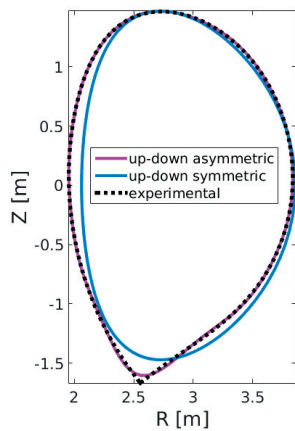


Figure 3.6 – Plot of the experimental LCFS of the JET shot 91610 against the Fourier constructed equilibria assuming up-down symmetry and asymmetry.

This subsection focuses on the influence of up-down asymmetric magnetic equilibria. Modifications to the LEMan code allow the use of any coordinate system to calculate the wave-propagation code. A previous issue with being constrained to using Boozer [33] coordinates was that this requires up-down symmetry. This requirement has now been relaxed so that flux surface geometry can now better match the experimental magnetic equilibrium, as shown in figure 3.6. In order to permit a fair comparison with FEMIC in figure 3.5, the same plasma conditions will be used to establish the influence of up-down symmetry on the wave-propagation and radial power deposition profiles.

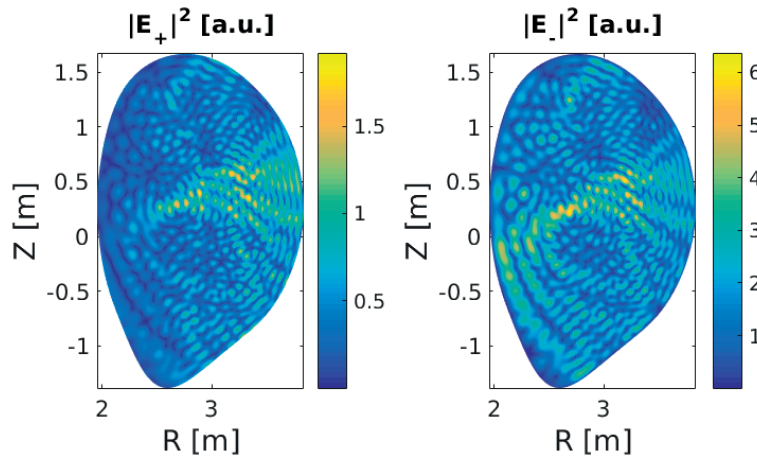


Figure 3.7 – A comparison of the absolute electric field left)  $E^+$  and right)  $E^-$  for an up-down asymmetric magnetic equilibrium using the LEMan code.

For the wave electric field amplitude (figure 3.7), similar behaviour is displayed by the up-down symmetric and asymmetric cases. For example, the  $E^-$  amplitude tends to propagate through the core and downwards in the  $Z$ -plane where strong dispersion occurs approaching the LCFS. The  $E^+$  amplitude also has a similar behaviour. For example, it penetrates through the core and is then strongly damped. Figure 3.8 illustrates the poloidal and toroidal summated 1D power deposition profiles of the RF-wave. Stronger peaking is found towards the core region for the up-down asymmetric case. Stronger differences in the RF-heating performance are expected when comparing the Fokker-Planck particle simulations of RF-heating for up-down asymmetric and symmetric equilibria, due to FOW and particle orbit topology effects.

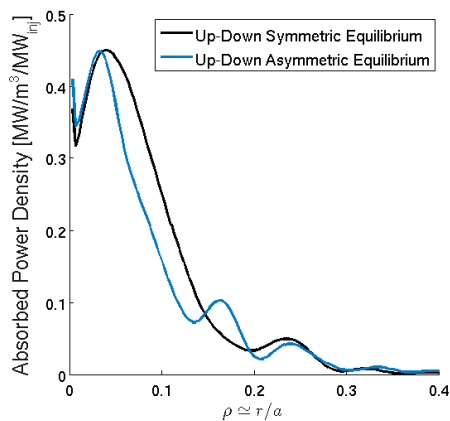


Figure 3.8 – A comparison of the wave power deposition for an up-down asymmetric and symmetric magnetic equilibrium.

3.4.2 RF-Power Absorption in Minority Species Heating Scenarios

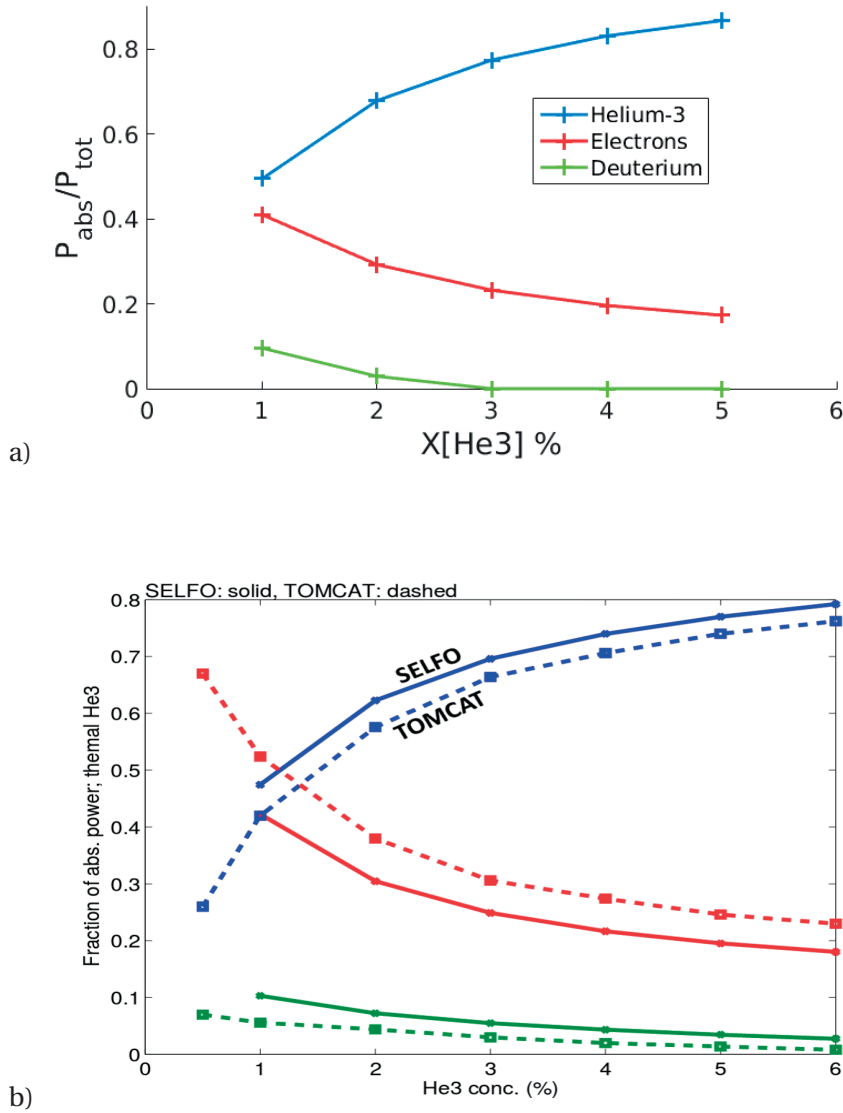


Figure 3.9 – RF-Power absorbed by the plasma with respect to the minority species concentration ( $n_j/n_e$ ) for a helium-3 minority heating scheme, comparing the results using the SCENIC (a) and SELFO and TOMCAT (b) codes. Blue lines show the helium-3 RF-absorption, red lines the electron RF-absorption and green lines the deuterium RF-absorption.

Harmonic effects are not only present in harmonic RF-heating with a single species plasma, but also in minority heating scenarios that are commonly applied in experiments. Figure 3.9 shows the results of a benchmarking comparison of JET shot number 86614 between three different codes: SCENIC, SELFO [27] and TOMCAT [34]. The concentration of the minority Helium-3 species was varied and the RF-power absorption of the different species

was investigated. SELFO is very similar to SCENIC. It self-consistently simulates the effect of the evolution of the fast ion distribution on wave-propagation and vice-versa. The major differences are the simplified magnetic geometry (simplified toroidal approximation of the CHEASE equilibrium [35]), the calculation of FLR terms in the dielectric tensor in the wave-propagation code LION [36] and the orbit averaged QLO implemented in the Fokker Planck code. The TOMCAT code is a 1D code which nevertheless includes mode-conversion effects in the RF-wave propagation and absorption. Neither SELFO nor SCENIC include mode conversion effects. The damping on the electron population shown in figure 3.9b) obtained by TOMCAT is only partially explained by the inclusion of mode-conversion effects (which is usually around 5% for small minority concentrations). It might be due to 2D magnetic geometry effects not being included in TOMCAT. SCENIC and SELFO show more similar trends with respect to the minority concentration. The main differences are the disappearance of energy transferred to the deuterium population through second harmonic heating in the SCENIC code, with more energy being absorbed by the minority helium-3 species. These small differences could be due to the influence of numerically implementing the full magnetic geometry in SCENIC, or the dielectric tensor calculation, or the RF-antenna model applied, or all of these effects.

### 3.5 RF-Antenna

This section is concerned with the numerical implementation of the realistic RF-antenna geometry into SCENIC, and how such a representation can be used to represent antenna configurations used in tokamak and stellarator devices. The model includes the effect of ‘RF-phasing’, which is a common heating method in tokamak ICRF experiments. It requires multiple RF-antenna straps. With the combination of different phases in the antenna current for each strap, parallel propagating RF-waves can be produced.

#### 3.5.1 In Tokamak Geometries

Numerical modelling of some 2D tokamak geometries has already been presented in [37]. Hence only a brief summary of the implementation is presented here. In tokamak geometries, the toroidal symmetry of the system allows the toroidal decomposition of the wave induced by the RF-antenna such that:

$$\vec{j}_{ant} = j_{n_\phi}(n_\phi)G(s)G(\theta)e^{in_\phi\phi}\vec{e}_{ant}. \quad (3.5.1)$$

$$G_\alpha(\alpha) = f_B\left(\frac{\alpha - \alpha_1}{\alpha_2 - \alpha_1}\right)(1 - \chi_\alpha^2)^2, \quad (3.5.2)$$

with

$$\chi_\alpha = \left(2\frac{\alpha - \alpha_1}{\alpha_2 - \alpha_1} - 1\right) \quad (3.5.3)$$



### Chapter 3. Numerical Advancements and Application for ICRF Optimisation

where  $j_{n_\phi}$  is the current density amplitude factor, and  $n_\phi$  is the toroidal wave-mode number. Note it is assumed in 3.5.1 that  $s$  and  $\theta$  geometry effects are separable. The current density is therefore represented in radial and poloidal geometry by the combination of a box function  $f_B$  and a polynomial function. Via decomposition in terms of a series of antenna straps, the resulting antenna current density spectrum away from the antenna is given as [34]:

$$j_{n_\phi} = \sum_k j_k \frac{\sin(\frac{n_\phi}{R} W_k)}{\frac{n_\phi}{R} W_k} \exp\left(-\frac{n_\phi d}{R}\right), \quad (3.5.4)$$

$$j_k(n_\phi) = j_{0k} \exp\left(i \frac{n_\phi}{R} z_k + i \phi_k\right). \quad (3.5.5)$$

The RF-antenna geometry is expressed through the strap location  $z_k$ , the phasing of the antenna  $\phi_k$ , the distance between the antenna  $d$  and the plasma and the half width of the amplitude  $W_k$ . A plot of this toroidal decomposition of the JET antenna is given in figure 3.10 (left). The current density amplitude of the antenna is therefore strongly dependant on the choice of toroidal wave mode number. Figure 3.10 also indicates that in tokamak devices there are dominant values of  $k_{\parallel}$  emitted by the RF-antenna. Many codes assume that  $k_{\parallel}$  is a function of the major radius. In particular that  $k_{\parallel} \simeq n_\phi / R$ . However, this neglects the influence of the poloidal up-shift effect which enters due to the poloidal derivative of the electric field scalar potential

$$i k_{\parallel} = \frac{1}{B\Phi} \vec{B} \cdot \nabla \Phi = \frac{\psi'}{\Phi B \sqrt{g}} \left( \frac{1}{q} \frac{\partial}{\partial \theta} + \frac{\partial}{\partial \phi} \right) \Phi. \quad (3.5.6)$$

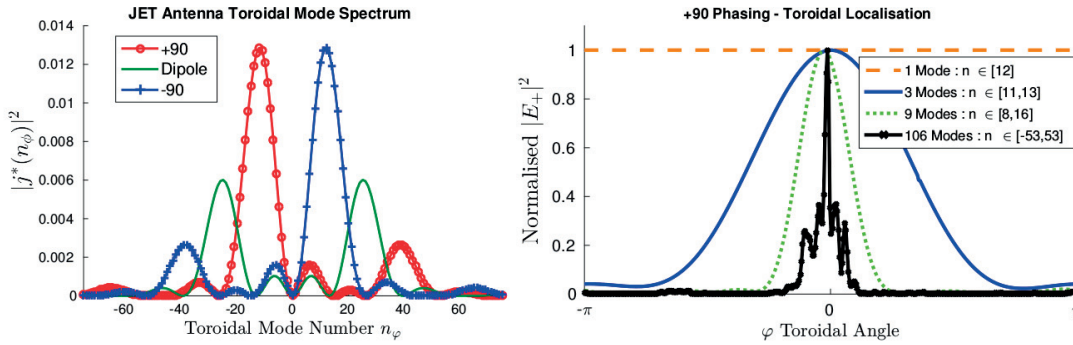


Figure 3.10 – The toroidal decomposition of the JET antenna. Left) the current amplitude per toroidal wave mode number for +90, -90 and dipole phasing. Right) the toroidal dependence of the electric field  $E_+$  for +90 phasing for various selections of Fourier harmonics  $n_\phi$ .

LEMMan [6] includes the poloidal up-shift through the iterative method described in section 3.1.2. Equation 3.5.1 and figure 3.10 illustrate the improved toroidal localisation of the cur-



rent density with the inclusion of more Fourier harmonics. Using equation 3.5.4 and figure 3.10, this would imply that for +90 antenna phasing, the 3 most dominant modes would be [+11, +12, +13]. For the superposition of a large number of toroidal wave modes, the electric field amplitude becomes further localised in toroidal space, as reflected in figure 3.10 (right). Once the wave propagation has been calculated by LEMan for each toroidal wave mode, this electric field is used by VENUS-LEVIS in the QLO Monte-Carlo operator (see section 2.4.4). Section 2.4.4 also mentions the importance of not including toroidal wave mode numbers that would result in a failure of quasi-linear diffusion theory. Numerical errors introduced by a failure in the Monte-Carlo QLO can be described by the following example: to simulate the modes  $n_\phi \in [+11, +12, +13]$  in VENUS-LEVIS, Monte-Carlo velocity kicks should not be applied by the QLO for all three of these mode numbers as the corresponding  $k_\parallel$  values are too close to one another. The numerical method resulting in the least computational time and resources is to take the LEMan simulations of the prominent  $n_\phi$  peaks of figure 3.10 (left) and apply the normalisation coefficients according to equation 3.5.4, given in table 3.2.

Dipole		+90		-90	
$n_\phi$	$J_{n_\phi}$	$n_\phi$	$J_{n_\phi}$	$n_\phi$	$J_{n_\phi}$
+27	0.006	+12	0.013	-12	0.013
-27	0.006	-39	0.0026	+39	0.0026
-6	0.001	7	0.0016	-7	0.0016
+6	0.001				

Table 3.2 – Details of the relative amplitudes that should be provided to the QLO in the Venus-LEVIS code.

An alternative method could be used to enhance the toroidal localisation of the wave by combining the wave modes around the current density peaks shown in figure 3.10. The corresponding QLO kicks would then be given using the dominant  $k_\parallel$  from the current density peak. Note that for +90 phasing, the negative  $n_\phi$  value needs to be included to ensure that the RF-pinch effect is not exaggerated. The RF-Pinch effect has been well described in [38] and simulations of this effect with the SCENIC package in [39]. This is a phenomenon that has been observed to arise in 2D tokamak scenarios. The quasi-linear velocity diffusion described in equation 2.4.32 can be written in terms of the parallel canonical momentum,

$$\Delta p_\phi = \frac{n_\phi}{\omega} \Delta E, \quad (3.5.7)$$

with

$$p_\phi = -Z\psi_\phi + \frac{B_\phi}{|B|} v_\parallel m = \text{const.} \quad (3.5.8)$$

Resonant trapped particles tend to align their bounce tips to the resonant surface, as discussed in section 2.4.4. At the bounce tip  $v_\parallel \rightarrow 0$ . A change in  $p_\phi$  directly results in radial particle

movement through a change in the toroidal magnetic flux according to:

$$\Delta\psi_\phi \simeq -\frac{\Delta p_\phi}{Z} = -\frac{n_\phi}{Z\omega} \Delta E. \quad (3.5.9)$$

Note that values of  $\psi_\phi$  are negative. For +90 antenna phasing, the particle RF-diffusion radially ‘pinches’ resonant particles inwards, and for -90 phasing the particles are pushed radially outwards. Experiments with a strong preferential  $k_\parallel$  value can improve the radial confinement of fast particles using this method. This leads to the production of higher energetic particles for +90 than standard dipole phasing, as well as to drive higher toroidal fast ion currents. The production of highly energetic particles leads, however, to a reduced heating performance (collisional power) [40, 41].

#### 3.5.2 In Stellarator Geometries

In 3D geometries, the principal method that has been used in the simulations performed for this thesis is described in section 4.5.1 of [37]. The antenna is modelled using the divergence free antenna expression

$$\vec{j}_{ant} = \nabla s \times \nabla(G_s(s)G_\theta(\theta)G_\phi(\phi)). \quad (3.5.10)$$

As a combination of a box and polynomial function in (s,u,v), it is therefore not possible to study antenna phasing in stellarators. Localisation in the toroidal, poloidal and radial directions is therefore dependant upon the number of Fourier modes and grid size of the LEMAN calculation. This has been the method used throughout all simulations of W7-X. In order to increase the number of Fourier modes used by the code, a new approach called the ‘toroidal mode family coupling’ should be used for future wave-propagation simulations in field-periodic devices. The method has been applied to the AORSA [42] code, described in [43]. The basic concept is to utilise the toroidal periodicity of the magnetic equilibrium to separate toroidal Fourier mode spectrums with respect to the field periodicity in the toroidal direction. Using this methods allows the number of Fourier modes to be increased by the number of toroidal field periods in the simulated stellarator or heliotron. In W7-X there are 5 toroidal field periods. For  $N_{FP}$  number of field periods, a boundary condition must also apply such that:  $\vec{E}^L(R, Z, 2\pi/N_{FP}) = \vec{E}^L(R, Z, 0)e^{i(2\pi/N_{FP})L}$ , for  $0 \leq L \leq N_{FP} - 1$ . Using this boundary condition, the Fourier decomposition of the electric field can be written in the following way:

$$\vec{E} = \frac{1}{N_{FP}} \sum_{L=0}^{N_{FP}-1} e^{2\pi i(L/N_{FP})(p-1)} \sum_{j,k,n} \vec{E}^L(j, k, n) e^{i[k_j x + k_k y + (nN_{FP}+L)\{\phi - (2\pi/N_{FP})(p-1)\}]}, \quad (3.5.11)$$

with  $j, k, n \in \mathbb{Z}$ . The introduction of the integer sequence  $p = 1, N_{FP} + 1, 2N_{FP} + 1, \dots$  allows a separation of the toroidal mode coupling in the wave equation 2.2.1. The Fourier mode decomposition of the electric field allows the wave propagation to be represented by the

following:

$$\begin{aligned} & \sum_u [k_u E_u^L(j, k, n) k_v - k_u^2 E_u^L(j, k, n) + \omega \mu_0 \sigma_{uv}(j, k, n) E_u^L(j, k, n)] + \frac{\omega^2}{c^2} E_v^L(j, k, n), \\ & = -i \omega \mu_0 J_v^{ant}(j, k, n) \frac{1}{N_{FP}} \sum_{L=0}^{N_{FP}-1} e^{2\pi i (L/N_{FP})(p-1)}, \end{aligned} \quad (3.5.12)$$

$$u, v \in \{x, y, \phi\} \text{ and } k_u \in \{k_j, k_k, n\}.$$

Each term in this equation can be assumed to have a periodicity according to the number of field periods. This permits the separation of each term such that toroidal modes can be grouped as multiples of the field period  $N_p$ . This implies that toroidal mode number  $\hat{n}$  will only interact with the set of toroidal modes  $\hat{n} + N_{FP}n$ , for  $n \in \mathbb{Z}$ . Therefore, wave-propagation in toroidally periodic reactors is simulated by the LEMAN code with  $N_p$  separate simulations, with toroidal mode numbers  $\{p, N_{FP} + p, 2N_{FP} + p, \dots\}$  for  $p \in \{1, \dots, N_{FP}\}$ . The resulting electric field is the superposition of all  $N_{FP}$  wave-fields, weighted by an amplitude factor. An example of such a simulation is shown in figure 3.11.

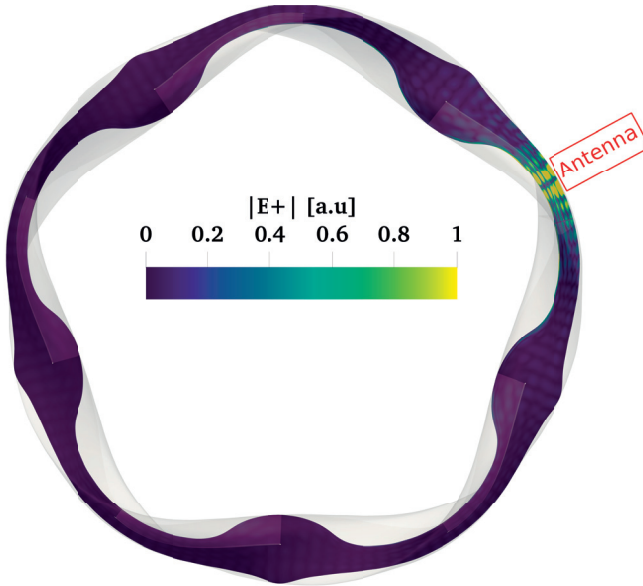


Figure 3.11 – Superposition of the electric field amplitude  $|E^+|$  for the five toroidal field periods of W7-X, simulating minority species heating (D(H) with X[H]=2%) in the high mirror equilibrium.

W7-X is foreseen to eventually have two ICRF antennas installed. The W7-X antennas, described in [44], permit only certain heating scenarios, focused mainly around minority species

and harmonic heating. The carbon wall prevents minority heating of deuterium. The first antenna, to be commissioned during the W7-X OP2 experimental campaign foreseen to commence in 2020, consists of two straps with a combined power output of 1.5MW, located at  $\theta = 0.117$ rad. The range of frequencies that the antenna will operate at is 25-38MHz, which allows on-axis fundamental minority heating of both helium-3 and hydrogen, for full-magnetic field experiments:  $B_0 \approx 2.5T$ . The second antenna has not been fully designed yet, but the latest idea is to have an operational frequency range to heat the plasma species at the second and third harmonics, depending on the desired resonant species.

### 3.6 Minority Species Heating

This section will focus on the application of the SCENIC code to exploit the implementations of the numerical updates mentioned in sections 3.1-3.5, in addition to exploiting the unique qualities of the SCENIC package such as FOW and anisotropic effects. Important parameters that affect the properties and performance are explored.

#### 3.6.1 JET

Details of the ICRF system installed on JET are found in [45]. This section focuses on the high-performance 92398 shot. This pulse achieved the highest neutron production since the ITER-like wall was installed.

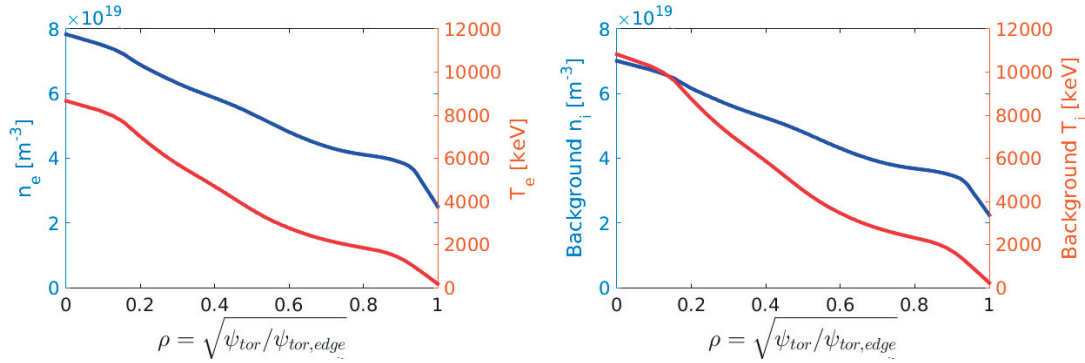


Figure 3.12 – The plasma profiles for the JET experimental shot number 92398 averaged over time 47.9 seconds. Left) background electron density and temperature profiles, right) background deuterium density and temperature profiles.

The density and temperature profiles are reproduced in figure 3.12 at the time  $t = 47.9 \pm 0.2$ s. Extracted from JET data (EFTF: MSE constrained EFIT), the experiment has the following values: vacuum magnetic field strength on axis ( $R_0 = 3.05$ m) of  $B_0 = 2.7T$ ,  $P_{RF} = 4.5$ MW,  $I_p = 2.2$ MA. The experimental deployed H minority heating in a D plasma with  $X[H] \approx 2.5\%$ . Impurity traces of  $X[Be]=0.5\%$  is assumed. The values  $Z_{eff} = 1.25$  and  $T_e = 1.25T_i$  were applied in the numerical simulations for the baseline simulation. Finally, the safety factor is shown in

figure 3.13.

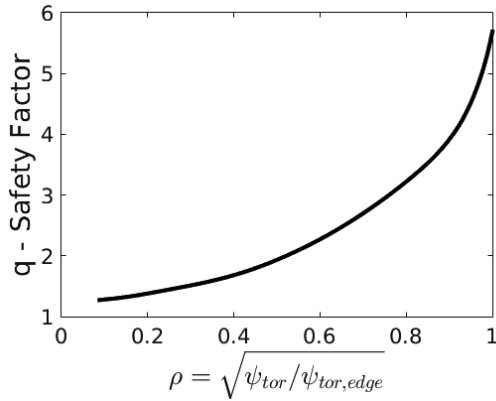


Figure 3.13 – The plasma safety factor profile for the JET experimental shot number 92398 averaged over time  $47.9 \pm 0.2$  seconds.

This section will vary important parameters that influence the RF-heating characteristics and performance. The aim of this is to progress towards the optimisation of RF minority heating schemes in tokamak reactors, and to investigate why varying such parameters can influence the heating method. The parameters varied are the minority species, minority concentration, antenna frequency, plasma current, antenna power and the influence of impurities.

### Resonant Species

ICRF minority heating experiments in deuterium background plasmas often use hydrogen or helium-3 as a resonant species. The minority concentrations are usually so small that without the presence of the RF-wave, the minority species has a negligible influence on the magnetic equilibrium. In the presence of the RF-wave, if the resonant species develops a significant fast ion population then the fast ion pressure and anisotropy can modify the magnetic equilibrium, the wave-propagation and the collisional power transferred to the background plasma. The build up of significant fast ion pressure and anisotropy depends on many factors. For the wave propagation, equation 2.2.20 predicts that the limit of the polarisation of the wave at the resonance layer is  $1/7$  or  $1/3$  for D(He3) and D(H) respectively. The distance between the L-cut-off (equation 2.2.10) and the ion-ion hybrid resonance layer (equation 2.2.4) is modified with respect to the charge of the resonant species as well as its concentration. If the distance between these two layers is too large then power is transferred to electrons through mode-conversion effects. This is typically why the minority concentration is less for helium-3 (1-3%) than for hydrogen (1-5%) experiments. The accurate calculation of the cut-off and absorption regions required the update of the LEMan code to calculate  $k_{\perp}$  using the hot plasma dispersion relation (section 3.1.2). One of the strongest influences of the species used for minority heating is through the collisionality of the particle with the background. The

collisionality scales with  $Z^2/m_a$ . The collisionality to the background plasma of hydrogen is 3/4 that of helium-3 for the same temperature and density. The species charge to mass ratio also influences the QLO, which in turn influences the anisotropy profiles. Comparing experiments of the same magnetic field strength, resonant species with higher charge to mass ratios require different antenna frequencies in order to ensure on-axis resonance. According to equation 2.4.32, this also results in a reduced parallel diffusion due to the  $1/\Omega_\alpha$  factor. This leads to larger on-axis particle anisotropies for helium-3 than for hydrogen, as shown in figure 3.17. In practice, whether this happens depends upon parameters such as the RF-antenna power (section 3.6.1) and the species concentration (section 3.6.1).

#### Minority Concentration

This section will study minority concentrations below 5%. Above this concentration, depending on the background plasma species mixture, leads to more power transferred to the electrons through mode-conversion effects. This is caused by the increase in distance between the L-cut-off and the ion-ion hybrid resonance layer. These effects cannot be simulated by the SCENIC package and therefore studies will be limited to small concentrations. Even for small minority populations, the concentration significantly influences the power absorption of the RF-wave on the different plasma species present. If  $T_i$  is large enough (as in 92398), using hydrogen as the minority species in a deuterium background plasma results in a considerable amount of the RF-power absorbed by the deuterium through the second harmonic, shown in figure 3.14. This figure shows that for low concentrations of hydrogen, deuterium second harmonic heating absorbs the majority of the RF-power. Increasing the hydrogen to larger concentrations increases the RF-power absorption such that the two have equal absorption at  $X[H]=2\%$ . Simulations of the RF-power absorption on different species in D(H) minority species ICRH JET experiments show a similar trend for varying hydrogen concentrations [46, 47]. Power absorption by harmonics is an FLR effect. Calculating accurately the second harmonic deuterium and the electron absorption through TTMP effects required the update of the LEMan dielectric tensor calculation (section 3.1). This means that for high plasma temperatures, the amount of energy absorbed by the deuterium would increase further if the hydrogen concentration is kept low (<5%).

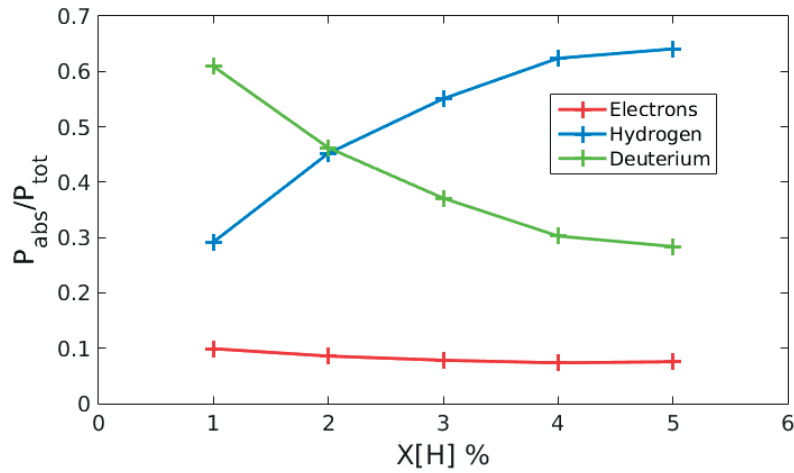


Figure 3.14 – RF-Power absorbed by the plasma with respect to the species concentration for a hydrogen minority heating scheme.

In helium-3 minority heating schemes, figure 3.15 shows that the minority species absorbs the majority of the RF-power for all concentrations over deuterium and electrons. This is because the fundamental deuterium resonant surface is on the HFS of the helium-3 resonance, and the second harmonic deuterium resonant layer is outside the LCFS. Due to the specific geometry and plasma conditions the absorption on the electrons is lower than seen in JET shot 86614 (see section 3.4).

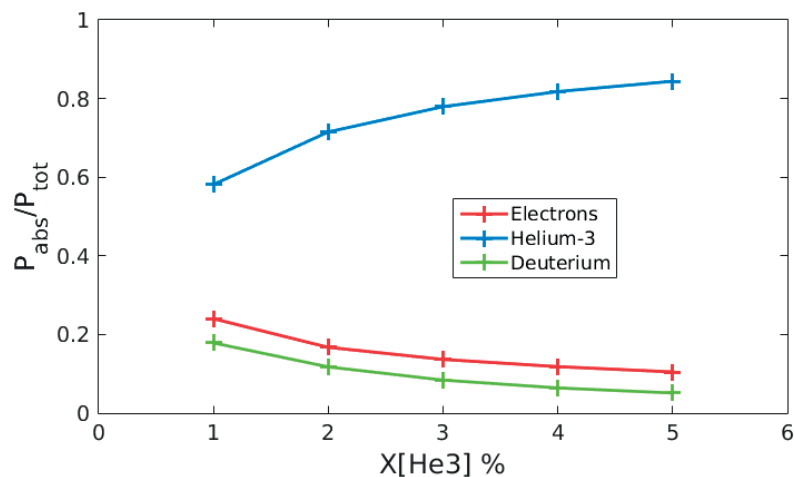


Figure 3.15 – RF-Power absorbed by the plasma species with respect to the species concentration for a helium-3 minority heating scheme. JET (92398):  $B_0 = 2.7\text{T}$ ,  $f = 42.5\text{MHz}$ .

With respect to the particle dynamics, the power transferred from the wave to the particle also

### Chapter 3. Numerical Advancements and Application for ICRF Optimisation

depends on how many particles are present. Larger minority concentrations tend to result in reduced highly energetic ion populations, illustrated in figure 3.16. This figure also demonstrates the influence of the increase in collisionality when using helium-3 minority species, resulting in less energetic fast ion populations as compared to the hydrogen simulations.

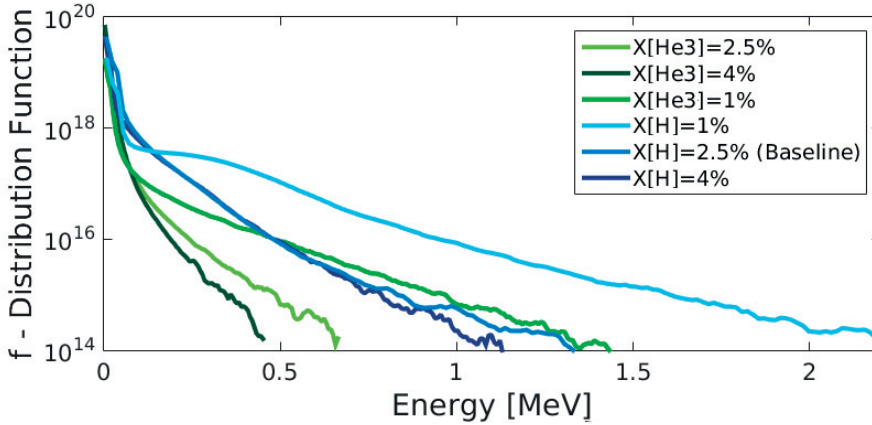


Figure 3.16 – Particle distribution as a function of energy, comparing simulations of minority heating with hydrogen and helium-3 of varying concentrations.

The production of energetic ion populations also influences the anisotropy profiles, shown in figure 3.17. An increase in the energetic population of resonant particles indicates stronger wave-particle interactions, and as standard ICRF heating scenarios heat preferentially in the perpendicular direction, this induces strong anisotropy of the minority distribution function. For both helium-3 and hydrogen, the anisotropy profiles decrease across the entire radial direction with respect to an increase in the minority species concentration. The secondary ‘bumps’ in the profile located at  $\rho \approx 0.65$  for both helium-3 and hydrogen are finite orbit width effects which are retained by the Fokker Planck code VENUS-LEVIS [15].

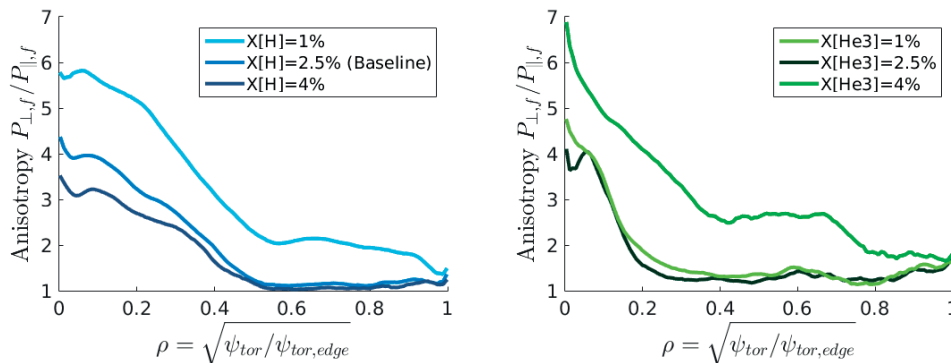


Figure 3.17 – Fast ion ( $E > 7T_e(s)$ ) anisotropy profiles of the minority species, comparing the influence of the species concentration for left) hydrogen and right) helium-3.



A comparison of the particle distribution as a function of energy of helium-3 and hydrogen is shown in figure 3.16, which would imply anisotropy profiles to be lower for helium-3 than for hydrogen. This is in fact the opposite of the result, shown in figure 3.17. As the magnetic field strength on axis is the same for both helium-3 and hydrogen, the antenna frequency required to heat helium-3 is lower than that for hydrogen. According to equation 2.4.32, this increases the RF-power transferred to the perpendicular velocity as compared to the parallel direction.

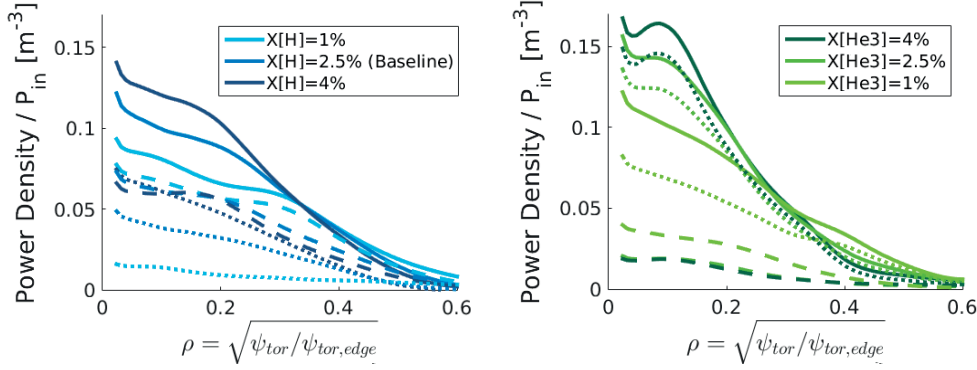


Figure 3.18 – The normalised collisional power transfer from the minority species to the background plasma, left) hydrogen and right) helium-3. Solid lines indicate the total power, dotted lines the power transferred to the background ions and dashed to electrons.  $P_{in} = 4.5MW$ .

Equations 3.5.9 and 2.4.30 show that the RF-pinch is stronger for minority species with a higher atomic mass (assuming the same  $B_0$ ), resulting in an increase in anisotropy. Evidence to support that the collisionality is reduced for particles located at outer radial values is shown in the power transferred to the background plasma, figure 3.18. Despite the high anisotropy for this secondary ‘bump’, the collisional heating power is predominantly transferred in the core region for all minority concentrations, for both hydrogen and helium-3 resonant species. The collisional power also reflects the higher collisionality of the helium-3 minority species with the background ions and electrons. The dotted lines in figure 3.18 illustrate the power transferred to the background ions. The high collisionality and also equation 3.6.1 provide evidence for why the majority of the collisional power is transferred to the background ions by the helium-3 if the energetic populations are not significantly large. With  $X[He3] = 1\%$  highly energetic populations are produced by the RF heating, resulting in larger power transferred to the ions for  $X[He3] = 4$  than 1%. For the case of hydrogen as the minority species, shown in figure 3.18 (left), the average fast ion energy is roughly that of  $E_{crit}$  for  $X[H]=4\%$ . This is reflected by the electron and ion background collisional power transfer being equal. Decreasing the minority species concentration leads to an increase in the highly energetic ion population and this exceeds the value of  $E_{crit}$ , such that more power is transferred to the background ions for  $X[H] = 4\%$  than 6%. The collisional power is not always transferred directly to the core region,

but depends also on the resonant surface, a parameter controlled by the antenna frequency. The minority species implemented in the experiment was 2.5% hydrogen. This value will now be fixed in order to investigate the influence of other important parameters.

$B_{res}$  Resonant Surface

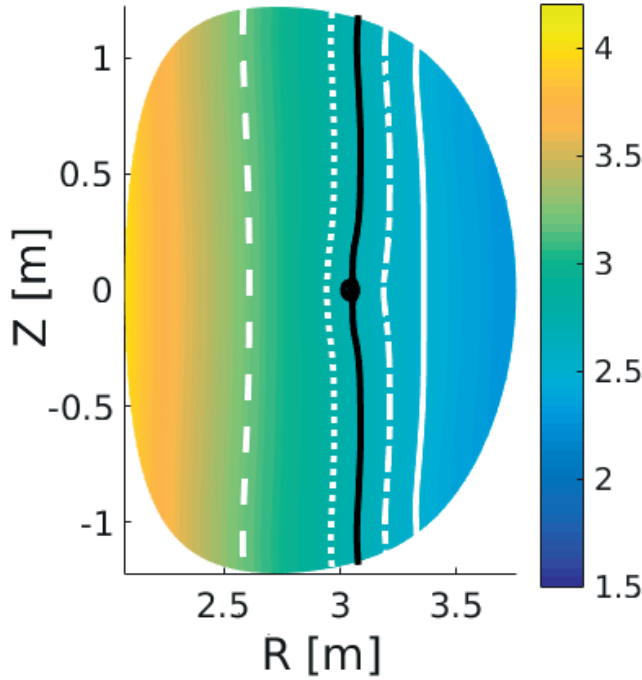


Figure 3.19 – 2D contour plot of the magnetic field strength  $|B|$ . The solid black line corresponds to the position of the cold ion-cyclotron resonance layer  $\omega_{ant} = \Omega_c$  for the baseline case  $|B_{res}| = 2.7\text{T}$ , the solid white line  $|B_{res}| = 2.5\text{T}$ , dot-dashed line  $|B_{res}| = 2.6\text{T}$ , dotted line  $|B_{res}| = 2.8\text{T}$  and the dashed line  $|B_{res}| = 3.2\text{T}$ .

In RF-heating experiments with off-axis power deposition, the same RF-antenna frequency is normally applied as would be for on-axis heating, but the magnetic field strength on axis is modified, such that the ICRF heating is off-axis. The characteristics of the RF generators and the geometry of the transmission lines connecting to the antennas impose a discrete set of frequencies that can be employed for best system performance. In this numerical work the RF-antenna frequency is varied corresponding to the magnetic resonant surface in the range  $B_{res} \in \{2.5, 2.6, 2.7, 2.8, 3.2\}\text{T}$ . Experimentally, the RF-antenna frequency would not be modified but the toroidal magnetic field strength on axis would be varied such that the magnetic field strength at the magnetic axis would be approximately  $B_0 \in \{2.9, 2.8, 2.7, 2.6, 2.3\}\text{T}$  respectively. The resonant surface, as described in section 2.2.2, influences RF-power absorption significantly. An important consequence of varying the antenna frequency for fixed  $B_0$  is the amount

of power transferred to the background species, shown in figure 3.20.

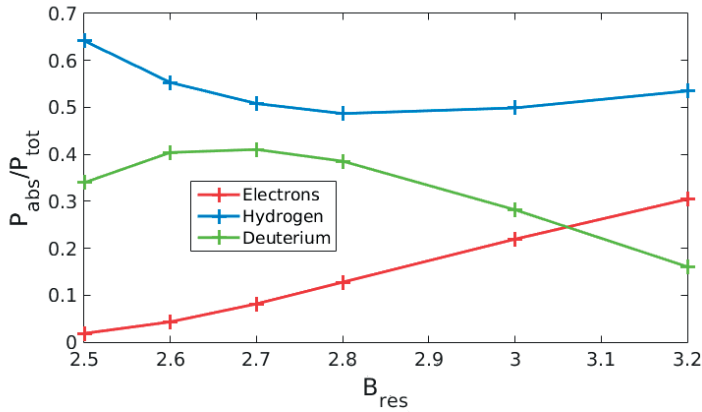


Figure 3.20 – RF-Power absorbed by the different plasma species as a function of the resonance location.

For the plasma conditions of the JET experiment 92398 described in this section, the electrons are the only species that can absorb RF-power away from fundamental or harmonic resonant surfaces except for large FOW effects. Electron absorption is through Landau damping or FLR effects such as eTTMP. HFS heating results in the wave travelling further through the plasma before reaching the resonant surface. This results in a larger amount of heating power transferred to the electrons, with LFS resulting in the lowest electron power absorption. The RF-power absorbed by deuterium through the second harmonic heating is peaked on axis where the temperature is highest. This is because harmonic heating is an FLR effect and therefore is more efficient at higher temperatures.

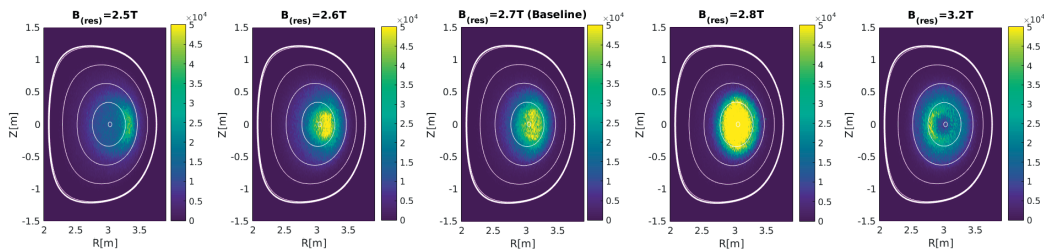


Figure 3.21 – 2D-contour plots of the fast ion pressure in the poloidal plane, summed over the toroidal angle.

Trapped RF-resonant particles tend to align themselves to the resonant surface. Displacing this surface from the magnetic axis towards the high or low field side of the tokamak influences the resulting fast ion pressure of the minority species. This is shown in figure 3.21. The 2D-contour plot clearly shows that the localisation of the fast ion pressure is shifted to the LFS for an

### Chapter 3. Numerical Advancements and Application for ICRF Optimisation

antenna frequency located at  $B_0 = 2.5T$  and to the HFS for  $B_0 = 3.2T$ . The closer the resonant surface is to the magnetic axis, the larger the fast ion pressure in the core. This influence is also seen in the energy distribution of the minority species, figure 3.22. This indicates that the antenna frequency at this moment in time during the shot was not fully optimised. If this value had been increased to  $B_{res} = 2.8T$ , then the population of RF-produced energetic particles above  $E > 0.15\text{MeV}$  would have been significantly larger compared to the other values of  $B_{res}$  simulated. In the region of  $0.15 < E < 0.4\text{MeV}$ , the particle distribution as a function of energy is a function of the distance of the resonant layer to the magnetic axis, such that LFS ( $B_{res} = 2.5T$ ) and HFS ( $B_{res} = 3.2T$ ) have the lowest concentration of particles within these energy values. For larger values of energy, this is no longer the case. Generating extremely energetic ions  $E > 0.5\text{MeV}$  is achieved in significantly larger numbers through heating towards the HFS. This can be explained by considering the anisotropy profiles and particle orbit types produced by varying  $B_{res}$ , such that more trapped particles remain in resonance with the RF-wave.

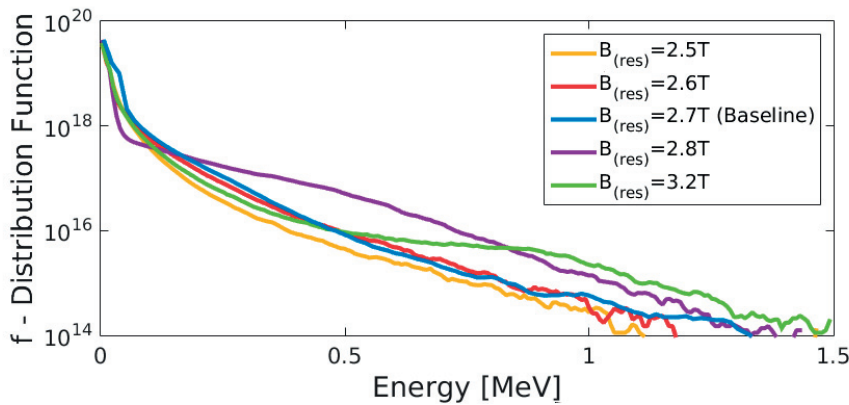


Figure 3.22 – Particle distribution as a function of energy for varying RF-antenna frequencies.

The anisotropy profiles (figure 3.23) indicate that anisotropy is inversely proportional to  $B_{res}$ . This relationship is actually complicated and requires an understanding of the orbit types produced by LFS, on-axis and HFS heating. The trapped-passing fraction is also relevant, since it changes strongly with local inverse aspect ratio. The passing and trapped populations produced are modified by modifying  $B_{res}$  relative to the on-axis  $B_0$ . As a percentage of the total fast particle distribution, larger passing populations result in lower anisotropy, whereas larger trapped populations have the inverse effect.

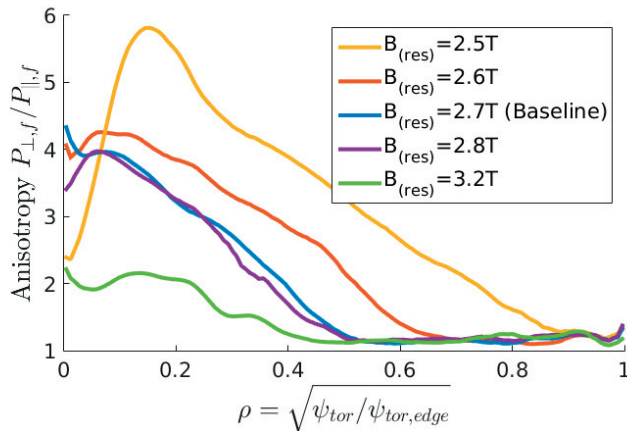


Figure 3.23 – Fast ion ( $E > 7T_e$ ) anisotropy profiles of the minority species, comparing the influence of varying the ion cyclotron resonance position in the plasma.

The orbit types of the fast particles can be measured using the principle of the conservation of toroidal momentum, as shown in section 2.4.1. The total number of co and counter passing and trapped particles as a percentage of the entire fast particle population is given in figure 3.24 for various  $B_{res}$ .

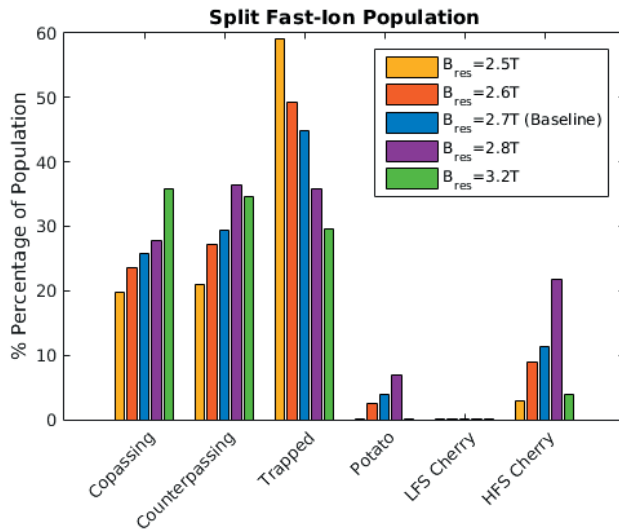


Figure 3.24 – Identification of the orbit types of the fast ( $E > 7T_e$ ) ions as a percentage of the total fast particles. Note that Potato and LFS cherry orbits are included in the trapped percentage and HFS cherry in the counter-passing.

With resonance on the LFS, trapped particles that align their bounce tips to the resonant surface will become deeply trapped. This results in large values of anisotropy. With HFS

### Chapter 3. Numerical Advancements and Application for ICRF Optimisation

resonance, trapped particles will be barely trapped, and anisotropy will approach unity. Clearly, when orbit widths are large, the latter simple explanation is complicated by exotic orbits.

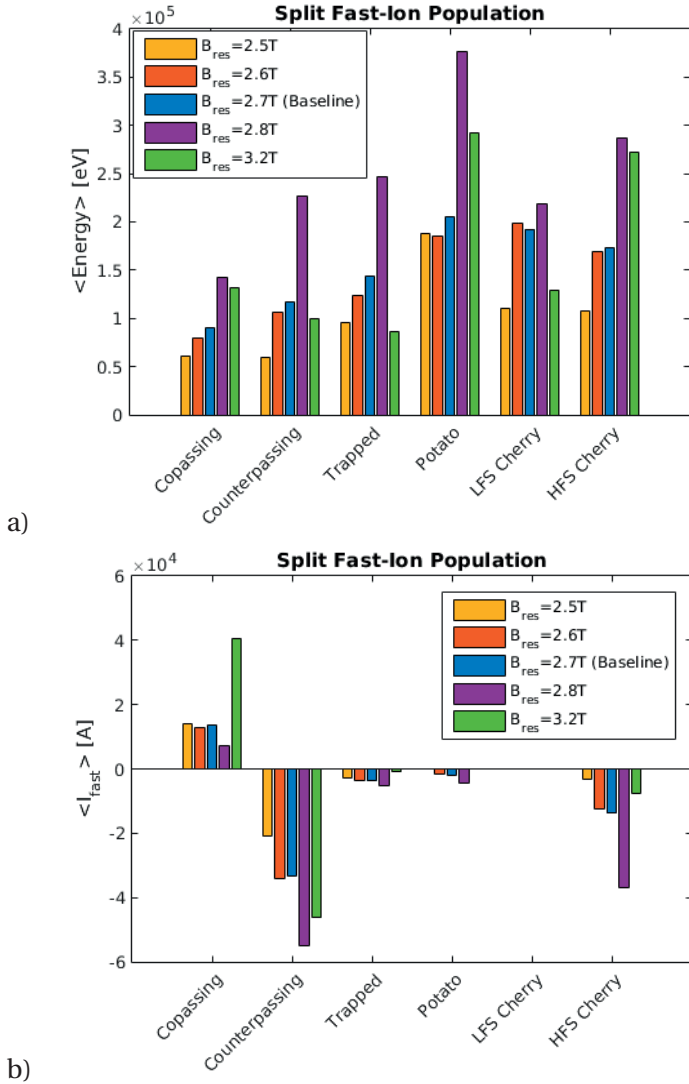


Figure 3.25 – The average energies and current contribution of each of the orbit types identified in figure 3.24.

Histograms of these exotic orbits for various  $B_{res}$  is shown in figure 3.24. The RF-pinch 3.5.1 effect is strong for  $B_{res} = 2.8T$ . Sufficient heating power results in the production of potato and HFS cherry orbit populations (the latter being an exotic orbit type that is counter-passing). Thus the counter-passing population also increases with an increase in  $B_{res}$ , except in the case where exotic orbits are heavily produced due to the RF-pinch effect. The number of passing particles plays a key role in RF-current drive (ICCD). Trapped particles oscillate between moving in the co and counter passing directs, and even despite the net toroidal precession

drift, the resultant current contribution is low. This is reflected in figure 3.25. The potato orbit is a highly energetic trapped particle. Its radial drift is large enough that the magnetic axis is enclosed inside the particle orbit, whereas for a thermal trapped particle this does not occur. Despite the extremely high average energy and non-negligible concentrations of the potato orbits, the current induced from such orbits is also small.

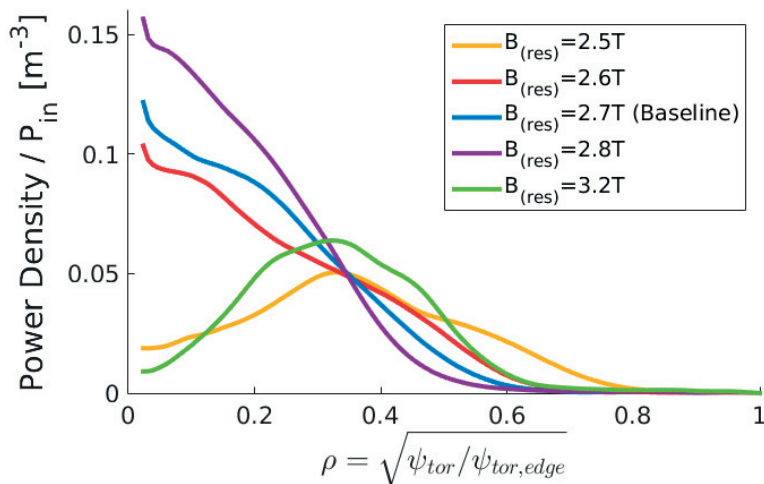


Figure 3.26 – Total absorbed RF-wave power, comparing the influence of varying the ion cyclotron resonance position in the plasma.

As shown from the simulation of  $B_{res} = 2.8T$ , tailoring the resonance position can also optimise RF-current drive due to the orbits produced. In addition to the RF-current drive, the radial location of the RF-power deposition is of crucial importance for the performance of ICRE. The collisional power deposition (figure 3.26) shows that moving the magnetic resonant surface by  $\pm 0.1T$  from the axis ( $B_0 = 2.7T$ ) still results in peaked on-axis background plasma heating. However, the values  $B_{res} = 2.5T$  and  $3.2T$  result in off-axis heating deposition.

### Plasma Current $I_p$ Scan

Modifying the plasma current also has a large impact on the orbits of fast particles. At risk of having a current driven unstable MHD mode, increasing  $I_p$  is difficult to achieve experimentally unless the change in  $I_p$  is matched by a change in  $B_0$  (so as to keep the q-profile fixed). Nevertheless, if  $B_0$  is held constant, varying  $I_p$  changes the curvature of the field lines (modifying q).

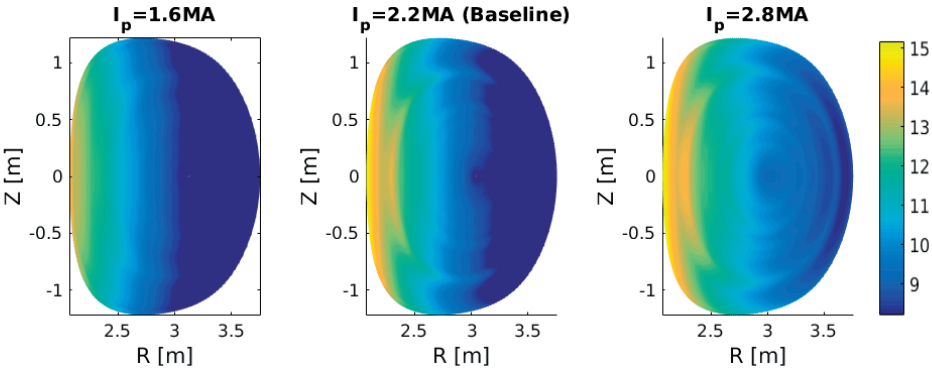


Figure 3.27 – The parallel wave-vector  $|k_{||}|$  comparing the influence of different values of the plasma current.

Curvature of the field lines influences the propagation of RF-waves in the plasma, notably the parallel propagation, shown in figure 3.27.

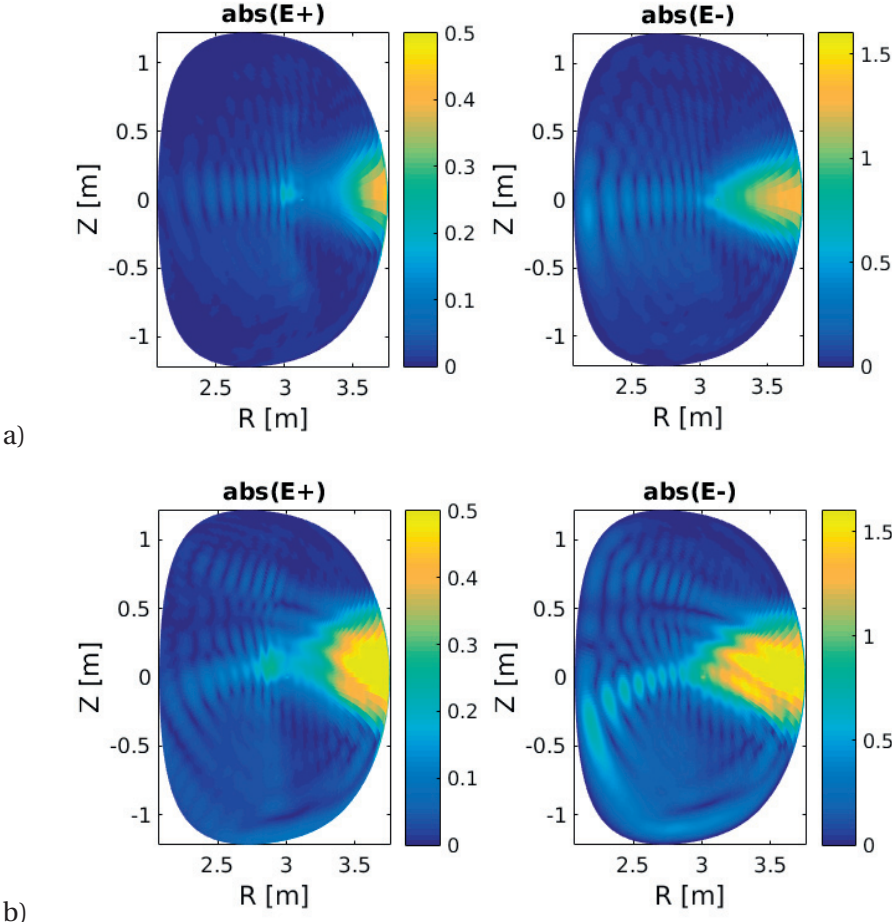




Figure 3.28 – Electric field components for the RF-wave propagation for fixed  $B_0$  varying plasma current: a)  $I_p = 1.6\text{MA}$  and b)  $I_p = 2.8\text{MA}$ .

As the plasma current increases, so does the contribution of the poloidal up-shift (equation 3.5.6) to  $k_{\parallel}$ . The curvature of the magnetic field lines and the influence of the poloidal magnetic field is visible in the propagation of the electric field into the plasma, shown in figure 3.28. The effects of the increase in poloidal magnetic field and field line bending impacts the RF-wave radial absorption profile, illustrated in figure 3.29. On-axis absorbed power peaking is proportional to the plasma current. The increase in plasma current increases the parallel wave-vector, which reduces the distance between the L-cutoff and ion-ion hybrid resonant layers. This is due to the reduced magnitude of L and S in comparison with  $n_{\parallel}^2$  in equation 2.2.8.

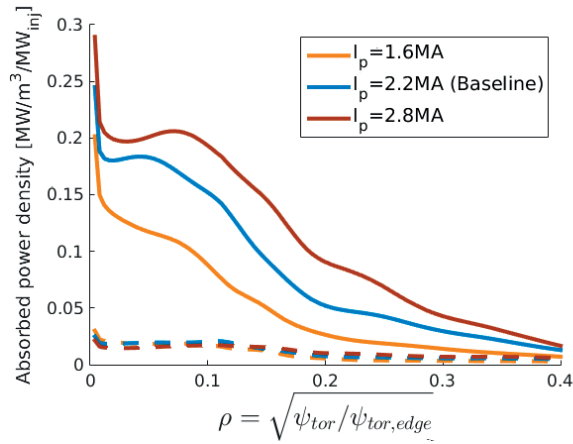


Figure 3.29 – RF-power absorption density normalised by the injected power for varying plasma current values  $I_p$ . Dashed lines represent the normalised absorbed power on the background electrons.

Increasing the plasma current also results in improved particle confinement through a reduced radial diffusion. This can be seen from the equations for the grad-B and curvature drift (equations 2.4.8 and 2.4.9). The decrease in the particle drifts improves confinement of particles and energy for the resonant ions, shown in figure 3.30. The difference between the higher current simulations (shown in dashed lines) and lower current (dotted lines) is consistent with this.

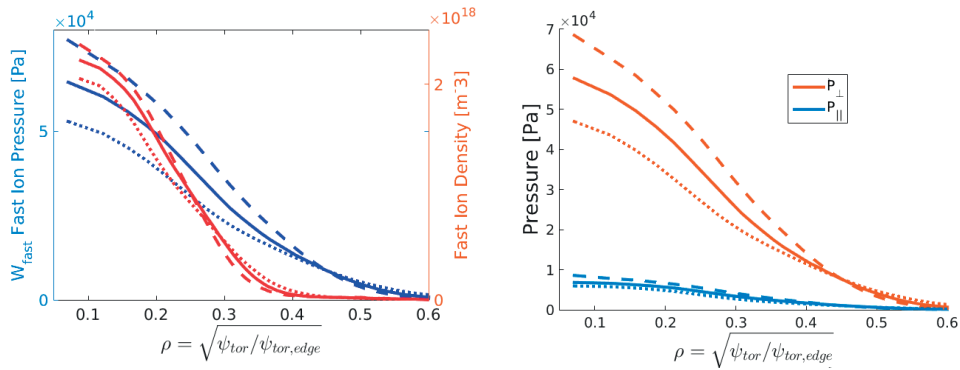


Figure 3.30 – Fast ion ( $E > 7T_e(s)$ ) density and temperature profiles of the minority species (left), including the parallel and perpendicular components of the pressure (right). Comparing the influence of varying the plasma current  $I_p$ . Dotted lines are  $I_p = 1.6\text{MA}$ , solid lines  $I_p = 2.2\text{MA}$  (baseline) and dashed lines  $I_p = 2.8\text{MA}$ .

The improvement in confinement for increasing  $I_p$  is shown in figure 3.31. It plots the energy distributions of the three simulations, indicating a significant increase in the highly energetic particle population for  $I_p = 2.8\text{MW}$ .

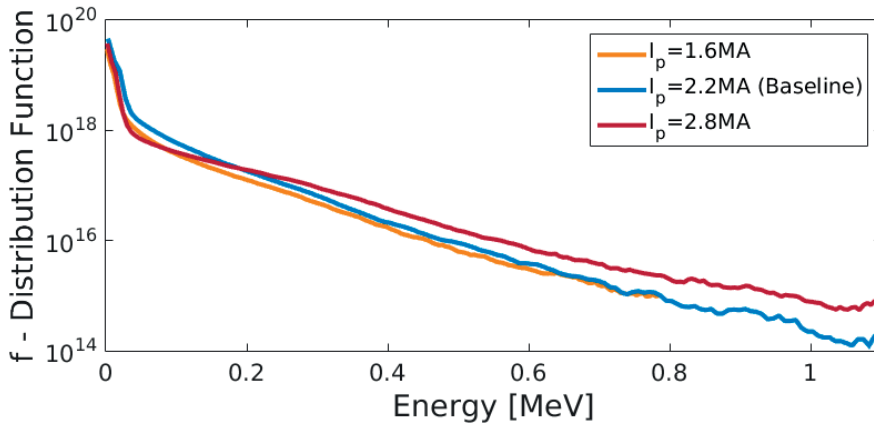


Figure 3.31 – Particle distribution as a function of energy for varying the plasma current  $I_p$ .

Figure 3.32 shows that for anisotropy values at  $\rho > 0.1$ , the low plasma current simulation results in high anisotropy values over a broad radial expanse. This is due to the increase in particle orbit drifts for a lower plasma current, enhancing the radial drift motion energetic particles over the bounce period.

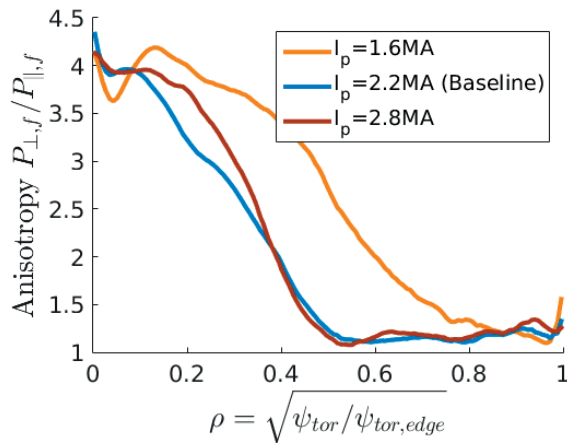


Figure 3.32 – Fast ion ( $E > 7T_e(s)$ ) anisotropy profiles of the minority species, comparing the influence of varying the plasma current  $I_p$ .

The influence of the plasma current on the plasma heating is shown in figure 3.33. The total power transferred to the electrons in the core region is higher for increased plasma current, whereas the power transferred on the ions remains approximately constant. This implies that the increase in plasma current helps to improve the confinement of the energetic ions with  $E > E_{crit}$ .

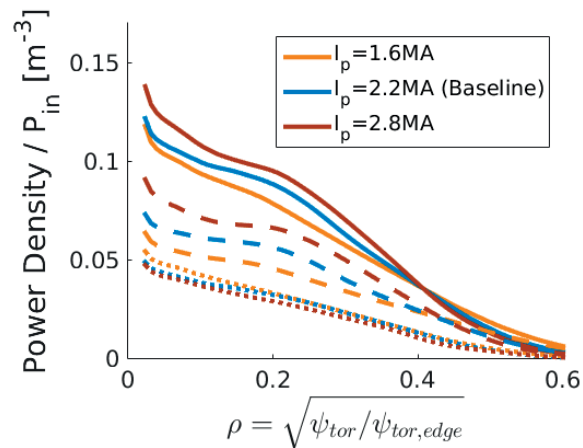


Figure 3.33 – The collisional power transfer from the minority species to the background plasma, comparing the influence of the plasma current. Dotted lines indicate power transferred to the background ions and dashed to electrons.

Influence of Coupled Antenna Power

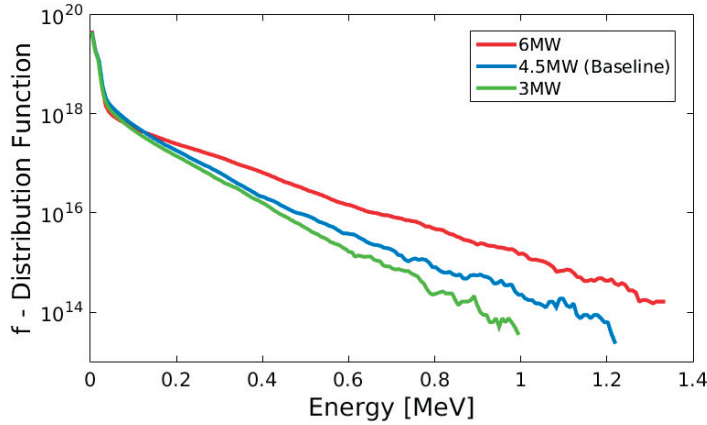


Figure 3.34 – The simulated particle particle distribution as a function of energy for JET shot number 92398 comparing different values of the coupled RF-antenna power.

For the first iteration of the SCENIC package, the antenna power does not affect the calculations of the magnetic equilibrium or the wave-propagation. The electric field calculated in LEMan is normalised in VENUS-LEVIS to ensure the antenna power equals a given value (the coupled RF-power is usually assumed or dictated by the experimental value). Wave-propagation is therefore unaffected by the RF-antenna power when the fast pressure and anisotropy are neglected.

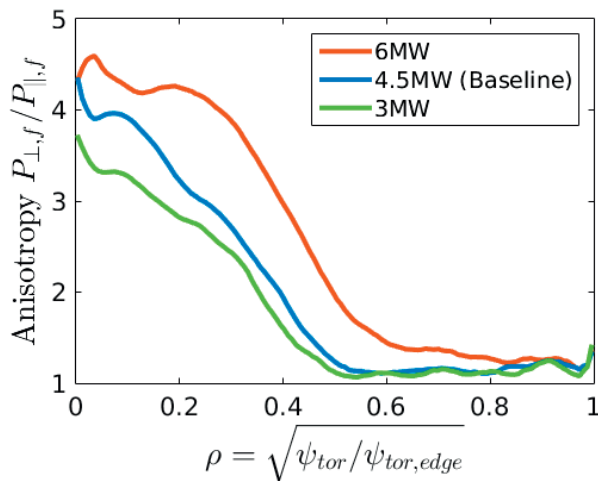


Figure 3.35 – Radial profile of the anisotropy of the fast ions ( $E > 7T_e$ )

In the VENUS-LEVIS code, the influence of the antenna power on the fast particle distribution

is non-linear. This is because, as the antenna power is increased, the energy transferred to the resonant particles augments, but with the increase in energy of a particle, the collisionality significantly decreases. This allows the possibility for higher energetic particles to be produced but at the potential cost that larger particle losses can also occur. Evidence for this can be found in figures 4.23-4.24 in [37]. The energy distribution for various values of coupled RF-power is given in figure 3.34.

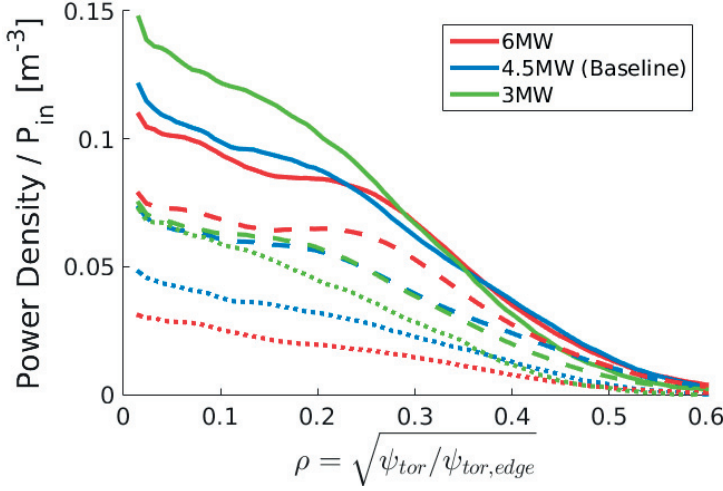


Figure 3.36 – Radial profile of the normalised (with the total input power) collisional power deposition comparing different values of coupled RF-power. Dashed lines represent power transferred to electrons and dotted lines to all background ion species.

As mentioned before, particles heated by ICRF using the minority species heating scheme are strongly heated in the perpendicular direction. The degree of anisotropy produced by the perpendicular heating is clearly proportional to the coupled RF-power. A plot of this is shown in figure 3.35. ICRF heating performance is determined by the amount of heating power transferred from the minority species to the total background population. This is reflected by the normalised collisional power loss from the minority species, shown in figure 3.36. The total power transferred to the background species might initially seem the inverse to what might be predicted. However, as the highly energetic resonant ion population increases, the collisionality between these particles and the background plasma decreases. The power transferred to the ions (dotted line) is also inversely proportional to the antenna power. This is because of  $E_{crit}$ , the energy limit beyond which the collisionality of a particle with the background electrons is stronger than that of the ions,

$$E_{crit} = 14.8 A_{res} T_e \left[ \sum_{\alpha} \frac{n_{\alpha} Z_{\alpha}^2}{n_e A_{\alpha}} \right]^{2/3}, \quad (3.6.1)$$

with  $A$  the atomic mass number, ‘res’ for the resonant minority species and the summation

over  $\alpha$  indicating the influence of all background and impurity ion species. For 6MW antenna power, the energetic particles produced collide more with the electrons than the ions. This is also reflected by the dashed line in figure 3.36: the collisional power transferred on the electrons is higher for the 6MW antenna power simulation.

#### Influence of Impurities

The JET tokamak has changed the wall and divertor material to what is known as the ‘ITER-like wall’, consisting of beryllium-9 wall and tungsten divertor. The best plasma performance in JET was achieved for the fully carbon wall and divertor. The reasons for the change from a fully carbon wall and divertor are numerous, but one reason is the deposit of radioactive hydrocarbon ‘soot’ (the radioactivity comes from the tritium-carbon molecules). The hydrocarbon chemical bonds are easily formed, easily transported (the resulting composite is light) and are difficult to remove once deposited. The reasons why the current material choice results in worse performance are also numerous. The Bremsstrahlung radiative power from high-Z impurities results in a significant increase in the power loss. Plasma disruptions have been experimentally observed to occur from high-Z impurity concentration in the plasma core, causing radiative collapse [48]. Carbon impurity in JET with the full carbon wall and divertor has previously been shown to significantly impact deuterium minority heating experiments such that mode-conversion effects lead to majority electron power absorption [48]. This is because carbon and deuterium have the same charge-to-mass ratio. For 3% carbon and deuterium in the plasma, this would be the equivalent of a 21% deuterium minority heating scheme, thus mode-conversion effects would dominate RF-power absorption. In the 92398 JET experiment, the most significant impurities present were beryllium-9, Nickel-59 and Tungsten-138. The presence of Ni comes from some of the plasma diagnostics used during experiments. This section shows that impurities also influence the RF-heating performance. The inclusion of impurity species into the SCENIC calculations is only possible due to the update to the LEMan code to extend the wave calculation to include an unlimited number of plasma species. The baseline simulation has included the impurity concentration  $X[\text{Be}]=0.5\%$ . This following section introduces the RF-heating performance when further impurities are included. One simulation calculates the inclusion of the impurities  $X[\text{Be}]=0.5\%$  and  $X[\text{Ni}]=0.5\%$ , and another for  $X[\text{Be}]=0.5\%$ ,  $X[\text{Ni}]=0.5\%$  and  $X[\text{W}]=0.5\%$ . The background deuterium plasma density was adjusted for each simulation to maintain quasineutrality. This results in a  $Z_{eff}$  of 1.6 and 1.7 respectively, whereas the baseline simulation is  $Z_{eff} = 1.24$ . The density and temperature profiles of the impurities is assumed to be the same as shown in figure 3.12 (right).

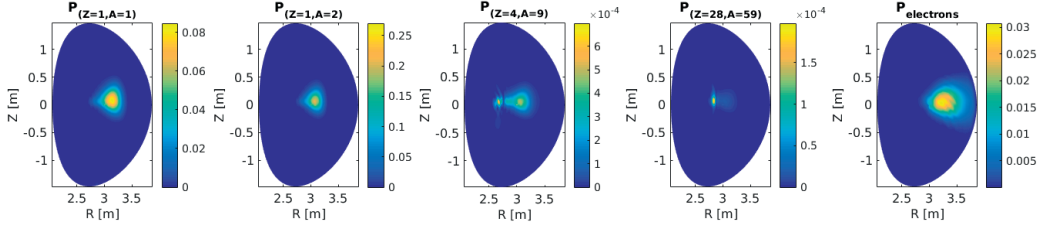


Figure 3.37 – Radial RF-power absorption density profiles normalised to the input power, varying the impurity content  $Z_{eff}$ .

Concerning the RF wave absorption, the inclusion of Ni or W impurities has an almost negligible impact: nickel absorbs less than 0.1% and tungsten less than 0.001%. The tungsten absorption is significantly smaller due to the charge-to-mass ratio lying outside of the LCFS. 2D contour plots of the RF-power absorption for the tungsten  $Z_{eff} = 1.7$  simulation is shown in figure 3.37. The power absorbed by tungsten is not included as the absorption was negligible. The power absorbed by Be and Ni is through the second harmonic. The presence of heavy impurities, depending upon the charge-to-mass ratio, can impact the wave through the displacement of the cut-off and resonances. This can be seen through the dispersion relation  $n_{\perp}$ , figure 3.38. Due to the negligible influence of the tungsten RF-absorption, figure 3.38 is plotted comparing only the baseline  $Z_{eff} = 1.24$  simulation with the tungsten  $Z_{eff} = 1.7$  simulation. As the dispersion relation depends strongly on the magnetic field strength which is inversely proportional to the major radius, the plot is made comparing the dispersion relation at  $\theta = 0$  and  $\theta = \pi$ .

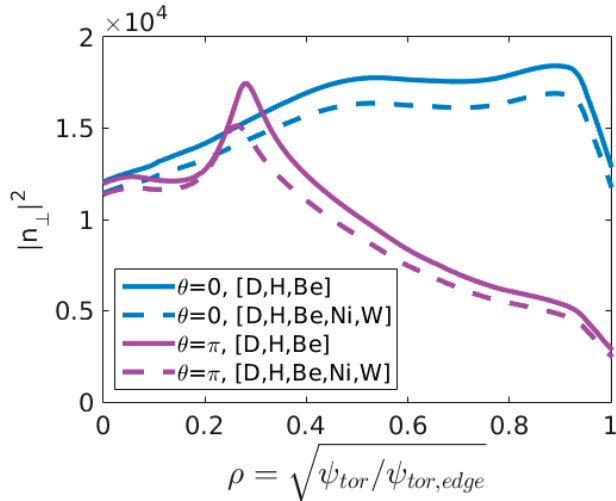


Figure 3.38 – Plots of the perpendicular refractive index  $|n_{\perp}|^2$  in the major radius direction, plotting the values along the line  $\theta = 0$  and  $\theta = \pi$ . The influence of the impurity content  $Z_{eff}$  is compared.

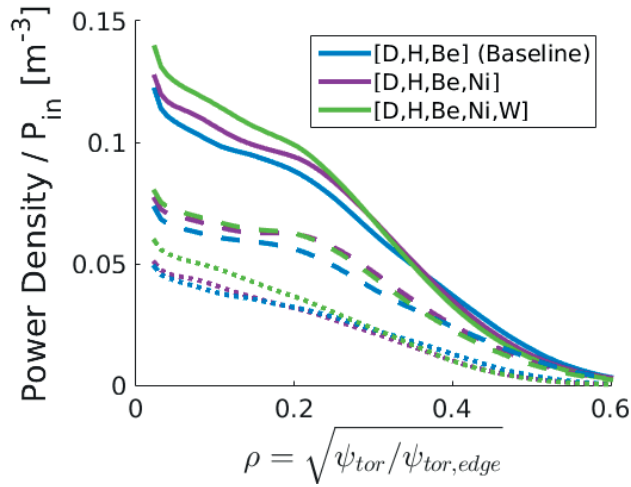


Figure 3.39 – The collisional power transfer from the minority species to the background plasma, comparing the influence of the impurity content  $Z_{eff}$ . Dotted lines indicate power transferred to the background ions and dashed to electrons.

The presence of Ni and W in the plasma acts to modify the total perpendicular refractive index  $n_{\perp}$  to make the wave more opaque. The impurities also radially displace the cut-off and resonance regions, which can be shown using the cold plasma dispersion relation equations defined in section 2.2.1. This will modify the polarisation of the wave in the resonance layer. The accuracy of the calculation of  $n_{\perp}$  has been improved by the update of the LEMan code to apply the hot plasma dispersion function in the iteration of the dielectric tensor calculation using  $k_{\perp}$ .

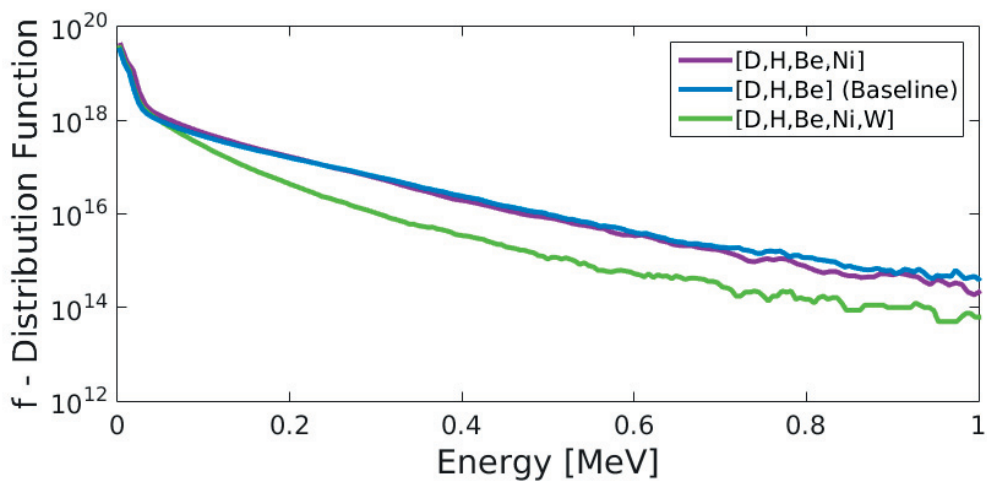


Figure 3.40 – Particle distribution as a function of energy for varying plasma impurity content.



The more obvious effect that impurities will have on the RF-heating is through the increase in collisionality between the resonant particles and the background ions. Figure 3.39 shows the amount of power transferred to the background plasma. The total collisional power and the power transferred solely to the background ions in the core region is proportional to  $Z_{eff}$ . In addition to this, the collisional power transferred to the electrons is larger than that of the baseline or Ni included simulations. An explanation for this can be given using the particle distribution as a function of energy in figure 3.40. A combination of the  $Z_{\alpha}^2$  dependence of  $E_{crit}$  and the reduced population of highly energetic resonant ions in the simulations that include tungsten influence the electron collisional power transfer. The resulting particle distribution as a function of energy (figure 3.40) illustrates the significant influence the tungsten has on the production of energetic particles. The increase of  $Z_{eff}$  on the RF-heating is also clear in the anisotropy profiles: figure 3.41. Collisionality and a modification of the RF-polarisation at the resonance layer reduce the anisotropy in the core region. This is then inverted beyond  $\rho > 0.25$ , presumably due to the influence of the impurities on RF-propagation and thus polarisation.

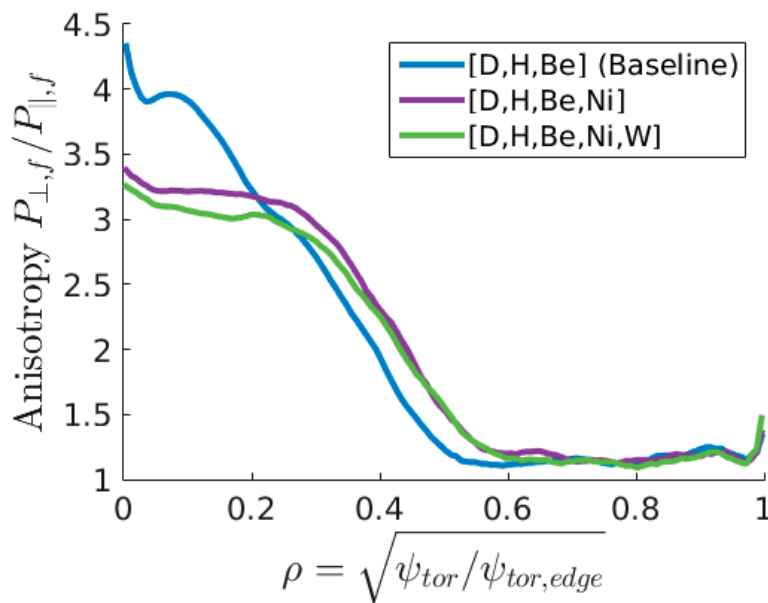


Figure 3.41 – Fast ion ( $E > 7T_e(s)$ ) anisotropy profiles of the minority species, comparing the influence of varying the impurity content  $Z_{eff}$ .

### Second Harmonic Deuterium Parasitic Absorption

The background deuterium species was shown in figure 3.14 to absorb, via second harmonic ion cyclotron heating, approximately a third of the RF-power by the LEMan code for a minority heating scheme with  $X[H]=2.5\%$ . Providing the LEMan wave calculation to the VENUS-LEVIS QLO, the evolution of the deuterium distribution function can also be calculated. A scan of the RF-power is performed to evaluate the effectiveness of the harmonic heating. Figure

3.42 shows the comparison between the harmonic deuterium heating and the  $P_{RF,H} = 3\text{MW}$  minority species hydrogen heated scenario, which corresponds to the value modified by the RF-absorption. For the actual experimental conditions with  $P_{RF,D} = 1.5\text{MW}$ , the energetic particle population is significantly reduced compared to the minority species hydrogen scheme, whereby the minority heating produces MeV range particles. Even with 6MW of power transferred to the deuterium population via harmonic heating, the largest energies produced are predicted at approximately 0.12MeV.

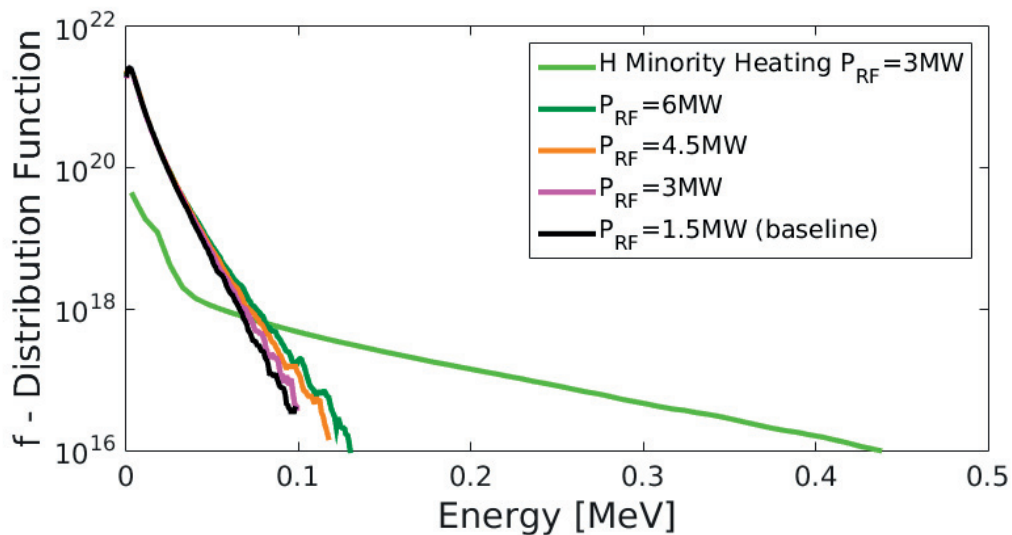


Figure 3.42 – Particle distribution as a function of energy from second harmonic deuterium heating with  $P_{RF} = 1.5\text{MW}$  for JET shot number 92398, comparing different RF-antenna power values.

The fast ion anisotropy is similar for all second harmonic simulations and considerably lower than as generated by the minority heating scheme, shown in figure 3.44. This indicates the difficulty of the harmonic heating to generate energetic particles, which are heated preferentially in the perpendicular direction by the ICRF heating.

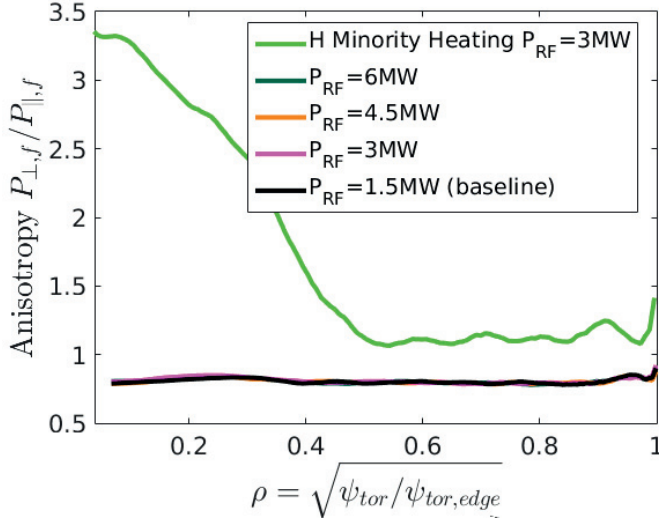


Figure 3.43 – Fast ion ( $E > 7T_e(s)$ ) anisotropy profiles of the majority deuterium species heated via harmonic heating, comparing the influence of varying the antenna power  $P_{RF}$ .

There is no significant difference between the fast ion densities and pressures for varying Rf-antenna power. These values are so low that the splitting method is only isolating the normal Maxwellian particles that are not produced by RF-heating. The fast ion pressure generated by the minority heating scheme is considerably larger than by second harmonic heating.

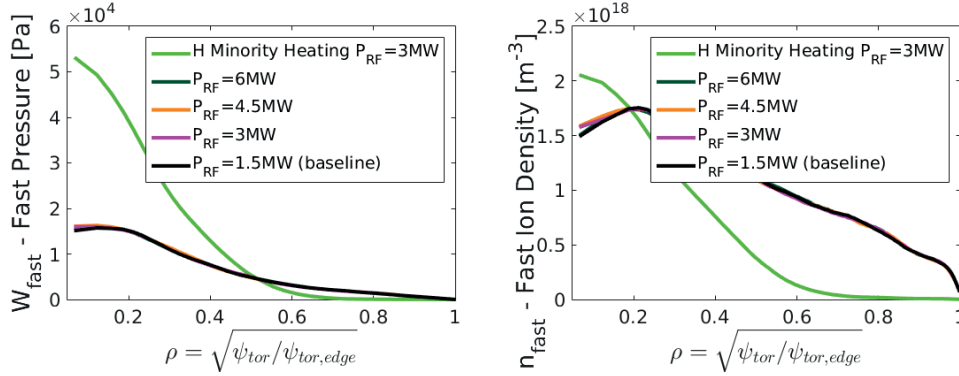


Figure 3.44 – Fast ion ( $E > 7T_e(s)$ ) left) pressure and right) density profiles of the majority deuterium species heated via harmonic heating, comparing the influence of varying the antenna power  $P_{RF}$ .

The maximum of the collisional power density transferred to the background is predicted to be larger than for the minority species scheme. The number of particles that can resonate with the RF-wave is very large, and therefore the average transfer of RF-energy given to each resonant particle is very small. This results in particles not being able to gain energies that exceed the thermal background. The benefits of this is that the collisional power transfer to

the background is very large. Increasing the RF-antenna power increases the power delivered to the plasma core.

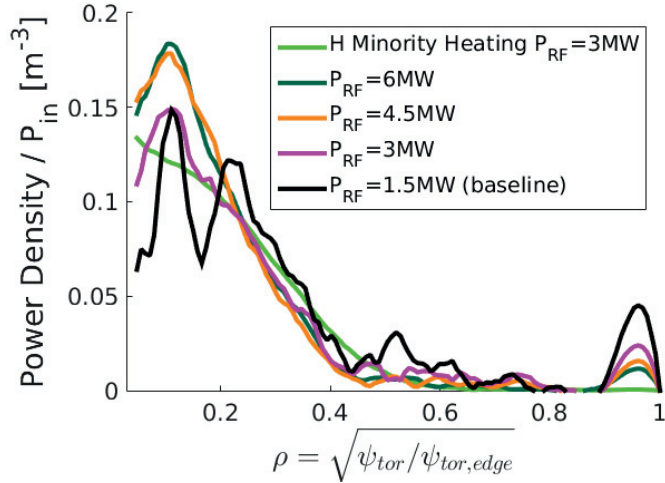


Figure 3.45 – The collisional power transfer of the majority deuterium species heated via harmonic heating to the background plasma, comparing the influence of the RF-antenna power.

The Fokker Planck VENUS-LEVIS simulations made for these deuterium harmonic heating results used markers with significantly larger weight size than in the minority species heating simulations of the JET shot 92398. This is because the total deuterium concentration in the experiment was very large ( $X[D]>85\%$ ), resulting in reduced statistics for the highly energetic particles. One possible issue with the results, such as shown in the particle distribution as a function of energy (figure 3.42), is that highly energetic particles may be produced but at quantities lower than the numerical resolution of these simulations. The Bessel functions in equation 2.4.30 use  $J_1(Y)$  and  $J_{-1}(Y)$  for fundamental harmonic heating and  $J_1(Y)$  and  $J_{-1}(Y)$  for second harmonic heating. Second harmonic heating requires a statistically significant number of particles that have large  $Y = k_{\perp}\rho_{\perp}$  values. Future work should involve investigating the role of increasing the  $E_{max}$  value in VENUS-LEVIS used to generate the numerical marker population from the background profiles.

### Lost Particle Populations

The lost particle population can represent the efficiency of the heating system, and statistics of the losses can help to optimise heating schemes. However, as seen in table 3.3, the relative concentrations of the particle and energy losses are very small. This is why up to this section, losses in the simulations made on JET experiment 92398 had not been mentioned: losses in this experiment did not play a crucial role in the RF-heating performance. Increasing the antenna power increases the lost power and particle losses, whereas increasing the plasma current has the inverse effect. Increasing the minority species concentration lead to lower

highly energetic particle populations and thus increased collisionality between the minority species and the background plasma. Enhanced collisionality results in larger radial diffusion over collisional time-scales and thus larger losses. Further evidence for this is from simulating the presence of tungsten impurities in the plasma. Varying the antenna frequency does not significantly alter the fast particle losses.

Simulation	$P_{lost}/P_{input}$ %	$N_{lost}$ %
Baseline	0.11	2.51
$I_p = 1.6\text{MA}$	0.22	3.38
$I_p = 2.8\text{MA}$	0.06	1.56
$B_{res} = 2.5\text{T}$	0.12	2.52
$B_{res} = 2.6\text{T}$	0.11	2.50
$B_{res} = 2.8\text{T}$	0.13	2.53
$B_{res} = 3.2\text{T}$	0.14	2.48
$Z_{eff} = 1.62$	0.12	2.50
$Z_{eff} = 1.74$	0.25	4.94
3MW	0.09	2.1
6MW	0.2	4.25
$X[H] = 1\%$	0.09	0.91
$X[H] = 4\%$	0.16	3.64
$X[He3] = 1\%$	0.06	1.36
$X[He3] = 2.5\%$	0.12	3.11
$X[He3] = 4\%$	0.18	4.81

Table 3.3 – The lost power and particle percentages for each of the simulations calculated for the JET shot 92398.

### Summary

Updates to the LEMan code, as well as the unique capabilities of the SCENIC package have been exploited to investigate the performance of the ICRF minority species heating scenario. The SCENIC package self-consistently retains anisotropic effects, and FOW effects are calculated by the VENUS-LEVIS code which influences the fast-ion pressure profiles used to self-consistently iterate through the magnetic equilibrium and wave-propagation. Inclusion of anisotropic and FOW effects have been shown to be of crucial importance when calculating the RF-heating performance for varying parameters such as the plasma current  $I_p$  or the coupled RF-power. Energetic ion orbit widths decrease when increasing the plasma current (for fixed  $B_0$ ) and increase when increasing  $P_{RF}$ . The anisotropy is observed to increase proportionally to the energetic particle orbit width. Simulations varying the RF-resonant surface  $B_{res}$  also benefit from the inclusion of anisotropy and FOW effects, ensuring a more precise calculation of the RF-induced exotic orbit types and the radial profile of the collisional power transfer to the background. Updating the dielectric tensor of LEMan permits the accurate calculation of the RF-absorbed power on the different plasma species. When varying the resonant surface

location, improved calculation of the dielectric tensor was shown to be of crucial importance to evaluate the RF-absorbed power partition on the electrons and the deuterium as compared to the hydrogen. The minority species and concentration was also found to strongly influence the RF-power absorption on the electrons and deuterium. The inclusion of FLR effects into the dielectric tensor was also exploited to calculate the wave-calculation and Fokker-Planck evolution of the second harmonic parasitic deuterium absorption. Extending the LEMan code to calculate the wave-propagation for an unlimited number of plasma species, the influence of impurities on ICRF was evaluated. The inclusion of high-Z impurities in the simulations was seen to reduce the perpendicular refractive index  $n_{\perp}^2$ . The accurate calculation of which required the update of the LEMan code to calculate  $k_{\perp}$  using the hot plasma dispersion relation.

#### 3.6.2 W7-X

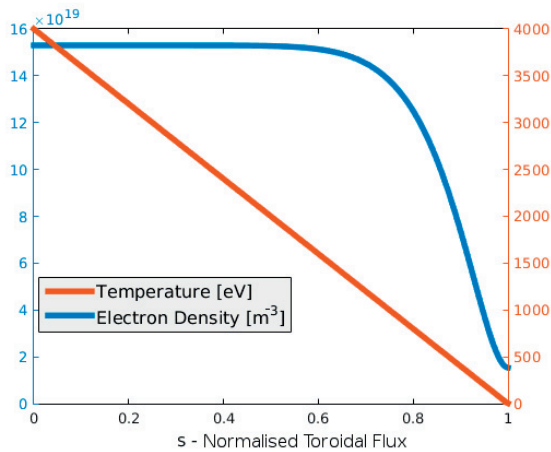


Figure 3.46 – Electron density and temperature profiles used for the minority heating simulations of W7-X.

The following section will focus on comparing the standard minority heating scheme of He4(H) heating with  $X[H] = 2\%$  in W7-X. Studying the influence of the 3D magnetic geometry for three equilibria: the low, standard and high toroidal mirror configurations is described in section 2.1.3. The plasma profiles used in this work are analytic and correspond to what might be expected in future W7-X experiments; figure 3.46. This includes a zero plasma current profile. These profiles were also used in [49].

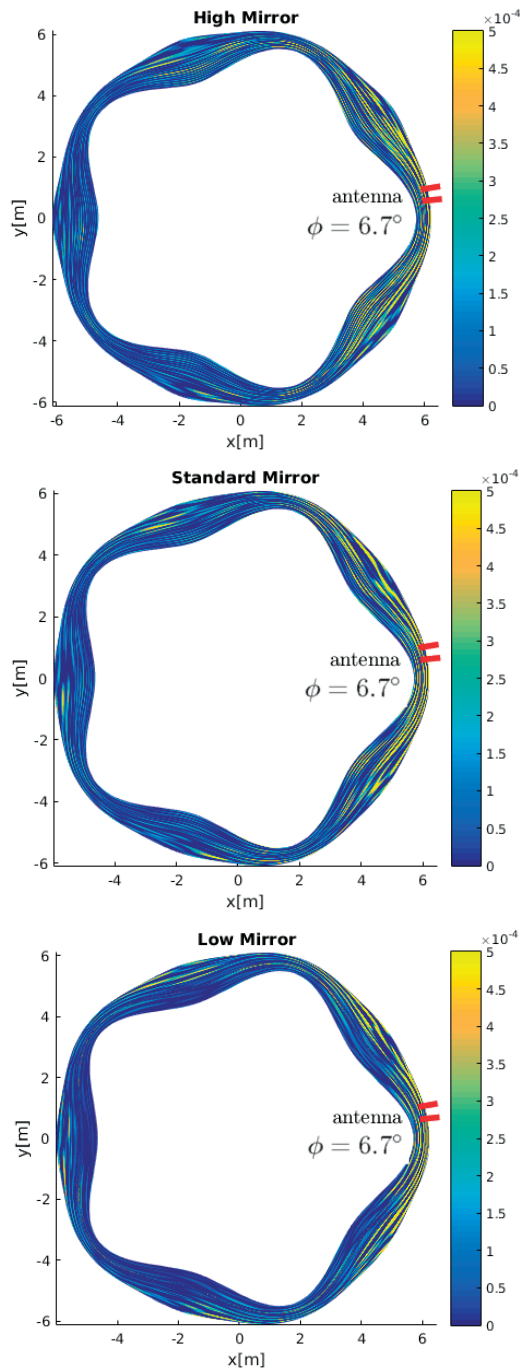


Figure 3.47 – Electric field component  $|E_+|$  in arbitrary units, comparing a) high mirror, b) standard mirror and c) low mirror magnetic configurations.

The choice of helium-4 as the background plasma species is due to restrictions on the neutron generation preventing the use of deuterium in W7-X for the first few experimental campaigns. An additional assumption due to the uncertainty in the experimental performance of W7-X

is  $T_i = T_e$ . The wave propagation for each toroidal mirror configuration is given in figure 3.47. Due to the large toroidal magnetic mirror, the high mirror configuration has a reduced electric field amplitude in toroidal field periods away from the RF-antenna region. The low mirror configuration has the lowest electric field amplitude when comparing values inside the magnetic axis  $R(\pi/2 < \theta < 3\pi/2)$ . This indicates strong single-pass absorption of the wave, due to the resonant layer remaining close to the magnetic axis for all toroidal angles.

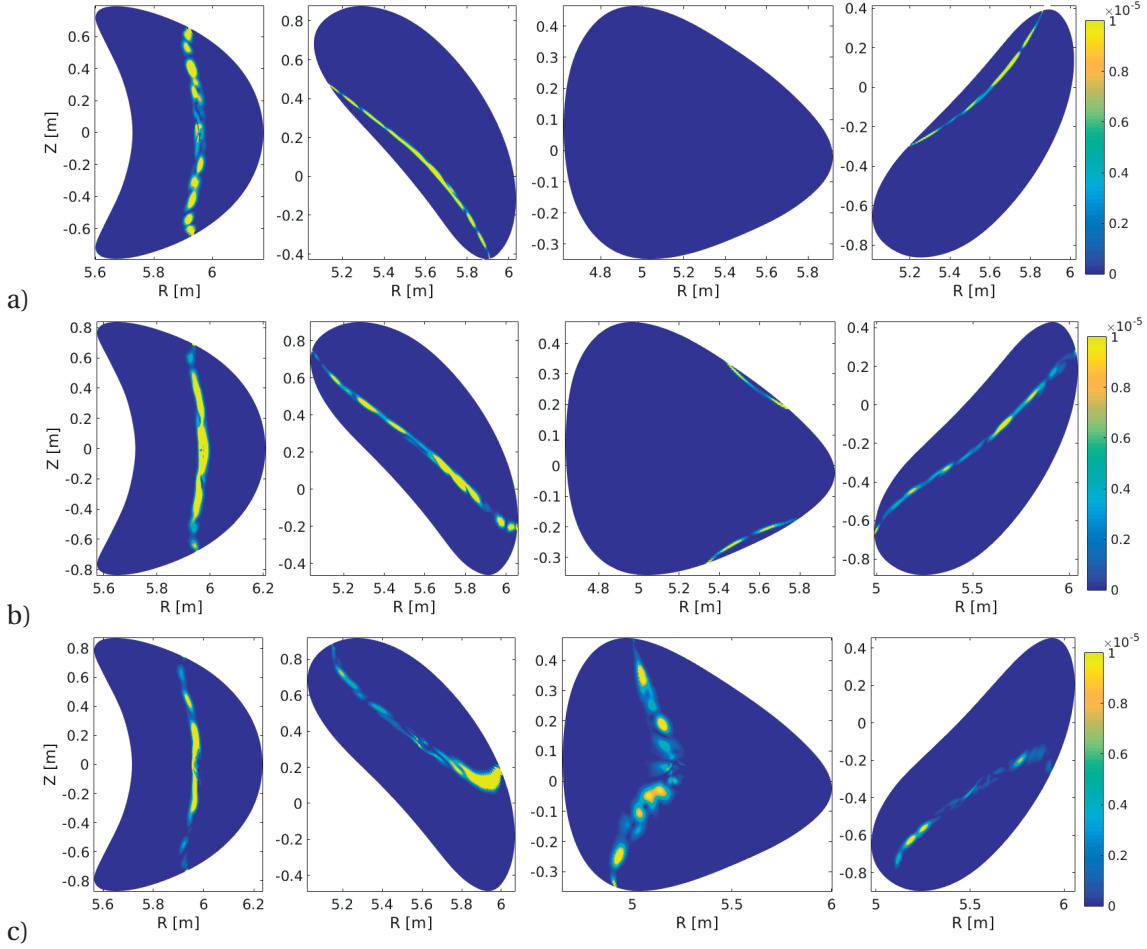


Figure 3.48 – Contour plots of the total absorbed power [a.u.] predicted for the minority species heating scheme. Plots of the poloidal cross-sections at  $\varphi = [0, \pi/10, \pi/5, 3\pi/10]$  are given for a) high, b) standard and c) low toroidal magnetic mirror configurations.

Figure 3.48 shows the total absolute power predicted by the LEMan wave code. The location of the antenna is very close to the mirror position at the toroidal angle  $\varphi = 0$ . The simulation at  $\varphi = 0$  is shown in the far left contour plots of figure 3.48. Strong RF-absorption of the wave by the resonant species would result in a larger absorption at toroidal angles closer to the antenna such as  $\varphi = 0$  or  $\pi/10$ . For the low mirror, the power is more concentrated in the core region than the standard or high mirror. For the high mirror, for most toroidal angles, most of the power is located towards the edge of the plasma. With respect to the triangular



toroidal section ( $\varphi = \pi/5$ ), it is clear that the low mirror is the only equilibrium to permit on axis resonance in the core at toroidal regions far from the antenna. As the antenna is located between  $\varphi = 0$  and  $\pi/10$ , the total power absorption at  $\varphi = \pi/10$  tends to be larger than at  $\varphi = 3\pi/10$ .

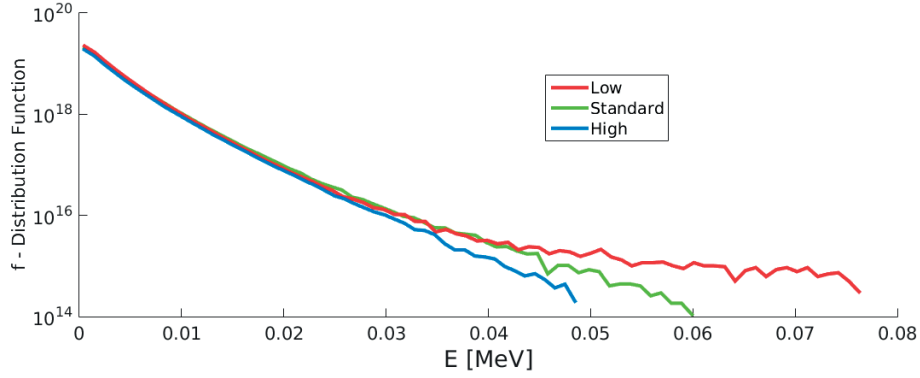


Figure 3.49 – Particle distribution as a function of energy of the minority species, comparing the influence of the magnetic equilibrium.

One common limit of tokamaks is known as the Greenwald density limit. The Greenwald limit does not exist for stellarator devices, allowing flat-top shaped, high density background plasma profiles. This results in high collisionality which increases the difficulty of an RF-resonant particle from becoming supra-thermal. This is reflected in the particle distribution as a function of energy plotted in figure 3.49 where very few energetic particles  $E > 50\text{keV}$  are generated. The almost linear curve of the high mirror equilibrium indicates that the particle distribution is nearly Maxwellian. Only the standard and low mirror equilibria develop (weakly) non-Maxwellian fast ion distributions.

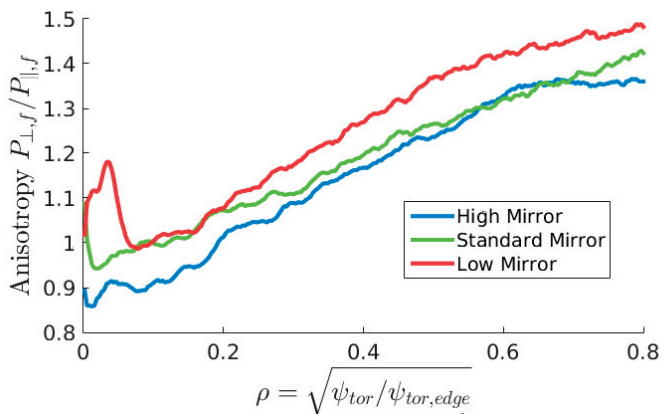


Figure 3.50 – Fast ion ( $E > 5T_e(s)$ ) anisotropy profiles of the minority species, comparing the influence of the magnetic equilibrium.

The concentrations of fast ion particles are very small, which is consistent with the anisotropy

profiles in figure 3.50. The link between anisotropy profiles and energetic tails was also explored in the JET simulations of section 3.6.1 varying the coupled RF-power. The anisotropy increases proportionally with  $\rho$  due to particle trapping in the presence of magnetic wells which become more enhanced towards the LCFS. This provides further evidence that the high collisionality profiles prevent the generation of highly energetic particles using the standard minority heating scheme.

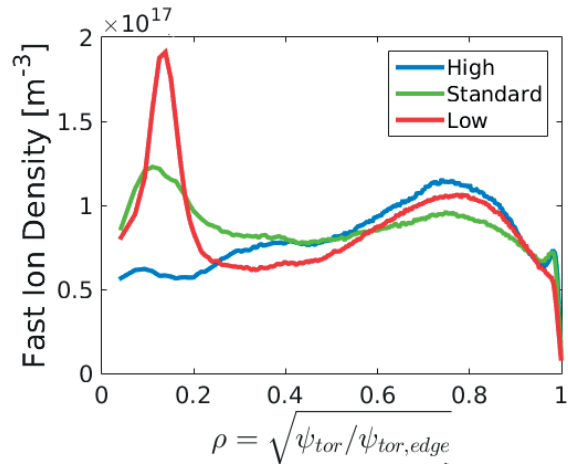


Figure 3.51 – Fast ion ( $E > 5T_e(s)$ ) density for minority species heating in diverse W7X magnetic equilibrium.

The fast ion density profiles have large off-axis values for all equilibria (figure 3.51). The fast ion density profiles indicate that only the standard and low mirror equilibria produce on-axis peaked energetic resonant ion densities.

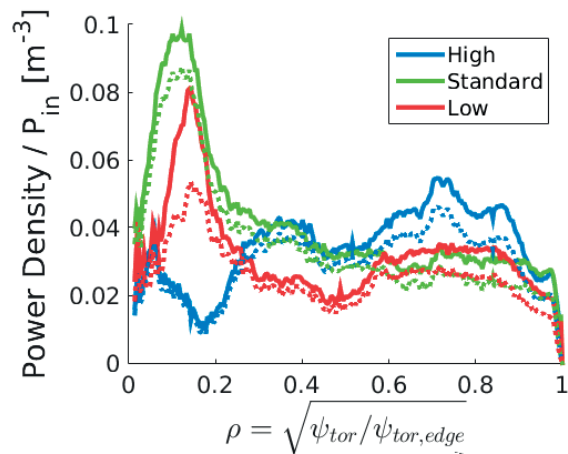


Figure 3.52 – The collisional power transfer from the minority species to the background plasma, comparing the influence of the magnetic equilibrium. Dotted lines indicate power transferred to the background ions.  $P_{in} = 1.5\text{MW}$ .

The radial collisional power density reflects the off-axis power transfer of the fast ion density, shown in figure 3.52. Information on the lost particle power and densities, as well as the

Mirror	$P_{cols}/P_{in}$ %	$P_{lost}/P_{in}$ %	Lost Particles %
High	99.92	0.08	2.42
Standard	99.78	0.22	3.30
Low	99.27	0.72	3.48

Table 3.4 – The lost power and particle percentages for ICRF heating in W7X for the different magnetic mirror configurations.

collisional power integrated over the entire volume are given by table 3.4. The combination of the toroidal magnetic mirror effect and the differences in energetic particle populations lead to a proportionality between the toroidal mirror and the power lost due to particle losses. These losses are located close to the RF-antenna toroidal field period, as shown in figure 3.53. The losses are considerably higher for the low mirror due also to the poor optimisation of this magnetic configuration for fast ions.

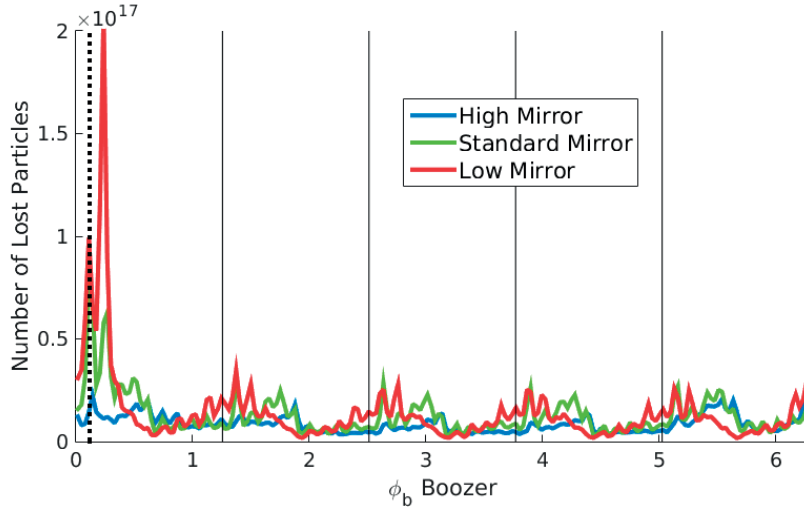


Figure 3.53 – Toroidal plot of the losses produced from minority species heating in various W7-X toroidal mirror configurations.

The distribution of lost particles in  $\lambda - E$  space explains some of the different characteristics of RF-heating in varying toroidal magnetic mirror stellarator equilibria (figure 3.54). The number of energetic particles produced for  $E > 40\text{keV}$  is very low for the high mirror. This results in the low saturation of the contour plot figure 3.54 (a). For the standard (figure 3.54 (b)) and low mirror (figure 3.54 (c)), the losses are significantly larger. For all three magnetic equilibria, the lost particles have  $\lambda \sim 0$ , corresponding to deeply trapped particles.

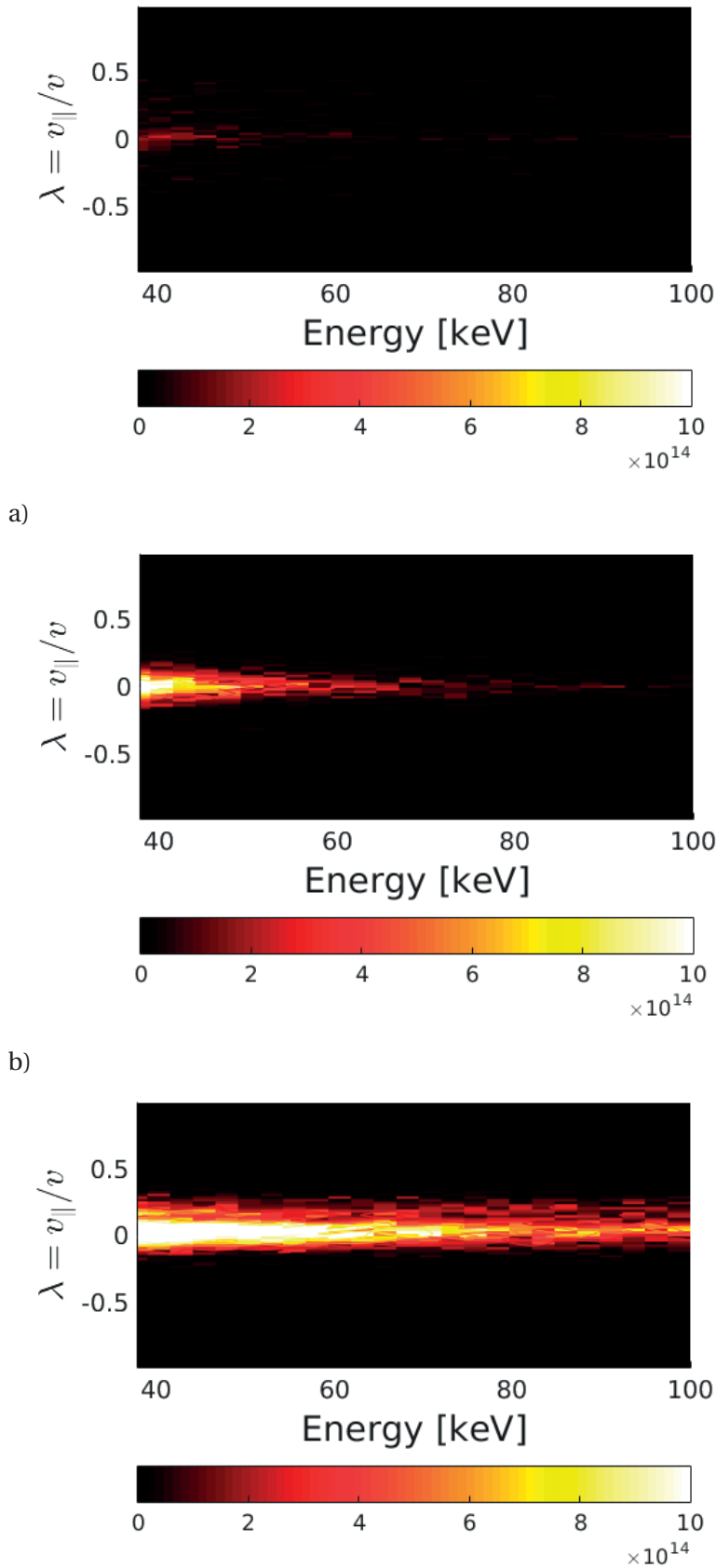


Figure 3.54 – Contour plots of the particle distribution in pitch angle-energy space for the minority species heating scheme for the a) high, b) standard and c) low mirror configurations.

Exploiting the unique capabilities of the SCENIC package, further studies of the parasitic second harmonic helium-4 absorption of the ICRF power should be made. It is not expected that second harmonic heating of the majority helium-4 species would result in the production of highly energetic particles or fast ion anisotropies. However, the collisional power density produced from second harmonic helium-4 heating should be evaluated to predict the full heating performance of the RF-heating scheme when applied to W7-X.

#### 3.6.3 RF in the Presence of Helical Cores

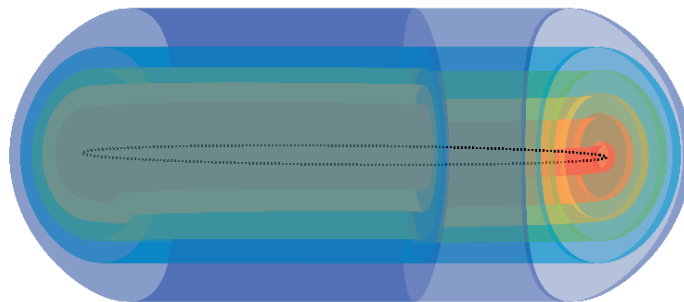


Figure 3.55 – Nested flux surfaces of the 3D internal helical deformation in an ITER hybrid scenario magnetic equilibrium. Dotted line illustrates the magnetic axis.

Tokamaks have been known to produce non-linearly saturated 3D internal helical equilibrium structures [50, 51]. Hybrid scenario experiments may have negative (or extended low shear) magnetic shear within the core region. For baseline scenarios, the presence of sawteeth modes can force the  $q_{min}$  value to approach unity at the radial position where the magnetic shear is lowest. After the unstable sawtooth mode, the plasma can saturate to form an internal kink mode around the radial region of low magnetic shear, whilst maintaining a toroidally axisymmetric outer mantle between this region and the LCFS, shown in figure 3.55. This section explores the influence of this internal helical deformation on the performance of a standard hybrid scenario experiment in the ITER tokamak. The profiles for such a configuration are found in [52, 53] and the magnetic equilibrium is from the work of W. A. Cooper [54] with  $I_p = 13.5\text{MA}$ . The toroidal displacement of the magnetic axis from  $\{R_{00}, Z_{00}\}$  is shown in figure 3.56. The core toroidal plasma flow velocity is predicted to be of the order of 10-30km/s. The magnetic equilibrium will therefore rotate toroidally around the tokamak. The position of the RF-antenna with respect to the internal kink mode therefore changes in time. Due to the large major radius, this results in a time-scale that is much longer than that of the wave-propagation such that  $\tau_{RF} \ll \tau_{\phi} \ll \tau_{col}$ , where  $\tau_{\phi}$  is the time-scale for the plasma fluid to complete one toroidal period of the device. For these conditions, the SCENIC code can be used to calculate the RF-propagation assuming a static magnetic equilibrium.

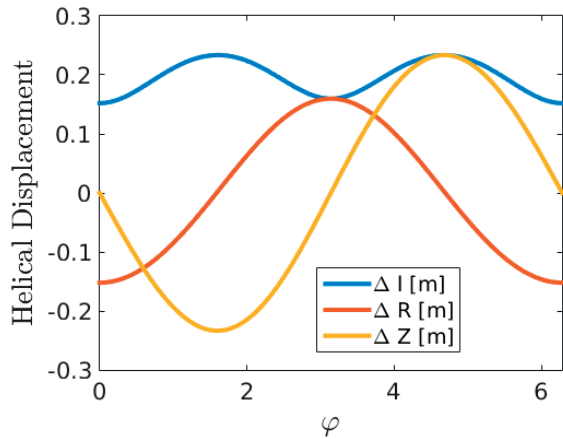


Figure 3.56 – The radial ( $\Delta R$ ), vertical ( $\Delta Z$ ) and total ( $\sqrt{\Delta R^2 + \Delta Z^2}$ ) displacement of the helical core from  $(R_{00}, Z_{00})$ .

Varying the toroidal location of the RF-antenna, the influence of the displaced magnetic axis and 3D magnetic equilibrium on the penetration and propagation of the RF-wave can be calculated using the LEMan code.

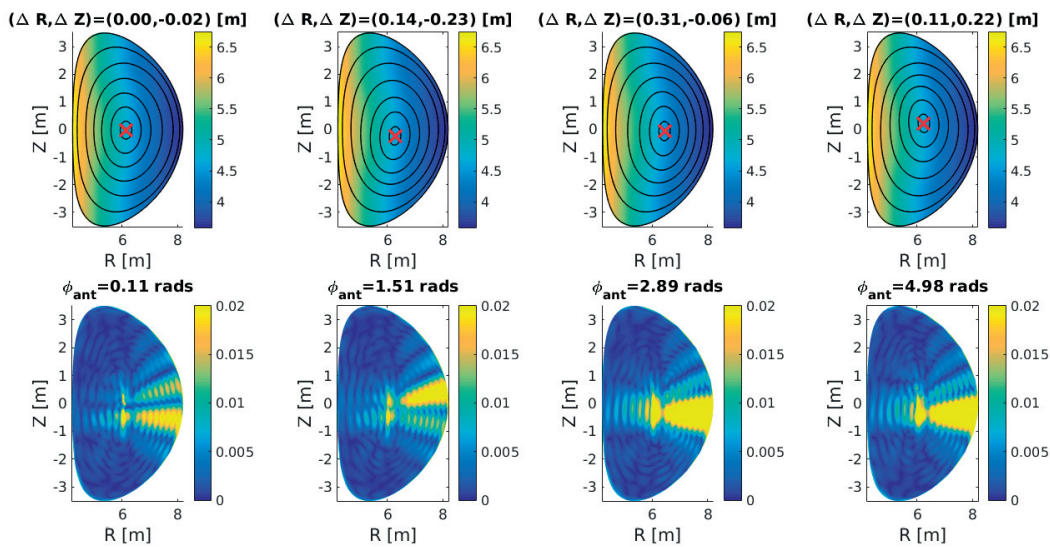


Figure 3.57 – Toroidal plane slices of  $|E_+|$  (in arbitrary units) for different toroidal positions in the ITER tokamak in the presence of an internal helical kink mode, varying the toroidal antenna location.

The wave propagation is calculated as if the helical mode was a locked mode with respect to the vessel wall, with the RF-antenna located at varying toroidal positions with respect to

the mode. The separation of time-scales implies that this calculation is approximately the same as when the toroidal rotation is included. Nonetheless, experiments on the ASDEX-Upgrade tokamak have generated non-linear saturated locked helical core modes using the Resonant Magnetic Perturbation (RMP) coils (*private communication with J.P. Graves, 2018*). This scenario would correspond exactly to that of the simulations made here.

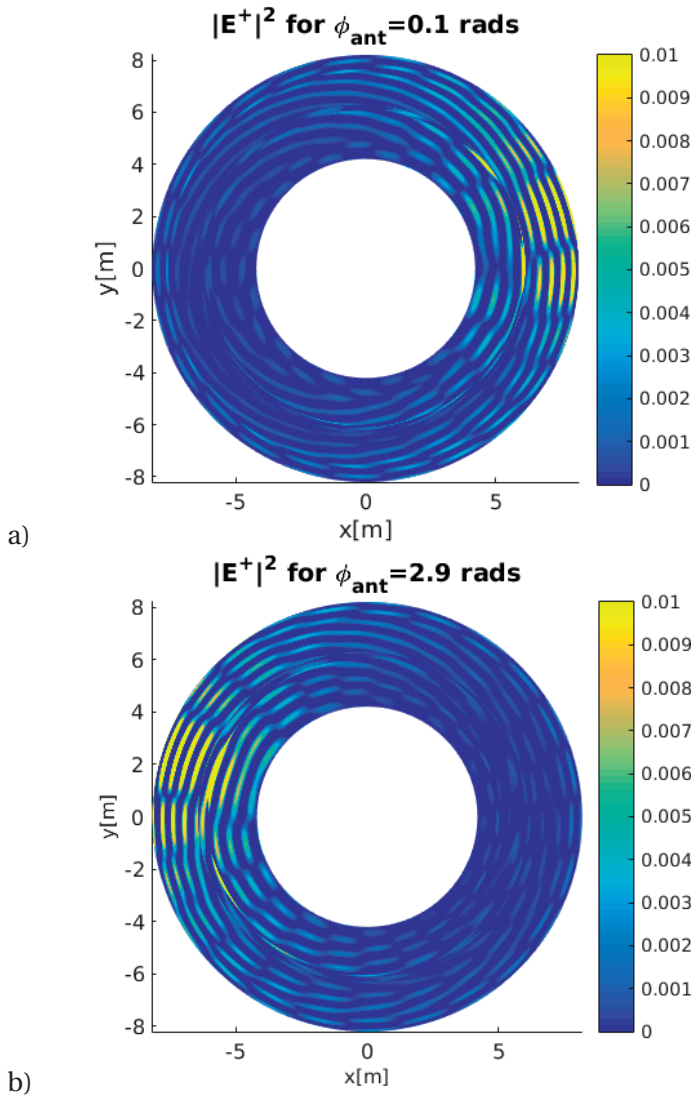


Figure 3.58 –  $|E_+|$  (in arbitrary units) in the  $Z = 0$  plane in the ITER tokamak in the presence of an internal helical kink mode, varying the toroidal antenna location: a) 0.11 rads and b) 2.89 rads.

One of the common RF-heating schemes to be used in the early phases of ITER will be minority heating D(H) or He4(H), with concentrations between 1 – 3%.

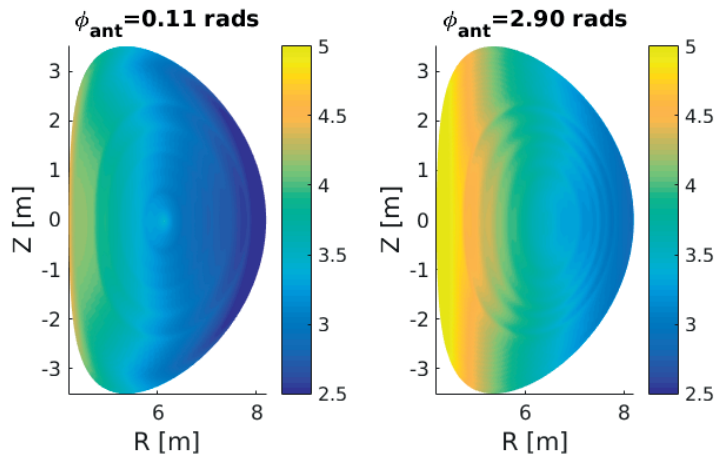


Figure 3.59 – Toroidal plane slices of  $k_{\parallel} [m^{-1}]$  for different toroidal positions in the ITER tokamak in the presence of an internal helical kink mode for  $\phi_{ant} = 0.11$  rads (left) and 2.90 rads (right). The toroidal location of the contour plots is at the toroidal angle of the RF-antenna.

The work presented here simulates  $X[H] = 2\%$ . The calculation also includes the influence of the second harmonic deuterium absorption. The tilting of the magnetic axis by the helical core has obvious effects on the wave-propagation from the antenna. Figure 3.57 shows the differences in the wave-propagation when the RF-antenna is located at different locations with respect to the helical deformation. The direction of propagation of the wave from the antenna penetrates into the plasma at different angles depending on the relative position of the shifted magnetic axis. The magnitude of the electric field is also displaced and modified by the angle of propagation. In comparing two of these antenna positions: 0.11 and 2.89 radians, from a slice in the poloidal plane along the  $Z = 0$  plane, the wave propagation can be seen to penetrate further into the HFS of the device at  $\phi_{ant} = 2.89$  rads, figure 3.58.

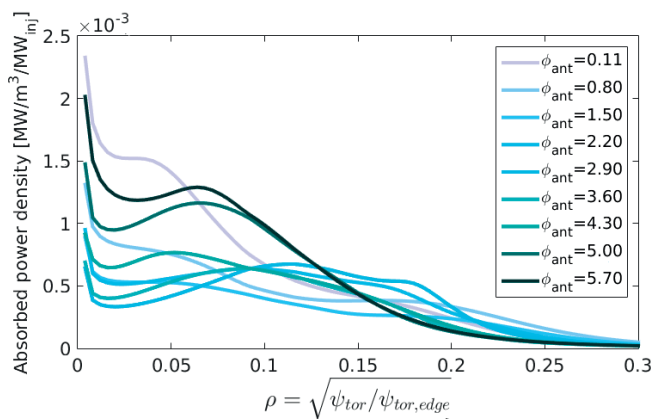


Figure 3.60 – Total RF-power absorption density for an array of different antenna positions.



The wave is also toroidally more localised and propagates with a larger parallel velocity for  $\phi_{ant} = 2.90$  rads, shown by plotting  $k_{\parallel}$  in front of the antenna cross section: figure 3.59. The wave-propagation directly influences the power deposition and absorption by the background plasma. Figure 3.60 reveals that the on-axis peaking of this power deposition can be shifted off-axis by up to half a metre for different  $\phi_{ant}$  values. More importantly, the peak values of the power absorption are 3.5 times larger at  $\phi_{ant} = 0.11$  rads than at 2.90 rads. This directly impacts the efficiency of the RF-wave. Future work will involve running the VENUS-LEVIS code to simulate the fast ion heating and confinement in the helical core equilibrium.

### 3.7 Summary

The presence of ion cyclotron range of frequency waves in 2D and 3D magnetised plasmas has been presented in this chapter. Such waves are generated from driving currents in the RF-antenna, producing an electric field that propagates into the plasma. Resonance between the wave and the particle occurs near the resonant surface, which is normally close to where the particle cyclotron frequency matches the frequency of the RF-wave driven by the antenna. Reflection and absorption of the wave is dictated by the dielectric tensor, which has been updated in the LEMan code to include finite Larmor radius effects and improved calculation of the perpendicular wave-vector using the full hot dispersion relation. Code validation involved comparison with a reduced, second order FLR dielectric tensor. Additional validation was performed through benchmarking with the codes TORIC, PION, FEMIC, SELFO and TOMCAT[30, 32, 31, 27, 34]. The results showed good agreement. Inclusion of FLR effects into the dielectric tensor allows the investigation of harmonic heating and improved the RF-power absorption calculations that are presented for JET and W7-X applications in this chapter.

Selecting JET experimental shot number 92398, the SCENIC code was used over a broad parameter scan to investigate some important influences on ICRF performance and properties. Choice of the charge-to-mass ratio of the resonant species strongly influences ICRF. The presence of the majority background deuterium in hydrogen minority experiments reduces the RF-power absorbed by the minority species due to harmonic heating. For low hydrogen concentrations the majority of the power is directly absorbed by the deuterium. The fast hydrogen ions transfer most of the RF-power to the electrons, so when hydrogen absorption is dominant, electron heating dominates over heating transferred to other background species. For low concentration, helium-3 minority heating results in larger ion heating than hydrogen minority heating. However, higher concentrations have been shown to enter into the mode conversion regime where electron heating re-dominates the RF-power absorption [48]. The most important differences observed are due to the different collisionality for helium-3 and hydrogen, leading to lower energetic particle populations for helium-3 heating. This results in larger core collisional power transferred to the background plasma ions. Simulations varying the antenna frequency relative to the resonant ion cyclotron frequency in the core have been shown. Changes to the location of the resonant layer leads to modified RF-power deposition. Electron absorption is increased proportionally with the distance the wave must

### Chapter 3. Numerical Advancements and Application for ICRF Optimisation

---

travel through the plasma to the minority species resonant layer due to enhanced ELD and TTMP effects. Second harmonic deuterium RF-absorption is increased when the fundamental minority species resonant surface is located in regions of higher temperature. Thus, second harmonic deuterium RF-power absorption peaks for on-axis heating. 2D fast ion pressure profiles revealed strong localisation of the pressure profiles in the vicinity of the resonant surface, with the total fast ion pressure highest for on-axis heating. Altering the resonant surface location also strongly influences the number of co and counter passing and trapped particle populations. HFS heating resulted in an increase in passing populations, which may result in driving larger ICCD depending on the relative concentration and energies of co and counter passing particles. Simulating a scan of plasma currents indicates strong modification of the RF-wave propagation through the parallel wave-vector, increasing RF-power absorption in the core for higher  $I_p$ . Energetic particle core confinement is also improved for increasing plasma current. The reduced FOW of the energetic ion and lower collisionality allows energetic ions to remain in resonance, resulting in an increase in the fast ion density and pressure. The RF-antenna power was varied, such that the energetic ion populations and fast ion anisotropy increase proportionally to the RF-power. This reduces the collisional power transferred to the background ions depending on the total RF-power. Including the presence of impurities in the simulations is shown to have a significant influence on the collisionality. The presence of small amounts of tungsten and nickel reduce significantly fast ion populations and increases the collisional power lost from the resonant ion population. Calculation of the Fokker-Planck evolution of parasitic harmonic heating of deuterium in the baseline simulation was also performed, illustrating highly isotropic distributions with minimal energetic particle generation. The collisional power transfer to the background ions was observed to be larger than for the minority heating scheme and localised in the plasma core. Possible issues with the numerical marker resolution of the large ( $X[D]>85\%$ ) deuterium concentrations should be explored to investigate the energetic particle generation at lower densities (below  $10^{16}$ ).

This chapter also investigated ICRF in 3D magnetic geometries. Simulations of the minority species scheme in the W7-X stellarator were presented for varying toroidal magnetic mirror equilibria. The toroidal variation of the magnetic field strength at the magnetic axis was observed to have a significant impact on the heating performance. The low mirror configuration has the resonant surface located approximately on-axis for all toroidal angles, allowing on-axis wave-particle energy exchange along the magnetic axis everywhere. The absence of this resonant surface in the high mirror near to the triangular toroidal section leads to significantly worse heating performance. The high collisionality of the plasma profiles expected to be used in future W7-X experiments leads to low anisotropy profiles that are almost unity in the core. The high collisionality prevents the generation of highly energetic particles but results in large collisional power profiles to the ions, which are peaked on axis for the standard and low mirror configurations only. The losses have been identified to be dominated by strongly trapped particles, which is a well known disadvantage to stellarator devices. ICRF wave propagation and absorption has also been studied in a 3D ITER tokamak equilibrium, where the presence of a helical internal kink-like mode was explored. The presence of the mode significantly

varies the wave propagation and power absorption on each plasma species, depending on the shifted magnetic axis location with respect to the RF-antenna. The maximum core RF-power deposition was roughly 4 times the minimum value, flattening the radial peaking profile for certain helical core amplitudes.



## 4 Numerical Advancements and Applications for NBI

In this chapter the ionisation and particle evolution physics of NBI is presented using the VENUS-NBI module [14]. The VENUS-NBI module has been updated to calculate NBI deposition in 3D magnetic geometry, include an accurate W7-X beam injection geometry and use equal marker weights for numerical resolution. The code is applied to evaluate the performance of NBI in the three different W7-X toroidal magnetic mirror stellarator configurations described in 2.1.3. A new method is also introduced to distinctly separate the slowing down beam distribution from the diluted thermal content. While not so important for the NBI heating and fast ion confinement studies in this chapter, this will be important for the advanced heating scheme physics of chapter 5, when synergetic RF-NBI effects become important.

### 4.1 Simulating NBI heating

The VENUS-NBI module was originally developed in [14] and improved in [55]. This code is used to simulate the neutral beam deposition. Equation 2.3.1 is solved based upon the equilibrium LCFS and plasma profiles. Work using a combination of this module and the VENUS-LEVIS code has already extensively studied for 2D and 3D tokamak scenarios, the latter simulating NBI confinement and performance in the presence of a helical internal kink-like mode[55]. Initial investigations into the beam ion confinement were also made in [56]. The limitations of this work were the poor representation of the W7-X NBI geometry, the inability of the VENUS-NBI module to account for 3D LCFS equilibria and the use of unequal-weighted numerical markers. The VENUS-NBI module has been modified to account for all three of these factors.

#### 4.1.1 Equal Marker Weighting

Applying equal weights to the markers in the VENUS-LEVIS code was originally implemented such that the beam line  $l$  was discretised to have  $N$  markers equally distanced between the entry and exit point of the beam line into the plasma. The numerical resolution of which is therefore reduced, as towards the end of the beam line there are not very many particles penetrating, resulting in markers with extremely small weightings. Markers that were located

near the peak of the beam penetration would have a weighting three orders of magnitude larger than the smallest weighted markers. When calculating the collisional power and densities the presence of such large variations of markers, required many numerical markers for good numerical resolution. This has now been accounted for such that the markers are unequally spaced along the beam line but have equal numerical weighting.

### 4.1.2 Voxelisation Method

In order to identify whether an NBI particle exists within the 3D LCFS of the plasma, the code has been updated to use a process known as voxelisation. Previously, the code could only handle 2D LCFS shapes, assuming a toroidally symmetric form to calculate the beam penetration. The parity count method [57] is applied. The methodology of which is highlighted in the following steps:

1. Discretise the LCFS into triangular 'mesh' elements.
2. Build a 3D cubic grid in cartesian coordinates that entirely encompasses the LCFS triangular surface mesh.
3. Choose a direction to ray trace along, e.g. x direction.
4. Reduce computational cost by finding tri-elements close to cubic-nodes along  $x_i$ : find elements that have maximum y and z values that are above  $y_i$  and  $z_i$  and minimum values of y and z directions are below  $y_i$  and  $z_i$ .
5. Use the plane equations for each tri-element (using the normal vector) to find if and where the x-direction line  $x_i$  intersects the tri-element surface.
6. Moving along  $x_i$  direction, for each value of x along this line, count the number of times the ray has crossed a tri-element.
7. Nodes located where the ray has crossed an odd number of times are located within the LCFS and even number of times outside the LCFS.
8. Repeat along the x direction but over all y and z gridpoints
9. The grid of points in x, y and z can be used to form a mesh of cubic elements.
10. Beam particles are grouped inside voxel elements. If the cube is not located inside the plasma then the particle weighting is set to zero so that VENUS-LEVIS does not simulate it.

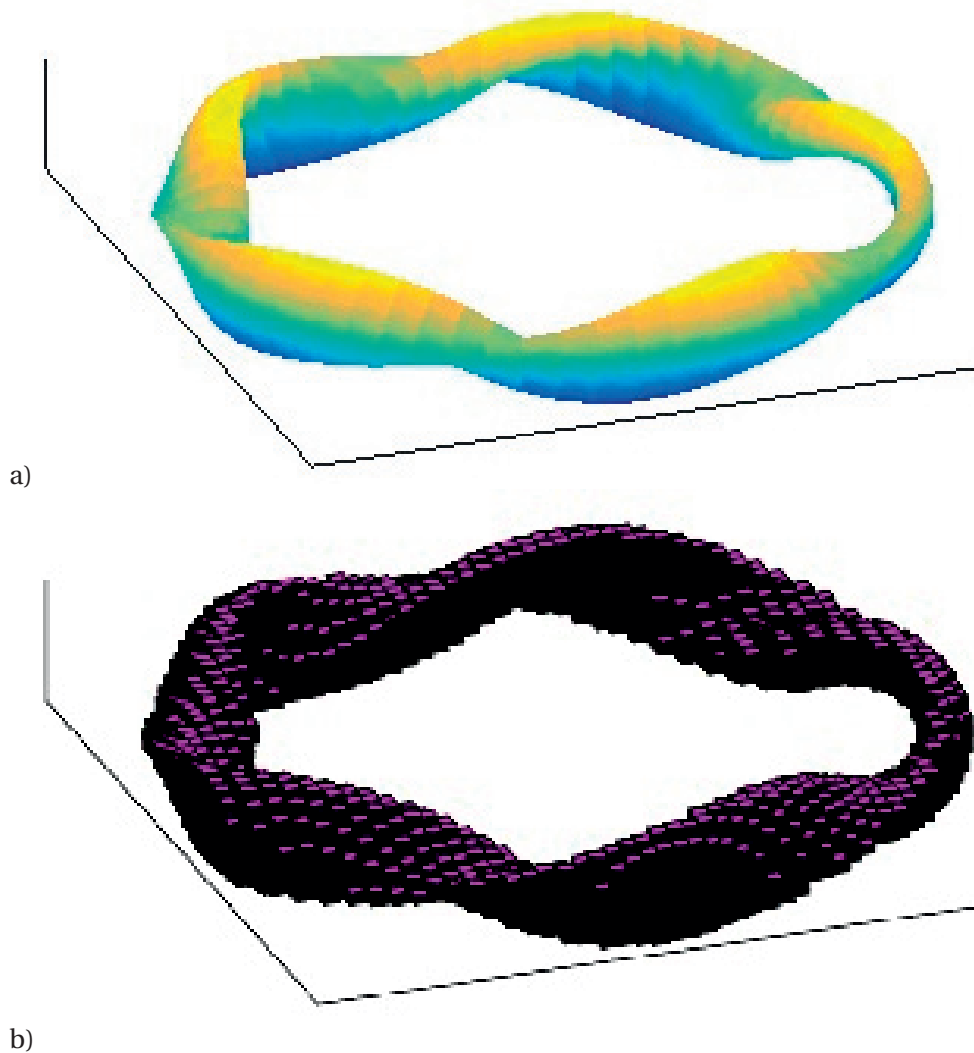


Figure 4.1 – The voxelisation process: left) the LCFS of the W7-X high mirror equilibrium, right) voxelisation of the surface on a coarse grid for visualisation purposes.

Using the parity count method reduces the computational time required, as all voxels along the ray can be identified in parallel. This also reduces the problem to searching with only  $N \times N$  rays. An example of the voxelised mesh is shown in figure 4.1.

#### 4.1.3 Benchmarking

NBI code benchmarking was performed with both the NBI ionisation code and the Fokker Planck code for slowing down NBI simulations using VENUS-LEVIS in the W7-X stellarator. Figure 4.2 shows a comparison of the NBI beam ionisation as a function of the major radius for all four NBI PINI's. The results indicate that compared to other codes, SCENIC has lower ionisation on the outboard side  $R > 6\text{m}$ . If a particle penetrates through the LCFS on the

inboard side, the code marks that particle as out of the plasma and gives the marker zero weighting. This is reflected in the steep drop in the number of bins beyond  $R > 6\text{m}$ . As figure 4.2 is a histogram, the normalisation of the number of bins is higher for VENUS-LEVIS because there are less markers at  $R > 6\text{m}$ . The beam ionisation of SCENIC could also be influenced by the numerical implementation of the PINI geometry, which is more simplistic than other codes. In addition to this, the equations used to calculate the cross sections could be replaced by a data-lookup table of the experimentally evaluated cross-sections for the different beam species and energies.

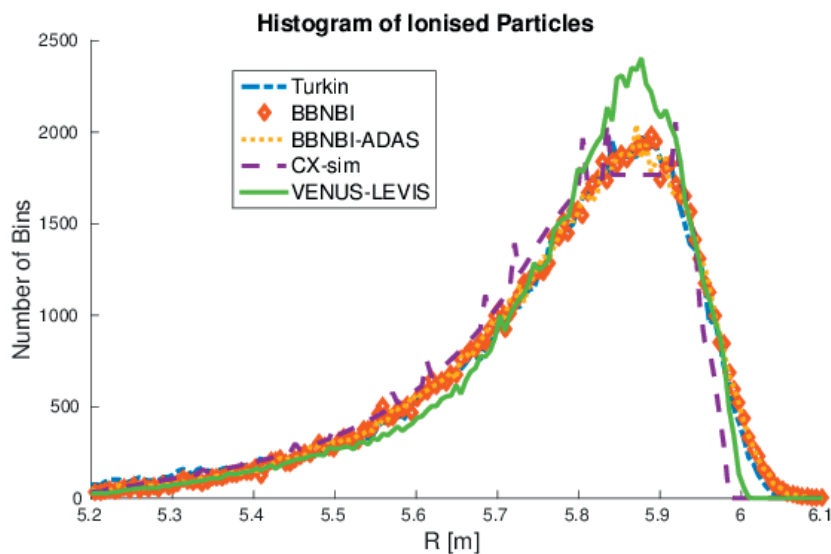


Figure 4.2 – NBI beam ionisation (arbitrary units) as a function of the major radius, comparing the results predicted by different codes. Simulations made for the high-mirror W7-X magnetic configuration.

Using the NBI ionisation marker population generated by the VENUS-NBI code, by injecting these particles at the same time and recording the number of lost particles in time, one can compare the Fokker Planck codes. The comparison is made in order to compare the implementation of the numerical discretisation of the magnetic geometry and the Monte-Carlo collision operators of the codes. These simulations were also used to compare the influence of the radial electric field on the particle confinement. VENUS-LEVIS is the only code that uses the Fourier-spline technique in the toroidal and poloidal directions, the other two codes use cubic-spline methods which are less precise when discretising the magnetic field onto a 3D grid before splining. Thus use of the Fourier-spline technique in VENUS-LEVIS ensures increased precision in the conservation of the magnetic moment  $\mu$ . This leads to a larger number of lost particles than the cubic-spline based codes ASCOT and ANTS, shown in figure 4.3. Using a more precise magnetic equilibrium splining technique and conservation of magnetic moment ensures that the particle motion in the intricate 3D geometry is more accurately evaluated. Deeply trapped particles perform super-banana orbits along magnetic



wells and are lost from the system, a process that requires precise calculation of the background magnetic geometry. The increase in particle losses for VENUS-LEVIS could be explained by the increase in precision of the particle motion. Upon the inclusion of the radial electric field, the particles that would have been lost in magnetic wells in the VENUS-LEVIS calculations will then have improved confinement and thus significantly reduce the beam losses, also observed. Figure 4.3 implies that VENUS-LEVIS simulations in W7-X without the presence of the radial electric field could be significantly less reliable than simulations that include this factor.

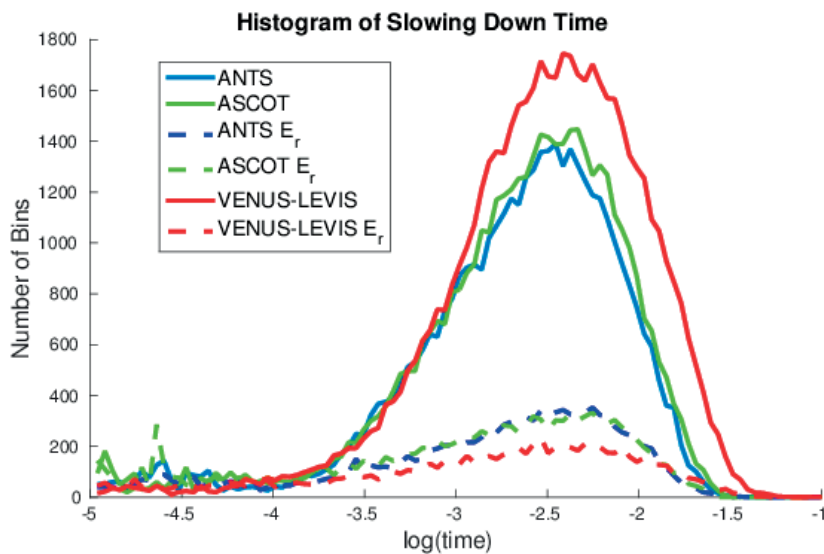


Figure 4.3 – Lost NBI particles in time (arbitrary units), comparing the codes ANTS, VENUS-LEVIS and ASCOT, with and without the presence of the radial electric field. Simulations made for the high-mirror W7-X magnetic configuration.

## 4.2 W7-X

W7-X has two NBI modules installed, N120 and N121, each with four beam injectors. N120 and N121 are located at  $(R, Z, \phi) = (6.750, -0.305, 0.993)$  and  $(R, Z, \phi) = (6.750, 0.305, 1.520)$  respectively. A complete description of the geometry and the system parameters are given in [58]. One of the optimisation criteria of the W7-X stellarator design is to minimise the plasma current. Therefore, the two modules inject in toroidally opposing directions. Figure 4.4 shows the injectors that will be applied within the first two experimental campaigns OP1 and 2 on W7-X, highlighted with red circles. The injectors on each module are directed at different poloidal angles such that the beam deposition is more normal for the injectors 3 and 7, with a power of 1.64MW each, and is more tangential for the injectors 4 and 8, with a power of 1.78MW each. The power fraction that is given to each ion molecular species is shown in table 2.3.

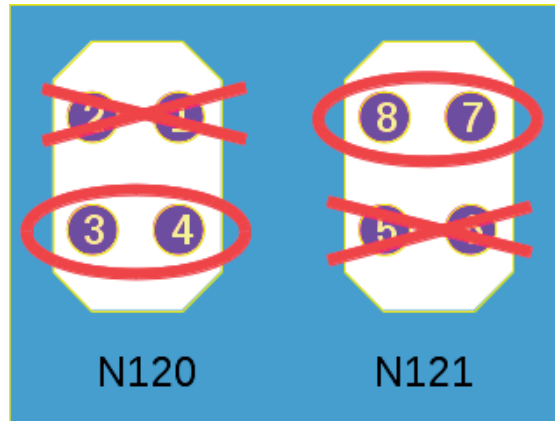


Figure 4.4 – Illustrations of the two W7-X NBI modules, the injectors that have been used in this work have been circled in red, corresponding to the injectors that will be applied during upcoming experimental campaigns.

#### 4.2.1 NBI Ionisation

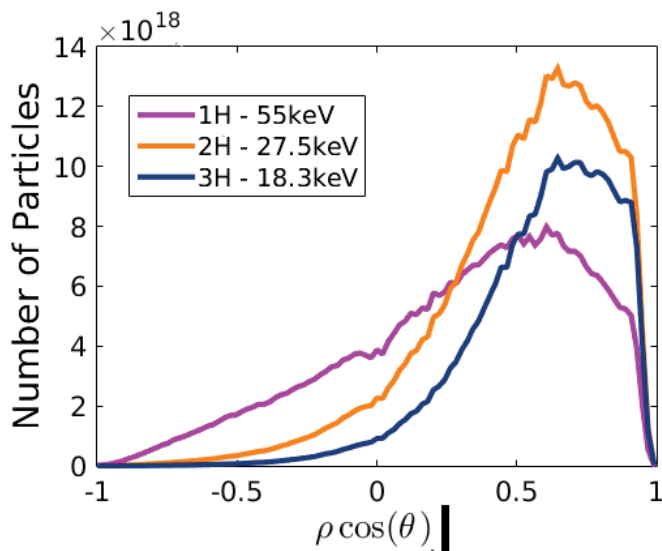


Figure 4.5 – NBI beam ionisation (arbitrary units) as a function of the major radius for each of the NBI beam hydrogen molecular ion fractions in the standard mirror W7-X configuration.

For the flat-top background density profiles illustrated in 3.46, penetration into the plasma results in off-axis NBI ionisation deposition, shown in figure 4.5. The pseudo-major radius parameter  $\rho \cos(\theta)$  visualises the number of particles across the major radial direction but without the influence of the toroidal magnetic flux surface distortion. The results show that the first ion molecule penetrates furthest into the plasma due to the higher beam particle energy 55keV. The use of NBI in the W7-X stellarator is difficult because of the magnetic flux

surface distortion as a function of the toroidal angle. In addition to the large major radius and small minor radius of the machine, this makes it difficult to find beam line trajectories that result in good core NBI penetration at high densities. The low NBI energy injection value 55keV chosen for W7-X allows NBI to be used at lower densities without large shine through losses.

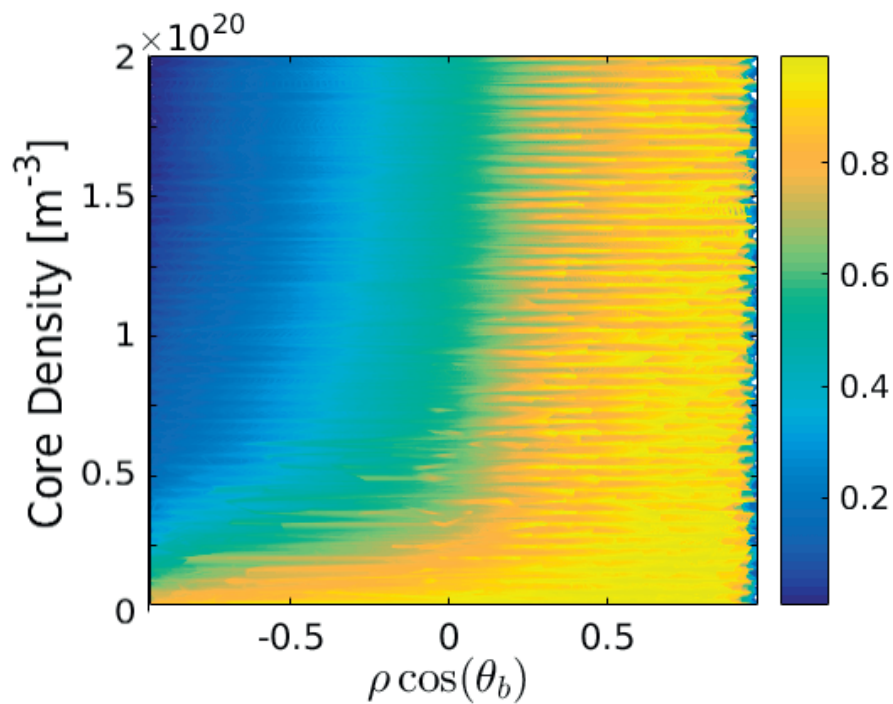


Figure 4.6 – Contour plot of the number of particles ionised along the major radius-like direction for varying electron core densities. The colourbar axis is normalised by the maximum per  $n_{e,0}$  value.

For a given injector geometry, NBI penetration depth is strongly dependent upon the density profiles and not so much upon the temperature. By modifying the core density value, figure 4.6 shows the normalised (with respect to the maximum value) peak in NBI particle deposition. The results indicate that for strong on-axis NBI deposition the plasma background densities would have to be lower than  $10^{19}$ , which would result in a large shine-through. However, due to the volume effect when calculating the particle densities, core NBI deposition still occurs.

### 4.2.2 NBI Losses

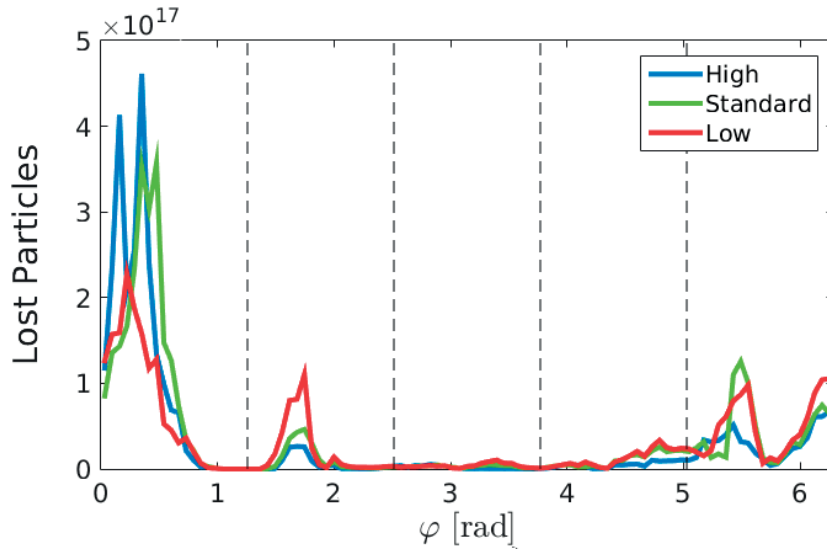


Figure 4.7 – Comparison of the first and multiple orbit NBI losses as a function of the toroidal angle for the three toroidal magnetic mirror configurations.

Taking the marker distribution generated by the VENUS-NBI module, NBI confinement can be studied and compared across the three magnetic equilibria foreseen to be implemented in W7-X experiments. Figure 4.7 shows the first and multiple orbit losses  $t < 0.5 \times 10^{-3}$ s. Losses over such a short period of time are highly influenced by the initialisation of the beam distribution, as on time-scales smaller than collisional time-scales, energetic beam ions perform only one or a few orbits. The toroidal locations of the losses are very similar across the three equilibria. The low mirror configuration has lower minimum and maximum magnetic field strength values compared to the high and standard mirror as particles are less likely to toroidally bounce in the low mirror, resulting in slightly fewer first and multiple orbit losses. Above time-scales of  $t > 5 \times 10^{-3}$ , the particles diffuse due to the presence of collisions with the background plasma. These diffusive losses are independent of the toroidal field period. Figures 4.8 a) and b) show the beam particle losses with and without Coulomb collisions respectively, which gives an insight into the beam particle losses attributed to the magnetic equilibrium only or to the influence of Coulomb scattering of the ion. The Coulomb collisions result in a toroidal spreading of the losses, by pushing particles into magnetic wells of negative curvature where deeply trapped beam ions perform super-banana orbits until exiting the LCFS. The toroidal location of the beam ion losses without the presence of Coulomb collisions is similar across high and standard mirror, whereas with the inclusion of Coulomb collisions the difference in the peak loss values across the magnetic equilibria increase significantly with respect to the toroidal angle.

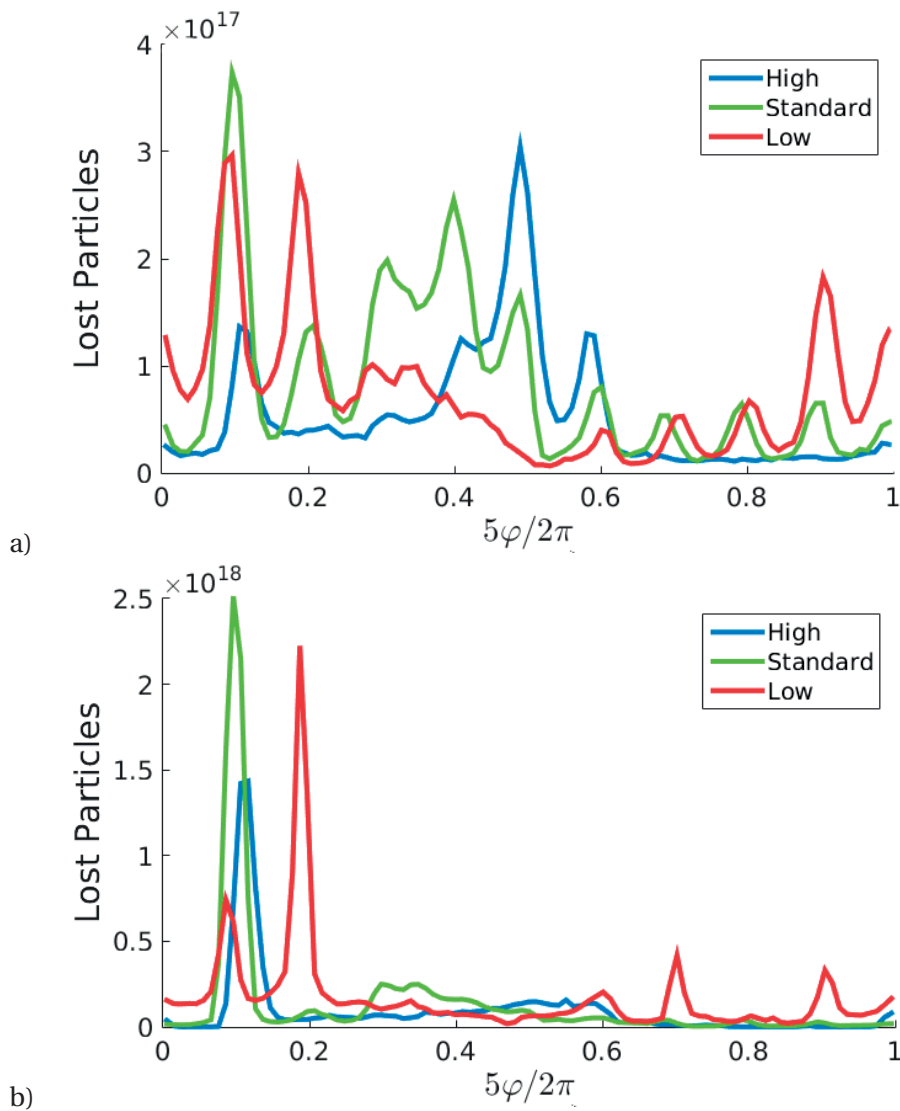


Figure 4.8 – Diffusive NBI losses summed over all toroidal field periods, comparing the different toroidal magnetic mirror configurations a) including the presence of Coulomb collisions, b) without Coulomb collisions.

The high and standard configurations result in large toroidal bounce motion which prevents ion toroidal precession, produces deeply trapped particles and so particles are lost near the toroidal bounce point at  $5\varphi/2\pi \sim 0.12$ . With the initial position of a marker known from the NBI ionisation code, time scales for losses of markers at any initial flux surface can be evaluated by comparing the time taken to reach the LCFS.

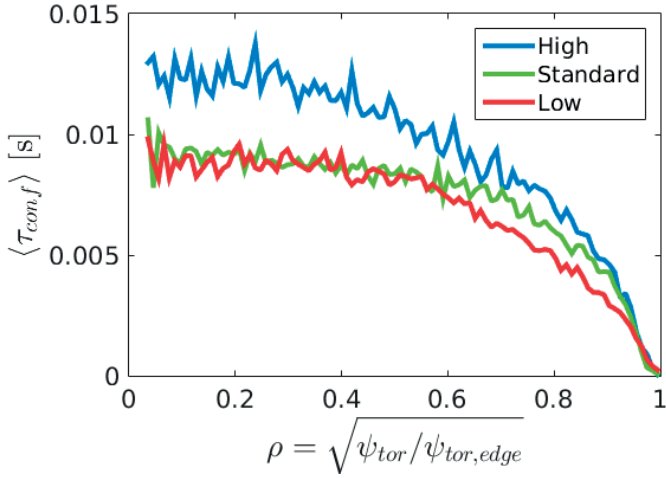


Figure 4.9 – Confinement time of the fast beam particles as a function of the initial radial position of the beam particle ionisation.

Figure 4.9 shows the confinement time as a radial function, showing the significantly improved performance of the high mirror configuration for confining the energetic beam ions.

Mirror	$P_{cols}/P_{in}$ %	$P_{lost}/P_{in}$ %	Lost Particles %
High	68.5	11.8	16.2
Standard	61.2	20.2	24.7
Low	61.0	20.6	25.3

Table 4.1 – The lost power and particle percentages for NBI heating in W7X for the different magnetic mirror configurations in the presence of Coulomb collisions, including the radial ambipolar electric field  $E_r$ .

### 4.2.3 Slowing Down Distribution

NBI is not just a heating source but also a source of particles. Once an NBI particle thermalises, it becomes part of the background plasma. The injected beam particles that are located inside the plasma can therefore be separated to define two distributions: an energetic part which slows down on the background plasma and a thermal concentration which remains in the plasma after thermalisation. The thermalised part of the beam is therefore a plasma dilution concentration. The transport physics related to these particles is complex, including neoclassical flows, turbulence, the presence of MHD modes, etc. These physical processes are not calculated by the VENUS-LEVIS code, but some effects of which can be included ad hoc. The background plasma profiles that are used by the SCENIC package are assumed to be the density and temperature profiles that include (as a flux-surface average) the influence of anomalous and neoclassical transport effects, that can either be taken from experimental conditions or from transport codes such as TRANSP[59]. The background plasma profiles are

assumed to be steady-state. Simulations of NBI in this thesis assume that the NBI injection has been included in the generation of the plasma profiles. This assumption allows VENUS-NBI slowing down simulations to be made without recalculating the resulting influence of NBI on the modification of the background plasma profile form. For steady-state plasmas with NBI injection, after multiple slowing down time scales the thermalised beam concentration can therefore be assumed to have the same density (with differing concentrations) and temperature profiles as the background ions. However, if the background majority ion species is a different species to the injected beam, modification of the concentration of the background ion density is made (ensuring quasi-neutrality) to accommodate for the NBI beam dilution factor. The dilution factor should be given by experimental predictions of the total densities of the beam species (which would therefore include both the thermal and slowing down components) if available. A measurement of the ion concentrations are usually inferred by analysis of multiple experimental diagnostics such as Thomson scattering (for the electron density), photodiodes (to observe the amplitude of the emitted visible light from the ion species), neutron spectroscopy (for the energetic particle distributions) and the neutral particle analyser (NPA).

There are two numerical approaches applied in this thesis to evaluate the NBI population using the VENUS-LEVIS code. There are two populations defined: the slowing down beam distribution and the thermalised dilution distribution. The slowing down distribution is defined as the particles that have been injected into the plasma but have not collided with the background plasma enough to reach thermal temperature (thermal defined as  $T_e(s)$  with  $s$  the flux surface position of the beam ion). The numerical approach applied by VENUS-LEVIS to determine only the slowing down beam distribution in velocity and physical space is similar to the ASCOT code[60]. The pressure and density profiles of this distribution will be discontinuous with the background plasma. The discontinuity can be observed by plotting the density of slowing down particles close to thermal energies, which will not match the form of the Maxwellian background plasma density. The continuity of the NBI distribution with the background density profiles is important for advanced RF-NBI heating scenarios presented in chapter 5. One of the numerical approaches made to calculate NBI in VENUS-LEVIS is through the separation of the slowing down distribution, referred to as the slowing down calculation. The second method involves the calculation of the NBI distribution to include thermalised particles such that the total beam density profile approximately matches the form (but not amplitude of) the background ion density profile.

### **Time-Independent NBI**

One method that can be used to evaluate the source term of beam particles that NBI provides to a plasma is through calculating time-independent simulations. Experimentally, NBI beam ions are constantly injected in time. The time-independent VENUS-LEVIS NBI method injects all NBI beam ion numerical markers at the start of the simulation. The distribution function is evaluated as the markers collisionally slow down on the background. When a

## Chapter 4. Numerical Advancements and Applications for NBI

---

marker approaches thermalisation or reaches the LCFS it is removed from the simulation. Accurate description of the slowing down distribution requires large numbers of diagnostics (also referred to as marker binning/snapshots in time). By the end of the simulation all the numerical markers are either thermalised or have left the LCFS. Increasing the simulation time therefore produces the same slowing down distribution provided that the number of diagnostics is sufficient to statistically sample the slowing down process. The time-dependence is then reintroduced by a normalisation of the marker weight with respect to the time the NBI experiment would last. For example, injection of 4MW of an NBI hydrogen beam with the fractions 0.52,0.3 and 0.18 of H1,H2 and H3 ion molecules over 0.1 seconds of an experiment would inject  $\sim 3.7 \times 10^{19}$  ions into the system. Applying the NBI for 0.2 seconds would inject double this concentration, etc. Simulating with one million numerical markers results in a numerical weight of  $3.7 \times 10^{13}$  for each marker for 0.1 second NBI predictions. The method is summarised as follows:

- Evaluate the NBI beam ionisation deposition.
- Inject all markers at t=0 in the VENUS-LEVIS simulation.
- Take ‘snapshots’ of the particles continuously over time and bin the markers in order to determine the evolution of the plasma distributions in velocity and physical space over time.
- When a particle slows down such that the energy matches the local thermal electron temperature or reaches the LCFS it is removed from the simulation.
- Run the simulation until no more energetic numerical markers exist within the LCFS.
- Normalise the marker weights according to the amount of NBI power injected over the time scale of the NBI.



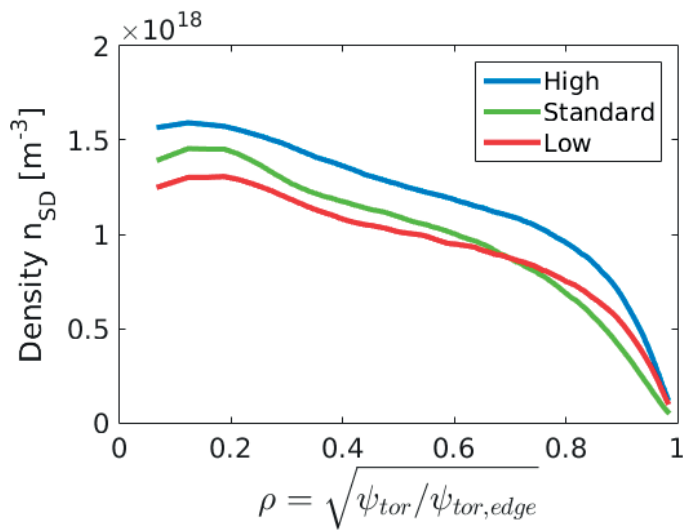


Figure 4.10 – Slowing down beam ion density as a radial function comparing the different toroidal magnetic mirror configurations for  $t_{fin} = 0.2s$ .

Simulations using this method result in the slowing down radial density profile shown in figure 4.10. This agrees with the confinement time figure (4.9) indicating the improved energetic beam ion confinement in the high mirror equilibrium. This is corroborated in figure 4.11 for the energetic ion distribution with respect to energy, showing more energetic ions near the injection energies ([55,27.5,18.3]keV) for the high mirror case.

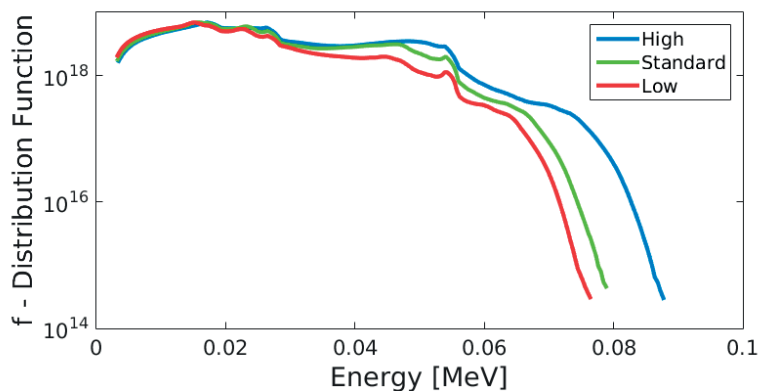


Figure 4.11 – Particle distribution as a function of energy of the resulting slowing down NBI population for the different toroidal magnetic mirror configurations for  $t_{fin} = 0.2s$ , not including dilution effects.

The pressure profile of the slowing down beam ions, shown in figure 4.12, reflects the lower collisionality of the particles in the core region, resulting in peaked pressure distributions.

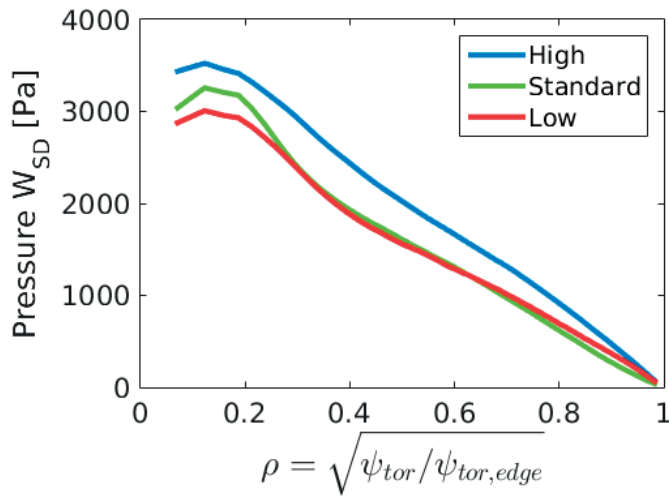


Figure 4.12 – Particle pressure of the slowing down beam ions as a radial function comparing the different toroidal magnetic mirror configurations for  $t_{fin} = 0.2s$ .

### Dilution Method

One of the issues with removing the thermalised particles is the discontinuity created in the energetic distribution function, both in phase space as in real space. Previous work [61] used a different method that will become important in section 5.2, which includes the measurable degree of dilution due to the presence of NBI. This method requires constant injection of particles throughout the simulation:

- Evaluate the NBI beam ionisation deposition.
- Calculate the longest collisional time-scale (Background collisions with 1st ionic molecule - of highest energy - in the core).
- Normalise the marker weights according to the amount of NBI power injected over this time-scale.
- Inject markers continuously through the VENUS-LEVIS simulation.
- After multiple slowing down times, the simulation will have a mixture of freshly injected beam ions and fully thermalised beam ions.
- If one wishes to distinguish between fast and thermalised ions (e.g. to take moments of the distribution using the anisotropic Bi-Maxwellian for the fast component), the ‘fast’ ion definition is taken as for ICRF simulations: particles with  $E > nT_e$  are considered as fast.

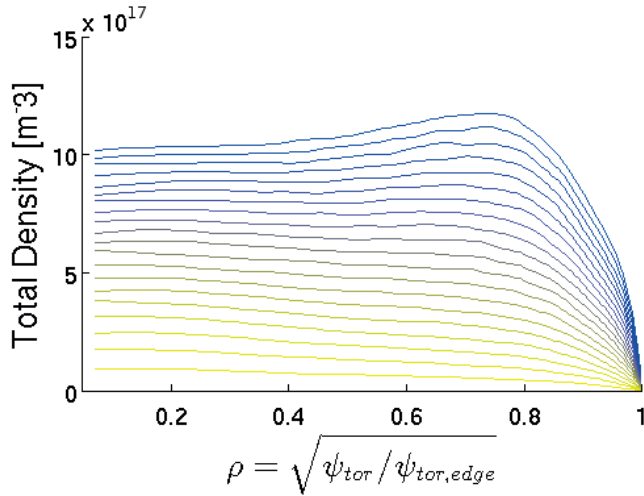


Figure 4.13 – Beam dilution accumulation in the SCENIC code for a simulation of 0.2s in the high mirror equilibrium. This leads to erroneous thermal particle transport. Darker colours represent later time periods of the simulation.

If the thermalised NBI particles are not removed from the simulation, then this method results in continuous accumulation of particles in the simulation. This occurs if thermalised ions do not transport fast enough to balance the injected ions (in a real experiment this balance does take place, but in the simulation we do not have all the realistic transport channels present in the experiment). This constant accumulation is shown in figure 4.13. The simulation time taken for this figure leads to erroneous calculation of the thermalised beam particle transport, resulting in an off-axis peaking of the density. The differences in running simulations of 0.1, 0.2 and 0.3 seconds in the high mirror are shown in figure 4.14 (left).

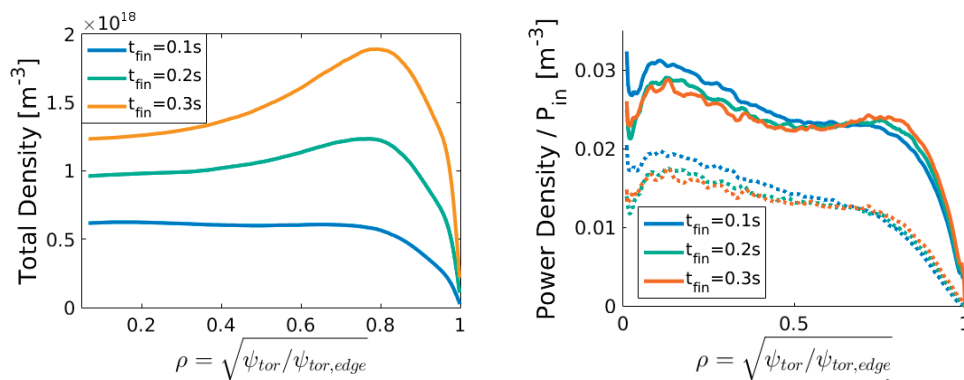


Figure 4.14 – Beam dilution effects in the high mirror equilibrium with respect to simulation time for left) total density and right) collisional power density. Dotted lines correspond to power transferred to the background ions.  $P_{in} = 6.84\text{MW}$ .

The slowing down time of the most energetic beam ions is  $\sim 0.03\text{s}$ . This leads to the conclusion

that in order to use the dilution method, the simulation run time should be limited to be at most  $\sim 0.1$  seconds such that the density profile form matches approximately that of the background plasma profiles. The radial transport influence of the dilution factor also influences the off-axis component of the collisional power transfer, illustrated by figure 4.14 (right).

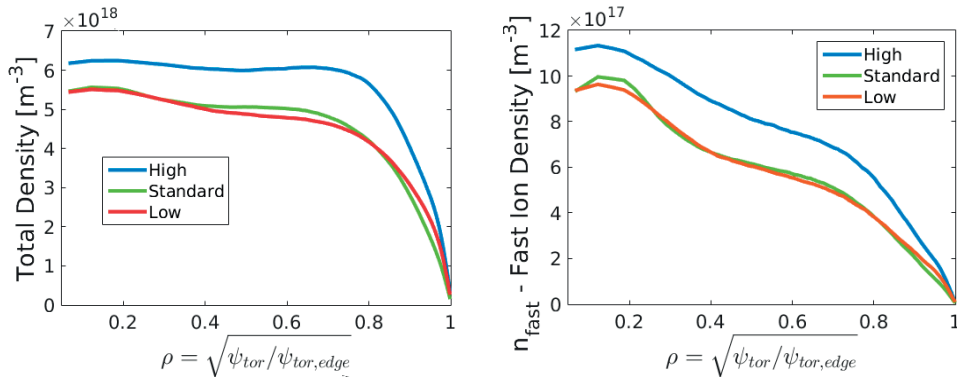


Figure 4.15 – Beam population density for left) total population including thermal and right) fast ( $E > 5T_e$ ) beam density, comparing the different toroidal magnetic mirror configurations.

Simulating the NBI over a simulation time of 0.1s in the high, standard and low mirror corresponds to 3-4 slowing down timescales for the energetic beam ions. Figures 4.15 and 4.16 compare the profiles of the total accumulated and the fast ion  $E > 5T_e$  density and pressure respectively, for each of the magnetic mirror configurations. The total accumulation profiles have similar forms to the background plasma profiles.

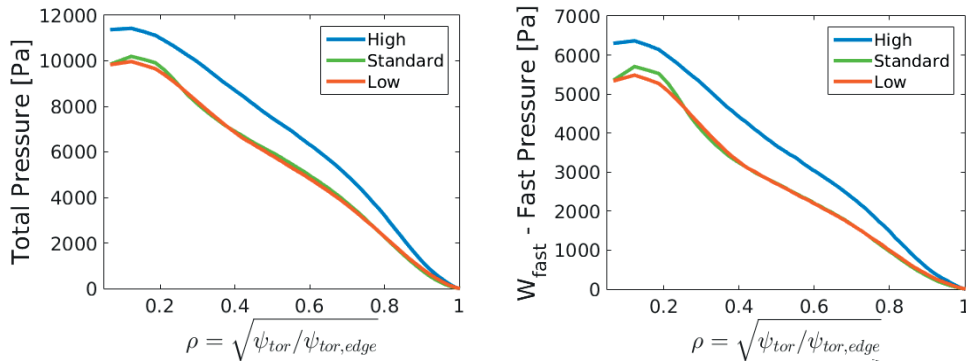


Figure 4.16 – Beam population pressure for left) total population including thermal and right) fast ( $E > 5T_e$ ) beam pressure, comparing the different toroidal magnetic mirror configurations.

Both the density and pressure moments indicate little differences between the low and standard mirror configurations, for the total and the fast ion profiles. A significant difference is

observed for the high mirror confinement of total and energetic beam ions. Despite the fast ( $E > 5T_e$ ) ion density being roughly 6-7 times smaller than the total measured, this energetic ion population carries roughly half the total energy as shown in figure 4.16.

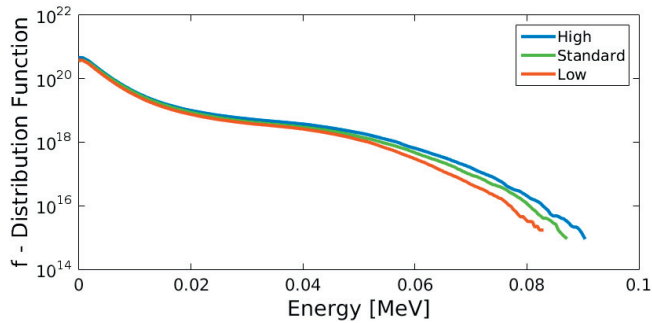


Figure 4.17 – The total energy distribution including NBI beam slowing down and the thermal dilution population, comparing the different toroidal magnetic mirror configurations.

The energetic distribution function, shown in figure 4.17, reflects how the dilution method results in a continuous, smooth energy distribution which can be split into a thermal and fast population and fitted with a Maxwellian and bi-Maxwellian analytical distribution functions respectively. The high mirror equilibrium has improved confinement, in particular for the highly energetic beam ions, with the largest losses for the low mirror configuration.

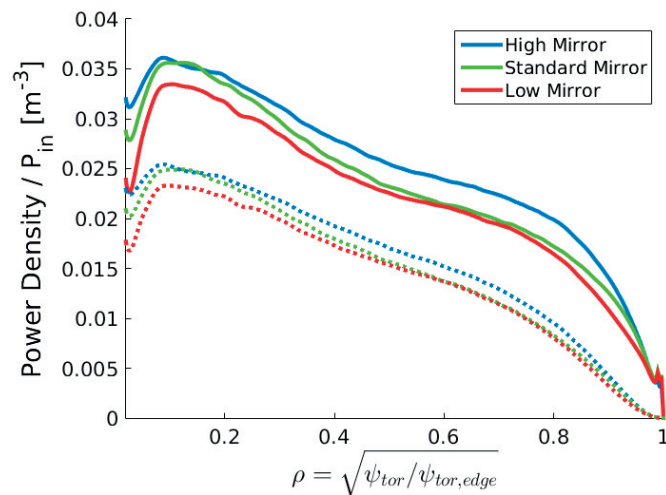


Figure 4.18 – The collisional power transfer density for the fast splitting method, comparing the different toroidal magnetic mirror configurations. Solid line corresponds to the total power transferred to all plasma species, dotted to background ions only.  $P_{in} = 6.84\text{MW}$ .

Collisional power transfer from the beam ions to the background plasma is shown in figure

4.18. The slight increase in the number of thermal and fast particles in the core is observed to increase the collisional power density in the plasma core for the standard mirror over the low mirror. The high mirror shows larger  $P_{col}$ , especially for outer radial flux surfaces.

### 4.3 Summary

This chapter investigates the physics of NBI through numerical simulations. The VENUS-NBI module has been developed throughout this work, such that the current status permits the calculation of NBI beam ionisation into 3D magnetic geometries, including W7-X NBI geometry, and uses equal-weighted numerical markers for increased numerical resolution. Benchmarking was made for both the ionisation and slowing down of NBI ions in the W7-X high mirror equilibrium for a large variety of other codes, showing good comparisons. The updated code package has been applied to the W7-X stellarator, comparing the low, standard and high toroidal magnetic mirror configurations. The beam ionisation was found to be virtually the same for all three configurations, since the plasma profiles are the same. Shine through losses are 10.63, 10.67 and 10.6% for the high, standard and low mirror respectively at densities of  $1.5 \times 10^{20} m^{-3}$ , indicating the similarities. The ionisation leads to large numbers of particles deposited on the outboard side for plasma densities above  $10^{19}/m^3$  due to the high plasma collisionality. However, due to the volume effect, flux surface averaging the deposition leads to on-axis peaked profiles for the first ionic molecules. Second and third ionic molecule ionisation is peaked off axis, as the penetration distance is proportional to the particle energy. Fokker Planck simulations following the time-evolution of the NBI beam ions in VENUS-LEVIS indicate that the first and multiple orbit (for  $t < 0.5 \times 10^{-3}s$ ) losses are similar across the three equilibria. The low mirror has reduced losses due to the allowed toroidal precession of trapped particles. For larger time-scales  $t > 5 \times 10^{-3}s$ , diffusive losses occur. The presence of Coulomb collisions on the diffusive losses tends to spread and increase the number of beam ion losses over a broader expanse of toroidal angles. With the inclusion of Coulomb collisions the toroidal loss regions are found to be very different between the mirror configurations, caused by the different magnetic loss wells and bounce tip behaviour created by the specific magnetic geometries. The high mirror was found to have the longest particle confinement time for all radial positions, resulting in improved numbers of particles near the injection energy and higher beam ion densities. Two different methods to evaluate the NBI slowing down distributions have been presented, one that injects all numerical markers into the simulation at once and removes all markers that have thermalised from the calculation, and the other method that injects constantly and thus accounts for thermal particle dilution. Using the method of constant injection over multiple slowing down time-scales results in a continuous energy distribution, but requires extra care to stop the simulation in time not to overestimate (or accumulate) the thermalised beam population. This would be more representative of the NBI beam species during experiments providing the simulation is stopped at a time so as to match the form (but not amplitude of) the background plasma profiles. The method involving the removal of thermal particles results in discontinuities in the energetic distribution function as a flux surface function. Results from both methods illustrate a significant improvement of

NBI particle and energy confinement, as well as collisional power transfer to the background plasma for the high mirror equilibrium. The differences between the low and standard mirror are mainly visible in the core where the standard mirror collisionally transfers more power to the background plasma. For all three magnetic mirror equilibria, the majority of the NBI heating power is transferred to the ions due to the low NBI injector energies.





## 5 Advanced Heating Schemes

The main aims of this thesis are to enhance and broaden an understanding of fast ion auxiliary heating methods, permitting the conception and development of advanced heating scenarios. In creating and applying novel RF and NBI heating schemes, the aim is to produce more efficient power transfer to the plasma core ions to increase plasma fusion production conditions and to generate fast ion particles to be used to study alpha particle confinement. This chapter shows the numerical results obtained in calculating advanced scenarios with the SCENIC package. The two advanced heating schemes presented in this chapter rely on a specific choice of the majority and resonant charge-to-mass ratios. These are the 3-ion species and synergetic RF-NBI Doppler shifted resonance heating scenarios. The 3-ion species scheme is described in [62]. The RF-NBI Doppler shifted resonance heating is described in [63] for deuterium NBI heating in a deuterium majority plasma, and in [64] for deuterium NBI heating in a hydrogen majority plasma (where the deuterium NBI ions play the role of a fast minority species). Experimentally, both scenarios have been explored in tokamaks such as JET, but never before in stellarators. With the experimental application of the RF-antenna to be made ready for the OP2 experimental campaign foreseen to take place in 2020, it is of crucial importance to predict which method might result in the greatest performance with respect to background plasma collisional heating and arguably even more importantly, energetic particle generation for mock up alpha particle confinement studies. The section on synergetic RF-NBI Doppler shifted resonance heating scenario also includes simulations of the JET shot 91256 which applied this method in a majority hydrogen plasma. Comparisons with the experiment are made by comparing with the TOFOR (neutron time of flight diagnostic).

### 5.1 3-Ion Species Heating Scheme

As indicated by equation 2.2.18, for a single species plasma the polarisation at the resonant surface goes to zero, resulting in inefficient wave-particle absorption. The minority species heating scheme utilises a small concentration of a secondary plasma species in order to move the ion-ion hybrid resonant layer (where  $S - n_{\parallel}^2 \rightarrow 0$  in equation 2.2.4) from the region where the polarisation is zero. However, as shown in equation 2.2.20, the polarisation has an upper limit at the wave-particle resonant surface. The advanced ICRF heating ‘3-ion species’

## Chapter 5. Advanced Heating Schemes

---

scheme has been proposed in [62] to circumvent this upper polarisation limit. The plasma is composed of two different majority species (that impose the dielectric properties of the plasma and the main wave polarisation) and a very small concentration of a third minority species. The application of this small quantity of the third species allows particle resonance close to the L-cutoff layer (equation 2.2.10) where the polarisation is maximised:

$$\left| \frac{E_+}{E_-} \right|^2 \gg 1. \quad (5.1.1)$$

The wave absorption  $n_{\perp}^2 < 0$  occurs in a region dictated by the charge mass ratio of the three species as well as the relative species concentrations. In order to have the minority species located near the L-cutoff, the charge to mass ratio of the three species must result in a ‘sandwiching’ of the third species such that:

$$(Z/A)_{M(1)} < (Z/A)_{min} < (Z/A)_{M(2)} \quad (5.1.2)$$

The concentration of the third species (*min*) also influences the polarisation at the wave-particle resonant surface. An approximated method to calculate the fraction of the third species required for strong wave absorption was proposed in [65]:

$$f_{M_1}^* \simeq \frac{\tilde{Z}_{min} - \tilde{Z}_{M_1}}{\tilde{Z}_{M_2} - \tilde{Z}_{M_1}} - \frac{(\tilde{Z}_{M_2} - \tilde{Z}_{min})(\tilde{Z}_{min} - \tilde{Z}_{M_1})}{\tilde{Z}_{M_2} - \tilde{Z}_{M_1}} \zeta, \quad (5.1.3)$$

with  $\tilde{Z}_{\alpha}$  the charge to mass ratio  $(Z/A)_{\alpha}$  and the parameter  $\zeta$  influenced by parameters such as the major radius, electron density and parallel wave number of the RF wave. This thesis focuses on the application of the 3-ion species in the W7-X stellarator. The results of the 3-ion species applied to 2D JET tokamak equilibria using the SCENIC package has been published in [66].

### 5.1.1 W7-X

Using the same electron profiles shown in figure 3.46, using a H-(3He)-4He scheme, the plasma concentrations taken were  $X[\text{H}]=68\%$ ,  $X[4\text{He}]=15.9\%$  and  $X[3\text{He}]=0.1\%$ . The total absolute power predicted by the LEMan wave code is shown in figure 5.1. Comparing with the same plot for the minority species scheme in figure 3.48, the power absorption in the plasma core of the bean section ( $\varphi = 0$ ) is significantly more focused for the 3-ion species scenario. The improved absorption of the wave near to the RF-antenna is also implied by the significant decrease in the absorbed power at  $\varphi = 3\pi/10$  for all mirror equilibria. It is seen that the electric field is strongly damped before reaching this toroidal angle.

### 5.1. 3-Ion Species Heating Scheme

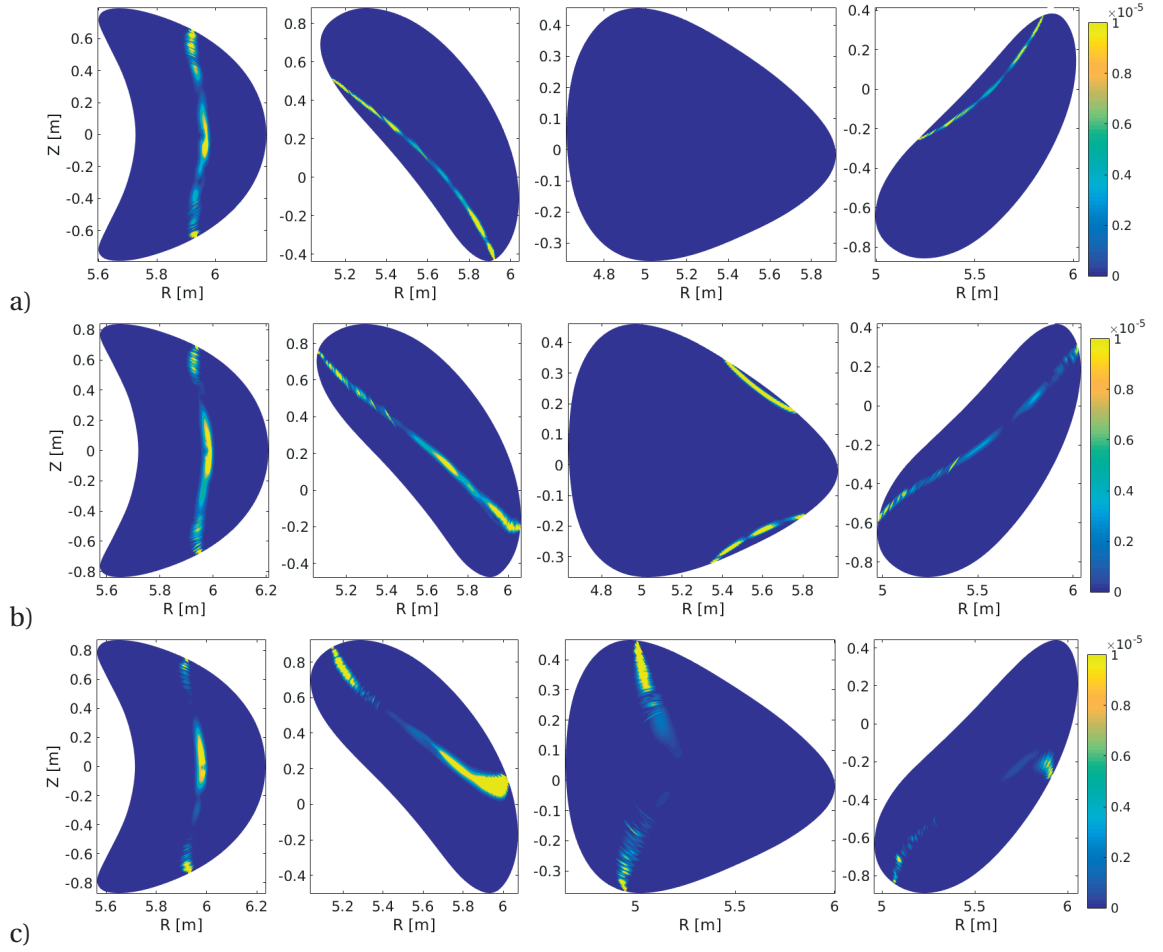


Figure 5.1 – Contour plots of the total absorbed power [a.u.] for the 3-ion species heating scheme. Plots of the poloidal cross-sections at  $\varphi = [0, \pi/10, \pi/5, 3\pi/10]$  are given for a) high, b) standard and c) low toroidal magnetic mirror configurations.

Fokker-Planck simulations with the 3-ion species RF-wave show strong dependence on the toroidal magnetic mirror value, reflected by the particle distribution as a function of energy in figure 5.2. The most energetic ions produced in the low mirror equilibrium are up to almost 0.5MeV. For the standard and high mirror these values are up to  $\sim 0.16$ MeV. The RF-resonant surface in the standard mirror remains close to the magnetic axis over a broader range of toroidal angles than for the high mirror, resulting in a greater number of particles at higher energies than the high mirror.

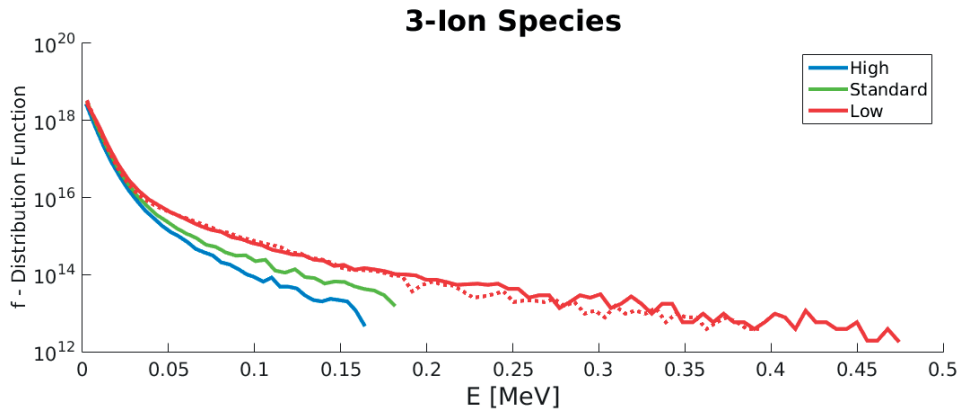


Figure 5.2 – Particle distribution as a function of energy of the 3-ion species heating scheme, comparing the influence of the magnetic equilibrium. Dashed red line shows low mirror off-axis ( $B_{res} = 2.6T$ ) simulation.

Above 0.1MeV, the low mirror has approximately one order of magnitude more energetic particles than for the high mirror. This reflects the significant influence of the magnetic mirror factor on the RF-resonant surface. Compared to the minority species scenario shown in figure 3.49, the 3-ion species heating scheme generates significantly higher energetic particles, for all magnetic equilibria. This is expected, since the field polarisation near the ion cyclotron resonance is favourable and the concentration of resonant ion species is very low compared to the two majority background species. The low mirror equilibrium could be used to study the confinement of highly energetic trapped particles heated by ICRF.

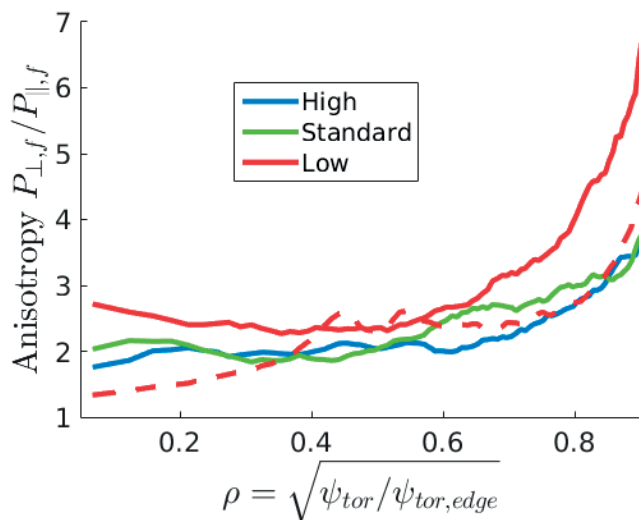


Figure 5.3 – Fast ion ( $E > 5T_e(s)$ ) anisotropy profiles of the 3-ion species heating scheme, comparing the influence of the magnetic equilibrium. Dashed red line shows low mirror off-axis ( $B_{res} = 2.6T$ ) simulation.

The anisotropy profiles in figure 5.3 provide further evidence for the improved RF-absorption of the low mirror due to the global increase in anisotropy. The edge anisotropy values for all equilibria are significantly larger than in the core for all equilibria, due to the increase in particle trapping from the magnetic equilibrium for large values of  $\rho$ . Calculation of the performance and behaviour of off-axis (with respect to the cyclotron frequency on axis at the antenna toroidal location) 3-ion species heating scheme has also been simulated in the low mirror equilibrium with  $B_{res} = 2.6T$ , which corresponds to HFS heating. Heating the low mirror off-axis reflects the influence of RF-heating on energetic particle confinement, which will be described at the end of this section. The performance of the on and off-axis RF heating in the low mirror to produce energetic resonant ion populations is similar, with particles generated up to almost 0.5MeV. The anisotropy profiles of figure 5.2 also indicate the improved performance of the 3-ion species compared to the minority species scenario to generate fast particles. Anisotropy is found to be higher in the on-axis low mirror than the standard or high mirror for all radial values. The anisotropy is significantly higher in the outer regions of the plasma due to the large radial motion of the trapped energetic particles generated by the RF-heating. Evidence for the increased radial transport is given later in this section.

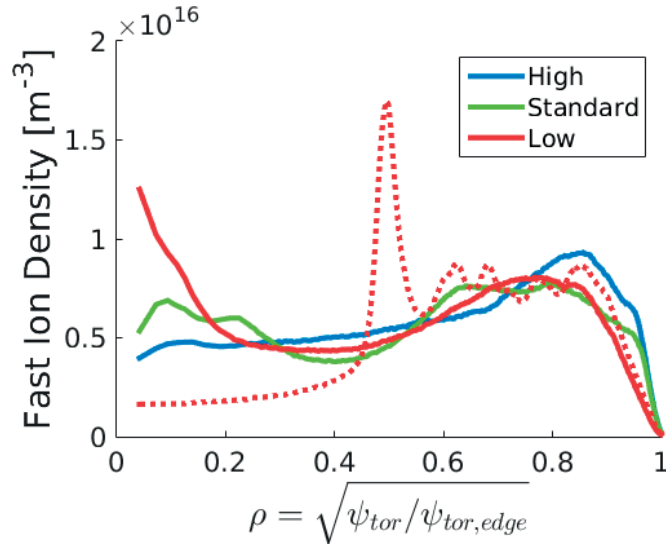


Figure 5.4 – Fast ion ( $E > 5T_e(s)$ ) density for the 3-ion species heating scheme in diverse W7-X magnetic equilibrium. Dashed red line shows low mirror off-axis ( $B_{res} = 2.6T$ ) simulation.

Moving the location of the resonant RF-surface to the HFS results in anisotropy profiles that are approximately unity in the core but peak to the same value as the core anisotropy value in

the on-axis low mirror case at the location of the resonance at  $\rho \sim 0.5$ . Further discussion of the anisotropy is made later in this section. With respect to the fast ion density profiles shown in figure 5.4, the on-axis 3-ion species heating in the low mirror is the only equilibrium peaked on-axis. All three equilibria generate significant off-axis components. It is also important to note the extremely low concentrations of fast ion particles in the core: the high mirror fast ion core concentration is less than  $10^{-5}\%$  of the background electron density. Experimental delivery and detection of such minute concentrations is not currently feasible. The collisional power deposition density profiles in figure 5.5 follow roughly the same form as the density profiles in figure 5.4. As compared to the minority species heating scenario, the 3-ion species fails to transfer as much total power to the background (to generate fast particles for alpha particle studies rather than bulk ion heating). This is reflected in table 5.1, illustrating the significant increase in lost power due to poor confinement of deeply trapped energetic particles. The shape of the collisional power transfer profiles is not ideal to be used for heating performance, as increasing the ion temperature at the plasma edge could result in instabilities or degraded plasma confinement.

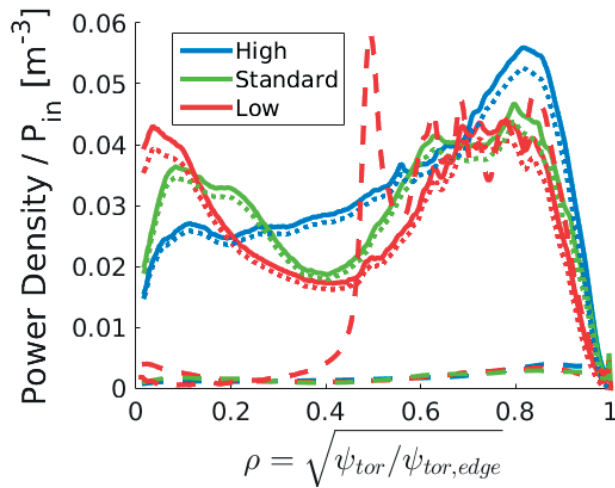


Figure 5.5 – The collisional power transfer from the minority 3-ion species to the background plasma, comparing the influence of the magnetic equilibrium. Dotted lines indicate power transferred to the background ions and dashed to electrons. Dashed red line shows low mirror off-axis ( $B_{res} = 2.6\text{T}$ ) simulation.

The distribution of particles in energy-pitch angle space is shown in figure 5.6. This illustrates the role of ICRF to heat the resonant particles predominantly in the perpendicular direction as would be expected. Figure 5.6 (a) indicates that the energetic population generated in the high mirror equilibrium has a more isotropic profile in pitch angle space than the low or standard mirror configurations. This is due to the resonant surface existing near the plasma core over a very narrow toroidal angle range, such that energetic particles collide more with the background plasma in between toroidal bounce periods, increasing the pitch angle scattering.

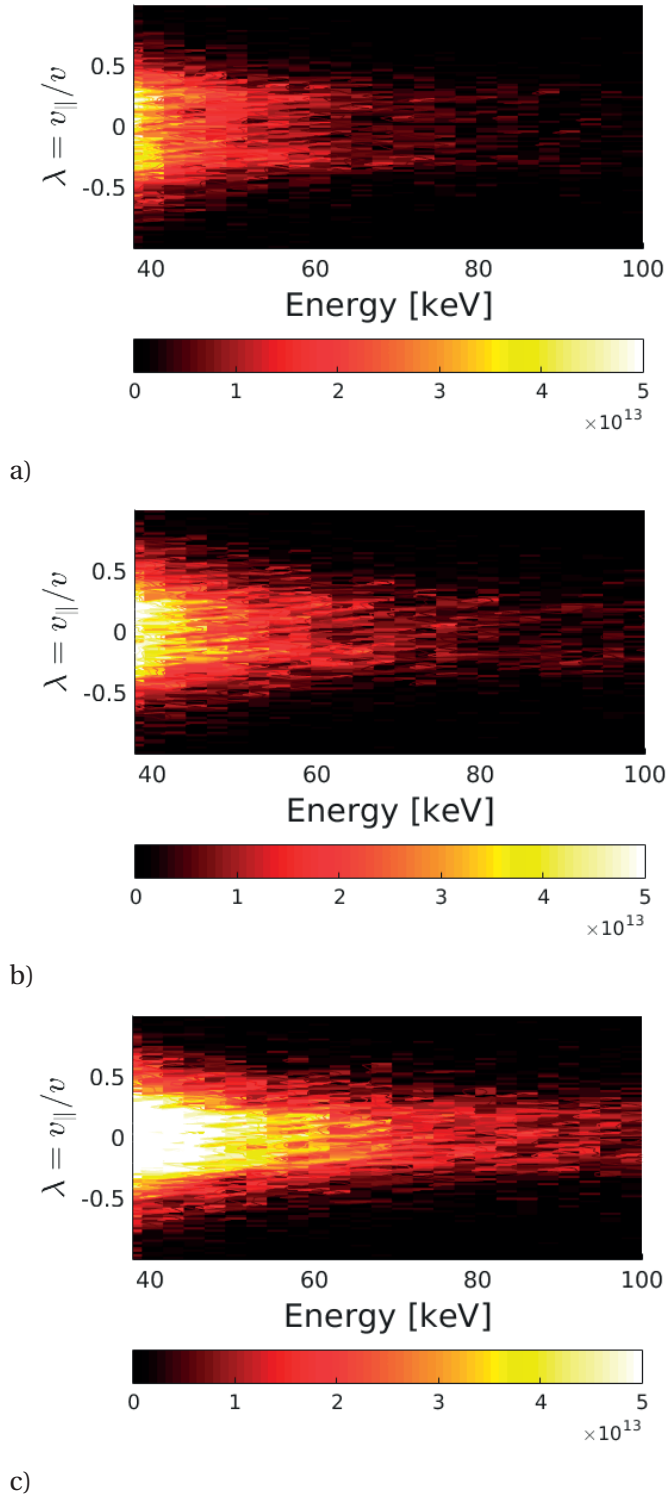
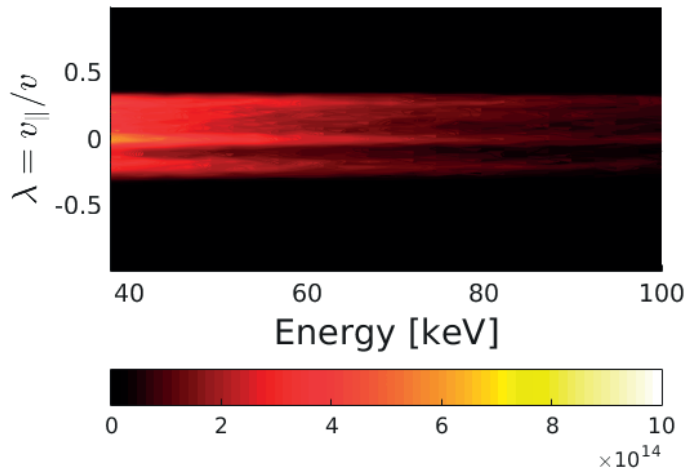


Figure 5.6 – Energy-pitch angle ( $E - \lambda$ ) space histogram contour plot of the converged marker population for the 3-ion species heating scheme for: a) high, b) standard and c) low mirror magnetic configurations.

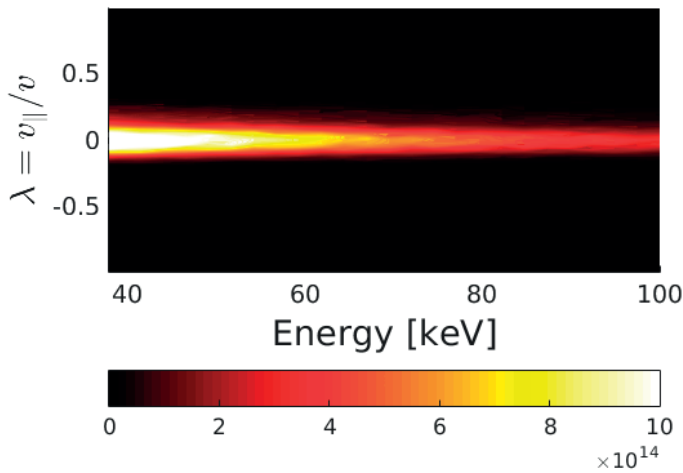
## Chapter 5. Advanced Heating Schemes

---

Generating the same contour plot for the lost particles further illustrates the large pitch angle scattering present for the 3-ion species heating in the high mirror. For the low and standard mirror, there is a clear peaking of lost particles at the point  $v_{\parallel} = 0$ , which corresponds to deeply trapped particles. The asymmetry in  $\lambda$  is due to the toroidal location of the RF-antenna ( $\phi \sim 0.117$  rads) with respect to the magnetic geometry. Regions of increased magnetic curvature result in large radial drifts. The co-directional particles (trapped or passing) that are heated by the ICRF antenna will experience different drifts to the counter-directional particles. This results in a net loss pattern that is asymmetric in pitch angle. This asymmetry is further increased with an increase in the number of particles that toroidally bounce near the RF-antenna, reflected by the differences in the energetic particle losses in pitch angle space when comparing the low and high mirror.

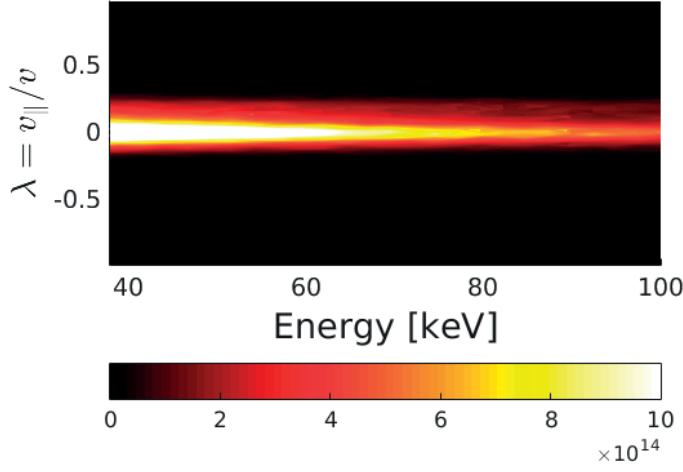


a)



b)





c)

Figure 5.7 – Energy-pitch angle ( $E - \lambda$ ) space histogram contour plot of the lost population for the 3-ion species heating scheme for: a) high, b) standard and c) low mirror magnetic configurations.

### RF-Resonant Surface and Energetic Particle Confinement

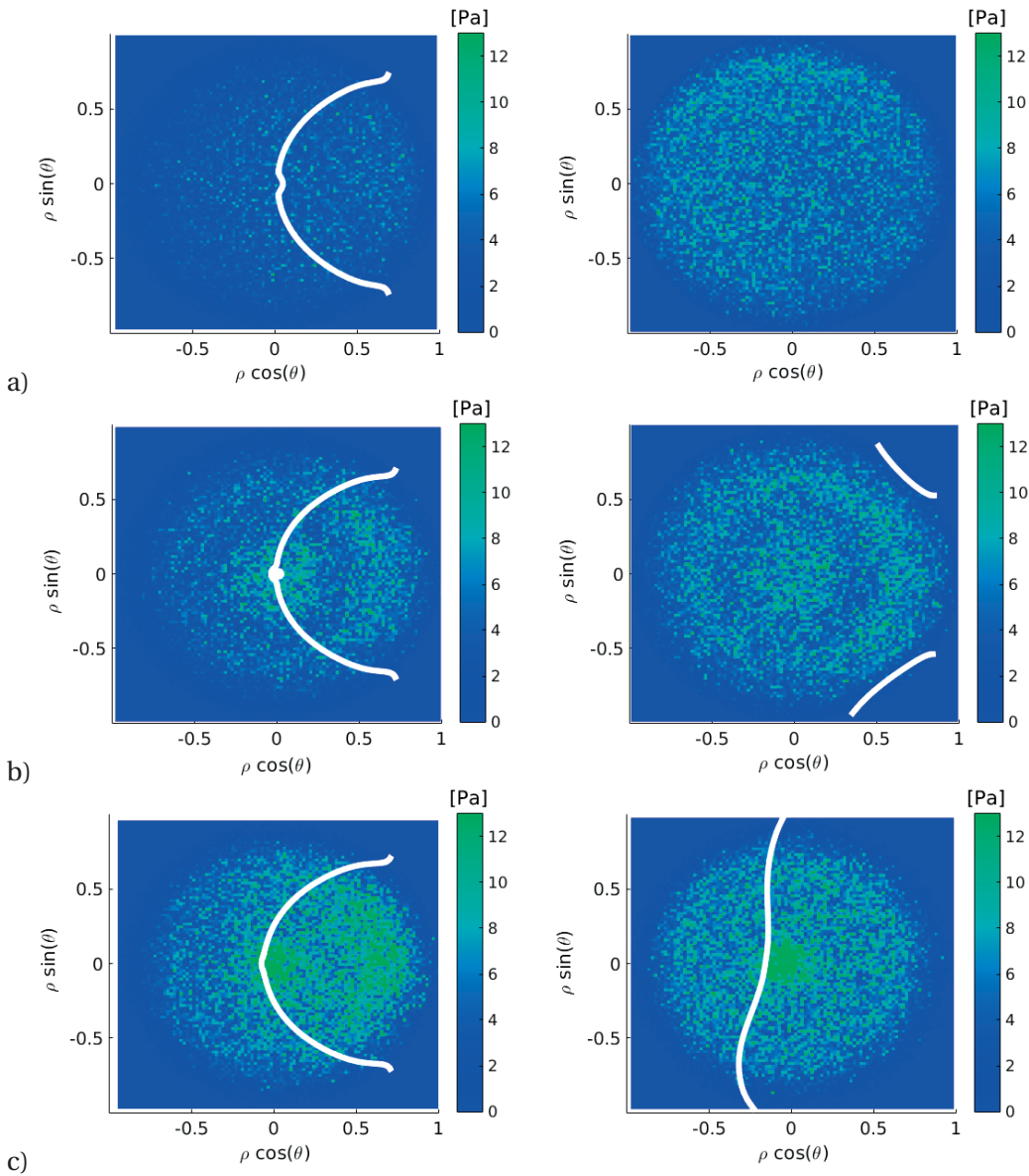
The confinement of deeply trapped energetic particles in the different magnetic equilibria can be assessed via the degree to which highly energetic ions are produced. Observing the influence of the displacement of the RF-resonant surface on the high, standard and low mirror configurations, a HFS resonance simulation was calculated for the low mirror to explore further the influence of the resonant surface on ICRF heating in 3D magnetic geometries. Figure 5.2 illustrates that similar highly energetic particle populations can be produced with HFS heating in the low mirror. With regards to the fast ion density peaking, shown in figure 5.4, the fast ion population is strongly peaked at the location of the resonant surface, with considerably lower concentrations in the plasma core for all on-axis simulations. The density outside this region is also increased, implying that once the energetic trapped particles are produced at outer radial positions, the strong radial drift encourages increased trapped particle losses. This is reflected in table 5.1.

Mirror	$P_{cols}/P_{in}$ %	$P_{lost}/P_{in}$ %	Lost Particles %
High	93.4	6.6	12.0
Standard	89.7	10.3	14.8
Low (on-ax)	81.9	18.1	13.3
Low (off-ax)	79.1	20.9	18.7

Table 5.1 – The lost power and particle percentages for the 3-ion species scheme in W7-X for the different toroidal magnetic mirror configurations.

## Chapter 5. Advanced Heating Schemes

Insight into the influence of ICRF on particle trapping and confinement can be illustrated by plotting the fast ion pressure in front of the RF-antenna ( $\varphi \sim 0$ ) compared to the triangular section ( $\varphi \sim \pi/5$ ). These plots are generated by remapping to circular flux surfaces,  $y = \sqrt{s} \sin\theta$ ,  $x = \sqrt{s} \cos\theta$  with  $\theta$  the VMEC poloidal angle. As was shown in the fast ion density plots (figure 5.4), the fast ion pressure is peaked on axis. However, an explanation for the large off-axis component can be inferred from the large pressure build up in front of the antenna ( $\theta = 0.117\text{rads}$ ) for the on-axis low mirror configuration shown in figure 5.8 c) (left). The bounce tips of the particles can also be be seen to align to the magnetic resonant surface (white lines), a phenomenon which was shown to occur in tokamaks in section 2.4.4. This behaviour can also be observed in the standard mirror equilibrium in figure 5.8 b) (left).



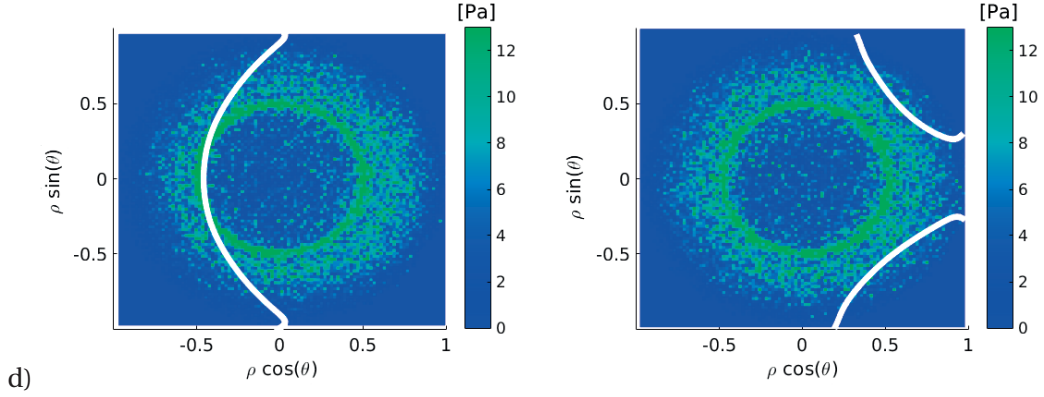


Figure 5.8 – Fast ion ( $E > 5T_e(s)$ ) pressure plots for the 3-ion species heating scheme for: a) high, b) standard, c) low and d) low HFS mirror RF-heating. Left) Bean  $\varphi = 0 \pm 0.2$  section, right) triangular  $\varphi = \pi/5 \pm 0.2$  section. The line of resonance of the  $B_{res}$  contour is indicated by the solid line.

Simulations with the HFS resonance in the low mirror equilibrium also indicate an alignment of RF-resonant particles to the resonant surface, resulting in a strong pressure peaking at the radial location of the resonant layer. This peaking is also caused by the influence of ICRF on the radial particle confinement, as shown in figure 5.9.

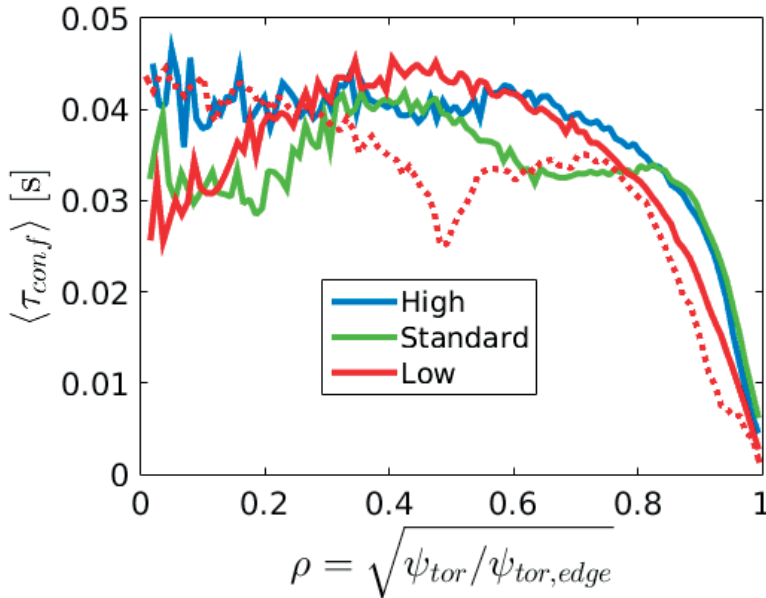


Figure 5.9 – The confinement time of the 3-ion species particles as a function of the initial radial position of the marker, averaged over the entire marker population. Dashed red line shows low mirror off-axis ( $B_{res} = 2.6T$ ) simulation.

The particle confinement is estimated using the following method: upon reaching a converged energy state in the Fokker Planck code calculation, the simulation is then run over particle loss time-scales. Knowing the particle's initial radial position and the time it takes to become lost, an average confinement time can be generated for the fast ions as a radial function. The HFS low mirror simulation has similar transport properties to the high mirror equilibrium in the core region because particles do not interact with the RF-wave at such radial values. The regions where the number of highly energetic trapped particles increases is reflected by a reduced average confinement time. This further illustrates the issues the stellarator fusion approach must overcome in order to design an efficient commercial fusion reactor.

### 5.2 RF-NBI Synergetic heating Scheme

Synergetic ICRF heating of NBI beam ions has been applied in tokamak, stellarator and heliotron experiments over the past decade [64, 63, 67, 68]. In experiments such as at JET [69, 63], a clear increase in the D-D neutron rate as well as an enhancement of the slowing down beam population ( $T_i < E < E_{beam}$ ) was measured. Most synergetic RF-NBI experiments have applied fundamental and harmonic frequencies to the beam ions such that the appropriate on-axis resonant frequency was  $\omega_a \sim n\Omega_{c,res}$ . For the application of the fundamental frequency, if the injected ions are the same element as the majority species, then power absorption is low due to poor wave polarisation. The poor performance can be explained by consideration of the plasma dilution caused by NBI fueling. Concentrations of thermalised NBI ions can be up to  $\sim 20\%$  of the electron density. If all beam particles would be at thermal energies, applying the minority species heating with concentrations of this amount would result in almost all power being transferred to the electrons via wave mode-conversion. Moreover, if the main plasma ions are lighter than the injected beam species (a so called 'inverted' ICRF scenario), a LFS cut-off would hinder the wave to reach the resonant layer of the thermalised beam particles, resulting in poor heating on thermalised beam particles. However, because of the large energy of the injected beam ions, their Doppler-shifted ion cyclotron resonance,  $\omega = \Omega_c \pm k_{\parallel} v_{\parallel}$ , is located beyond the cut-off generated by the thermalised beam population, producing efficient absorption of the RF-wave power. In this respect, the thermalised beam ions even help to enhance RF-absorption on the beam species, due to the strong RF-field polarisation near the cut-off. Upon ionisation, the NBI beam resembles a delta function in velocity space, with  $v_{\parallel,b}$  and  $v_{\perp,b}$  dictated by the beam injection geometry. Using the simplification  $k_{\parallel} \sim n_{\phi}/R$ , the  $k_{\parallel} v_{\parallel}$  factor in the ICRF resonance condition will be approximately a magnetic field contour for the beam ions. This allows a clear separation between the thermalised and (recently ionised) beam particle resonant surfaces. In a two-species hydrogen-deuterium plasma, three prominent RF-resonant surfaces are present: the majority background, the thermalised beam dilution concentration and the recently ionised beam population. The presence of the Doppler-shifted beam resonance layer near to the LFS cut-off results in a maximisation of the polarisation, similar to the 3-ion species scheme. This results in improved RF-power absorption by the resonant beam species. Unlike the 3-ion species scheme, however, adjustment of the concentration of the third species is not possible as the beam injection energy and power is not

flexible. A distinction between the synergetic RF-NBI heating experiments should be made. Those in [69, 63] use the same element as the injected beam, and in [64], a majority species with a different charge-to-mass ratio is used. In order to heat the NBI ions on-axis, the latter experiment applied the RF-antenna frequency to resonate with the value  $\omega_a \sim n\Omega_{c,res} + k_{\parallel}v_{\parallel}$  on-axis, thus the Doppler effect modifies the frequency applied. Manipulating the resonance condition and using the approximation for the parallel wave-number  $k_{\parallel} \sim n_{\phi}/R$  in tokamak devices,

$$\Delta R \simeq \frac{n_{\phi}v_{\parallel,beam}}{\omega_a}, \quad (5.2.1)$$

then with deuterium injection of energy  $E \sim 100\text{keV}$ , pitch angle  $\lambda \sim 0.62$  and dipole antenna phasing such that  $n_{\phi} \sim \pm 27$ , the Doppler shift is approximately  $\Delta R \sim 35 - 40\text{cm}$  [63].

As mentioned previously, using RF-produced energetic particles to simulate alpha particle confinement studies requires particles with isotropic velocity distributions. The Doppler shifted resonance synergetic RF-NBI heating scheme is ideal as the resonant particles are heated more in the parallel velocity than the other RF schemes mentioned in this thesis, which heat preferentially in the perpendicular direction. The pitch angle collisional scattering of the particles depends on the value of the pitch-angle, shown in equation 2.4.22, producing distribution functions more isotropic in pitch angle. This results in a broader, more isotropic particle distribution in velocity space than traditional ICRF schemes. Evidence for the increase in the heating transferred in the parallel direction of this heating scheme is given by multiple factors described in this section.

Injecting energetic NBI ions at values of  $\lambda = v_{\parallel}/v$  significantly increases the heating in the parallel velocity. This is reflected by the QLO term  $\mathcal{Q}_{\perp,RF}\partial^2 f_{0,\alpha}/\partial v_{\perp}^2$  in equation 2.4.23. The value of  $\mathcal{Q}_{\perp,RF}$ , shown in equation 2.4.29, is increased at the resonance location with this heating scheme. This is due to the enhanced wave polarisation at the resonance due to the location of the ‘third’ species (the Doppler-shifted beam population) near to the L-cutoff layer, as for the 3-ion species scheme. Additionally,  $\mathcal{Q}_{\perp,RF}$  is enhanced as the resonant beam ions have much larger Larmor radii, increasing the absorption via the Bessel functions in the QLO. The delta-function beam distribution can be approximated as a narrow Maxwellian distribution function:

$$f_{NBI} = \frac{S_{NBI}}{\sqrt{2\pi}(v_{\perp,b}\tan\theta)^2} e^{-\frac{(v_{\perp}-v_{\perp,b})^2}{2(v_{\perp,b}\tan\theta)^2}}, \quad (5.2.2)$$

with  $S_{NBI}$  the source number of particles injected by the NBI and  $\theta$  the NBI beam spreading angle. Considering  $df_{0,\alpha}/dt = \mathcal{Q}_{\perp,RF}\partial^2 f_{0,\alpha}/\partial v_{\perp}^2$ , then comparing the second derivative of the distribution function with that of a thermal Maxwellian species results in time-scales  $\tau_{NBI}/\tau_{th} = v_{\perp,b}\tan\theta/v_{\perp,th} \ll 1$ . The generation of energetic particles is dependant upon the relative time-scales of the particle resonance compared to collisionality time-scales. The

energy transfer of the RF-wave to the beam population compared to a thermal population is therefore over much shorter time-scales. This implies that this RF-NBI method may be advantageous in the generation of highly energetic particles. Further evidence for the increased RF-heating in the parallel direction is given by equations 2.2.13 and 2.2.14, which compare the range of values of the parallel velocity where wave-particle resonance can occur between RF-heating on-axis ( $\omega_a = n\Omega_c(s=0)$ ), and the Doppler shifted position for RF-NBI Doppler shifted resonance heating ( $\omega_a = n\Omega_c + k_{\parallel} v_{\parallel}$ ). These two equations illustrate that in the core region of the plasma in front of the RF-antenna, there is no possibility for trapped ( $v_{\parallel} \sim 0$ ) thermal particles to absorb energy from the wave for the Doppler-shifted resonance RF-NBI scheme. This is due to the application of an antenna frequency which includes the strong Doppler shift of the beam ions. Modifying the RF-antenna frequency such that strong wave-particle energy transfer occurs in a region where  $\omega_a \neq n\Omega_c(s=0)$  results in a larger parallel velocity energy transfer, reflected by equation 2.4.33.

Having given a brief introduction on the unique properties of the synergetic RF-NBI heating scheme, the remainder of this subsection is written as follows: a presentation of the simulation methodology is given in 5.2.1, explaining the two approaches taken. Both these methods rely on a reliable fitting between the Fokker Planck NBI slowing down marker population and the density, temperature and anisotropy moments of the SCENIC bi-Maxwellian distribution function for the wave-propagation calculation. Section 5.2.1 shows comparisons between the raw marker data and the moments. The first numerical results using this heating scheme are shown in the JET tokamak using the shot number 91256, for RF-heating of deuterium NBI ions in a hydrogen majority plasma (thus an inverted scheme [48]). Comparison with experiment is made using the TOFOR diagnostic. The final part of this section shows the numerical results for RF-heating of hydrogen NBI beam ions in a helium-4 majority plasma (thus a standard or non-inverted scheme) in the W7-X device, using the two different numerical approaches shown in section 5.2.1. Using the low, standard and high mirror magnetic configurations described in chapter 2, a parameter scan of the antenna frequency and the background density concentration of the beam element is made.

### 5.2.1 Numerical Methods

To simulate the interaction between ICRF and NBI, a necessary requirement is the constant injection of freshly ionised beam particles during the course of the simulation. Pure ICRF heating simulations always contain a constant number of markers at all times, which can no longer be maintained for RF-NBI heating scenarios. As described in chapter 4, constantly injecting markers throughout the simulation results in a steady increase of the particle population in the simulation unless the input particles are balanced by the lost particles. This would require significant percentage losses of the thermalised NBI beam ions over the simulated timescales. We do not model the appropriate transport channels for thermalised ions in the SCENIC code. We therefore have to contain the simulations so that the thermalised population is in reasonable agreement with experimental or theoretical predictions. Two approaches are



made to simulate synergetic RF-NBI heating using the SCENIC package: the dilution method and the fast-splitting method.

### Dilution Method

In both tokamak and stellarator devices, transport of thermal particles is very complicated when considering neoclassical and turbulent diffusion effects. SCENIC does not include the effects of such transport. Highly energetic particles tend to average out turbulent transport over a gyro-orbit[70], and neoclassical effects have been shown to have only a small influence on the particle radial transport[71]. Section 4.2.3 explored the effects of running the slowing down NBI simulations for time periods whereby the plasma profiles (in particular, the density) become unphysical. The conclusion of that section was that for the W7-X plasma profiles used in this thesis, a simulation time limit of  $3-4\tau_{SD}$  (for these profiles: 0.1 seconds) should be used to obtain a total beam particle density profile form that resembles the background plasma profiles. The advantages of such a method are that the RF-interaction between the wave and thermal particles is also inherently included, and that the particle distribution as a function of energy is continuous. This will be shown to be very important in RF-NBI simulations. If the experimental total percentage concentration of the beam species is known, then the weighting of injected markers can be adjusted to ensure a final total beam concentration (including the thermalised population) that matches the experimental value. The simulation can therefore be run to constantly increase the number of markers present in the simulation. The final marker distribution therefore corresponds to the converged state if the power transferred to the background converges in time throughout the simulation. The approach of this method is as follows:

1. Calculate the NBI ionisation deposition marker population using VENUS-NBI (chapter 4).
2. Adjust the marker weighting according to the NBI power over multiple slowing down time scales.
3. Run marker population in VENUS-LEVIS.
4. Calculate the total remaining population concentration at the end of the simulation.
5. Adjust the marker weighting to match the experimental and numerical concentrations.
6. Modify background bulk ion density profile (for a fixed electron density profile) to account for dilution concentration (this ensures quasi-neutrality).
7. Rerun VENUS-LEVIS using original NBI ionisation deposition.
8. Repeat points 2-7 until convergence.

## Chapter 5. Advanced Heating Schemes

---

9. Split the fast and thermal particles for the bi-Maxwellian distribution function fitting and provide the bi-Maxwellian fast and Maxwellian thermal moments to the LEMan wave propagation code.
10. Rerun VENUS-LEVIS with RF-wave, using original NBI ionisation deposition.
11. Repeat points 9-10 until either the empirical dilution is reached or before the profiles become distorted due to incorrect calculation of thermal particle transport.

### Fast-Splitting Method

An alternative approach is proposed which avoids the thermalised beam particles (and thus the question of thermal particle transport) in the VENUS-LEVIS simulation. The main difference between this and the dilution method is that beam ions that approach electron thermal temperatures ( $E < 1.5T_e$ ) are removed from the simulation. The background profiles are artificially adjusted to include a thermal beam species concentration for the LEMan calculation. The method is outlined as follows:

1. Calculate the NBI ionisation deposition marker population using VENUS-NBI.
2. Run VENUS-LEVIS using the NBI method removing the thermalised population, outlined in section 4.2.3.
3. In place of the removal of thermalised beam population, deploy a Maxwellian population that helps to match the measured/expected dilution. Adjust ion concentrations to maintain quasi-neutrality (for a fixed electron density profile).
4. Adjust artificially the background profiles to account for a certain thermal beam species dilution concentration.
5. Apply the bi-Maxwellian distribution function fitting to the total slowing down beam population resulting from removing the thermal species.
6. Provide the bi-Maxwellian fast moments to the LEMan wave propagation code.
7. Rerun VENUS-LEVIS with the RF-wave QLO, continuously injecting markers, using original NBI ionisation deposition and continuing to remove thermalised particles.
8. Ensure that the collisional power, density and pressure of the marker distribution converges in time.

The disadvantages of this method are that the particle distribution as a function of energy will be discontinuous on every flux surface and that there is no possible means for the wave to interact with the thermal population through the QLO in VENUS-LEVIS. A physical interpretation of this is that the RF-power is assumed to be mostly deposited on-axis in front of the antenna where thermal particles cannot receive energy from the wave. This assumption



is valid in tokamaks, but in stellarators this might not be the case. As an outlook for future research applying this method, LEMan wave simulations using the toroidal family mode method (see section 3.5) could be used to explore the validity of such an assumption.

### Applying the Bi-Maxwellian Distribution Function

Another assumption made using these two methods is that the bi-Maxwellian distribution function well represents the density, temperature and anisotropy moments of the marker population. Equation 2.5.2-2.5.4 are shown as 2D functions in  $B$  and  $s$ . Figure 5.10 indicates that for Wendelstein 7-X the Bi-Maxwellian density moments for the high, standard and low mirror correspond well to the actual marker population.

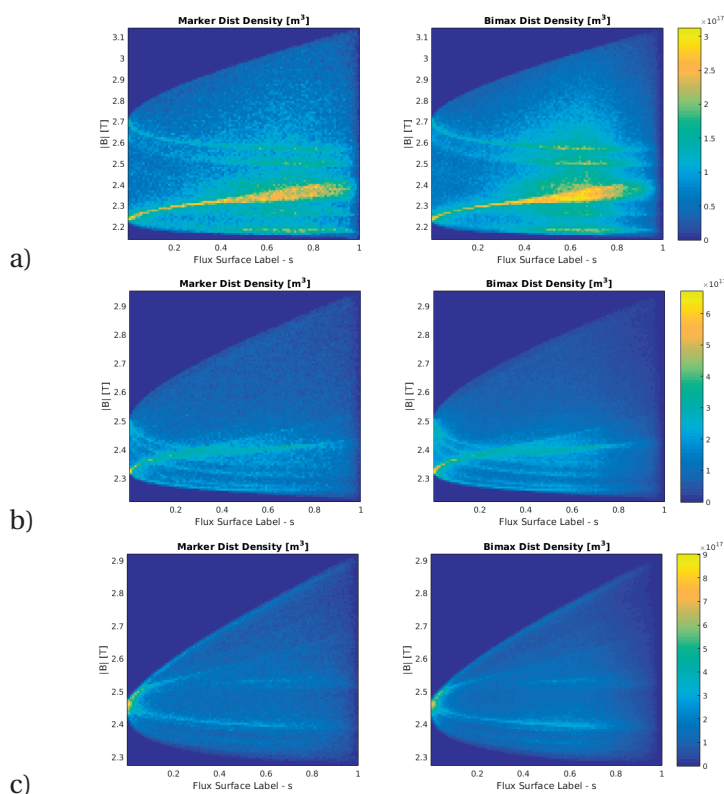


Figure 5.10 – Comparison between the density moment (right) of the Bi-Maxwellian distribution function and the marker population (left) for the NBI slowing down distribution, for a) high, b) standard and c) low mirror W7-X magnetic configurations.

### 5.2.2 JET Shot 91256

The Doppler shifted resonance synergetic RF-NBI heating (inverted) scenario was recently applied to the JET tokamak in shot 91256. The results were promising, as shown in [64]. The plasma was majority hydrogen, with deuterium the NBI injected population, leading to an inverted ICRF scenario. The dilution factor is approximately  $X[D_{th}] \sim 8 - 10\%$ . The fast NBI beam population was predicted to be  $X[D_{NBI}] \sim 2 - 4\%$ . Therefore, the  $H - (D_{NBI}) - D$  Doppler

shifted heating scheme was applied.

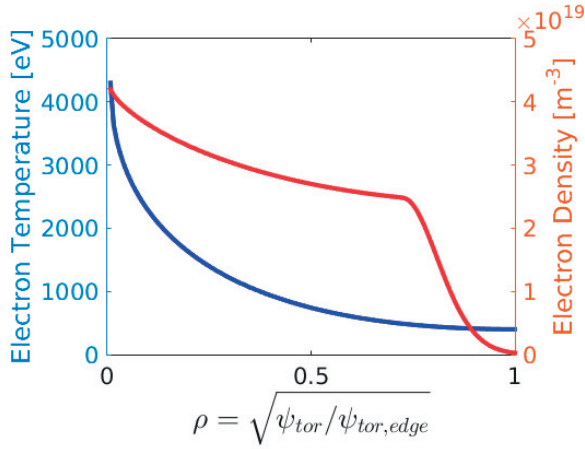


Figure 5.11 – Electron density and pressure profiles for the 91256 JET experiment at t=50.9s.

The electron plasma profiles used to simulate the experiment are shown in figure 5.11, which correspond to the time period t=50.9s. Additionally, a beryllium impurity concentration of 0.5% was assumed. The magnetic field on axis was  $B_0 = 2.82\text{T}$ , plasma current  $I_p = 1.9\text{MA}$  and the Doppler-shifted RF-antenna frequency applied was 25MHz. The ion temperature  $T_{i,0} = 3.5\text{keV}$ . The JET NBI beam injector modules applied were 8.7 and 8.8, which are both co-current.

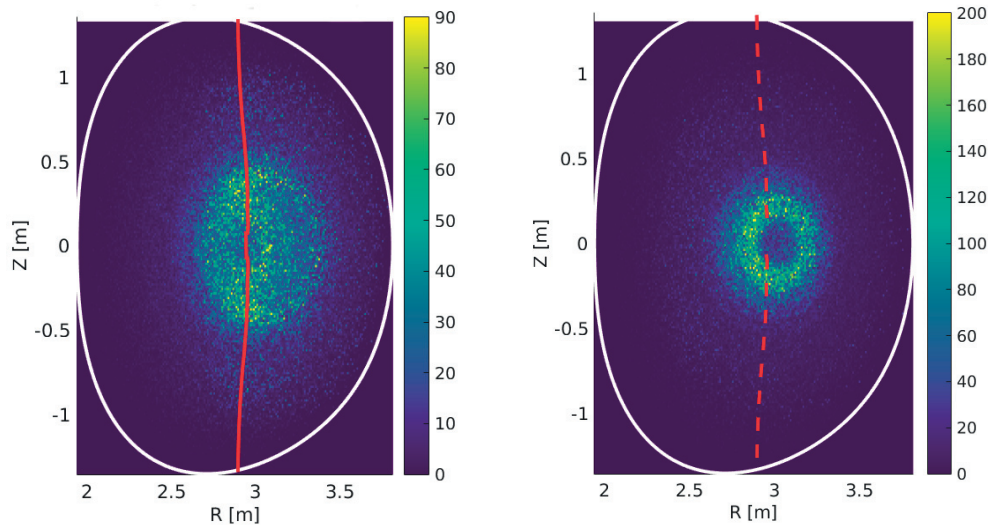


Figure 5.12 – Fast ion ( $E > 7T_e$ ) pressure comparing left) on-axis  $\omega = \Omega_c(s = 0)$  minority heating RF-NBI with right) Doppler shifted resonance  $\omega = \Omega_c(s = 0) + k_{\parallel}(s = 0)v_{\parallel}$  RF-NBI synergistic heating. The solid red line indicates the on-axis resonant surface  $\omega_a = \Omega_c$ , the dashed red line corresponds to the resonant surface for  $\omega_a = \Omega_c + v_{\parallel,b}k_{\parallel}$ , with  $v_{\parallel,b} \sim 2 \times 10^6\text{m/s}$ . Note the different colourbar axis limits between the two plots.

As mentioned previously, to prevent unphysical accumulation or the miscalculation of the thermalised beam population, the appropriate numerical method must be chosen to simulate synergetic RF-NBI heating. In the next section on the W7-X we compare the results from the dilution and fast splitting methods. For the JET simulations, the dilution method has been applied as the thermal beam concentrations were experimentally calculated based on the JET diagnostics, such that  $X[D_{th}] \sim 10\%$ . Incoherent Thomson scattering leads to calculations of the electron density and temperature, which, in combination with charge exchange (CX) and neutron emission spectroscopy (MPR), was used to infer the thermal deuterium core density to be  $X[D_{th}] \sim 10\%$ . The VENUS-LEVIS synergetic RF-NBI simulations for the shot number 91256 were therefore run until the thermal particle accumulation reached 10%, to match the predicted concentrations made from experimental observations. Two simulations were made for this experimental shot for varying antenna frequency. A comparison of the results predicted by SCENIC using the Doppler-shifted resonance with  $\omega_a = 25\text{MHz}$  was made with the equivalent on-axis minority species-like heating scheme with  $\omega_a = 21\text{MHz}$ . The on-axis simulation does not represent what would happen experimentally, firstly because the RF-antenna frequency range at JET means that 21MHz is not possible. More importantly, as mentioned in section 2.2, the minority species heating scheme with minority concentrations of 10-15% would not produce efficient minority ion heating. The SCENIC code cannot model such RF-wave dispersive effects. The on-axis simulation was undertaken purely to investigate the QLO velocity diffusion differences between the two RF-NBI schemes.

The influence of the Doppler shifted resonance on the parallel velocity diffusion can be seen directly in the fast ion pressure, figure 5.12. For the on-axis 21MHz simulation, the trapped particle orbits are visible through the 2D fast ion pressure contour plot. However, regarding the 25MHz Doppler shifted simulation, the passing particle orbits are clearly visible. Looking at the fast particle velocity space distributions in the core region  $\rho < 0.35$  for the two simulations in figure 5.13, the velocity distribution at  $\omega_a = 25\text{MHz}$  produces energetic particles with significantly larger parallel velocity values. The distributions are asymmetric in the parallel velocity direction because of the unbalanced NBI beam injection. The imbalance is visible for the on-axis velocity distribution via the bulge formed around  $(v_{\parallel}, v_{\perp}) \sim (2 \times 10^6, 2 \times 10^6)$ , which corresponds to the injection of the first molecular deuterium NBI ions (with  $E=100\text{keV}$ ). The asymmetry is much more obvious for the Doppler shifted resonance RF-NBI heating scheme. The vertical green lines shown in figure 5.13 indicate the range of the allowed parallel velocities which permit RF-resonance (see equation 2.2.13) and the black dotted lines the trapped-passing boundary. The range of parallel velocities to which wave-particle resonance is possible illustrates that particles with low parallel velocities cannot absorb energy from the wave for the Doppler shifted antenna frequency RF-NBI scheme. As trapped particles tend to resonate with the wave at the bounce point where  $v_{\parallel} \sim 0$ , passing particles are preferentially heated. At high energies  $v_{\perp} > 3 \times 10^6$ , the trapped-passing boundary illustrates that the majority of these particles are passing.

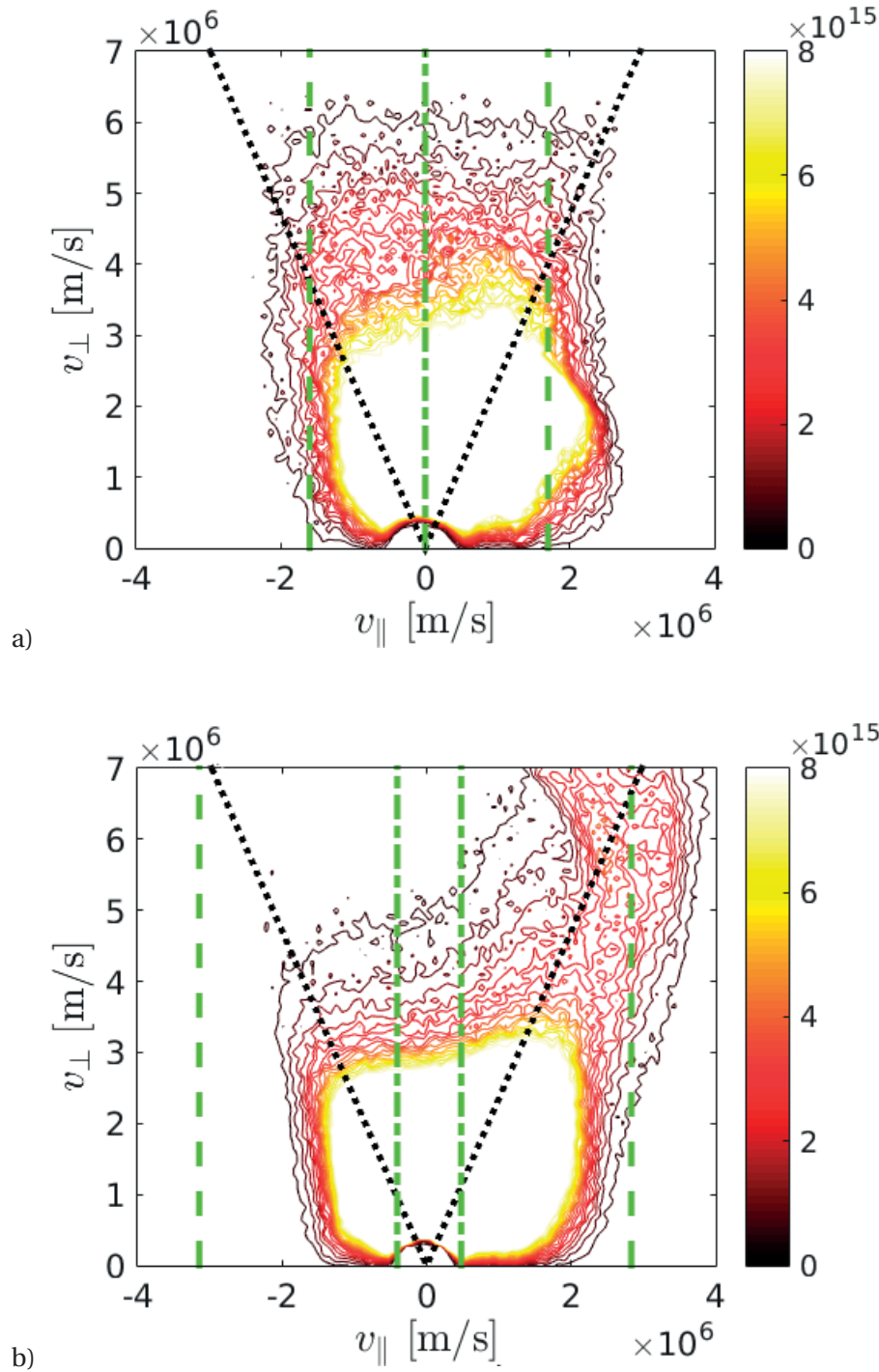


Figure 5.13 – 2D contour plots of the velocity space particle distributions comparing a) on-axis  $\omega_a = \Omega_c(s = 0)$  minority heating RF-NBI with b) Doppler shifted resonance RF-NBI synergetic heating. The NBI injection for 100keV single molecules of deuterium is  $\sim \{2 \times 10^6, 2 \times 10^6\}$ .

The SCENIC results for the RF-antenna frequency 25MHz simulation are compared against the experimental results using the TOFOR (Time-Of-Flight Optimised for Rate) diagnostic in figure

5.14. In order to make this comparison, energetic particles with  $E > 5T_e$  and that exist within the line-of-sight of the TOFOR detector are extracted. Calculations of the neutrons that would be produced by such an energetic population is made by a synthetic diagnostic which produces the associated time-of-flight (ns) of the neutrons produced by the RF-generated energetic population. The results compare well with the experiment. To improve the results, a scan of the background density could be performed to observe the balancing of the increased thermal deuterium concentration on the increase in collisionality with the increase in polarisation associated with the L-cutoff. Future work should also run the SCENIC code with neutron predictive calculations in order to normalise the y-axis of figure 5.14 to the experimentally observed neutron count.

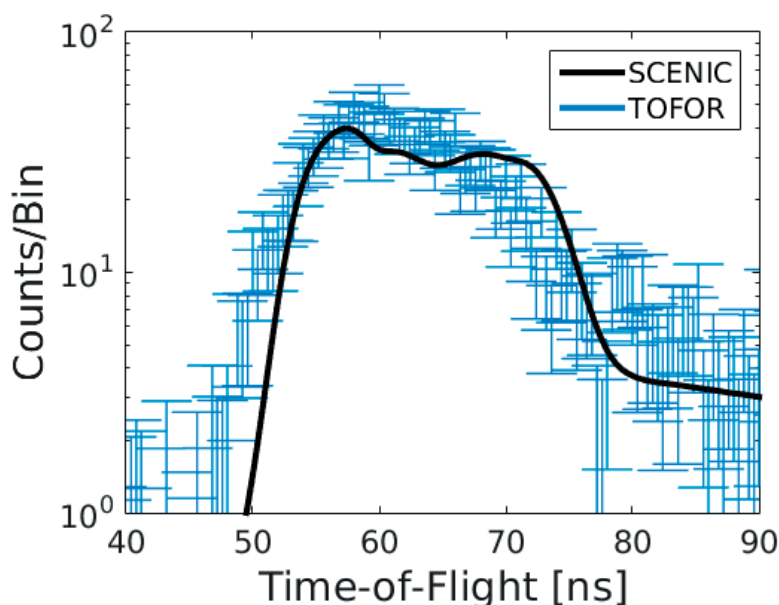
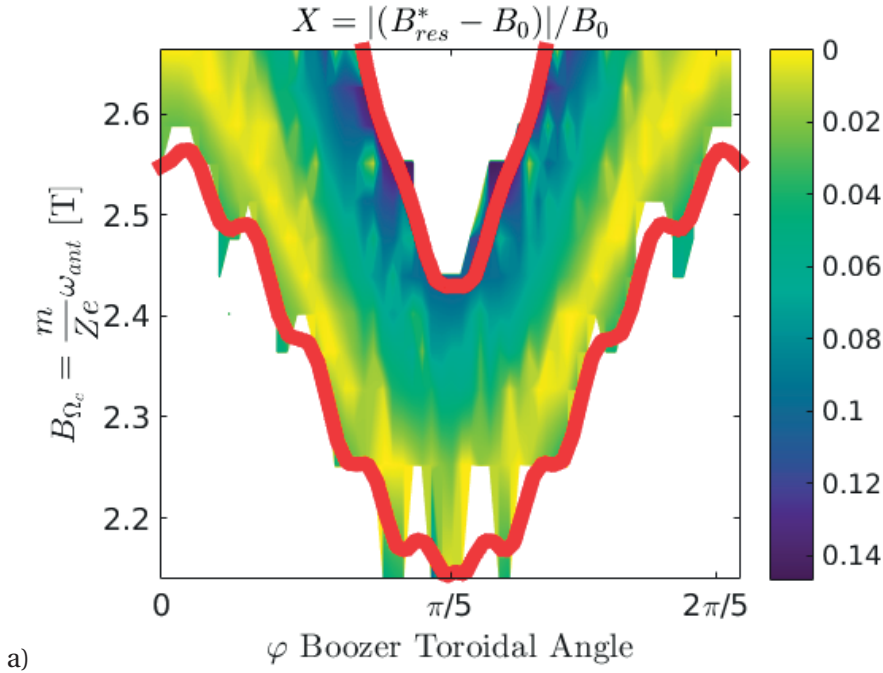


Figure 5.14 – Number of counts per bin (normalised) of the time of flight (ns) comparing the SCENIC predictions with the TOFOR experimental diagnostic of JET shot 91256.

### 5.2.3 W7-X

This section calculates the performance of the Doppler shifted resonance synergetic RF-NBI scheme for  $He4(H_{NBI})$ , using the same background electron density and temperature profiles as in previous W7-X simulations. This is not an inverted scheme since the beam ions are lighter than the background ions, where the fast wave cut-off is at the HFS of the ion cyclotron resonance layer. Due to the variation of the magnetic field strength along the magnetic axis for W7-X, the choice of RF-antenna frequency required for optimal heating performance is unknown. This is because the value of  $k_{\parallel}$  cannot be approximated as in toroidally symmetric magnetic fields. As shown previously, the production of highly energetic passing particles increases for an increase in the displacement of the resonant surface of the thermal ions from the magnetic axis. However, via consideration of the toroidal variation of the magnetic field

toroidal mirror term, limits to the choice of RF-antenna frequency can be calculated. This becomes important when considering the fundamental or harmonic resonance surfaces with the majority species. The freshly injected NBI beam ions injected into the plasma core have pitch angle values of  $\lambda = \pm 0.5$  and  $\pm 0.35$  for the tangential and normal NBI injector modules respectively. The approach taken in this work is to target the beam ions injected by the more tangential NBI injectors, which also have a slightly higher power (1.78MW instead of 1.64MW for the more normal injectors). In tokamak geometries, the approximation that  $k_{\parallel} \sim n_{\phi}/R$  is fairly accurate. However, in stellarators the poloidal up-shift effect, the 3D deformation of the flux surfaces and the toroidal variation of the magnetic field strength means that such an approximation is no longer valid. The numerical ‘cannonball’ method is applied, whereby a scan of the RF-antenna frequency is made. For each simulation in  $\omega_a$ , the parallel velocity close to the magnetic axis is extracted and averaged to evaluate the resonance condition  $\omega_a - \Omega_c - v_{\parallel} k_{\parallel}$ . Replacing  $\Omega_c = Z_{\alpha} B / m_{\alpha}$  allows to determine the magnetic field strength  $B_{res}^*$  at which resonance occurs for the beam particle  $v_{\parallel,b} = 2 \times 10^6$ . This value can be calculated at each toroidal cross-section and compared to the magnetic field strength on axis such that  $X(\phi) = |B_{res}^*(\phi) - B_{s=0}(\phi)| / B_0 = 0$  satisfies the resonance condition and energy is transferred from the wave to the beam ions. Contour plots of the variation of the parameter  $X$  with the toroidal angle and applied RF-antenna frequency are shown in figure 5.15. The toroidal magnetic field strength variation of the high mirror equilibrium strongly influences the resonance condition.





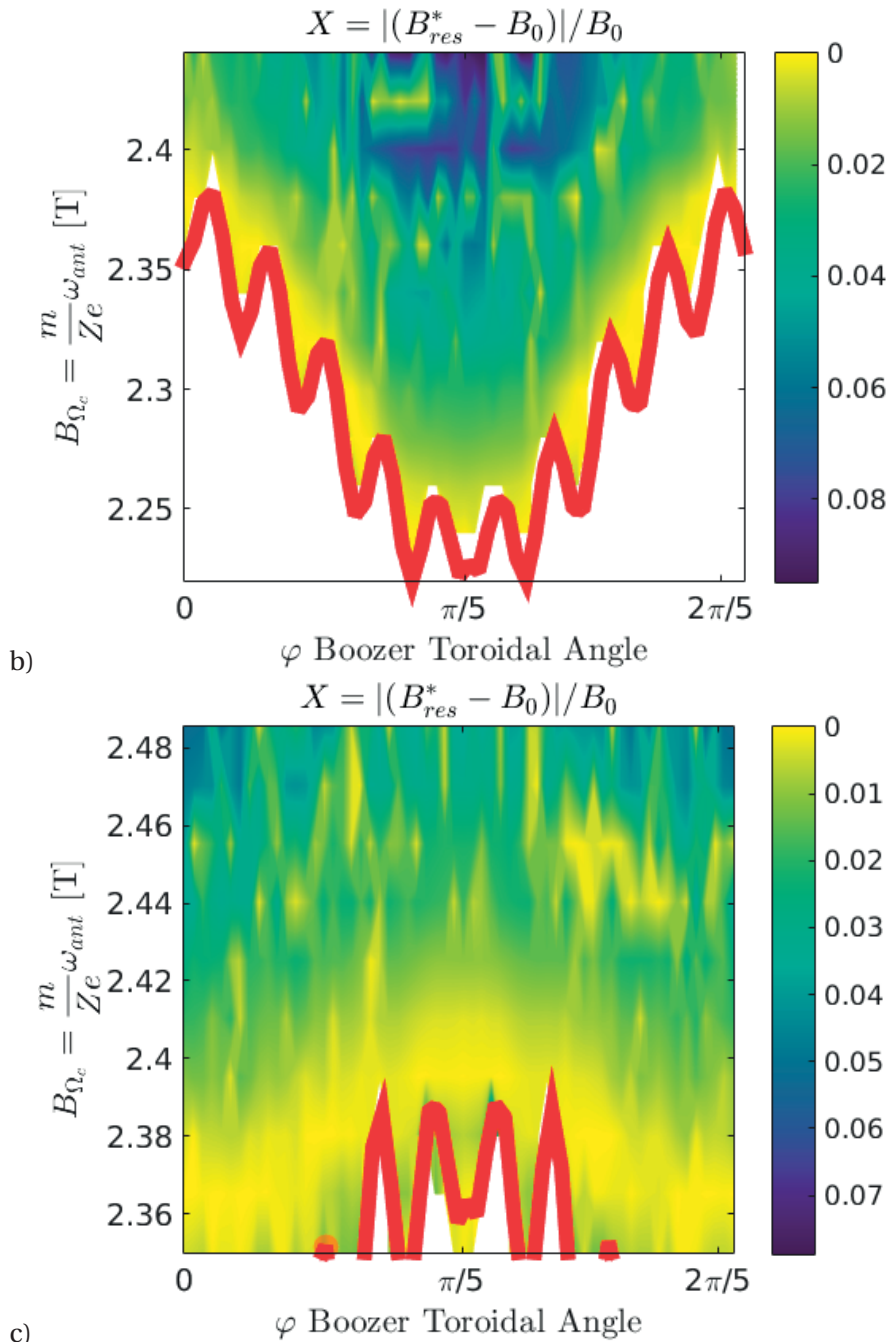


Figure 5.15 – Contour plots of the variation of the parameter  $X$  with the toroidal angle and magnetic field strength which corresponds to the resonant surface  $B_{res} = m_a \omega_a / Z_a$  for the a) high, b) standard and c) low toroidal magnetic mirror configurations. The red lines correspond to the limit within which the resonance position still exists within the plasma.

The choice of antenna frequency is varied for each of the magnetic mirror configurations due to the differences in the gradient of the magnetic field strength. For the low mirror,  $B_{res} = 2.37, 2.38$  and  $2.39$ T, for the standard mirror,  $B_{res} = 2.32, 2.34$  and  $2.36$ T and the high

## Chapter 5. Advanced Heating Schemes

mirror,  $B_{res} = 2.52, 2.55$  and  $2.58\text{T}$ . A focus will be made on the intermediate values  $2.38, 2.34$  and  $2.55\text{T}$  for the low, standard and high mirror equilibria respectively.

### Dilution Method

The simulations with the dilution method (described in 5.2.1) were run with the NBI slowing down simulations calculated for  $3-4\tau_{SD}$  ( $\sim 0.1$  seconds). This time was chosen in order to obtain a dilution factor of 3.67% which resulted in total beam particle density profiles of similar form to the background plasma profiles, as described in chapter 4.

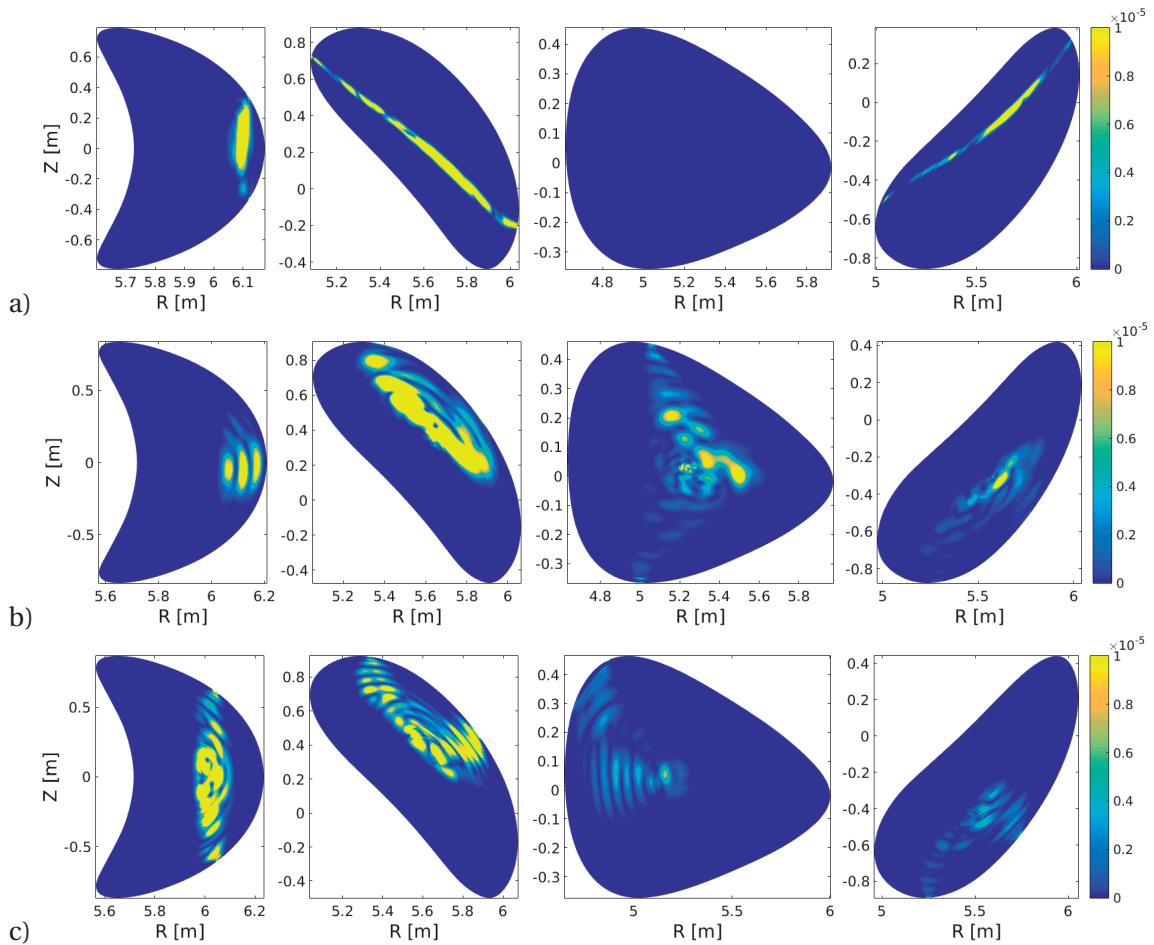


Figure 5.16 – Total absorbed RF-power density from the LEMan wave code. Plots of the poloidal cross-sections at  $\varphi = [0, \pi/10, \pi/5, 3\pi/10]$  are given for a) high, b) standard and c) low toroidal magnetic mirror configurations.

The beam thermal distribution calculated from the NBI simulations using the VENUS-LEVIS code was used to modify the background helium-4 population in order to maintain both quasi-neutrality and the background electron density. Feeding the moments of the fast and thermal NBI slowing down distribution into the wave-propagation code LEMan results in



the total absorbed RF-power density shown in figure 5.16. What is particularly noticeable, as compared with the same plots for the minority and 3-ion species schemes, is the observable Doppler-shift effect on the absorption. This broadening of the absorption is less visible in the high mirror configuration as the gradient of the magnetic field strength is much larger across flux surfaces, compacting the resonances together. Absorption in the standard mirror is closer to the magnetic axis over the toroidal angles than for the minority or 3-ion species schemes. Calculating the Fokker Planck beam distribution evolution results in a significantly increased fast ion pressure and density compared to the minority and 3-ion species heating schemes, shown in figure 5.17. Additionally, the pressure and density maxima are in the core region. This is very advantageous for fusion reaction conditions. The benefits of the improved high energetic particle confinement observed in the high mirror configuration as compared to the low and standard configurations are also observed in the fast ion density plot, which is a significant improvement over the other heating schemes applied (see the off-axis maxima in figures 3.51 and 5.4 for the minority species and 3-ion species heating schemes respectively).

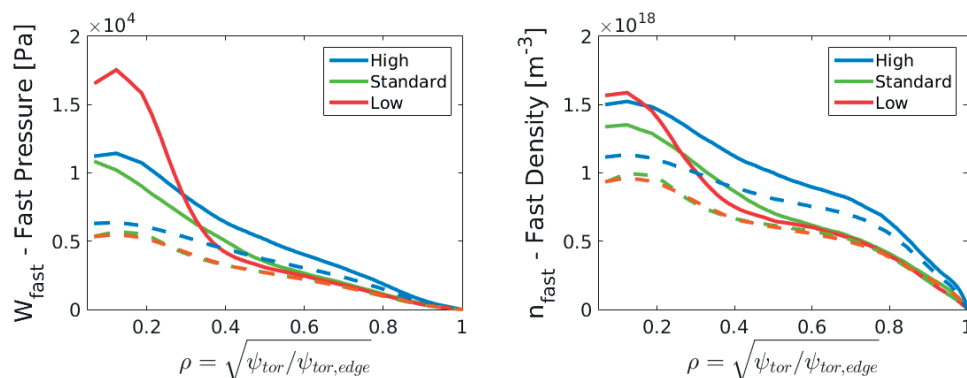


Figure 5.17 – Fast ion ( $E > 5T_e$ ) pressure and density plots for the a) high, b) standard and c) low toroidal magnetic mirror configurations. Dashed lines indicate the values for NBI only.

The energetic particle distribution of figure 5.18 reflects the ability of the Doppler shifted synergetic RF-NBI heating scheme to generate highly energetic particles that are almost in the MeV range. The performance of the low mirror to produce highly energetic particles, as in previous heating schemes, is increased significantly over the high and standard mirror equilibria. However, the high mirror outperforms the standard mirror for this heating scheme. The number of particles produced with energies over 0.2MeV is greatly reduced in the standard mirror, due to the location of the thermal particle resonant surface close to the magnetic axis, which compete with the fast beam ions. The number of energetic particles may therefore be more sensitive to the dilution concentration in the standard mirror. Figure 4.9 in section 4 indicated that the confinement of NBI ions is similar for the low and standard mirror within  $\rho < 0.6$ . Therefore, application of the Doppler shifted resonance RF-NBI heating results in reduced core particle confinement in the standard compared to the low mirror. Further evidence for this is given in figure 5.17 (right), which indicates increased radial drifts of the fast particles, reflected by the decrease in the fast ion density within  $\rho < 0.25$  and increased

fast ion density between  $0.25 < \rho < 0.6$ .

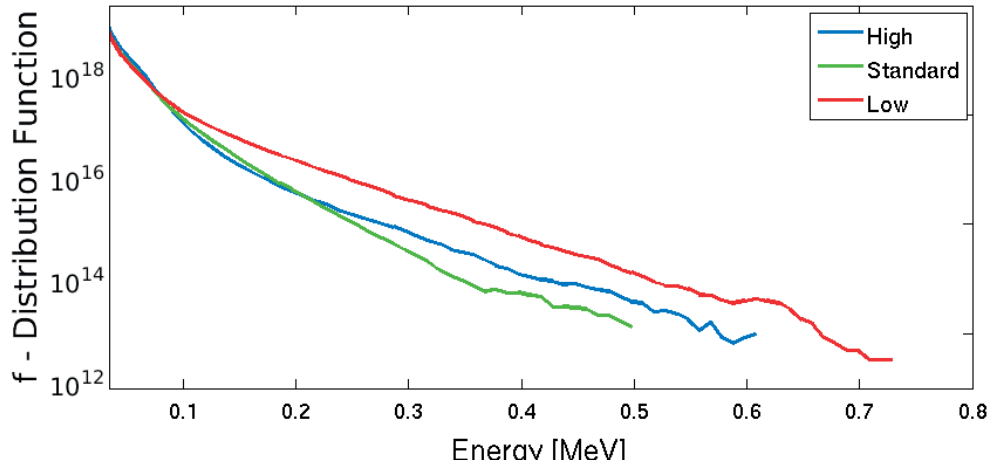


Figure 5.18 – Particle distribution as a function of energy, comparing the different magnetic mirror configurations.

The high mirror benefits from the thin resonance layer caused by the large gradient in the magnetic field strength across flux surfaces, localising the resonance such that the power is transferred over a narrow region.

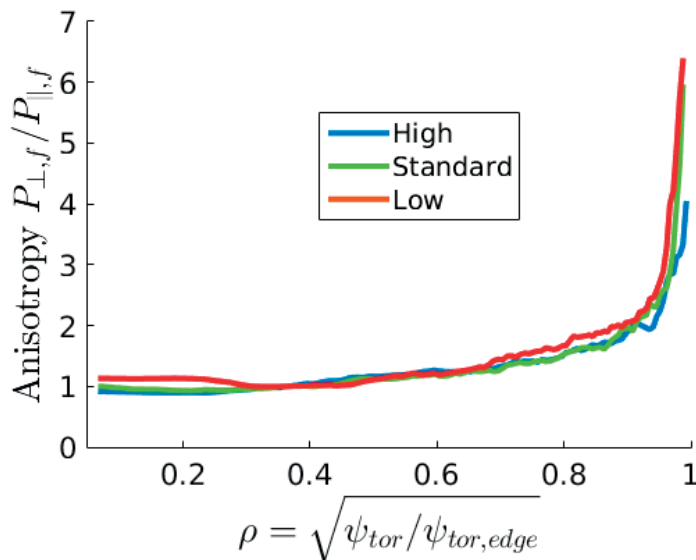
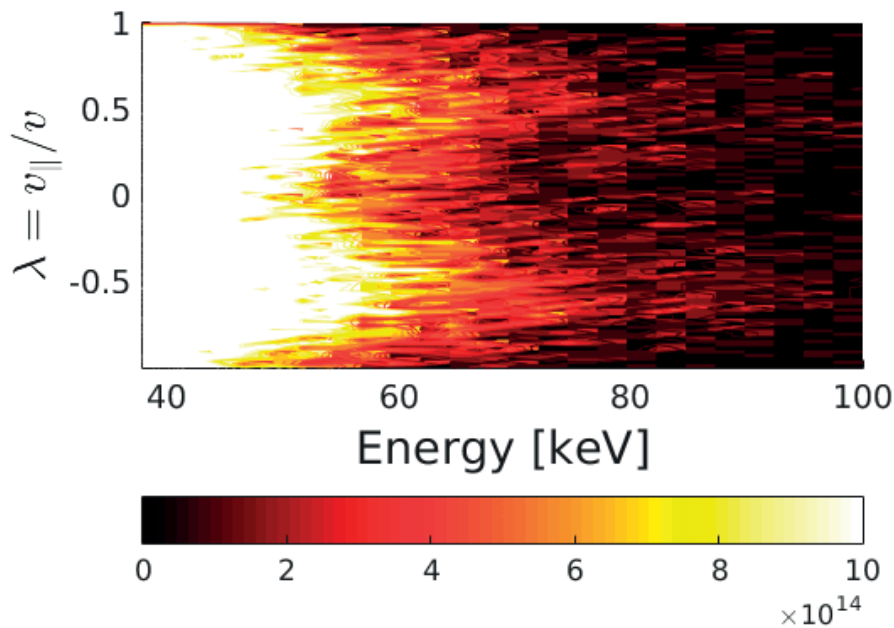


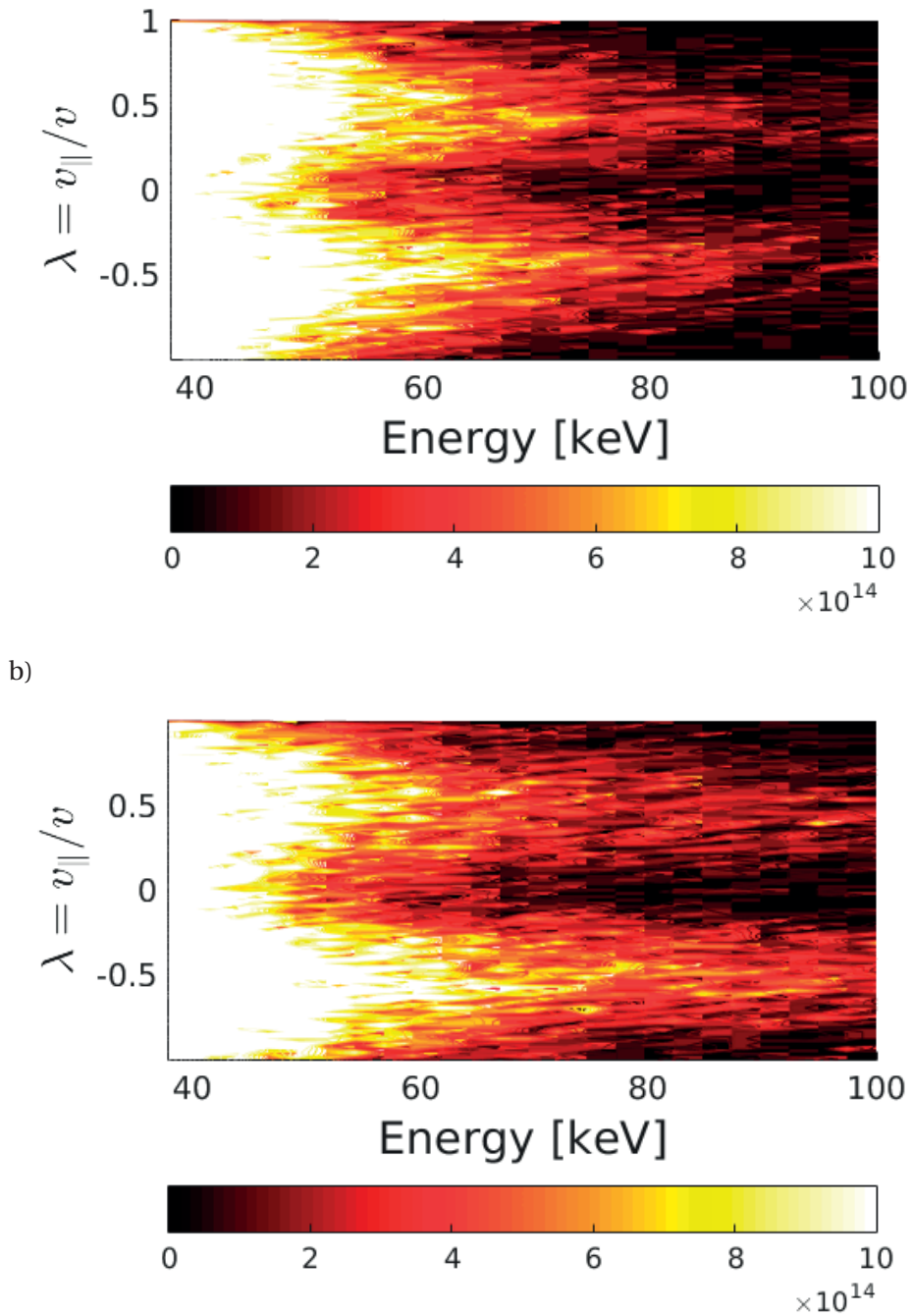
Figure 5.19 – Anisotropy profiles for the different magnetic mirror configurations.

For the pure RF heating schemes, the high mirror was found to be the worst performing magnetic configuration. Particles in the high mirror become toroidally trapped easier than for the low or standard mirror equilibria. The magnetic resonant surface also moves out of the

plasma in the triangular toroidal section. With the increase in parallel velocity diffusion for the RF-NBI heating scheme, the high mirror can produce and confine highly energetic resonant ion populations. One of the important properties of the Doppler shifted resonance synergetic RF-NBI heating scheme, described in the introduction, is the increase in parallel velocity diffusion as compared to pure RF-heating schemes. The anisotropy profiles in figure 5.19 illustrate that the fast particle parallel and perpendicular pressures are approximately equal up to  $\rho \approx 0.6$  and  $A < 2$  for nearly all of the plasma radius. The low values of anisotropic fast ion pressure in the core provide first evidence of the increase in parallel velocity diffusion in 3D magnetic geometries of the Doppler shifted resonance RF-NBI scheme, which seems to be almost independent of the toroidal magnetic mirror term. Further evidence for the increased parallel velocity diffusion obtained using this heating scheme is given by the energy-pitch angle contour plots of figure 5.20. The figure illustrates that for all three magnetic equilibria, an increase in parallel velocity from the Doppler shifted resonance is observed. As for the 2D JET simulations, the large pitch angle values also result in a broader pitch angle distribution due to the large pitch angle scattering from Coulomb collisions. The increase in the parallel velocity diffusion of the Doppler shifted resonance synergetic RF-NBI heating scheme, as compared to the pure RF minority species or 3-ion species heating schemes, produces resonant particles with large values of  $|\lambda|$  which have improved confinement over deeply trapped particles. These particles remain in resonance and therefore highly energetic ions can be produced in all toroidal magnetic mirror configurations.



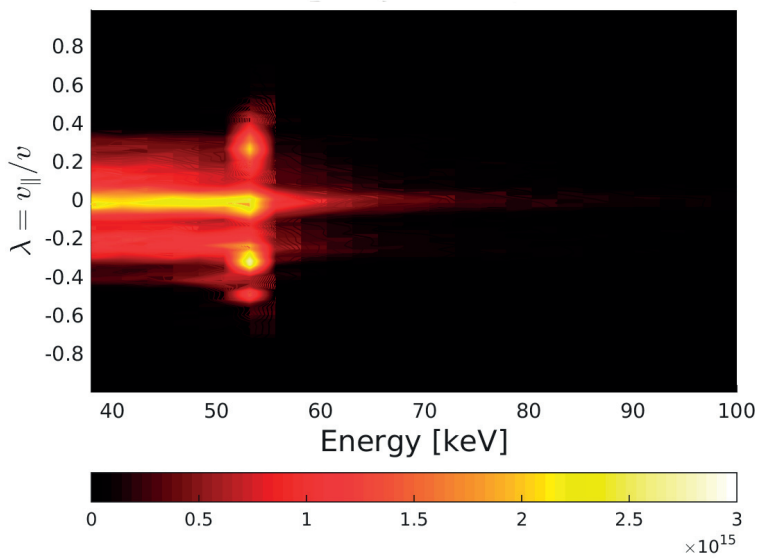
a)



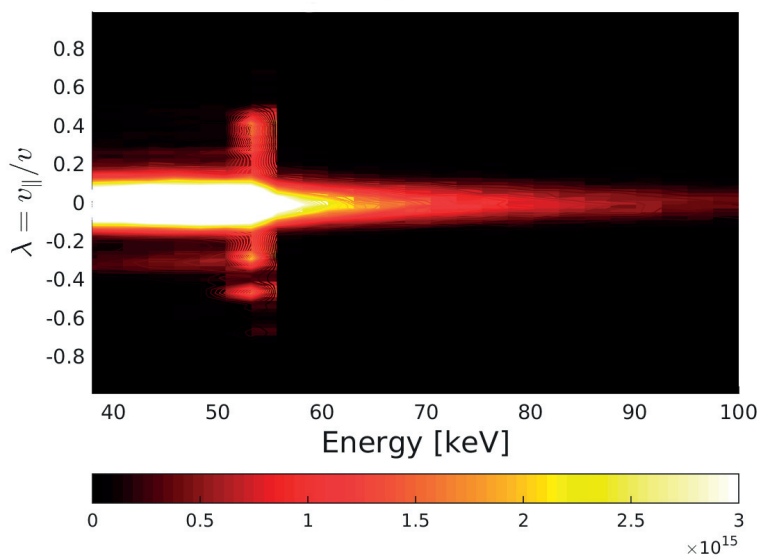
c)  
Figure 5.20 – Energy-pitch angle ( $E - \lambda$ ) space histogram contour plot of the resulting beam population for the a) high, b) standard and c) low mirror magnetic configurations.

Figure 5.20 (c) reflects an asymmetric pitch angle distribution for the low mirror configuration. The synergetic RF-NBI simulations are made using balanced NBI beam injection, and therefore

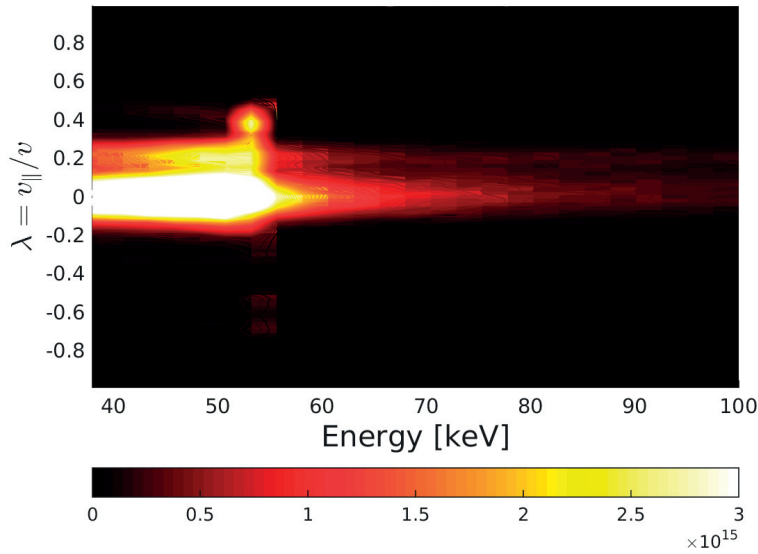
the Doppler shift should ensure that the pitch angle is approximately isotropic. The asymmetry in figure 5.20 (c) can be explained by considering orbit width effects. The radial orbit width of co and counter (to the magnetic field) energetic ions is significantly different at higher energies. In the low mirror configuration, this width difference is larger compared to the high or standard mirror due to the reduced magnetic field strength gradient across flux surfaces, and because particle velocities are generally larger.



a)



b)



c)

Figure 5.21 – Energy-pitch angle ( $E - \lambda$ ) space histogram contour plot of the lost population for the a) high, b) standard and c) low mirror magnetic configurations.

As shown in figure 5.21, the lost particle distribution is also asymmetric in pitch angle space in the low mirror equilibrium. A combination of the increased orbit width and the toroidal location of the RF-antenna could explain the increase in the losses of energetic resonant particles with  $\lambda \sim 0.2$ . The location of the RF-antenna is at  $\phi = 0.117$  rads, close to the region of increased magnetic curvature at the bean section  $\phi = 0$  rads where the particle radial drift is increased. The transfer of RF-power has different influences on the co-passing and counter-passing particles at the resonance location. Further work must be made to further investigate such effects.

Table 5.2 shows the total collisional and lost power and the number of lost particles resulting from the Doppler shifted resonance synergetic RF-NBI heating scheme. Compared to the pure NBI simulations, the total collisional power transfer to the background plasma is increased for the high mirror equilibrium by over 2%, but decreased by roughly 5-6% for both the low and standard configurations. The lost power and number of particles are increased significantly for all three equilibria compared to pure NBI simulations, due to the relatively poor confinement of highly energetic ions in W7-X. The high mirror continues to demonstrate improved energy and particle confinement over the low and standard equilibria.

Mirror	$P_{cols}/P_{in}$ %	$P_{lost}/P_{in}$ %	Lost Particles %
High	70.8	21.0	22.8
Standard	55.6	38.2	34.6
Low	56.2	38.2	30.8

Table 5.2 – The lost power and particle percentages for each of the simulations calculated for the Doppler-shifted resonance synergetic RF-NBI heating scheme in W7-X.

The total collisional power density profiles, shown in figure 5.22, show significantly improved core heating power (normalised to total heating power) to the pure RF heating schemes described earlier. The profiles are also considerably improved in terms of depositing the majority of the power into the plasma core region, without significant off-axis heating as observed for NBI and pure RF heating scenarios. This illustrates the significantly improved performance of the Doppler-shifted resonance synergetic RF-NBI heating scheme, potentially enhancing core fusion reaction conditions in the W7-X device, and allowing fast particle confinement studies.

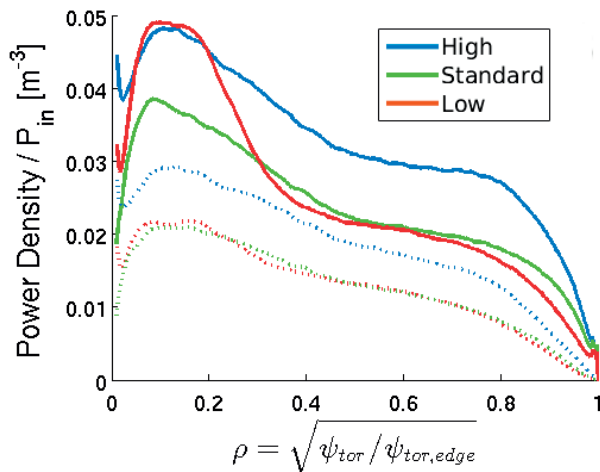


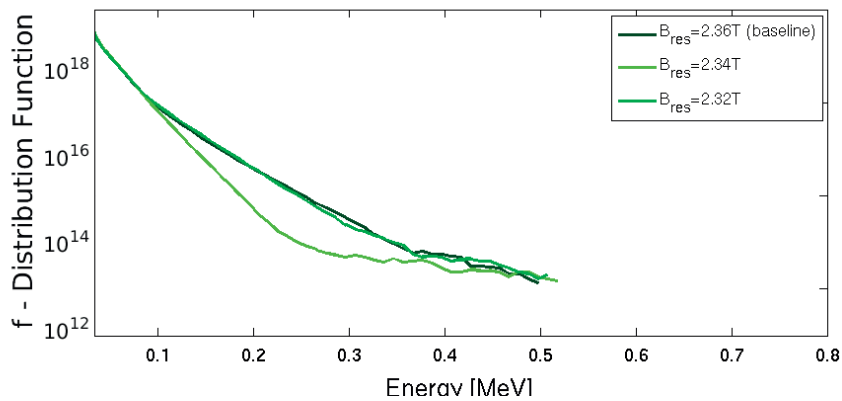
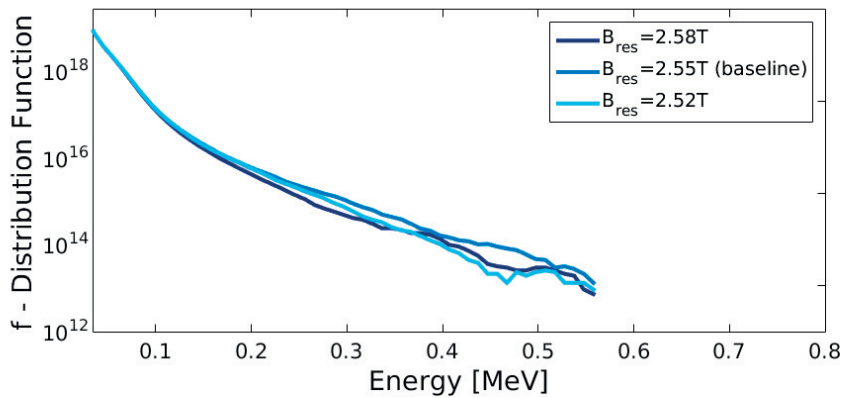
Figure 5.22 – Collisional power density to the background plasma, comparing the influence of the magnetic equilibrium. Dotted lines indicate power transferred to the background ions.  $P_{in} = 8.34\text{MW}$ .

### RF-Antenna Frequency Scan with the Dilution Method

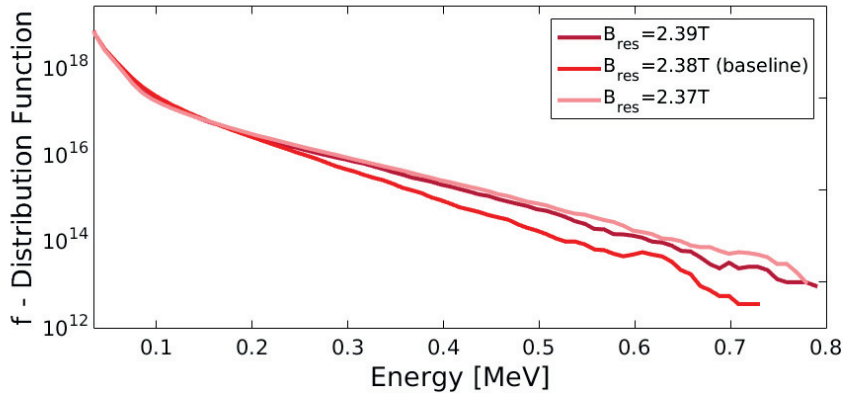
One of the known issues with ICRF is the experimental operational limits of the frequency range of the RF-antenna. In the JET tokamak, so called ‘sweet-spots’ are known for the antenna frequencies available, related to the permitted wave lengths possible to be transmitted along the transmission lines from the RF-field generators. The position of the resonant surface is typically fine-tuned by varying the axial magnetic field (at the same toroidal angle) due to RF-antenna frequency limitations. Due to secondary effects such as reflection of the RF-

## Chapter 5. Advanced Heating Schemes

wave in the plasma edge, limitations of the power supply, locations of edge ergodic surfaces, a certain degree of flexibility with respect to the RF-antenna is therefore required of ICRF heating schemes. In addition, we may not know the axial field prior to the experiment, since its value is determined by the plasma beta, toroidal curvature effects, etc. Hence, in this section the effects of small changes to the RF-antenna frequency are investigated. The influence of varying the RF-antenna frequency on the energy distribution is shown in figure 5.23. Large differences in the number of highly energetic population between the applied RF-antenna frequencies are observed for  $E > 0.1\text{MeV}$  for the  $B_{res} = 2.34\text{T}$  simulation in the standard mirror and  $E > 0.3\text{T}$  for the  $B_{res} = 2.38\text{T}$  simulation in the low mirror configuration. However, the value of the energy for the most energetic particle is still roughly the same for all equilibria. Further work is required in order to explain why these differences are present. It is necessary to perform a broader RF-antenna frequency scan to understand the extent to which this heating scheme is sensitive to this effect.



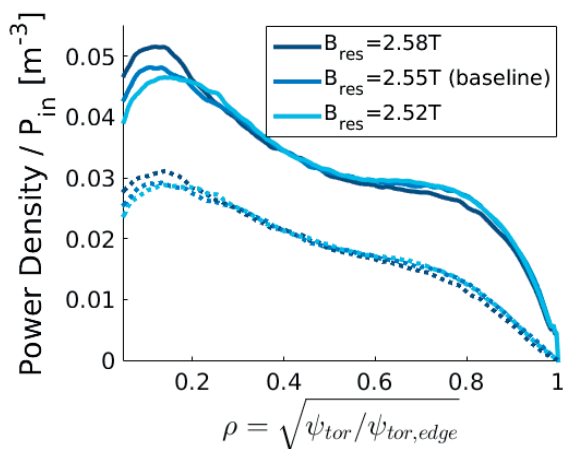




c)

Figure 5.23 – Particle distribution as a function of energy, comparing the influence of the RF-antenna frequency for the a) high, b) standard and c) low mirror configurations.

The influence of changing the RF-antenna frequency on the heating power transferred to the background plasma is less sensitive than for the production of highly energetic particle populations, reflected by figure 5.24. Compared to the NBI and pure RF heating scenarios presented previously in this thesis, the Doppler-shifted resonance heating synergetic RF-NBI scenario in the high mirror is predicted to be the best performing heating scheme for the plasma core region  $\rho < 0.25$ , and improvement compared to pure NBI occurs for all magnetic equilibria. In terms of the ion heating, the high mirror provides  $\sim 50\%$  larger core heating power than the standard or low mirror configurations. This is because of the improved energetic ion confinement. The electron heating is stronger for the low mirror configuration as compared to the high and standard equilibria. It is finally pointed out that the high mirror configuration is optimised for performance in high-beta plasmas for increased fusion reaction enhancement, such that improved heating properties in the high mirror equilibrium is particularly exciting.



a)

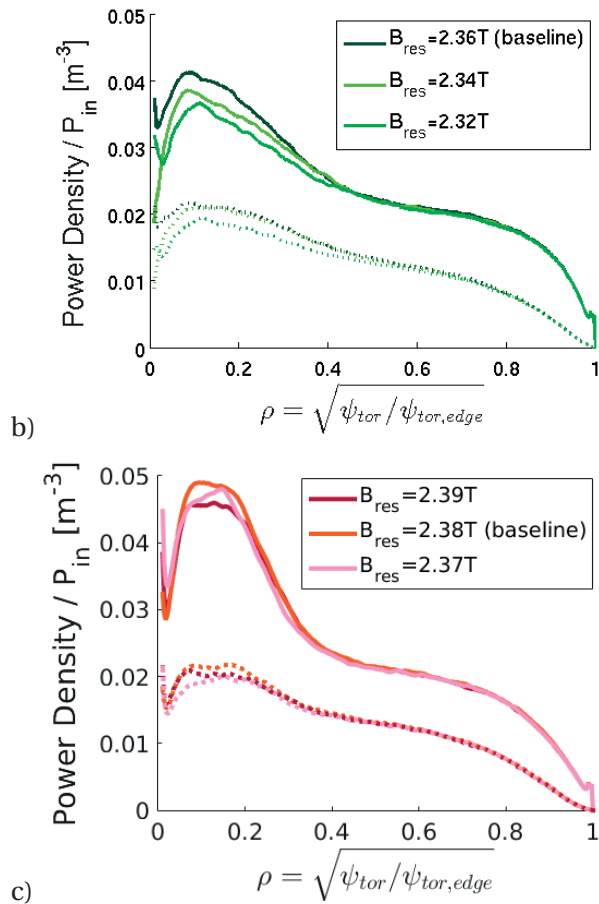


Figure 5.24 – Collisional power density to the background plasma, comparing the influence of the RF-antenna frequency for the a) high, b) standard and c) low mirror configurations. Dotted lines indicate power transferred to the background ions.  $P_{in} = 8.34\text{MW}$ .

### Convergence with the Dilution Method

In section 4.2.3, issues with the dilution method were presented, including an uncertainty on the convergence of the solution with respect to the density of thermal particles in time throughout the simulation. Figure 5.25 shows convergence in the total collisional power in time for both the high, standard and low mirror equilibria.

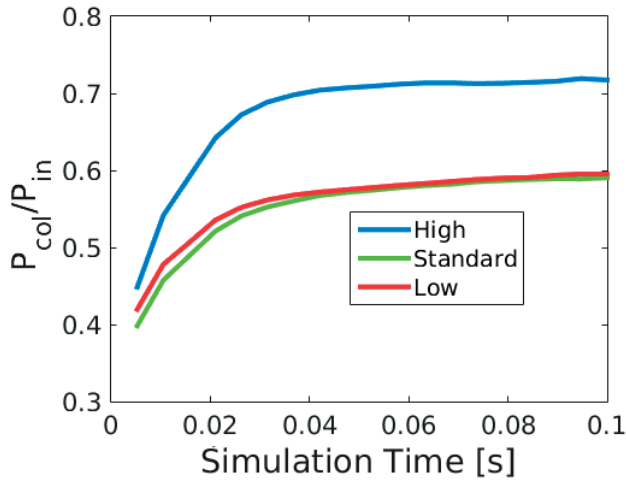


Figure 5.25 – Convergence of the total collisional power to the background plasma in time for the high, standard and low mirror equilibria, using the dilution method

The definition of convergence chosen for the dilution method is based upon two parameters: the collisional power in time and the NBI-only total density and pressure profiles. An additional scan to further increase the time of the simulation shows how the simulation time impacts not only the thermalised population, but the fast ion attributes too. Figure 5.26 shows the radial fast ion pressure and density profiles for increased simulation time, illustrating that using longer simulation times results in reduced fast ion pressure and density, as the thermalised hydrogen beam population is probably overestimated. The resulting core concentrations were 3.67, 5 and 6.67% for the simulation times 0.1, 0.2 and 0.3s respectively. Values of concentrations around 5% are probably much larger than those expected in the experiments.

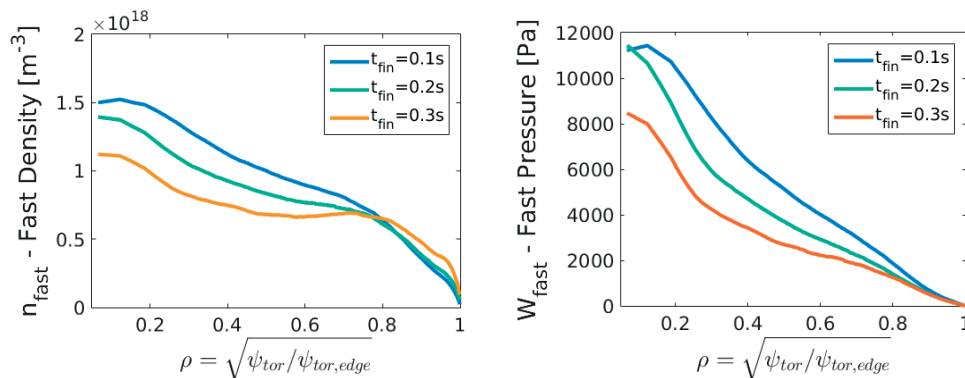


Figure 5.26 – Comparison of the fast ion ( $E > 5T_e$ ) density and pressure calculated using the dilution method for a variation of simulation duration times.

The particle distribution as a function of energy, shown in figure 5.27, illustrates a weak but visible effect of the simulation time on the production of highly energetic populations. As the dilution concentration increases the population of highly energetic particles decreases.

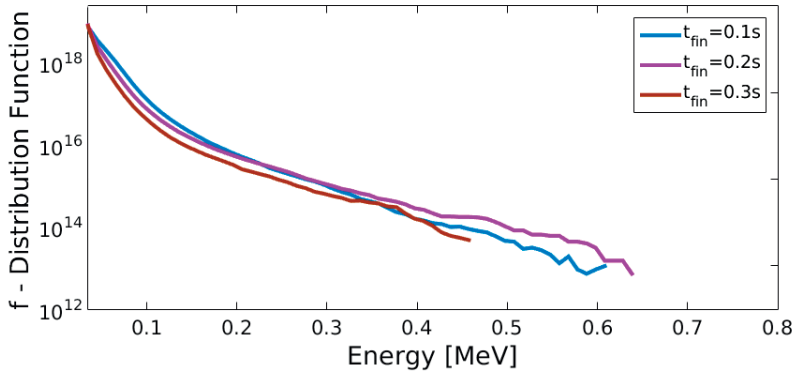


Figure 5.27 – Comparison of the particle distribution as a function of energy using the dilution method for a variation of simulation duration times.

The collisional power transferred to the background plasma is roughly the same for  $t_{fin} = 0.2$  and  $0.3s$ , both resulting in increased (overestimated) values near the plasma centre. This indicates that beyond a certain simulation time the variation in the numerical result decreases. With all this considered (i.e. the effect of simulation time on the results) we now investigate the alternative splitting method for W7-X.

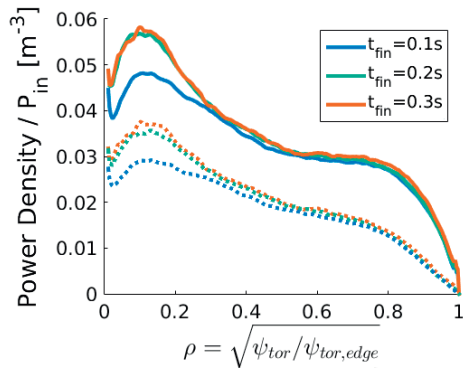


Figure 5.28 – Comparison of the normalised radial collisional power transfer using the dilution method for a variation of simulation duration times. Dotted lines reflect the collisional power transferred on the background ions.

### Fast-Splitting Method

As explained in section 4.2.3, transport of thermal ions is not accurately simulated in VENUS-LEVIS. By removing thermalised NBI particles from the simulation, such effects can be removed. Applying the fast-splitting method described in section 5.2.1, simulations are presented using the RF-antenna frequency corresponding to 2.38, 2.34 and 2.55T for the low, standard and high mirror equilibria respectively (same as chosen for the dilution method).

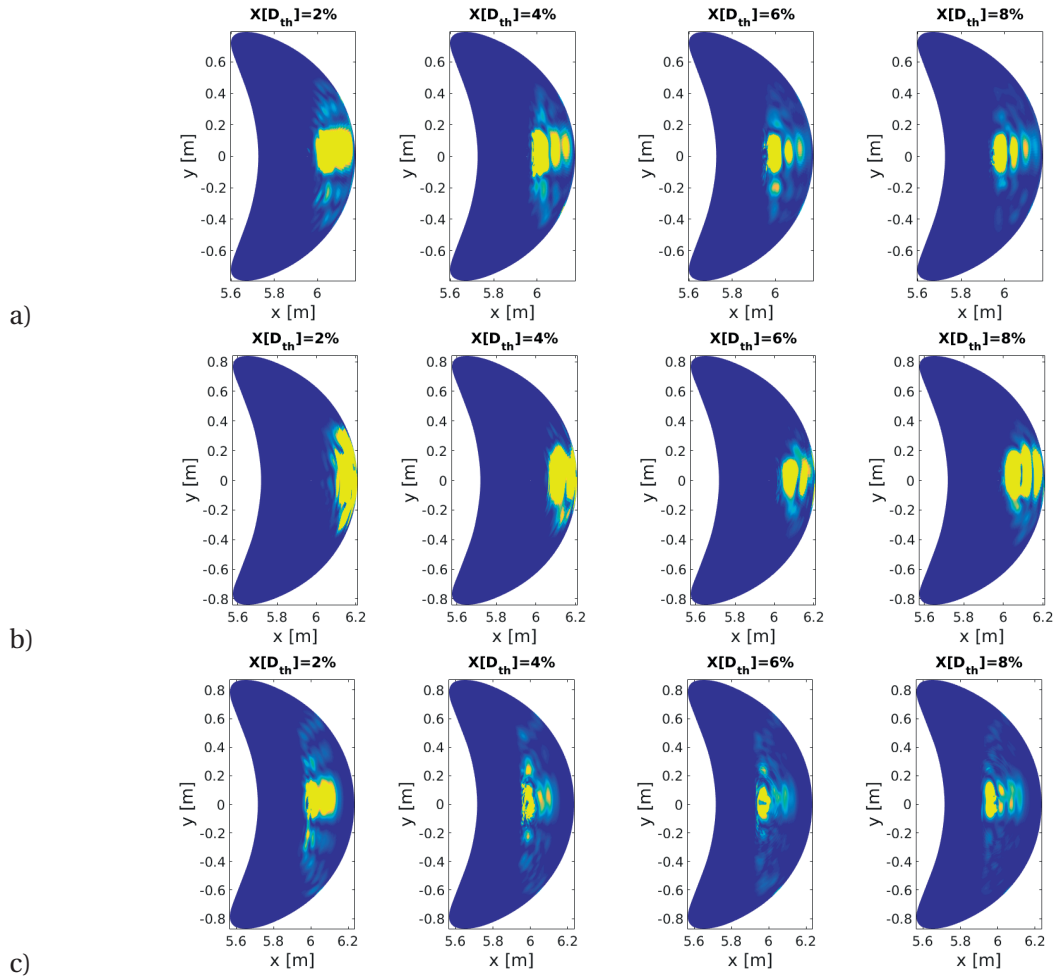


Figure 5.29 – Poloidal contour plots of the absorbed RF-power density from the LEMan wave code at  $\varphi = 0$  with varying background thermal beam species density of  $X[H_{th}] = 2, 4, 6, 8\%$  respectively: a) high, b) standard and c) low toroidal magnetic mirror configurations.

The variation of the background thermal beam species density significantly influences the radial absorbed power deposition, shown in figure 5.29. Optimisation of the wave polarisation is dictated by the L-cut-off shown in equation 2.2.10, which is significantly influenced by the density of the thermal beam species concentration. Larger concentrations tend to displace the L-cut-off further from the thermal beam species resonant surface. With the inclusion of the Doppler-shift for the beam species, there is an optimal concentration of the thermal beam species such that the associated resonant surface is located as close as possible to the L-cut-off layer where the polarisation is maximised. Figure 5.30 shows the total absorbed power density in the radial direction. The core values for the low and high mirror are significantly larger than for the standard mirror.

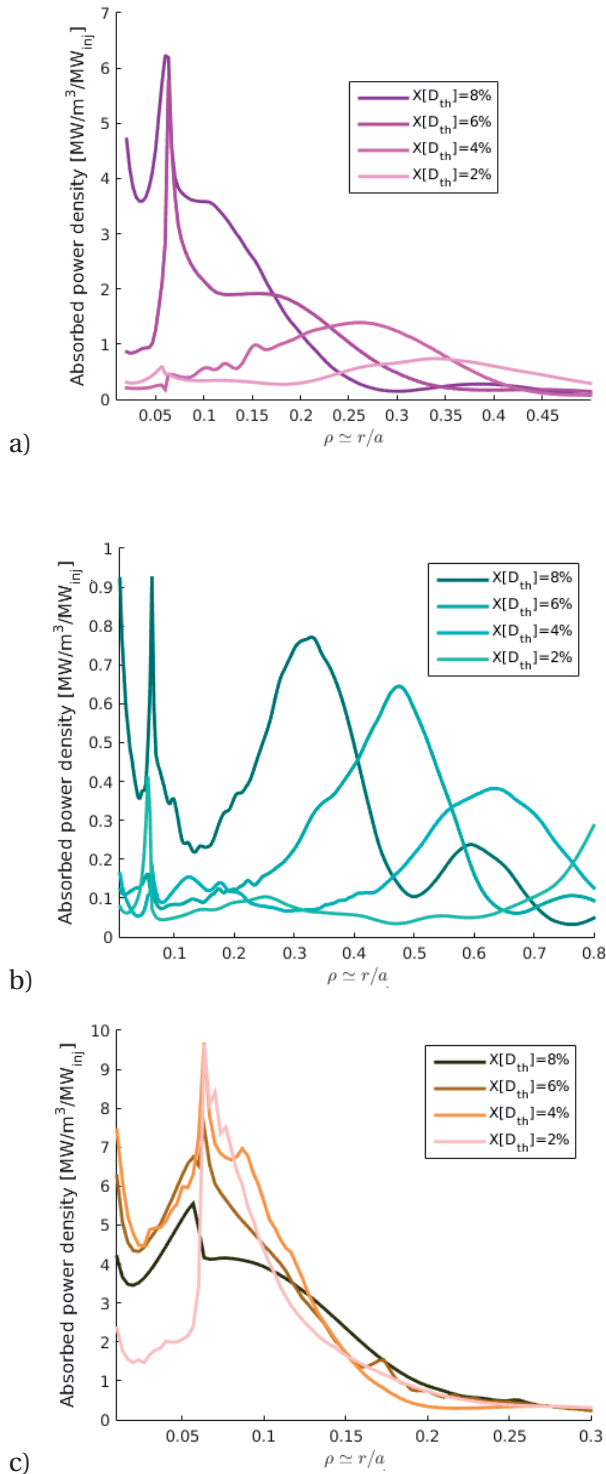
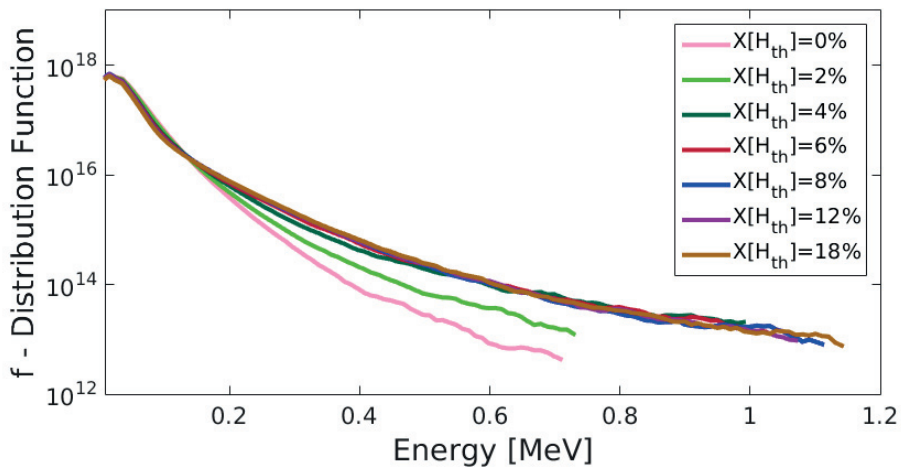


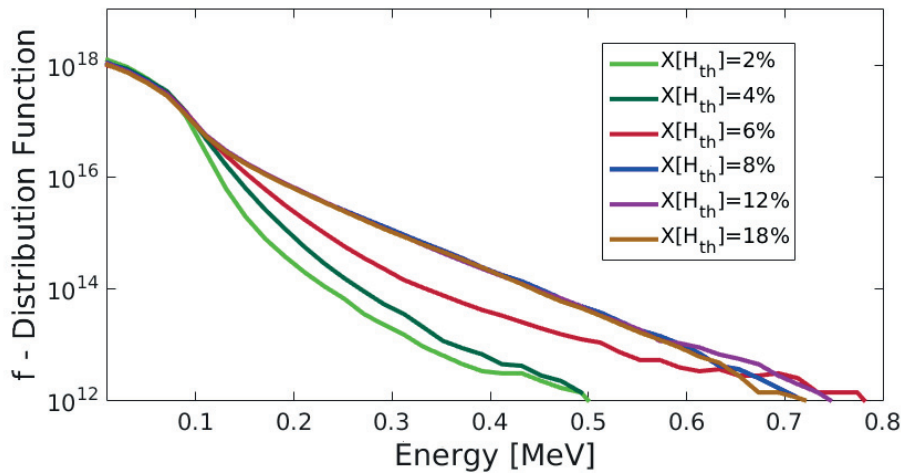
Figure 5.30 – Radial plots of the absorbed RF-power density from the LEMan wave code at  $\varphi = 0$  for the a) high, b) standard and c) low toroidal magnetic mirror configurations.

The energetic particle distributions for the high, standard and low mirror for the different ther-

mal beam species concentrations are given in figure 5.31. For all the magnetic configurations studied, the polarisation of the wave becomes more favourable for energetic particle production for large background thermal hydrogen densities. The particle distribution function seems to converge with respect to energy for thermal hydrogen values above  $X[D_{th}] \geq 8\%$  for all equilibria simulated. The benefit of more central RF-absorption for the  $X[D_{th}] \geq 8\%$  simulations is especially evident for the standard mirror case, shown in figure 5.31 (b), where a considerably larger highly energetic particle population is produced with energies up to  $\sim 0.8\text{MeV}$ . For the low mirror configuration, the splitting method predicts similar fast ion generation for all cases (except 2%), since the power absorption does not significantly vary. The improved confinement of NBI ions in the high mirror equilibrium is shown in figure 5.31 (a), as large concentrations of energetic particles are produced up to  $1.2\text{MeV}$ , considerably higher than for the standard or low mirror. The low mirror is similar to the standard mirror for particle energies below  $E < 0.2\text{MeV}$ . For  $E > 0.2\text{MeV}$ , the low mirror is the worst performing equilibrium due to the poor particle confinement of particles with large Larmor radii.



a)



b)

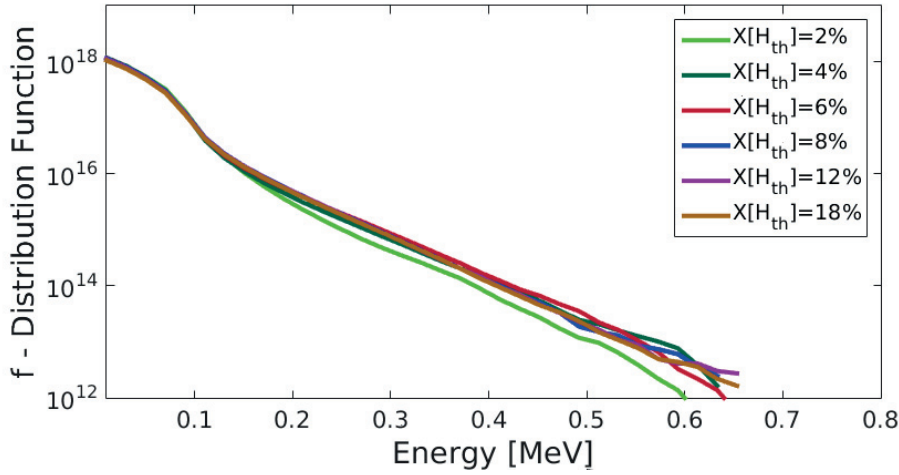
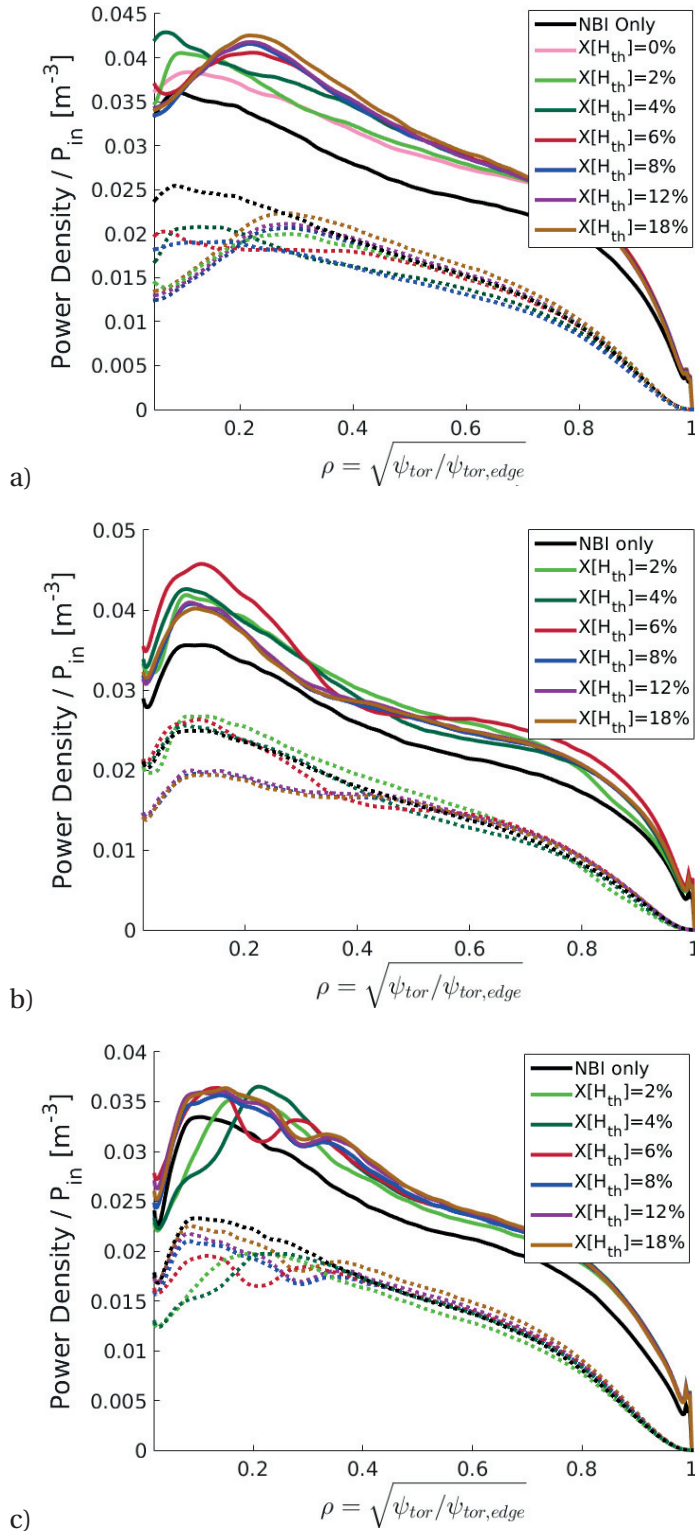


Figure 5.31 – Particle distribution as a function of energy, comparing the influence of the background thermal dilution concentration for the a) high, b) standard and c) low toroidal magnetic mirror configurations.

The collisional power transferred to the background from the synergetic RF-NBI heating scheme is shown in figure 5.32. For all equilibria, the normalised total heating power is increased in comparison with NBI only, noting that the NBI only plot is normalised with only 6.84MW of input power. This illustrates that the particle confinement must be increased with the addition of the ICRF, such that the confined particles remain in the plasma longer where their power is transferred over slowing down time-scales. The normalised heating power transferred to the electrons is increased for all equilibria for  $X[H_{th}] > 6\%$ , due to the reduced ion-beam collisionality at high energies. The variation of the background thermal density species concentration can be seen to converge for  $X[H_{th}] \geq 8\%$ . In the high mirror, low concentrations of thermal hydrogen result in improved on-axis collisional power transfer, which then moves off-axis for larger thermal concentrations. As illustrated by varying the antenna frequency in figure 5.24, this off-axis peaking is not associated with the location of the resonant layer but to the increased wave polarisation and the localisation of the RF-absorbed power peaking near the magnetic axis in front of the RF-antenna. As shown in figure 5.29, increasing the thermal hydrogen concentration leads to an increase in the focusing of the wave to become more localised in the equilibrium. This is due to the increase in wave-plasma absorption in the vicinity where the wave polarisation is maximised. For the low and standard mirror, the total collisional power is transferred in the core region due to the relative location of the resonant surface toroidally in the plasma near to the RF-antenna. The standard mirror has the largest collisional power transferred in the core for  $X[H_{th}] \leq 6\%$ , due to the reduced production of energetic ions that have a decreased collisionality with the background plasma. Unlike the high and standard mirror equilibria, the low mirror results in an improved collisional power transfer in the core for  $X[H_{th}] \geq 6\%$ . As the RF-resonant surface remains near the core for all toroidal angles, the wave polarisation and absorbed power is localised to the core region. This is not related to the concentration of energetic particles produced, which was found (see



figure 5.31) to converge for  $X[H_{th}] \geq 4\%$ .



## Chapter 5. Advanced Heating Schemes

Figure 5.32 – Collisional power density transferred from the slowing down NBI ions (with  $E > 1.5T_e$ ) to the background plasma, comparing the influence of the background thermal dilution concentration for the a) high, b) standard and c) low toroidal magnetic mirror configurations. Dashed lines indicate collisional power transferred to the ions and the solid black line represents the NBI only results (taken from figure 4.18). For the RF-NBI simulation  $P_{in} = 8.34\text{MW}$  and for the NBI only simulations  $P_{in} = 6.84\text{MW}$ .

### Convergence using the Fast-Splitting Method

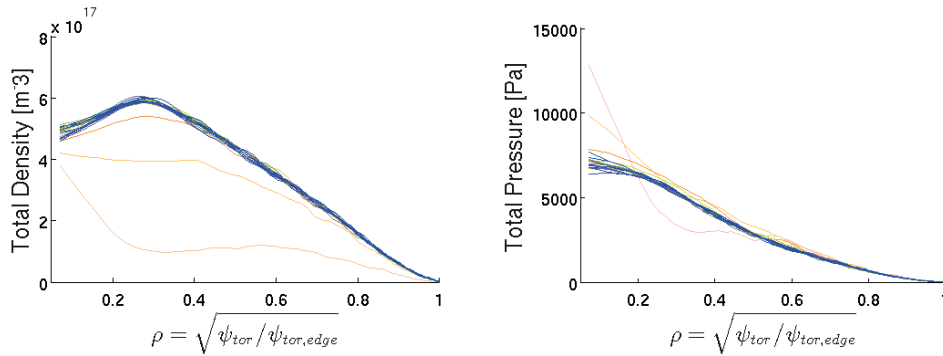


Figure 5.33 – Convergence in density and pressure for the fast-splitting method in the high mirror with  $X[D_{Th}] = 6\%$ . Lighter tone colours refer to earlier points in time during the simulation.

Figure 5.33 shows the convergence of the fast-splitting method for the total particle density and pressure of all the non-thermalised markers in the simulation, indicating good convergence in time.

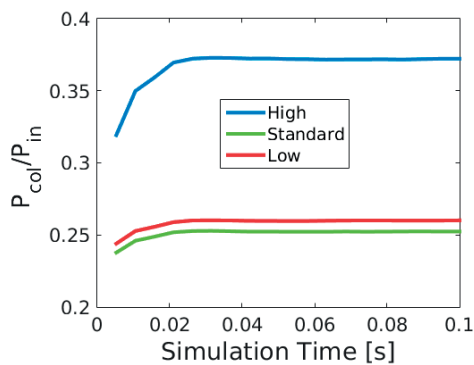


Figure 5.34 – Convergence of the total collisional power to the background plasma in time for the high, standard and low mirror equilibria, using the fast-splitting method.

The time evolution of the normalised total collisional power density is given in figure 5.34, also indicating a convergence of this method to simulate RF-NBI synergetic heating. Note that

the convergence of such simulations is faster than for the dilution method.

### Total Energy Distribution with the Fast Splitting Method

As mentioned previously, the fast-splitting method results in discontinuities due to the artificial removal of a background thermal population. Figure 5.35 shows the thermal and the background energy distributions used for the fast-splitting method applied to the high mirror configuration with  $X[D_{th}] = 4\%$ .

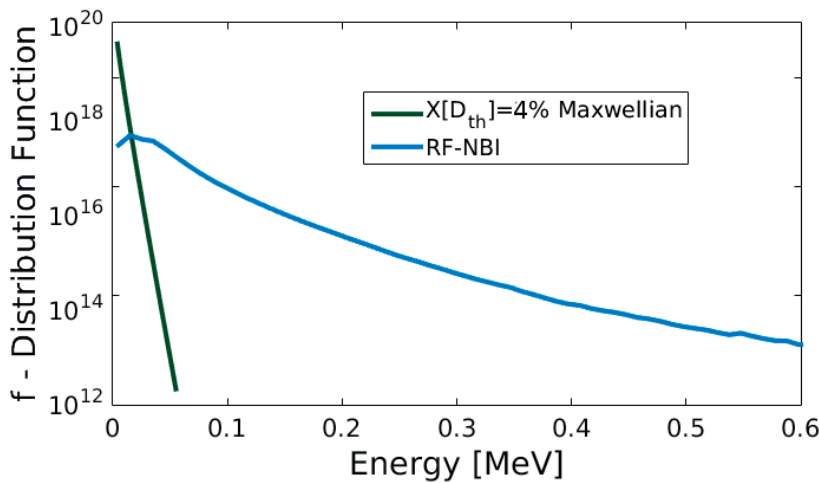


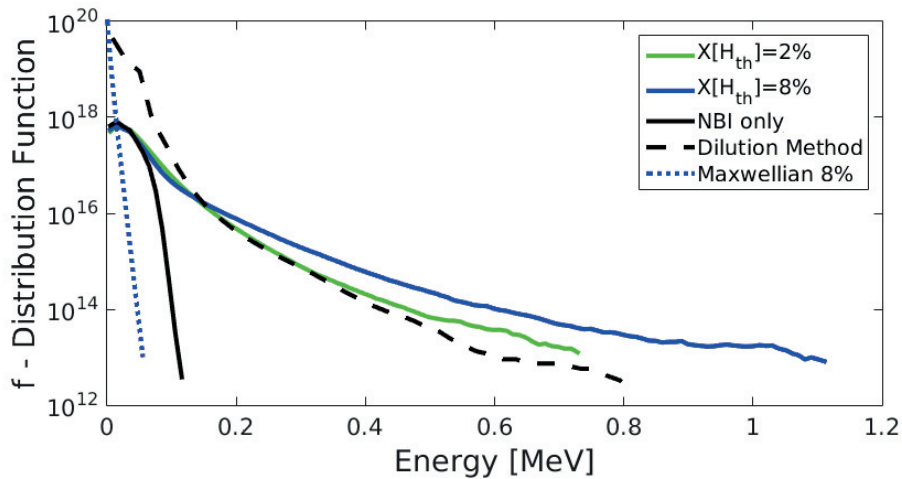
Figure 5.35 – The resulting particle distribution as a function of energy using the fast-splitting method in the high mirror equilibrium. This includes the background thermal density of 4% and the corresponding distribution of RF-heated slowing down NBI particles with such a background.

### Comparison of the Dilution and Fast Splitting Methods

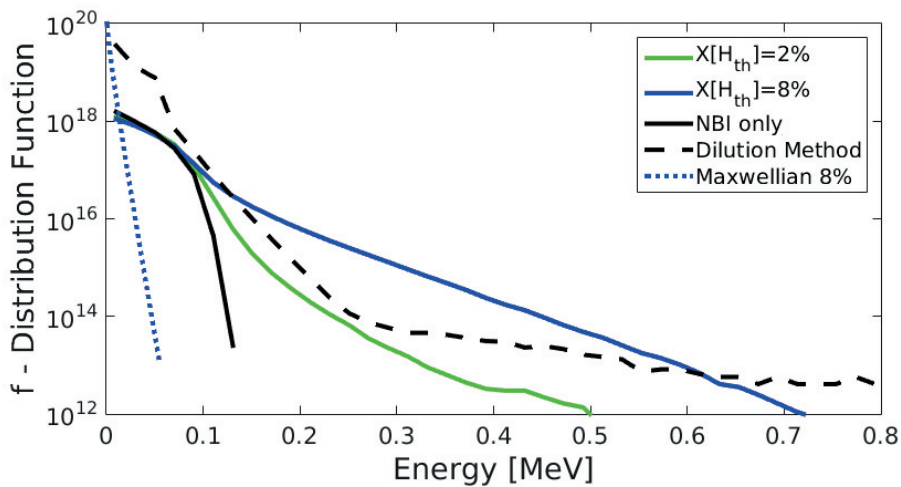
By comparing the dilution method with the fast splitting method for each equilibrium, shown in figure 5.36, the results illustrate that in the region of  $0 < E < 0.1\text{MeV}$ , the dilution method produces an increased number of energetic particles than the fast splitting method for all magnetic configurations studied. This is caused by the RF-acceleration of thermal particles that remain in the Fokker Planck calculation for the dilution method only. For a stronger comparison, the fast splitting method distribution function should also include a separate Fokker Planck calculation (using VENUS-LEVIS) of the RF-heating on the thermal hydrogen species. As shown in the JET simulations in section 5.2.2, the thermalised NBI particles are accelerated, but as the acceleration is predominantly in the perpendicular direction, these particles are easily lost from the system at energies that peak below 0.1MeV (evidence of this is shown in figure 5.21). With the inclusion of the thermal hydrogen resonance, the differences between the fast splitting and dilution method are expected to reduce. Comparison of the results using the fast-splitting and the dilution method show differences across the magnetic configuration. The large toroidal variation of the magnetic field strength in the high

## Chapter 5. Advanced Heating Schemes

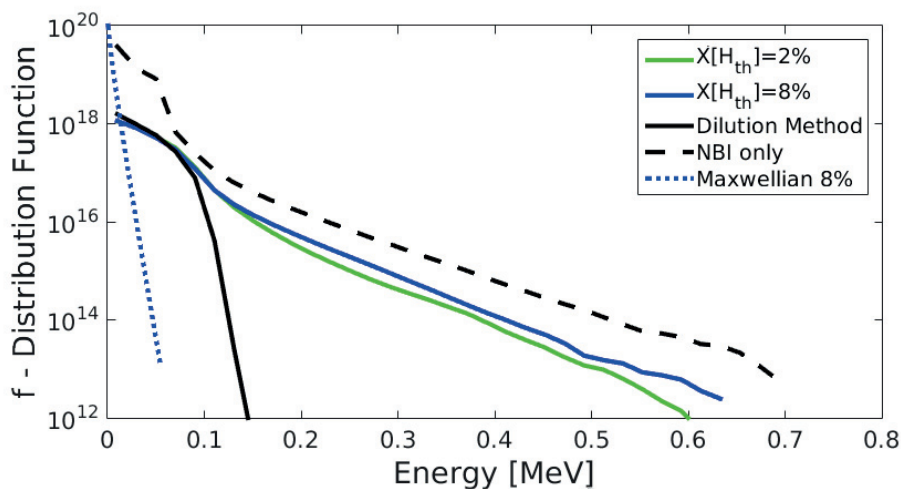
mirror results in an increased energy exchange between the wave and the thermal population, resulting in the dilution method predicting lower energy particles produced by the heating scheme. For the low mirror equilibrium, on the other hand, a larger population of freshly ionised NBI particles can resonate on-axis and thermal particles cannot absorb RF-power on axis, resulting in lower concentrations of highly energetic populations for the dilution method, as the QL energy kick is smaller due to the sharing of the RF-power between a larger population of resonant species.



a)



b)



c)

Figure 5.36 – Particle distribution as a function of energy, comparing the two different numerical methods for the calculation of synergetic RF-NBI synergetic heating: the dilution method and the fast splitting method (with  $X[H_{th}] = 2\%$  and  $8\%$ ) in the a) high, b) standard and c) low toroidal magnetic mirror configurations. The black solid line shows NBI only results, the dotted blue line from an analytical Maxwellian distribution function with  $X[H_{th}] = 8\%$ , and the black dashed line the results from the dilution method taken from figure 5.18.

As noted above, an advantage of the dilution method is that RF-resonance effects for thermalised ions are naturally included. These effects appear to be important. In addition, the distribution is continuous in all variables. The disadvantage of this method is that the thermalisation of the beam particle population leads to an accumulation of numerical markers in VENUS-LEVIS. This creates an issue with respect to the convergence of the simulation, which is determined when the thermal beam concentration matches the experimentally measured or predicted value. By retaining the thermalised beam ions in the simulation and using them as a definition for convergence, the dilution method also assumes that thermal particle transport is accurately calculated by the VENUS-LEVIS code. Unless neoclassical or anomalous transport effects are included, this assumption may not be valid, especially in W7-X equilibria. The fast splitting method assumes that the thermal beam population density and pressure takes the same form as the background plasma. However, with no accumulation of numerical markers, a convergence in NBI slowing down density and pressure is reached over multiple slowing down time-scales. The concentration of thermalised beam particles, however, is approximated by an analytical Maxwellian distribution with the same form as the majority background ion species. Unless the dilution concentration is known, a scan over thermalised beam concentrations is therefore required. Similarly, if using the dilution method, a scan of the simulation time would be required. Additionally, as particles with energy  $E < 1.5T_e$  are removed from the system with the fast splitting method, the particle distribution as a function of energy is discontinuous at thermal energies. The use of the two different methods appears to introduce either under or overestimations of the fast particle generation, depending on the magnetic configuration. With the inclusion of neoclassical transport in the dilution method, the thermal particles

would take the form of the background plasma profiles when no ICRH is applied. Therefore, to minimise the differences between the dilution and fast splitting method, VENUS-LEVIS could apply the predicted neoclassical transport coefficients that are calculated by codes such as DKES [19]. However, as VENUS-LEVIS simulations of W7-X equilibria do not currently include neoclassical or anomalous transport, the most appropriate method is stated to be the fast splitting method for stellarator equilibria where neoclassical transport influences strongly thermal particle motion.

### 5.3 Summary

Despite the 3-ion species heating scheme generating a population of highly energetic particles, the concentrations produced would be extremely difficult to detect experimentally. Additionally, as ICRF tends to heat particles predominantly in the perpendicular direction, hence producing highly anisotropic distributions, this heating scheme would not be entirely appropriate for alpha particle confinement studies. This is because alpha particles are generated isotropically in velocity space. Therefore, even with detectable energetic particle concentrations, the 3-ion species scheme would only produce particles that represent deeply trapped alpha particles. Furthermore, the populations of such energetic particle populations are so small that experimental detection would be difficult.

An alternative scheme referred to as the Doppler-shifted resonance synergetic RF-NBI heating has been explored. A mixture of QLO theory and numerical simulations indicates that this heating scheme can produce highly energetic ion populations that have more isotropic pitch-angle values than those of RF only heating methods. The Doppler-shifted resonance synergetic RF-NBI heating has been studied using two different approaches: the dilution and the fast splitting method. The Doppler shifted resonance synergetic RF-NBI (inverted) heating scheme (using deuterium NBI beams into hydrogen majority plasmas) was initially applied to the JET tokamak, using the dilution method, to study the basic physics of the scheme and to compare the results experimentally with the TOFOR diagnostic. The results show increased parallel velocity diffusion than the on-axis minority species heating scheme, and compare well to the experimental results. Simulations in W7-X, using hydrogen NBI beams in a helium-4 plasma (a standard or non-inverted scenario), for the low, standard and high mirror equilibria using both methods predict energetic particles in the MeV range ( $\sim 0.8 - 1.2\text{MeV}$ ). The sensitivity to the magnetic configuration is reduced as compared to scenarios with ICRF heating only. The core collisional power deposition predicted by the dilution method results in a significant improvement over the NBI and 3-ion species RF heating scenarios. Using this method also comparatively reduces the off-axis component present in all other heating schemes, providing more heating to the core region where the particle and energy confinement is improved. This synergetic RF-NBI heating scheme could be applied to W7-X to investigate alpha particle confinement or as a more effective plasma heating method than pure NBI or RF scenarios.

## 6 Conclusion and Outlook

Advancements in the understanding of ICRF and NBI heating have been made, permitting the optimisation and development of both standard and advanced heating schemes, in particular for 3D magnetic fusion devices. The SCENIC code package has been used to numerically calculate the 2D and 3D MHD ideal flux surface equilibria, the RF-wave propagation and absorption and the background plasma power transfer, fast ion generation, losses and transport in 3D magnetic equilibria. This chapter summarises the modifications to the SCENIC package and the results predicted for a range of heating schemes.

The first two chapters provide an introduction to tokamak and stellarator magnetic confinement fusion and the fast ion auxiliary heating methods: NBI and ICRF. By introducing the basic equations required to resolve such physics, the components of the SCENIC package are explained, demonstrating the numerical approach taken in the work.

Significant code modifications have been made to the SCENIC package, in particular the LEMan RF-wave code and the VENUS-NBI beam ionisation and deposition code. Chapter 3 explores the topic of ICRF and provides a more in-depth explanation of the relevant equations. Reflection and absorption of an RF-wave into a plasma is dictated by the dielectric tensor and the plasma dispersion relation. Updating the LEMan numerical calculation to include FLR effects results in more reliable power absorption calculations and permits the calculation of harmonic heating schemes, which was previously not possible in SCENIC. The perpendicular wave-vector  $k_{\perp}$  calculation by the LEMan code has been modified to be evaluated from the full hot plasma dispersion relation, as the full FLR order dielectric tensor contains and iterates over  $k_{\perp}$ , requiring a more accurate calculation of the wave that heats the resonant plasma species.

ICRF-only 2D tokamak calculations focus on the JET shot 92398, with a broad scan over variable plasma parameters. In terms of the wave propagation, the RF-power absorption is strongly dependent upon the species and concentration of the resonant species, influencing the power partition split between the electrons and the resonant species. If the resonant species has an integer multiple of the background majority charge-to-mass ratio, then sig-



## Chapter 6. Conclusion and Outlook

---

nificant RF-power can be absorbed via harmonic absorption. As shown by the scan in the RF-antenna frequency, parasitic harmonic absorption increases proportionally to the ion temperature at the resonance location, since this is an FLR effect. Maximal parasitic absorption results from on-axis resonance, yet maximal direct electron absorption is produced from HFS heating. The parallel wave-vector at the resonance is increased for an increased plasma current, which leads to an increase of RF-power in the core region. The presence of high-Z impurities was also shown to displace the mode-conversion layer, such that higher  $Z_{eff}$  leads to lower populations of energetic resonant ions. With respect to the production of highly energetic particles, lighter resonant species experience a lower collisionality with the background, leading to the generation of highly energetic particle populations. An increase in fast ion densities at high energies results in a larger collisional power transfer to the background electrons as compared to the ions. A higher plasma current is also the cause of reduced radial transport, resulting in larger energetic particle populations due to the increased confinement and concentration of resonant particles in the core. Increasing the RF-antenna power also increases the generation of highly energetic ions. Inclusion of high-Z impurities decreases the highly energetic particle population, due to higher plasma collisionality. The plasma heating power tends to be inversely proportional to the highly energetic particle population, as collisionality is reduced at higher energies. The anisotropy profiles were observed to be significantly dependent on the location of the resonant surface via modification of the RF-resonant surface in the major radius. Movement of the resonant surface causes different proportions of co and counter (to the magnetic field) passing and trapped particles in the plasma. The parasitic harmonic absorption was found to remain highly isotropic, resulting in very low concentrations of highly energetic particles. The radial collisional power deposition of the second harmonic parasitic deuterium heating is also dependent upon the amount of power absorbed from the RF-antenna.

The minority species heating scheme was also applied to 3D tokamak and stellarator geometries. Wave propagation and absorption studies have been made for the ITER tokamak in the presence of an internal kink-like long lived helical mode. The presence of this MHD mode results in a significant variation of the total RF-power absorbed in the core (by a factor of 4 depending on the location of the antenna relative to the phase of the kink). Results from the application of the minority species heating scheme to W7-X show low concentrations of fast ion particles due to the high collisionality of the background profiles. The radial profiles of the fast ion density, pressure and the collisional power density is very sensitive to the degree of toroidal magnetic mirroring, with large off-axis components. The best results were obtained with the low mirror configuration, but still  $E_{max} < 100\text{keV}$ .

Chapter 4 presents the calculations of the NBI ionisation and heating performance. Benchmarking of the ionisation and slowing down of the beam population compares well with other codes. The results are less sensitive to the toroidal magnetic mirror effect as compared to minority species RF heating. Improved particle and energy confinement is observed in the high mirror equilibrium. Due to the large, flat-top density profiles of W7-X, the majority of the



NBI ions ionise at the plasma edge, which results in  $\sim 10\%$  first and early orbit losses. With the volume effect of the flux surfaces, the pressure and density profiles are peaked on-axis. However, the collisional power transfer is comparably flat across flux surfaces with approximately equal electron and ion heating.

The development and investigation into advanced heating scenarios for W7-X is presented in chapter 5. The 3-ion species scheme uses extremely small concentrations (0.02% was simulated here) of a third species. The results indicate very low fast ion densities and pressures, with the generation of highly energetic particle populations sensitive to the toroidal magnetic mirror value of the magnetic flux surface equilibrium. Losses are large as pure RF-heating schemes preferentially heat resonant ions in the perpendicular direction, producing deeply trapped energetic particles which are then lost from the system. Only the low mirror configuration is shown to produce on-axis peaked collisional power transfer, with a significant part of the power transferred at the edge flux surfaces where the collisionality is larger. The second advanced fast ion auxiliary heating scheme explored is that of the Doppler-shifted resonance synergetic RF-NBI heating. Unlike the recent proof-of-principle JET experiments which used deuterium NBI ions in hydrogen plasmas, the proposed scenario for W7-X relies on hydrogen beam injection into helium-4 majority plasmas. The latter, being a non-inverted RF heating scheme, is expected to be less sensitive to the thermalised beam population than the inverted scheme tested in JET. For this scenario, at the RF-antenna toroidal location, the resonance occurs on-axis only for the freshly ionised beam particles, requiring an RF-antenna frequency for which the thermal beam species resonant surface is off-axis. This heating scheme produces energetic particle populations in the MeV range at concentrations two orders of magnitude larger than the 3-ion species scheme in W7-X. The results are significantly less sensitive to the equilibrium toroidal magnetic mirror term. The energetic particles produced are more isotropic in pitch-angle space because of the increase in parallel velocity diffusion specific to the Doppler shifted resonance synergetic RF-NBI heating scheme, which would be ideal for alpha particle confinement studies. The core heating power to the background plasma is significantly improved over pure-NBI heating, despite the larger lost power.

## 6.1 Outlook

In order to further advance the work presented in this thesis, several numerical updates should be implemented. For the ANIMEC code the magnetic flux surface equilibrium should be radially extended to include the plasma edge and first wall. Fast ion loss patterns and wall component heat loading should be evaluated. With this implementation, the RF-antenna could be numerically simulated to lie outside of the plasma LCFS in the LEMan code, which would lead to more accurate wave propagation and absorption calculation as well as RF wave-plasma coupling studies. Additional modifications to the LEMan code should include the implementation of the dielectric tensor for the fast ion population using the SCENIC zeroth order Vlasov Bi-Maxwellian distribution function. Allowing the calculation of self-consistent ICRF simulations with a full FLR dielectric tensor in the SCENIC package, which could be used

## Chapter 6. Conclusion and Outlook

---

for in-depth studies of higher harmonic RF-heating effects. The second W7-X RF-antenna is foreseen to heat plasma harmonics, with the update of the dielectric tensor, this could be calculated with LEMan. If a second W7-X antenna is installed, it might be tuned specifically for plasma harmonic heating. With the updates of the LEMan code presented in this thesis, the associated physics required in the dielectric tensor are now taken into account. The collisional operator of the VENUS-LEVIS code should also be updated (mentioned in 4.1.3) to include the displacement of the guiding centre. The toroidal mode family coupling approach described in section 3.5.2 could be used to more accurately calculate the RF-wave for ICRF simulations in VENUS-LEVIS. Currently, this must be accompanied by an increase in the number of numerical markers. This imposes serious memory requirements which currently cannot be met. Currently, the data file containing the RF-wave information for the QLO is currently stored on every MPI-task. For supercomputer nodes with 48 cores per node, this requires 48 copies of a file that is 32GB for a typical W7-X simulation. Utilising the shared memory MPI-3.0 modules would help to resolve such an issue.

To further explore the physics presented in this thesis, a particular emphasis should be made on some of the W7-X simulations. All W7-X work calculated in this thesis uses the same electron plasma density and pressure profiles. Sensitivity of the results to different profile shapes and impurity species should be evaluated. Additionally, inclusion of neoclassical flows into VENUS-LEVIS should be made such that the transport of thermal or particles with low collisionality corresponds to what is calculated in codes such as DKES [19]. The calculation of the parasitic harmonic and electron RF-power absorption should be made in future work, which should be calculated using the toroidal mode family stellarator antenna method described in section 3.5.2. With respect to the impurity concentrations, inclusion of 2-3% of carbon should be carried out in future SCENIC simulations of W7-X, which may influence the radial RF-power absorption profiles. A more extensive scan of the RF-antenna frequency should be evaluated for all ICRF heating schemes, for all magnetic mirror configurations. This is of particular importance in the default ICRF scheme: minority species heating. The Fokker-Planck evolution of the background majority ion distribution function from harmonic absorption of the RF-power should be calculated for the simulations of the minority species heating. One of the main challenges for harmonic heating in SCENIC is how to increase the marker resolution for low particle concentrations. Harmonic heating should also be simulated with a broad parameter scan in the JET tokamak, in order to optimise the performance also in 2D equilibria. Work on the ITER helical kink-like minority species heating should also be advanced to calculate the Fokker-Planck evolution of the minority species, to investigate the influence of the helical mode on the collisional power transfer and generation of energetic particle populations.

# Acknowledgements

Concerning the work done in this thesis, the first person I must acknowledge is Jojo. My vertically challenged friend of little patience, learning from you (both SCENIC and the French language) was not often pleasant. However, the work you did on the code was both outstanding and greatly under-appreciated. A great deal of this thesis was done thanks to you. After four years, as far as Anglo-French relations go, I admit that I might even consider you to be a friend.

To my supervisor Jon, I thank you for being so fair in your attitude to work. The support that you have given me over the four years will never be forgotten. In particular, towards the end of the thesis, the independence that you gave me and your confidence in my ability helped me to work hard and with confidence.

Many thanks to Dirk Van Eester, Ernesto Lerche, Thomas Johnson, Pablo Vallejos, Dani Gallart and Yevgen Kazakov for the lengthy discussions and taking the time to explain to me some of the intricacies of ICRF heating to me. It has been a true pleasure in working with all of you and I wish you all the best with your futures.

Every man must acknowledge the importance of their mother. In this respect I am extremely fortunate. Even having spent four years at EPFL, I have never met anyone so well-roundedly intelligent. You are a true source of inspiration, and there is nobody in this world that I respect more. To my papa, it was always important for me to hear your opinion on my life decisions so I could always do the opposite. A man of many fantastic traits, my favourite is your ability to encourage and install confidence in people to aim high and pursue their dreams. Your attitude to life and the way to treat and respect all human beings is something I truly admire. Jonny, over the years we have become increasingly close, and watching you get married was a proud moment of my life. Your never ceasing positivity and energy is a constant source of motivation. Rory, your curiosity in life is a flame that should never be extinguished, how fortunate you are to have such intense passions and interests, I'm sure you'll do something amazing with your future. Harry, when I started my thesis you were 14 years old... how you have changed! A cracking sense of humour and an eye for detail, I can't wait to see how your life unveils.

Des enormes bisous à tou-te-s mes potes de Lausanne. Umar, since the first night in the

## Acknowledgements

---

Great I knew I would be alright in Lausanne. You have been there through thick and thin. Heaven forbid I might have an Australian friend. Paola, senza di te, l'avrei sicuramente lasciato. Mi sei supportato quando non andava e ti ringrazio sempre. It has been fantastic being in the presence of someone so radiant with life and laughter. Oulfa, t'es quelqu'un clairement exceptionnelle et j'ai vraiment de la chance de te connaître. Intelligente dans toutes les senses, je sais pas comment t'es toujours autant modeste. Denys, je t'aime, mon chouchou. Sabine, la personne qui m'a appris cette langue, je me rappelle toujours des premiers tandems quand je captais rien. T'es quelqu'un très intelligente et fort d'esprit et je suis ravi de t'avoir dans ma vie. Pedro, you are a fantastic character full of passion and intensity, a person I empathise with enormously. I'm only sorry that you will clearly be deaf before the age of 40. Thanks to André for dealing with me in the office. The mixture of your kind heartedness and great sense of humour has been greatly appreciated. Andreia, t'es entrée dans ma vie vraiment au pire moment, mais comment ça m'a fait du bien ! Je vais jamais oublié toutes nos grasses matinées. Je me réjouis pour toutes les expériences qu'on partagera ensemble ! Je dois aussi remercier Jabir, Federico, Coralie, Alizée, Hugo, Davide, Laurie, Emmanuel, Sam Lanthaler, Carrie, Madhu, everyone else from the lab, mes amis d'Amnesty et d'UNIL Sans Frontières.

Finally, to Mayo, Aaron and Norrisey. We are all self-centred and brutal human beings that try desperately to live normal lives. Spending time hurling abuse at one-another and allowing the worst side of me to surface keeps the blood running in my veins. Thank God that you all exist. Jen, you have had the greatest influence on my life over the past decade, and what a special friendship we have formed, something I wish to cherish until my dying day. Thanks to Oly, Goodwin, Hickman, Ali, Chorr, Chatkinson, Chavier, Jo, Moran, Ryan, Josie, Lauren, Liam, John, Grandma, Granny Weed and Gar, and all my extended family and friends for your support.

# Bibliography

- [1] Y. Xu *Matter and Radiation at Extremes*, vol. 1, no. 4, pp. 192–200, 2016.
- [2] W. Cooper *et al. Comp. Phys. Comm.*, vol. 180, no. 9, pp. 1524–1533, 2009.
- [3] C. Beidler *et al. Nuc. Fus.*, vol. 51, no. 7, p. 076001, 2011.
- [4] S. Bingren, “A note on classification of icrf fast and slow waves,” tech. rep., 1999.
- [5] T. Stix, *Waves in plasmas*. Springer Science & Business Media, 1992.
- [6] N. Mellet *et al. Comp. Phys. Comm.*, vol. 182, p. 570, 2011.
- [7] R. Koch *Fusion science and technology*, vol. 45, no. 2T, pp. 183–192, 2004.
- [8] C. Boley *et al. Physical Review Letters*, vol. 52, no. 7, p. 534, 1984.
- [9] S. Suzuki *et al. Plasma Physics and Controlled Fusion*, vol. 40, no. 12, p. 2097, 1998.
- [10] T. Jones *et al. Fusion engineering and design*, vol. 47, no. 2-3, pp. 205–231, 1999.
- [11] D. Ćirić *et al. Fusion Engineering and Design*, vol. 86, no. 6-8, pp. 509–512, 2011.
- [12] P. McNeely *et al. Fusion Engineering and Design*, vol. 88, no. 6-8, pp. 1034–1037, 2013.
- [13] J. Wesson and D. Campbell, *Tokamaks*, vol. 149. Oxford University Press, 2011.
- [14] M. Albergante, “Interaction between fast ions and microturbulence in thermonuclear devices,” 2011.
- [15] D. Pfefferlé *et al. Comp. Phys. Comms.*, vol. 185, no. 12, pp. 3127 – 3140, 2014.
- [16] L. Eriksson and F. Porcelli *Plasma Physics and Controlled Fusion*, vol. 43, no. 4, p. R145, 2001.
- [17] C. Hsu and D. Sigmar *Physics of Fluids B: Plasma Physics*, vol. 4, no. 6, pp. 1492–1505, 1992.
- [18] W. Kernbichler *et al. Plasma and fusion research*, vol. 3, pp. S1061–S1061, 2008.
- [19] S. Hirshman *et al. Phys. Fluids*, vol. 29, no. 9, pp. 2951–2959, 1986.

## Bibliography

---

- [20] C. Kennel and F. Engelmann *The Physics of Fluids*, vol. 9, no. 12, pp. 2377–2388, 1966.
- [21] M. Jucker *et al.* *Plasma Physics and Controlled Fusion*, vol. 53, no. 5, p. 054010, 2011.
- [22] D. Swanson, *Plasma waves*. CRC Press, 2003.
- [23] W. Cooper *et al.* *Nuclear fusion*, vol. 46, no. 7, p. 683, 2006.
- [24] P. Popovich *et al.* *Fusion Science and Technology*, vol. 46, no. 2, pp. 342–347, 2004.
- [25] A. Walker, *Plasma waves in the magnetosphere*, vol. 24. Springer Science & Business Media, 2013.
- [26] B. Fried and S. Conte, *The plasma dispersion function: the Hilbert transform of the Gaussian*. Academic Press, 2015.
- [27] J. Hedin, J. Carlsson, T. Hellsten, and A. Jaun *Plasma physics and controlled fusion*, vol. 40, no. 6, p. 1085, 1998.
- [28] N. Mellet *et al.* *Computer Physics Communications*, vol. 182, no. 3, pp. 570–589, 2011.
- [29] D. Anderson *et al.* *The International Journal of Supercomputing Applications*, vol. 4, no. 3, pp. 34–47, 1990.
- [30] M. Brambilla *Plasma Physics and Controlled Fusion*, vol. 41, no. 1, p. 1, 1999.
- [31] T. Hellsten, T. Johnson, and P. Vallejos in *Journal of Physics: Conference Series*, vol. 561, p. 012010, IOP Publishing, 2014.
- [32] L. Eriksson, T. Hellsten, and U. Willén *Nuclear Fusion*, vol. 33, no. 7, p. 1037, 1993.
- [33] A. Boozer *The Physics of Fluids*, vol. 25, no. 3, 1982.
- [34] D. Van Eester and R. Koch *Plasma physics and controlled fusion*, vol. 40, no. 11, p. 1949, 1998.
- [35] H. Lütjens, A. Bondeson, and A. Roy *Computer Physics Communications*, vol. 69, no. 2, pp. 287 – 298, 1992.
- [36] L. Villard, K. Appert, R. Gruber, and J. Vaclavik *Computer Physics Reports*, vol. 4, no. 3-4, pp. 95–135, 1986.
- [37] J. Faustin, *Self-consistent interaction of fast particles and ICRF waves in 3D applications of fusion plasma devices*. PhD thesis, 2017.
- [38] T. Hellsten *et al.* *Nuclear Fusion*, vol. 44, no. 8, p. 892, 2004.
- [39] J. Graves *et al.* *Plasma Physics and Controlled Fusion*, vol. 57, no. 1, p. 014033, 2014.
- [40] M. Mantsinen *et al.* *Nuclear fusion*, vol. 40, no. 10, p. 1773, 2000.

- 
- [41] P. Lamalle *et al.* *Nuclear fusion*, vol. 46, no. 2, p. 391, 2006.
- [42] E. Jaeger *et al.* *Physics of Plasmas*, vol. 8, no. 5, pp. 1573–1583, 2001.
- [43] E. Jaeger *et al.* *Physics of Plasmas*, vol. 9, no. 5, pp. 1873–1881, 2002.
- [44] J. Ongena *et al.* *Physics of Plasmas*, vol. 21, no. 6, p. 061514, 2014.
- [45] A. Kaye *et al.* *Fusion Engineering and Design*, vol. 24, no. 1, pp. 1 – 21, 1994.
- [46] M. Goniche *et al.* *Plasma Physics and Controlled Fusion*, vol. 59, no. 5, p. 055001, 2017.
- [47] D. Gallart *et al.* *Nuclear Fusion*, 2018.
- [48] M. Mayoral *et al.* *Nuclear Fusion*, vol. 46, no. 7, p. S550, 2006.
- [49] J. Faustin *et al.* *Plasma Physics and Controlled Fusion*, vol. 58, no. 7, p. 074004, 2016.
- [50] A. Weller *et al.* *Physical review letters*, vol. 59, no. 20, p. 2303, 1987.
- [51] I. Chapman *et al.* *Nuclear Fusion*, vol. 50, no. 4, p. 045007, 2010.
- [52] C. Gormezano *et al.* *Plasma physics and controlled fusion*, vol. 46, no. 12B, p. B435, 2004.
- [53] C. Gormezano *et al.* *Nuclear Fusion*, vol. 47, no. 6, p. S285, 2007.
- [54] W. Cooper, J. Graves, and O. Sauter *Plasma Physics and Controlled Fusion*, vol. 53, no. 2, p. 024002, 2011.
- [55] D. Pfefferlé *et al.* *Nuclear Fusion*, vol. 54, no. 6, p. 064020, 2014.
- [56] J. Faustin *et al.* *Nuclear Fusion*, vol. 56, no. 9, p. 092006, 2016.
- [57] F. Nooruddin and G. Turk *IEEE Transactions on Visualization and Computer Graphics*, vol. 9, no. 2, pp. 191–205, 2003.
- [58] P. McNeely *et al.* *Fusion Engineering and Design*, vol. 88, no. 6-8, pp. 1034–1037, 2013.
- [59] R. Budny *et al.* *Nuclear Fusion*, vol. 32, no. 3, p. 429, 1992.
- [60] S. Äkäslompolo *et al.* *Nuclear Fusion*, vol. 58, no. 8, p. 082010, 2018.
- [61] H. Patten *et al.* *Plasma Physics and Controlled Fusion*, vol. 60, no. 8, 2018.
- [62] Y. O. Kazakov *et al.* *Nat. Phys.*, vol. 13, pp. 973–978, 2017.
- [63] E. Lerche *et al.* *Plasma Physics and Controlled Fusion*, vol. 51, no. 4, p. 044006, 2009.
- [64] J. Ongena *et al.* in *EPJ Web of Conferences*, vol. 157, p. 02006, EDP Sciences, 2017.
- [65] Y. O. Kazakov *et al.* *Nuc. Fus.*, vol. 55, p. 032001, 2015.
- [66] J. Faustin *et al.* *Plas. Phys. Contr. Fusion*, vol. 59, p. 084001, 2017.

## Bibliography

---

- [67] J. Eriksson *et al.* *Nuclear Fusion*, vol. 55, no. 12, p. 123026, 2015.
- [68] H. Kasahara, K. Saito, and T. Seki, “High harmonic fast wave heating and beam driven ion cyclotron emission behavior in the lhd,” tech. rep., National Inst. for Fusion Science, 2008.
- [69] A. Krasilnikov *et al.* *Plasma Physics and Controlled Fusion*, vol. 51, no. 4, p. 044005, 2009.
- [70] A. Fasoli *et al.* *Plasma Physics and Controlled Fusion*, vol. 52, no. 12, p. 124020, 2010.
- [71] C. Chang *et al.* *Physics of Fluids B: Plasma Physics*, vol. 2, no. 10, pp. 2383–2394, 1990.



---

## HAMISH PATTEN

Ch. de la Colline 6, Lausanne, CH 1007  
Nationality : British

+41788668983  
DOB : 14/09/1989

[hamish.patten@epfl.ch](mailto:hamish.patten@epfl.ch)

---

### SUMMARY

Computational physicist with strong problem solving and communication skills. Through numerical methods and experimental involvement, knowledge has been developed in numerical methods, theory of plasma physics and tokamak and stellarator magnetic confinement devices. Key strengths: scientific computing, code development, theoretical physics, science pedagogy and communication.

---

### EDUCATION

#### 2014-present PhD: Swiss Federal Institute of Technology (EPFL)

Theoretical and computational physics: “*Development and optimisation of advanced auxiliary ion heating schemes for 3D fusion plasma devices*”. The PhD involved development and application of the world-class SCENIC code package, used to simulate Ion Cyclotron Range of Frequency (ICRF) and Neutral Beam Injection (NBI) heating in 3D fusion plasma devices. This required a strong understanding of:

- **VENUS-LEVIS** - particle motion in 3D magnetic equilibria: Monte-Carlo algorithm, Quasi-Linear Operator, Particle-in-cell method, spline domain decomposition, Runge-Kutta time-evolution, Lagrangian mechanics.
- **LEMan** - Electromagnetic wave propagation and absorption in 3D magnetised plasmas: hot plasma dielectric tensor, finite element discretisation, large matrix inversion problems, Bessel function representation.

#### 2013-14 MSc Fusion Energy: Uni. of York - Distinction (thesis 78%)

Awarded a £5000 Scholarship for the MSc in Fusion Energy.

#### 2008-12 BSc & DIS: Loughborough Uni. - 1:1 (final year 84.5%)

£1000 merit-Based Scholarship provided by the Institute of Physics.

---

### ACADEMIC

- Member of Institute of Physics (IoP).
- Member of American Physical Society (APS).

#### [Publications - Peer Reviewed \(1<sup>st</sup> author | co-author\)](#)

H. Patten, *et al*, Plasma Physics and Controlled Fusion **60** 085009 (2018).

H. Patten, *et al*, Physical Review Letters, *submitted*.

H. Patten, *et al*, Computational Physics Communications, *in preparation*.

---

F. Casson, *et al*, Nuclear Fusion, *in preparation*.

W.A. Cooper, *et al*, Nuclear Fusion **58** 124002 (2018).

R. Dumont, *et al*, Nuclear Fusion **58** 082005 (2018).

J. Ongena, *et al*, EPJ Web of Conf. **157** 02006 (2017).

X. Litaudon, *et al*, Nuclear Fusion **57** 102001 (2017).

W. A. Cooper, *et al*, Plasma Physics Controlled Fusion **58** 064002 (2016).

W. A. Cooper, *et al*, Physics of Plasmas, **23** 040701 (2016).

---

### LANGUAGES

English (native), French (C1 level), Italian (B1 level).

---

### **Presentations - Invited**

- Workshop on Fast Ion Physics 22-23rd Jan. 2018, IPP-Greifswald, "Advanced Synergetic RF-NBI Heating in W7-X".
- Workshop on Fast Ion Physics 22-23rd Jan. 2018, IPP-Greifswald, "Finite Larmor Radius Effects in Hot Magnetised Plasmas".
- 643<sup>rd</sup> WE-Heraeus Seminar : Impact of 3D Magnetic Fields on Hot Plasmas, 22-24<sup>th</sup> May 2017, Physikzentrum Bad Honnef, "Interplay between stellarator magnetic topology and auxiliary heating schemes on fast particle confinement".
- EuroFusion Science Meeting : Simulations of fast ion generation and transport including 3D effects, 8<sup>th</sup> November 2017, CCFE Oxford, "Advanced RF-NBI synergetic heating in JET-ILW and W7-X for varied magnetic mirror equilibria".

---

### **COMPUTING**

Applying for time allocation as well as running simulations of millions of CPU hours on each of the world-class supercomputer facilities in Switzerland (CSCS), Italy (MARCONI), Japan (HELIOS) and Germany (IPP-Hydra), requiring MPI and OpenMP programming. Strong knowledge of scientific computing in Linux with a range of languages:

**Fortran, Matlab, Python, C++, MPI, OpenMP.**

---

### **WORK EXPERIENCE**

#### **2014-18 Teaching - Swiss Institute of Technology (6 semesters)**

Teaching assistant for 'Computational Physics' (In French).

#### **2013-14 Teaching and Marking - University of York (2 semesters)**

Teaching in the weekly seminar of 40 students in the modules 'Newtonian Mechanics', 'The Physics of Matter' and first year physics labs, as well as marking for 'Electrons in Solids'.

#### **2010-11 Finite Element Modelling - DSTL (1 year)**

Finite element modelling for applications to ballistics and vehicle armour.

---

### **VOLUNTEERING**

- **UNIL Sans Frontières : EPFL Liason Officer & Mentor (2017-18)**  
<https://www.asso-unil.ch/unilsansfrontieres/epfl-sans-frontieres/>  
Principal coordinator for EPFL.
- **Amnesty International UNIL : Treasurer (2017-18)**  
Also strongly involved in the sub-section 'Asylum and Migration'.
- **EVAM : General volunteer (2017-18)**  
Organisation of weekly activities with refugees and asylum seekers based in Lausanne, including music workshops, swimming and EPFL lab visits.
- **EPFL-FSB Running Club (2015-18)**  
Secured grants of over 5000CHF to subsidise and organise for the association members (~70 people) running events in Lausanne.

---

### **REFERENCES**

Dr. J. Graves Ecole Polytechnique Fédérale de Lausanne [jonathan.graves@epfl.ch](mailto:jonathan.graves@epfl.ch)  
Prof. A. Fasoli Ecole Polytechnique Fédérale de Lausanne [ambrogio.fasoli@epfl.ch](mailto:ambrogio.fasoli@epfl.ch)  
Prof. H. Wilson University of York [howard.wilson@york.ac.uk](mailto:howard.wilson@york.ac.uk)



